Studies on the Catalysis by New Solid Acid Catalysts and the Characterization(Dissertation_全文)

AUTHOR(S):

Yamamoto, Takashi

STUDIES ON THE CATALYSIS BY NEW SOLID ACID CATALYSTS AND THE CHARACTERIZATION

TAKASHI YAMAMOTO

1999

STUDIES ON THE CATALYSIS BY NEW SOLID ACID CATALYSTS AND THE CHARACTERIZATION

TAKASHI YAMAMOTO

DEPARTMENT OF MOLECULAR ENGINEERING
GRADUATE SCHOOL OF ENGINEERING
KYOTO UNIVERSITY

1999

Preface

The main themes of the present thesis are to clarify acidic property and the generation mechanism of some new solid acid catalysts. The present thesis consists of three parts. In the first part, acidic properties of siliceous FSM-16 were investigated. The second part describes acidic properties of silica-supported rare earth oxides and their structural characterizations. The generation mechanism has been proposed for a long time, but no one confirmed it. The last part is devoted to clarification of the role of Fe and Mn in Fe-, Mn-SO_4^{2-}/ZrO_2. SO_4^{2-}/ZrO_2, which promotes superacidic reactions at room temperature, is regarded as a promising catalyst in practice. Recently, it was reported that Fe and Mn promotion onto SO_4^{2-}/ZrO_2 enhances a catalytic activity of *n*-butane isomerization by three orders of magnitude, whereas the structures and roles of the promoters have not been clarified. As an appendix, the author applied X-ray absorption spectroscopy to characterize new-type homogeneous Lewis acid catalyst of ytterbium trifluoromethane-sulfonates.

The clue, which let the author start the series of investigations described in this thesis, is that he paid attention to the narrow pore-size distribution of mesoporous silica FSM-16 as a host of solid base particles. The original aim was to prepare homogeneous rare earth oxide particle inside the mesopore with narrow pore-size distribution, and to examine dependence of the particle size on "solid basicity". The author prepared mesoporous silica FSM-16 supported ytterbium oxide catalysts with various loading amounts; however, unexpected phenomena that siliceous FSM-16 itself enhances some acid-catalyzed reactions were found. Subsequently, specific acidic and structural characters were found on silica-supported ytterbium oxide catalysts. Therefore, the author focoused these new solid acid catalysts and investigated to clarify their acidic properties and the origins.

Catalytic processes are indispensable for modern chemical industry. Above all, the processes, to which catalyses by solid acids and bases are applied, occupy a special place. Petroleum, natural gas and coal are main resources for producing raw materials for almost all chemical products. To convert these resources, solid acid catalysts have been utilized in many important reactions such as cracking of hydrocarbons, conversion of methanol into hydrocarbons, isomerization, alkylation and acylation, oligomerization and polymerization, hydration and dehydration, hydrolysis and so forth. On the other hand, from the scientific point of view, chemistry of catalysis by solid acids and bases is considerably intriguing subject: developing new catalysts and catalysis systems, analyzing the states of catalysts and elucidating the new mechanisms and innovating the new catalysts and catalysis systems. Acid-base catalysis is always one of the main themes in International Congresses on Catalysis held every four years, and conferences on catalysis held somewhere in the world every year. Furthermore, a series of congresses focused on acid-base catalysis have been held every three years.

In 1795, Humphry Davy found that alcoholic vapor changed to other kind of a flammable gas over a heated natural clay. This phenomenon is one of the oldest discovery of catalysis by solids, and now is interpreted that ethanol was dehydrated to ethene over the clay.

A surface of solid material usually exhibits acid property. The first direct discovery of surface acid was reported by Kobayashi in 1901. Kobayashi found that the natural clay produced at Kita-Kabahara in Niigata Prefecture, Japan changed the blue color of wet Litmus paper to red. Natural clay minerals consist of mainly hydrated magnesium silicate and aluminosilicates, and the both are now generally accepted to be solid acids. The first solid acid catalyst industrially used on a large scale was activated natural clay, as a cracking catalyst in Houdry's process in 1936 (fixed-bed catalytic cracking; developed by Socony Vacuum Oil Co.). After 7 years, the moving-bed catalytic cracking process was developed by Socony Mobil Oil Company & Houdry Process Company. Almost at the same time, the first fluid catalytic cracking (FCC) process was realized by Standard Oil of Louisiana in 1942. In the cracking process, gasoline is produced from light oil distillates. Sulfuric acid-treated natural clay (mainly montmorillonite) was used for the first catalytic cracking process, however, iron impurity lowered selectivity to gasoline. It had already been known that co-precipitate of silica and alumina, and mixture of wet silica-gel and alumina-gel exhibit solid acidity. Then, amorphous silica-alumina (Al_2O_3; ca 14 wt%) catalyst was applied to the process in 1944. In 1954, Breck and Milton (Union Carbide Corp.) succeeded to synthesize A- and X-type zeolite; a family of crystalline aluminosilicates. Union Carbide Corp. and Socony Mobil Oil Co. reported in 1960 an excellent paraffin cracking ability of cation exchanged zeolite. In 1962, rare earth-exchanged hydrogen-Faujasite (RE-H-FAU) was firstly used for the cracking process by Socony Mobile Oil Company. This is an epoch-making progress in FCC processes because of highly superior of RE-H-FAU to amorphous silica-alumina in both activities and selectivities. And old type catalysts had been replaced by the zeolite-based catalysts. High performances of zeolite-catalysts drastically changed the facilities of catalytic cracking process as well. Since then, zeolite-based catalysts used for FCC process have been improved; to enhance selectivities, hydrothermal stability, stability to poisons such as SOx, Ni and V; to obtain high octane number; to decrease carbon-deposition.

Besides FCC catalysts, a large number of solid acids have been investigated and applied to industrial processes; *e.g.*, heteropoly acids, clay minerals, MFI-type zeolites, ion-exchange resins, metal sulfates and phosphates, sulfate-ion treated zirconia, mixed metal oxides, and so forth. On the other hands, generation mechanisms of the acidic properties have not been postulated, and many questions still remain unsolved. Even nowadays, novel solid acid catalysts have been found. The chemistry of solid acid catalyst has been in progress.

The present thesis is a summary of the author's studies on the catalysis and characterization of new solid acid catalysts, which have been carried out under the supervision of Professor Satohiro Yoshida at Department of Molecular Engineering, Graduate School of Engineering, Kyoto University during 1996-1999.

The author wishes to express his sincerest gratitude to Professor Satohiro Yoshida for his helpful guidance, valuable discussions and continual encouragement throughout this work. The author is deeply grateful to Professor Takuzo Funabiki for his instructive discussions and

heartily encouragement. Special acknowledgments should be made to Professor Tsunehiro Tanaka for his fruitful discussions and suggestions, helpful advises, continual encouragement. Thanks are made to Professor Sadao Hasegawa at Tokyo Gakugei University for the collaboration about Fe-, Mn-SO_4^{2-}/ZrO_2, which is described in Chapter 6. The author is owing to Professor Shu Kobayashi at Tokyo University and Dr. Tomoko Yoshida at Nagoya University for the collaboration and instructive discussions about $Yb(OTf)_3$ complexes, which is described in Chapter 7. Dr. Shinji Inagaki at Toyota Central R & D Labs., Inc. is acknowledged for his useful and lively discussions about FSM-16, and elemental analysis. The author is delightful to express his thanks to Dr. Ryuichiro Ohnishi at Hokkaido University for his helpful advises for carrying out α-pinene isomerization. Heartily thanks are made to Professor Masaharu Nomura at High Energy Accelerator Research Organization for the advise for recording XAFS spectra and to the staffs of Photon Factory at KEK for making the beam line available. Acknowledgments are made to Drs. Tomoya Uruga and Hajime Tanida at SPring-8 for their technical assistances for XAFS spectra measurements. The author would like to express his gratitude to the staffs at SPring-8 and the members of Broad Energy Band XAFS (BEB-XAFS; Drs. Shuichi Emura, Makoto Harada, Yoshiyuki Nakata, Masao Takahashi at Osaka University, Hidekazu Kimura at NEC, Osamu Kamishima, Yoshihiro Kubozono, Hironobu Maeda at Okayama University, and Yasuo Nishihata at JAERI) for making the beamline BL01B1 at SPring-8 available.

The author is deeply grateful to Mr. Takahiro Matsuyama for his collaboration and instructive discussions about supported rare-earth oxide catalysts, which are described in Chapters 3, 4, 5. Professor Hiromi Yamashita at Osaka Prefecture University, Drs. Yasuo Nishimura at Osaka National Research Institute, and Hisao Yoshida at Nagoya University are acknowledged for useful discussions and hearty encouragement. Thanks are made to Drs. Hirofumi Aritani at Kyoto Institute of Technology for his lively discussions and computational assistance, and Sakae Takenaka at Tokyo Institute of Technology for his useful discussions and assistance for measurements of FTIR, Raman and XAFS spectra, and glass work of apparatus. The author acknowledges Messrs. Yoshiumi Kohno for his fruitful discussions and computational assistance, and Ryoji Kuma for his assistance with TPD measurements. Thanks must be made to Secretary Miss Akiko Nakano for her kind official support. The author is indebted to all the members of the group of catalysis research led by Professor Yoshida.

Finally, the author would like to thank his parents, Masao and Kyoko, his grand mother Matsue, and his brothers Hiroshi and Takahiro for their understanding and encouragement.

Takashi Yamamoto

Kyoto,
June, 1999

CONTENTS

General Introduction

History of Acid and Base [1-6]

Since ancient times, catalysis itself has been familiar with the life of human kinds. Without special consciousness, people had been making use of catalyses for brewage of alcoholic beverages, vinegars and so forth. Catalyses began to be utilized on purpose in the early 13th century, and diethylether synthesis from ethanol had been carried out with sulfuric acid. In 1781, Parmentier found that starch decomposes to glucose by inorganic acids in those days. The first man that recognized the "catalysis" from a scientific point of view is Kirchhof. In 1811, he found that starch in heated water decomposes to sugars by addition of inorganic acids, whereas the inorganic acids remain unchanged. The word of "catalysis" was firstly proposed by J. J. Berzelius in 1836. W. Ostwald defined an improved definition about catalysis in 1901, *i.e.*, a catalyst is substance that never appears on the final products in a chemical reaction, but changes the reaction rate. So far, the concept proposed by Ostwald is recognized as the definition of catalyst.

The history of chemistry began with alchemy in medieval times of Europe. Accompanied by alchemy, chemistry about acid-base had improved because alchemists tried to alchemize common metals to gold, and inorganic acids were used to separate mixed metals. In the early 15th century, B. Valentinus firstly succeeded in fractional precipitation of metal ions with acids and bases, and detected iron in tin, copper in iron, silver in copper, and gold in silver. In the early 16th century, G. Agricola achieved to separate a mixture of gold and silver with nitric acid. Until the middle 17th century, character of acid had been recognized as follows; it tastes sour, is water soluble, and exhibits high solvation ability. In 1663, R. Boyle found that blue color of litmus paper changes to red by acids, and confirmed heat of neutralization. In 1774, Raoult first proposed a definition of bases. The proposed concept was that a base is a matter which produces a salt with an acid. H. Cavendish assumed a concept of equilibrium relationship among acids and bases in 1766. W. Lewis utilized plant pigments as acid-base indicators in the middle of 18th century. From 17th through late 19th century, many concepts about acid-base and their origins had been proposed by many scientists. A. L. Lavoisier named the substance, which was called as flame air (Feuerluft), as oxygen in 18th century, and insisted that oxygen is the origin of all acids. On the other hand, P. L. Dulong insisted that hydrogen is the common source of all acids, because hydrochloric acid had been proved to be non-oxygen acid by H. Davy. J. L. Gay-Lussac and P. L. Dulong newly proposed two kinds of acid-concepts in the early 18th century; one is oxygen-acid, the other is hydrogen-acids. The refined concept was proposed by J. Liebig in 1838. He stated as follows; acids are compounds containing hydrogen atoms, which could be replaced by metal ions. S. A. Arrhenius proposed a theory of electrolytic dissociation in 1886, and furthermore an ionic

theory and ionic product in 1887. This ionic theory is defined as that an acid dissociates to proton and acid residue, and a base dissociates to hydroxide ion and metal ion in aqueous solution. In 1888, W. Ostwald established the dilution law, by which strengths of many weak acids and bases can be determined. Then a concept of pH was introduced by S. P. L. Sørensen in 1909. However, these concepts were restricted within aqueous solution system, and could not apply to non-aqueous solution systems.

The memorial year about acid-base is 1923 when two important definitions were proposed. T. M. Lowry and J. N. Brønsted proposed independently a new acid-base definition; acids are substances that release proton, and bases are ones that accommodate proton. However, this new definition by Lowry-Brønsted could not explain the acidity of well-known acidic compounds such as of $SOCl_2$, $AlCl_3$, SO_3, BF_3 and so forth. Another definition was proposed by G. N. Lewis. According to his definition, acids shall accept a lone electron pair, and bases shall donate a lone electron pair. This definition includes the definition proposed by Lowry and Brønsted. After 1923, some definitions have been proposed. A definition proposed by H. Lux in 1939 was one focusing on donor-acceptor of O^{2-}. In 1947, H. Flood and T. Förland expanded the definition proposed by Lux. The Lux-Flood definition is often applied to molten salts and oxides, *i.e.*, acid acts as network former and base acts as network modifier.

At the present time, two acid-base definitions proposed by Lowry-Brønsted and Lewis are utilized for explanation acid-base phenomena. The Lewis's definition includes that of Lowry-Brønsted. All Brønsted base sites are also Lewis base sites. In a field of catalysis, a clarification of acid-base site is judged whether the corresponding site transfers a proton or an electron pair. Now, these two definitions used to make use of together in almost all cases.

Solid Acid and Acidity

Since Benesi measured acid strengths of many clays and cracking catalysts with Hammett indicators in 1956, Hammett function (H_0) and Hammett indicators have been utilized to evaluate acid strength and the distribution of solid acids (acidity), the method of which was established by Benesi.[7-9] The acid strength of a solid surface is defined as an ability of the surface to convert an adsorbed neutral base into its conjugate acid, quantitatively expressed by Hammett and Derup's H_0 function.[10] If a reaction proceeds by means of proton transfer from the surface to the adsorbate, the acid strength is expressed by H_0,

$$H_0 \equiv -\log \frac{a_{H^+} f_B}{f_{BH^+}} \qquad \text{or} \qquad H_0 = pK_a + \log[B] / [BH^+]$$

where a_{H^+} is the activity of proton [B] and [BH^+] are respectively the concentrations of neutral base (basic indicator) and its conjugate acid and, and f_B and f_{BH^+} the corresponding activity

coefficients. If a reaction takes place by means of electron pair transfer from the adsorbate to the surface, H_0 is expressed by

$$H_0 \equiv -\log \frac{a_A f_B}{f_{AB}} \qquad \text{or} \qquad H_0 = pK_a + \log[B]/[AB]$$

where a_A is the activity of a Lewis acid or electron pair acceptor, [AB] is the concentration of neutral base coupled with electron acceptor A.[11] The indicators used for a determination of acid strengths and amounts are listed in Table 1. The amounts of acid sites on a solid surface could be estimated by amine titration after determination of acid strength. For a titrant, *n*-buthylamine is recommended. Combining with Hammett indicators and amine titration method, the acid strength distribution of a solid surface could be evaluated.[12]

After Hammett and Derup proposed H_0 function for homogeneous systems in 1932, Hauser and Leggett observed a color reaction on aluminosilicate minerals attendant upon adsorption of various substances.[13] Weil-Malherbe and Weiss firstly recognized such the color reactions on aluminosilicates as phenomena related to acid.[14] The first scientist that expressed surface of solid with H_0 function is Walling.[11] Walling evaluated surface properties of some inorganic compounds besides aluminosilicates, and found that metal sulfates such as copper(II) and iron(III) exhibit solid acidity. Tamele performed a quantitative analysis of acid sites of alumina-silica cracking catalyst with *n*-buthylamine, using *p*-dimethylaminoazobenzene as an indicator. He found a linear relationship between catalytic activity for propylene polymerization and the number of acid sites.[15,16]

Nowadays, the estimation of acidity on catalyst surfaces has been widely performed with Hammett indicators and amine-titration method. However, some limitations and problems about these techniques are pointed out.[17] One problem is the difficulty to determine a point where the protonation equilibrium of an indicator attains. The most serious problem is the fact that it takes a very long time to achieve equilibrium, and it is rarely achieved. Both of them result in the wrong estimation of the number of corresponding acid sites.[18,19] Other serious problem is the possibility that the color arising from an acid form is produced by surface sites which are not catalycally active. For example, the evaluated maximum acid strengths with Hammett indicator were H_0 = -12.7 [20] or -14.52 [21] for ZrO_2. The evaluated acid strength of ZrO_2 is enough to catalyze *n*-butane skeletal isomerization, however, the reaction is never promoted. Although SO_4^{2-}/ZrO_2 is truly super-acid which catalyzes *n*-butane isomerization at room temperature, some spectroscopic characterizations indicate that the real maximum acid strength of SO_4^{2-}/ZrO_2 is comparable to that of HY [22] or 100% H_2SO_4.[23] Nevertheless the evaluated acid strength of SO_4^{2-}/ZrO_2 was H_0 = -16.04.[24] There are some limitations and exceptions for applying Hammett indicator to determine acid strength on solids. However, Hammett indicators still play an important role to characterize acid properties of solids combining with other characterizing methods, especially in qualitative analysis.

TABLE 1. Basic Indicators Used for the Measurement of Acid Strength

Indicators	Color		pK_a	Equivalent
	Base-form	Acid-form		(H_2SO_4) %
Neutral red	yellow	red	+6.8	8×10^{-8}
Methyl red	yellow	red	+4.8	
Phenylazonaphthylamine	yellow	red	+4.0	5×10^{-5}
p-(Dimethylamino)azobenezene	yellow	red	+3.3	3×10^{-4}
2-Amino-5-azotoluene	yellow	red	+2.0	5×10^{-3}
Benzeneazodiphenylamine	yellow	purple	+1.5	2×10^{-2}
Crystal violet	blue	yellow	+0.8	0.1
p-Nitrobenzeneazo(p'-nitro-diphenylamine)	orange	purple	+0.43	
Dicinnamalacetone	yellow	red	-3.0	48
Benzalacetophenone	colorless	yellow	-5.6	71
Anthraquinone	colorless	yellow	-8.2	90
2,4,6-Trinitroaniline	colorless	yellow	-10.10	98
p-Nitrotoluene	colorless	yellow	-11.35	
(100 % H_2SO_4)	-	-	-11.93	100
m-Nitrotoluene	colorless	yellow	-11.99	
p-Nitrofluorobenzene	colorless	yellow	-12.44	
m-Nitrochlorobenzene	colorless	yellow	-13.16	
2,4-Dinitrotoluene	colorless	yellow	-13.75	
2,4-Dinitrofluorobenzene	colorless	yellow	-14.52	
1,3,5-Trinitrotoluene	colorless	yellow	-16.04	

Novel Solid Acid Catalyst

Discovery of new catalysts and new reactions are desired at all times. A large number of various soild-acid catalysts are used for more than 100 industrial processes.[25] ZSM-5 and sulfated zirconia (SO_4^{2-}/ZrO_2) are representatives of the greatest discovery of solid acid catalysts in recent years. ZSM-5 is practically utilized and has replaced with other conventional catalysts. SO_4^{2-}/ZrO_2 is regarded as a promising catalyst in practice. In 1990s', there are plenty of reports about newly prepared catalysts and/or materials. The author believes that the most excellent discovery (preparation) of catalyst in 1990s' is mesoporous silica such as MCM-41 and FSM-16. The materials possess a variety of availability.

References

1 Tanabe, K.; Takeshita, T. *Acid-Base Catalysis*, Sangyo Tosho, Tokyo, 1966.

2 Tanabe, K. *Solid Acids and Bases*, Kodansha, Tokyo, 1970.

3 Tanabe, K. *Shokubai no Hataraki*, Kagaku Dojin, Kyoto, 1988.

4 Ohki, M.; Tanaka, M. *San Enki to Sanka Kangen*, Iwanami, Tokyo, 1979.

5 Keii, T. *Shokubai Kagaku*, Tokyo Kagaku Dojin, Tokyo, 1981.

6 Ohnishi, T. *Shokubai*, Dai Nihon Tosho, Tokyo, 1987.

7 Benesi, H. A. *J. Am. Chem. Soc.*, **1956**, *78*, 5490.

8 Benesi, H. A. *J. Phys. Chem.*, **1957**, *61*, 970.

9 Benesi, H. A.; Winquist, B. H. C. *Adv. Catal.*, **1978**, *27*, 97.

10 Hammett, L. P.; Deyrup, A. J. *J. Am. Chem. Soc.*, **1932**, *54*, 2721.

11 Walling, C. *J. Am. Chem. Soc.*, **1950**, *72*, 1164.

12 Tanabe, K.; Misono, M.; Ono, Y.; Hattori, H. *New Solid Acids and Bases*, Kodansha, Tokyo, **1989**, pp. 5-25.

13 Hauser, E. A.; Leggett, M. B. *J. Am. Chem. Soc.*, **1940**, *62*, 1811.

14 Weil-Malherbe, H.; Weiss, J. *J. Chem. Soc.*, **1948**, 2164.

15 Tamele, M. W. *Disc. Faraday Soc.*, **1950**, *8*, 270.

16 Johnson, O. *J. Phys. Chem.*, **1955**, *59*, 827.

17 Corma, A. *Chem. Rev.*, **1995**, *95*, 559.

18 Hattori, H. *Sekiyugakkaishi*, **1964**, *7*, 694.

19 Take, J.; Nomizo, Y.; Yoneda, Y. *Bull. Chem. Soc. Jpn.*, **1973**, *46*, 3568.

20 Mukaida, K.; Miyoshi, T.; Satoh, T. *Stud. Surf. Sci. Catal.*, **1989**, *90*, 363.

21 Chen, F. R.; Coudurier, G.; Joly, J.-F.; Vedrine, J. C. *J. Catal.*, **1993**, *143*, 616.

22 Adeeva, V.; de Haan, J. W.; Jänchen, J.; Lei, G. D.; Schünemann, V.; van de Ven, L. J. M.; Sachtler, W. M. H.; van Santen, R. A. *J. Catal.*, **1995**, *151*, 364.

23 Semmer, V.; Batamack, P.; DorEémieux-Morin, C.; Vincent, R.; Fraissard, J. *J. Catal.*, **1996**, *161*, 186.

24 Hino, M.; Arata, K. *J. Chem. Soc., Chem. Commun.*, **1980**, 851.

25 Tanabe, K.; Hölderich, W. F. *Appl. Catal. A*, **1999**, *181*, 399.

Part I

Acidic Property of Mesoporous Silica FSM-16

Introduction of Part I

Mesoporous Silica

Before 1990s', there were no mesoporous materials having narrow pore size distributions. Porous gels, pillared clays and USY zeolites possess large pores in a mesopore range, however, their sizes are not uniform and the distributions are very wide. Because newly synthesized mesoporous silicas, FSM-16 and MCM-41, possess large and uniform mesopores with extremely high surface areas (ca. 1000 m^2g^{-1}), much attentions have been paid for application of it, *i.e.*, catalysts, hosts for nano-structured compounds, absorbers, models to clarify of absorption properties in nano-ranges, and so forth.[1-3] The structure of FSM-16 is almost identical to that of MCM-41. Both of them possess uniform one dimensional pores which are hexagonally arrayed to form two dimensional structure. In general, qualities of mesoporous materials, and uniformities and regularities of the mesopores are characterized with XRD, nitrogen adsorption-desorption isotherm measurements and TEM micrograph observations. A TEM micrograph and an XRD pattern do not always reflect the whole structure of a sample. The disposition and/or coexistence of amorphous gels onto mesoporous materials often occurs, however, it can not be detected with XRD characterization. The deposited silica gel little affects an evaluated surface area of mesoporous materials. Typical features in the nitrogen adsorption-desorption isotherm, which are accompanied with capillary condensation and the hysteresis loop, are the most sensitive to the morphology and porosity. It is desirable to examine a structure of mesoporous materials with nitrogen adsorption isotherm experiments, accompanied by XRD characterizations.

In 1990, Kuroda *et al.* reported the first preparation of mesoporous silica with narrow pore size distribution and high specific surface area.[4,5] It was prepared from kanemite of layered polysilicate by an application of intercalation technique. The pore diameter was able to be controlled by changing alkyl-chain length of intercalates ($C_nH_{2n+1}(CH_3)_3N^+Cl^-$, n = 12, 14, 16, 18). At that time, the experimentally confirmed information about the structure of the mesoporous compounds is 1) its layered structure by TEM, and 2) three dimensional SiO_2 networks by XRD and ^{29}Si-MAS NMR. In 1993, hexagonal regular array of channels was confirmed for this new material with TEM micrograph, and a folding sheets' formation mechanism was proposed by Inagaki.[6] In fact, formation of intermediate lamellar silica-surfactant intercalate phase was detected with real-time *in situ* X-ray diffraction measurements.[7] On the basis of the model of folding silicate sheets of kanemite, this new material was named to FSM-16.[8,9] The addition of mesitylene in the mother suspension results in an expansion of the pore diameter.[10]

The pore wall thickness of FSM-16 was estimated to be 0.8-0.9 Å with XRD simulations, indicating that the wall consists of double SiO_4 layers.[11] The folding sheets'

mechanism indicates that the wall consists of both single and double silicate layers, indicating FSM-16 possesses two kinds of walls with different thickness. However, recent TEM characterization revealed that there are no differences in the wall thickness of any sides,[9,12] the value of which is 12 Å.[10] At the present stage, any spectroscopic differences between FSM-16 and amorphous silica gel were not confirmed with ^{29}Si-MAS NMR,[8,9,12,13] FTIR,[14] and Raman[15] characterizations. The precise mechanism of formation and pore wall structure of FSM-16 remain unknown.

In 1992, Mobile researchers reported a preparation of ordered mesoporous silica named MCM-41 (MCM; Mobile Composition of Matter) which possesses regular hexagonal arrays of uniform channels. TEM micrographs and Ar physisorption measurements of MCM-41 revealed that the pore size can be regulated in a very narrow distribution ranging 16 to 100 Å.[16] The pore size of MCM-41 was varied with alkyl-chain length of surfactants (alkyl-trimethylammonium salt),[17] and further addition of 1,3,5-trimethylbenzen [17] or 1,3,5-triisopropylbenzene,[18] as well as the case of FSM-16. On the other hand, the pore size and wall thickness of MCM-41 could be controlled by a proper choice of synthesis temperature and/or time, even if it was synthesized from one kind of surfactant (hexadecyl-trimethyammonium bromide).[19,20] Namba reported that a pore size of MCM-41 are able to be finely controlled by changing in a template mixture of hexadecyl trimethyammonium bromide / dodecyl trimethyl-ammonium bromide.[21] The long-range structural order and textural uniformity of MCM-41 are markedly improved if MCM-41 was synthesized with repeated pH adjusting.[22]

As a formation scheme of MCM-41, liquid-crystal templating mechanism was proposed.[16,17] The proposed mechanism was as follows: hexagonal arrays of cylindrical micelles form with the polar groups of the surfactants to the out side. Silicate species then occupy the spaces between cylinders and the final calcination step burns off the original organic material, leaving hallow cylinders of inorganic material. In contrast, another formation mechanism of MCM-41 was proposed by Stucky *et al.*[23] In their formation mechanism, firstly formed surfactant-silicate system of lamellar phase transforms to hexagonal mesophase. In fact this phase transformation was confirmed with TEM microscopy,[24] and ^{14}N-NMR characterization.[25] However, a time resolving *in situ* XRD experiment revealed that no intermediate phases are observed during a formation of the silica-surfactant mesophase that leads to MCM-41.[7] The reason why two kinds of different MCM-41 synthesis mechanisms have been demonstrated is the remarkable difference in their synthesis conditions. After all, the two quite different formation pathways of hexagonal mesophase give the same compound of MCM-41.

As other kinds of mesoporous silica molecular sieves, HMS [26,27] and MSU-1 [28] have been synthesized. HMS is synthesized with neutral primary amine surfactants (C_8-C_{18}; S^0) and neutral inorganic precursors (I^0), and MSU is synthesized with tetraethyl-orthosilicate and polyethylene oxide surfactant [$C_{11\text{-}15}H_{23\text{-}31}O$-$(CH_2CH_2O)_nH$]. In contrast to HMS and

MSU, MCM-41 is synthesized with long-chain quaternary ammonium cation surfactant (S^+) and anionic inorganic precursors (I^-).[29] HMS and MSU-1 possesses high surface area of ca. 1000 m^2g^{-1}, and relatively narrow pore size distributions. Both of MSU-1 and HMS exhibit only one d_{100} reflection in their XRD patterns, and capillary condensation over wide range of pressure in the nitrogen adsorption isotherms. XRD patterns and nitrogen adsorption-desorption isotherms indicate that the crystallinities and pore size uniformities and/or distributions seem to be inferior to those of MCM-41.

It is known that the value of thin pore wall thickness estimated with HRTEM is affected by a focus at a sample position. The wall structure of MCM-41 was investigated with molecular dynamics (MD) and simulations of XRD patterns.[30] The experimentally obtained XRD pattern was reproduced by a simulation when model MCM-41 structure possessed 44.6 Å of a_0 value and 10.9 Å of pore wall thickness. Under the condition, MD simulation demonstrated that the pore wall mainly consists of four and five membered rings, whereas the bulk silica mainly consists of six membered ring. When computational simulation is applied to reproduction of experimentally recorded XRD pattern of MCM-41, regularly arrayed hexagonal model structure has been usually assumed. However, recent investigation revealed that a special structure with a destroying hexagonal pore-arrays or a broader pore size distribution, effects only a minor influence on the simulated diffraction patterns against to the regular structure.[31] This result indicates a possibility that hexagonally arrayed pore structures of MCM-41 and FSM-16 are disordered. On the other hand, Elder *et al.* proposed a two-layered wall structure.[32] They recorded X-ray diffraction patterns of MCM-41 using synchrotron radiation, and simulated the recorded patterns with a model which consists of both dense and less dense walls, the thickness of which are 15.0-16.0 and 5.5-6.4 Å, respectively. Based on the results, the real pore diameter of calcined MCM-41 was estimated to be 13.9-14.8 Å, which was much smaller than those reported by the other research groups (ca. 30 Å). About large differences in pore wall thickness, they claimed that these earlier methods measured only an average wall thickness, which was assumed a simple two-region hole/wall model. As well as FSM-16, there are no evidences about structural differences among amorphous silica and MCM-41. Chen *et al.* reported that IR, Raman, ^{29}Si MAS- and CP- NMR spectra of MCM-41 are quite similar to those of amorphous silica.[33] The real structure of mesoporous silica such as MCM-41 and FSM-16 remains unknown, in particularly in the pore-structure and pore-wall thickness.

FSM-16 and MCM-41 exhibit high thermal stability up to 1273 K in the absence of moisture. In contrast, mesoporous silicas are mechanically unstable compared to zeolites, and the crystallinity is reduced by pressing.[34-36] Compared to FSM-16, MCM-41 exhibits low hydrothermal stability and the crystallinity is easily reduced.[37,38] To improve its hydrothermal stability, addition of cations into synthesis gels,[39,40] post-synthesis water treatment,[41] and postsynthesis sililation [42] were carried out. The reason for differences in the hydrothermal stability among FSM-16 and MCM-41 might be due to the pH values in the preparation step. MCM-41 is synthesized in an autoclave around pH = 12. In contrast, pH adjustment was

carried out in FSM-16 preparation procedure, pre- and post-adjusted values of which are 12 and 8.5, respectively. Two Si-OH condense to form Si-O-Si linkage at a lower pH at a preparation of FSM-16. The different pH values at the synthesis procedures might cause differences in the degree of Si-OH condensation, which reflects their structural stabilities.

Amorphous silica deposits easily on the surface of FSM-16 at the pH adjustment procedure. Prior to the pH adjustment from 12 to 8.5, removal of solved silicate species is indispensable for FSM-16 synthesis to obtain silica gel free FSM-16.[8] Nitrogen adsorption-desorption isotherm of MCM-41 scarcely shows hysteresis at high P/P_0 (P_0: saturated vapor pressure) region,[16,43] whereas that of FSM-16 exhibits small hysteresis above $P/P_0 = 0.5$ due to deposition of amorphous silica.[9,44] SEM characterizations revealed that the morphology of MCM-41 is a hexagonal prism,[16,17] while that of FSM-16 retains that of kanemite which does not possess regular morphology.[6] The differences in morphology might be affected by the preparation condition. MCM-41 crystallizes in an autoclave under a static condition. On the other hand, mother suspension of FSM-16 synthesis is in stirring all the time. As a result, secondary granular of FSM-16 might not reflect the hexagonally arrayed pore structure, in contrast to the case for MCM-41. Other possible reason is the deposition of amorphous silica. Although the secondary granular of FSM-16 and MCM-41 are quite different, XRD characterization has never revealed differences among them. There are no data reflecting differences in physical properties among them at the present stage.

Silica is generally a catalytically inert material, and the surface silanol groups are very weakly acidic in nature.[45] Therefore, FSM-16 and MCM-41 themselves are considered to be catalytically inactive. To generate catalytic activity of mesoporous silicas, introduction of other elements such as Al [17,23,46,47] and Ti [26,48,49] to the framework was performed by many researchers.[1,2,50] As other attempts to generate active sites on mesoporous silicas, grafting of organometallic compounds,[51-56] or supporting of transition metal oxides (Mn,[57] Mn,[58] Cs,[59] Cs and/or La,[60] Ge, Sn, Ti,[61] Fe [62]), and novel metal particles (Ru,[63] Rh[64,65] Pt,[66-69] Au [70]) and Pt wires [71,72] were examined. Using a large pore of FSM-16, ship-in-bottle synthesis of platinum carbonyl cluster, the size of which was too large to be accommodated into pores of conventional zeolites such as FAU, was carried out.[68, 69, 73,74] Al-contained mesoporous silica was applied for production of fine chemicals such as dimethylacetals [75] and Jasminaldehyde.[76] Shinoda *et al.* reported that Al-loaded FSM-16 exhibits excellent shape selectivity for meso-tetraarylporphyrin synthesis.[77]

In contrast to these efforts, catalyses over pure siliceous mesoporous silicas were found in 1997. The selective dehydration of 2-methylbut-3-yn-2-ol to 2-methylbut-3-yn-1-ene proceeded at 453 K over MCM-41.[78] Cumene cracking was catalyzed over FSM-16 at 673 K.[79] These two works did not focus the catalysis over siliceous mesoporous silicas, but those were used as reference samples or for a blank test. Nakajima *et al.* found that siliceous FSM-16 catalyzes Beckmann rearrangement of cyclohexanone oxime at 523-623 K without deactivation for 5 h.[80] The activities are higher than those of silica-alumina, HZSM-5, Na-ZSM-5, HX and

γ-Al_2O_3. Silica gel enhances this reaction with the same selectivity as that for FSM-16. Although the activity for silica gel was quite lower than that for FSM-16, differences in activities between FSM-16 and silica gel were not discussed. On the contrary, Sakata *et al.* found that siliceous FSM-16 accelerates a rate of degradation of plastic polymers into liquid hydrocarbons.[81,82] They concluded that non-acidic mesoporous silica acts as a radical-flask.

Although these significant data have been reported within recent several years, still the neutrality of FSM-16 and MCM-41 has been generally believed. In 1998, the present author found that FSM-16 enhances acid-catalyzed reactions and proposed that siliceous FSM-16 possesses acid sites.[14] Soon after our discovery, a similar catalytic behavior for acetalization of carbonyl groups was confirmed on siliceous MCM-41 by Iwamoto *et al.*[83] Their proposed active sites and the activity generation mechanism [84] were almost the same as ones proposed by the present author. Furthermore, photocatalyses over dehydrated FSM-16 were confirmed by Yoshida. FSM-16 evacuated at 1073 K catalyzes metathesis [85] and oxidation [86] of propene under photoirradiation, active sites of which are proposed to be produced by removal of hydroxyl groups. Amorphous silica itself catalyzes photomethathesis of alkenes [87,88] and photooxidation of propene,[89] however, FSM-16 exhibits higher activities than amorphous silica. They speculated that much amounts of surface silanol groups due to its large surface area and/or the wall structure of FSM-16 relate to higher catalytic activities than amorphous silica.

Until 1997, no one took in account for acid properties of siliceous mesoporous silicas. We opened and shed light to the new intrinsic properties of mesoporous silicas. The present part describes the discovery of the acid sites of FSM-16 and discusses its acid properties. In chapter 1, catalyses of but-1-ene and α-pinene isomerizations over siliceous FSM-16 were examined and the change of acidic property upon thermal treatment are reported. Relations among Brønsted acidic property of FSM-16, the surface silanol groups, and the structure were discussed. Chapter 2 describes a formation of Lewis acid sites on FSM-16 accompanied with a high-temperature treatment. Generation of Lewis acid sites and their acidic properties, and catalytic properties were examined with catalyses for methylamine synthesis and pyridine-adsorption-desorption experiments.

References

1 Corma, A. *Chem. Rev.*, **1997**, *97*, 2373.

2 Biz, S.; Occelli, M. L. *Catal. Rev. Sci. Eng.*, **1998**, *40*, 329.

3 Ciesla, U.; Schuth, F. *Microporous Mesoporous Mater.*, **1999**, *27*, 131, and references therein.

4 Yanagisawa, T.; Shimizu, T.; Kuroda, K.; Kato, C. *Bull. Chem. Soc. Jpn.*, **1990**, *63*, 988.

5 Yanagisawa, T.; Shimizu, T.; Kuroda, K.; Kato, C. *Bull. Chem. Soc. Jpn.*, **1990**, *63*, 1535.

6 Inagaki, S.; Fukushima, Y.; Kuroda, K. *J. Chem. Soc., Chem. Commun.*, **1993**, 680.

7 O'Brien, S.; Francis, R. J.; Price, S. J.; O'Hare, D.; Clark, S. M.; Okazaki, N.; Kuroda, K. *J. Chem. Soc., Chem. Commun.*, **1995**, 2423.

8 Inagaki, S.; Fukushima, Y.; Kuroda, K. *Stud. Surf. Sci. Catal.*, **1994**, *84*, 125.

9 Inagaki, S.; Koiwai, A.; Suzuki, N.; Fukushima, Y.; Kuroda, K. *Bull. Chem. Soc. Jpn.*, **1996**, *69*, 1449.

10 Inagaki, S.; Yamada, Y.; Fukushima, Y.; Kuroda, K. *Stud. Surf. Sci. Catal.*, **1995**, *92*, 143.

11 Inagaki, S.; Sakamoto, Y.; Fukushima, Y.; Terasaki, O. *Chem. Mater.*, **1996**, *8*, 2089.

12 Sakamoto, Y.; Inagaki, S.; Ohsuna, T.; Ohnishi, N.; Fukushima, Y.; Nozue, Y.; Terasaki, O. *Microporous Mesoporous Mater.*, **1998**, *21*, 589.

13 Fukushima, Y.; Inagaki, S. *J. Mat. Sci. Eng.*, **1996**, *A217/218*, 116.

14 Yamamoto, T.; Tanaka, T.; Funabiki, T.; Yoshida, S. *J. Phys. Chem. B*, **1998**, *102*, 5830.

15 Yamamoto, T.; Tanaka, T.; Funabiki, T.; Yoshida, S. unpublished results.

16 Kresge, C. T.; Lenowicz, M. E.; Roth, W. J.; Vartuli, J. C.; Beck, J. S. *Nature* **1992**, *359*, 710.

17 Beck, J. S.; Vartuli, J. C.; Roth, W. J.; Lenowicz, M. E.; Kresge, C. T.; Schmitt, K. D.; Chu, C. T-W.; Olson, D. H.; Sheppard, E. W.; McCullen, S. B.; Higgis, J. B.; Schlenker, J. L. *J. Am. Chem. Soc.* **1992**, *114*, 10834.

18 Namba, S.; Mochizuki, A. *Res. Chem. Intermed.*, **1998**, *24*, 5.

19 Cheng, C.-F.; Zhou, W.; Klinowski, J. *Chem. Phys. Lett.*, **1996**, *263*, 247.

20 Cheng, C.-F.; Zhou, W.; Park, D. H.; Klinowski, J.; Hargreaves, M.; Gladden, L. F. *J. Chem. Soc., Faraday Trans.*, **1997**, *93*, 359.

21 Namba, S.; Mochizuki, A.; Kito, M. *Chem. Lett.*, **1998**, 569.

22 Ryoo, R.; Kim, J. M.; *J. Chem. Soc., Chem. Commun.*, **1995**, 711.

23 Monnier, A.; Schüth, F.; Huo, Q.; Kumar, D.; Margolese, D.; Maxwell, R. S.; Stucky, G. D.; Krishnamuty, M.; Petroff, P.; Firouzi, A.; Janicke, M.; Chmelka, B. F. *Science* **1993**, *261*, 1299.

24 Alfredsson, W.; Keung, M.; Monnier, A.; Stucky, G. D.; Unger, K. K.; Schüth, F. *J. Chem. Soc., Chem. Commun.*, **1994**, 921.

25 Steel, A.; Carr, S. W.; Anderson, M. W. *J. Chem. Soc., Chem. Commun.*, **1994**, 1571.

26 Tanev, P. T.; Chibwe, M.; Pinnavaia, T. J. *Nature*, **1994**, *368*, 321.

27 Tanev, P. T.; Pinnavaia, T. J.; *Science*, **1995**, *267*, 865.

28 Bagshaw, S. A.; Prouzet, E.; Pinnavaia, T. J. *Science*, **1995**, *269*, 1242.
29 Huo, Q.; Margolese, D. I.; Ciesla, U.; Feng, P.; Gier, T. E.; Sieger, P.; Leon, R.; Petroff, P. M.; Schüth, F.; Stucky, G. D. *Nature*, **1994**, *368*, 317.
30 Feuston, B. P.; Higgins, J. B. *J. Phys. Chem.*, **1994**, *98*, 4459.
31 Schacht, S.; Janicke, M.; Schuth, F. *Microporous Mesoporous Mater.*, **1998**, *22*, 485.
32 Edler, K. J.; Reynolds, P. A.; White, J. W.; Cookson, D. *J. Chem. Soc., Faraday Trans.*, **1997**, *93*, 199.
33 Chen, C.-Y.; Li, H.-X.; Davis, M. E. *Microporous Mater.*, **1993**, *2*, 17.
34 Tatsumi, T.; Koyano, KA.; Tanaka, Y.; Nakata, S. *Chem. Lett.*, **1997**, 469.
35 Ishikawa, T.; Matsuda, M.; Yasukawa, A.; Kandori, K.; Inagaki, S.; Fukushima, Y.; Kondo, S. *J. Chem. Soc., Faraday Trans.*, **1996**, *92*, 1985.
36 Gusev, V. Y.; Feng, X.; Bu, Z.; Haller, G. L.; O'Brien, J. A. *J. Phys. Chem.*, **1996**, *100*, 1989.
37 Chen, C.-Y. ; Xiao, S.-Q.; Davis, M. E. *Microporous Mater.*, **1995**, *4*, 1.
38 Ryoo, R.; Kim, J. M.; Ko, C. H.; Shin, C. H. *J. Phys. Chem.*, **1996**, *100*, 17718.
39 Ryoo, R.; Jun, S. *J. Phys. Chem. B*, **1997**, *101*, 317.
40 Das, D.; Tsai, C.-M.; Cheng, S. *J. Chem. Soc., Chem. Commun,*, **1999**, 473.
41 Chen, L.; Horiuchi, T.; Mori, T.; Maeda, K. *J. Phys. Chem. B*, **1999**, *103*, 1216.
42 Koyano, KA.; Tatsumi, T.; Tanaka, Y.; Nakata, S. *J. Phys. Chem. B*, **1997**, *101*, 9436.
43 Branston, P. J.; Hall, P. G.; Sing, K. S. W. *J. Chem. Soc., Chem. Commun.* **1993**, 1257.
44 Branston, P. J.; Kaneko, K.; Setoyama, N.; Sing, K. S. W.; Inagaki, S.; Fukushima, Y. *Langmuir*, **1996**, *12*, 599.
45 Tanabe, K.; Misono, M.; Ono, Y.; Hattori, H. *New Solid Acids and Bases*, Kodansha, Tokyo, 1989, pp. 91-105.
46 Corma, A.; Fornes, V.; Navarro, M. T.; Pérez-Pariente, J. *J. Catal.* **1994**, 148, 569.
47 Inagaki, S.; Yamada, Y.; Fukushima, Y. *Stud. Surf. Sci. Catal.*, **1996**, *105*, 109.
48 Zhang, W.; Fröba, M.; Wang, J.; Tanev, P. T.; Wong, J.; Pinnavaia, T. J. *J. Am. Chem. Soc.* **1996**, *118*, 9164.
49 Corma, A.; Navarro, M. T.; Pérez-Pariente, J. *J. Chem. Soc., Chem. Commun.* **1994**, 147.
50 Sayari, A. *Chem. Mater.*, **1996**, *8*, 1840.
51 Maschmeyer, T.; Rey, F.; Sanker, G.; Thomas, J. M. *Nature*, **1995**, *378*, 159.
52 Tudor, J.; O'Hare, D. *Chem. Commun.*, **1997**, 603.
53 Liu, C.-J.; Li, S.-G.; Pang, W.-Q.; Che, C.-M. *Chem. Commun.*, **1997**, 65.
54 Mehnert, C. P.; Ying, J. Y. *Chem. Commun.*, **1997**, 2215.
55 Maquarrier, D. J.; Jackson, D. B. *Chem. Commun.*, **1997**, 1781; *ibid.*, **1997**, 1996.

56 O'Brien, S.; Tudor, J.; Barlow, S.; Drewitt, M. J.; Heyes, S. J.; O'Hare, D. *Chem. Commun.*, **1997**, 641.
57 Burch, R.; Cruise, N.; Gleeson, D.; Tsang, S. C. *Chem. Commun.*, **1996**, 951.
58 Sutra, P.; Brunel, D. *Chem. Commun.*, **1996**, 2485.
59 Corma, A.; Iborra, S.; Miquel, S.; Primo, J. *J. Catal.*, **1998**, *173*, 315.
60 Kloestra, K. R.; van Laren, M.; van Bekkum, H. *J. Chem. Soc., Faraday Trans.*, **1997**, *93*, 1211.
61 Oldroyd, R. D.; Sankar, G.; Thomas, J. M.; Özkaya, D. *J. Phys. Chem. B*, **1998**, *102*, 1849.
62 Abe, T.; Tachibana, Y.; Uematsu, T.; Iwamoto, M. *Chem. Commun.*, **1995**, 1617.
63 Fishel, C. T.; Davis, R. J.; Garces, J. M. *J. Catal.*, **1996**, *163*, 148.
64 Muluktla, R. S.; Asakura, K.; Namba, S.; Iwasawa, Y. *Chem. Commun.*, **1998**, 1425.
65 Muluktla, R. S.; Asakura, K.; Kogure, T.; Namba, S.; Iwasawa, Y. *Phys. Chem. Chem. Phys.*, **1999**, *1*, 2027.
66 Junges, U.; Jacobs, W.; Voigt-Martin, I.; Krutzsch, B.; Schüth, F. *Chem. Commun.*, **1995**, 2283.
67 Ryoo, R.; Ko, C. H.; Kim, J. M.; Howe, R. *Catal. Lett.*, **1996**, *37*, 29.
68 Yamamoto, T.; Shido, T.; Inagaki, S.; Fukushima, Y.; Ichikawa, M. *J. Am. Chem. Soc.*, **1996**, *118*, 5810.
69 Yamamoto, T.; Shido, T.; Inagaki, S.; Fukushima, Y.; Ichikawa, M. *J. Phys. Chem. B*, **1998**, *102*, 3866,
70 Okumura, M.; Tsubota, S.; Iwamoto, M.; Haruta, M. *Chem. Lett.*, **1998**, 315.
71 Sasaki, M.; Osada, M.; Sugimoto, N.; Inagaki, S.; Fukushima, Y.; Fukuoka, A.; Ichikawa, M. *Microporous Mesoporous Mater.*, **1998**, *21*, 597.
72 Ko, C. H.; Ryoo, R. *Chem. Commun.*, **1996**, 2467.
73 Ichikawa, M.; Yamamoto, T.; Pan, W.; Shido, T. *Stud. Surf. Sci. Catal.*, **1997**, *105*, 679.
74 Sasaki, M.; Osada, M.; Higashimoto, N.; Yamamoto, T.; Fukuoka, A.; Ichikawa, M. *J. Mol. Catal. A*, **1999**, *141*, 223.
75 Climent, M. J.; Corma, A.; Iborra, S.; Navarro, M. C.; Primo, J. *J. Catal.*, **1996**, *161*, 783.
76 Climent, M. J.; Corma, A.; Guil-López, R.; Iborra, S.; Primo, J. *J. Catal.*, **1998**, *175*, 70.
77 Shinoda, T.; Onaka, Y.; Onaka, M. *J. Chem. Soc., Chem. Commun.*, **1995**, 1801.
78 Galarneau, A.; Barodawalla, A.; Pinnavaia, T. J. *Chem. Commun.* **1997**, 1661.
79 Hamaguchi, K.; Hattori, H. *React. Kinet. Catal. Lett.*, **1997**, *61*, 13.
80 Nakajima, T.; Nakajima, T.; Mishima, S. *Nippon Kagaku Kaishi*, **1997**, 565.

81 Sakata, Y.; Uddin, M. A.; Muto, A.; Kanada, Y.; Koizumi, K.; Murata, K. *J. Anal. Appl. Pyrolysis*, **1997**, *43*, 15.

82 Uddin, M. A.; Sakata, Y.; Muto, A.; Shiraga, Y.; Koizumi, K.; Kanada, Y.; Murata, K. *Microporous Mesoporous Mater*,, **1998**, *21*, 557.

83 Tanaka, Y.; Sawamura, N.; Iwamoto, M. *Tetrahedron Lett.*, **1998**, *175*, 1998.

84 Sawamura, N.; Tanaka, Y.; Namba, S.; Iwamoto, M. "The 56th National Meeting of the Chemical Society of Japan,", Yokohama, March, **1999**, Abstr., I, p. 312.

85 Yoshida, H.; Kimura, K.; Inaki, Y.; Hattori, T. *Chem. Commun.*, **1997**, 129.

86 Yoshida, H.; Murata, C.; Inaki, Y.; Hattori, T. *Chem. Lett.*, **1998**, 1121.

87 Yoshida, H.; Tanaka, T.; Matsuo, S.; Funabiki, T.; Yoshida, S. *J. Chem. Soc., Chem. Commun.*, **1995**, 761.

88 Tanaka, T.; Matsuo, S.; Maeda, T.; Yoshida, H.; Yoshida, S. *Appl. Surf. Sci.*, **1997**, *121/122*, 296.

89 Yoshida, H.; Tanaka, T.; Yamamoto, M.; Yoshida, T.; Funabiki, T.; Yoshida, S. *J. Catal.* **1997**, *171*, 351.

Chapter 1

Characterization of Brønsted Acid Sites on FSM-16

Abstract

Siliceous FSM-16 possesses acid sites to catalyze but-1-ene isomerization to produce but-2-ene (*cis /crans* = 1.4 - 1.7) at 323 K and 2,6,6- trimethylbicyclo[3.1.1]hept-2-ene (α-pinene) isomerization at 303 K. Catalytic activity was dependent upon heat treatment and reached a maximum at 673 K. The maximum acid strength was invariably H_0 = -3.0 independent of the pretreatment temperatures. The acidity was much reduced by calcination at higher temperatures, but restored by water treatment at 353 K as long as the FSM-16 retained its structure.

Introduction

FSM-16,[1] MCM-41[2,3] and HMS[4] are mesoporous silicas with narrow pore size distribution, high specific surface area, and high thermal stability up to 1273 K. These materials, synthesized with cetyltrimethylammonium salts, have a quite similar structure, a unique adsorption isotherm of nitrogen, high BET specific surface area, a narrow pore size distribution, and a high pore volume, although the XRD pattern of HMS is slightly different from the others. While XRD patterns of FSM-16 and MCM-41 may exhibit up to four well-defined peaks, that of HMS exhibits only one broad peak attributed to the 100 reflection.[5] The main difference between FSM-16 and MCM-41 is the synthesis procedure and formation mechanism. Mobil researchers proposed the formation mechanism of M41S materials, such as MCM-41, based on a liquid crystal templating model. The folding sheets mechanism was proposed for FSM-16: intercalation of surfactants to layered polysilicate kanemite with a primary *d* spacing of 10 Å and then the folding of layers to form the specific hexagonal structure. On the other hand, Monnier et al. proposed a layered intermediate with a primary *d* spacing of 31 Å for the formation of MCM-41.[6] In fact, an in situ XRD study showed that the intermediate lamellar silica-surfactant intercalate was formed during the synthesis of FSM-16 from kanemite, whereas no intermediate phases were observed during the formation of MCM-41.[7]

Silica is a generally catalytically inert material, and the surface silanol groups are very weakly acidic in nature.[8] Therefore, FSM-16 and MCM-41 themselves are considered inactive catalytically, and the introduction of Al to the framework was often performed to generate acidity.[3, 6, 9-13] Other metals or cations are also added to FSM-16 and MCM-41 to generate catalytic activity, as exemplified by incorporation of transition metal cations such as Ti to the framework,[5,14-16] introduction of metal cations by ion exchange,[17] direct incorporation of novel metals via synthesis gel,[18] and introduction of catalytically active species into pores,[19-23] and so forth.

Here, we report that siliceous FSM-16 catalyzes isomerization of but-1-ene and 2,6,6-trimethylbicyclo[3.1.1]hept-2-ene (α-pinene) at 323 and 303 K, respectively. Isomerizations of terpenes such as the rearrangement of α-pinene to 2,2-dimethyl-3-methylenebicyclo-[2.2.1]-heptane (camphene)[24] and the migration of olefinic bonds of 1-methyl-4-(1-methylethynyl)-cyclohexene (limonene)[25] were known to be acid catalyzed reactions. In contrast, solid bases such as CaO and SrO catalyze isomerization of α-pinene to produce 6,6-dimethyl-2-methylenebicyclo[3.1.1]heptane (β-pinene), selectively.[26] Therefore, isomerization of α-pinene is an excellent test reaction for acid-base properties of a catalyst.

Recently, catalysis by siliceous mesoporous materials was reported. The selective dehydration of 2-methylbut-3-yn-2-ol to 2-methylbut-3-yn-1-ene proceeded at 453 K over MCM-41.[27] Cumene cracking was catalyzed over FSM-16 at 673 K.[28] Furthermore, Yoshida et al. reported that FSM-16 evacuated at 873 K catalyzes metathesis of propene under

photoirradiation.[29] However, the first two papers did not focus on the catalytic properties of siliceous mesoporous materials. There have been no reports discussing the acidic properties of siliceous mesoporous materials.

Experimental Section

Materials

FSM-16 was synthesized according to Inagaki's method.[30] Prior to calcination, the Si/Na atomic ratio of water glass (Osaka Keiso Co., LTD; SiO_2 = 31.93, Na_2O = 15.37, Al = 0.0098, Fe = 0.0028 wt %; Si/Al = 1463 atomic ratio) was adjusted to 1.00 by addition of NaOH solution (Wako Pure Chem. Ind., LTD). During synthesis, water glass successively changed to δ-$Na_2Si_2O_5$, kanemite ($NaHSi_2O_5 \cdot 3H_2O$), and finally FSM-16 via three steps. $[C_{16}H_{33}(CH_3)_3N]Br$ (Tokyo Chem. Ind. Co., LTD) was used as a template. The ion exchange of kanemite to produce FSM-16 was carried out as follows. At the beginning of ion exchange of kanemite, the concentration of template was 0.10 M and a molar ratio of the template to Si of kanemite was adjusted to 0.2. The ion exchange was carried out at 343 K for 3 h with stirring. After cooling to room temperature, the solid was filtered off and then dispersed in distilled water again. After adjustment of pH to the 8.5 with 2 M HCl, it was heated up to 343 K and stirred for 6 h while maintaining the pH at 8.5. Finally, ion-exchanged kanemite (FSM-16) was calcined in a dry air stream at 823 K for 6 h. The yield of FSM-16 based on SiO_2 was 24%. After calcination, FSM-16 was ground to powder under 100 mesh. The XRD pattern (d_{100}; 38 Å), the BET specific surface area (1078 $m^2\ g^{-1}$), the N_2 adsorption isotherm, the pore volume (0.73 $cm^3\ g^{-1}$; estimated by *t*-plot), and the pore diameter (27.6 Å; estimated by the Clanston-Inkley method) were quite similar to those reported in the literature.[30,31]

Calcined and rehydrated FSM-16 was also prepared because a hydration state of FSM-16 is closely related to catalytic activities, as would be described below. Rehydrated catalysts were prepared via two steps. Before rehydration, FSM-16 was calcined once in a dry air stream at 1173 or 1373 K for 2 h (FSM-1173, FSM-1373). At the next step, the calcined FSM-16 was treated with water at 353 K for 4 h with stirring, followed by calcination at 773 K for 5 h (FSM-1173H, FSM-1373H).

Silicon oxide hydrate ($H_2Si_2O_5$) was synthesized from kanemite,[32] which was the same material as used for FSM-16 synthesis. Kanemite dispersed in distilled water was converted to $H_2Si_2O_5$ keeping the pH at 1.2 at room temperature. Adjustment of the pH was performed with 2 M HCl, and the condition was maintained for 24 h with stirring. The precipitate was washed with distilled water until Cl^- was free based on $AgNO_3$ test. It was dried at 343 K for 12 h followed by calcination at 773 K for 5 h. Formation of $H_2Si_2O_5$ crystal was confirmed by XRD (JCPDS file No. 27-606) for the dried sample, which became

amorphous upon calcination at 773 K. TG-DTA analysis showed that $H_2Si_2O_5$ released the interlayer water molecules around at 473 K, and the loss of interlayer water should account for the loss of crystallinity. This phenomenon was consistent with previous works.[33] Al-doped δ-$Na_2Si_2O_5$ and $H_2Si_2O_5$ were also synthesized. To adjust the Si/Al atomic ratio to be 16, whose value was to form 5 wt % of Al_2O_3 containing SiO_2-Al_2O_3 as a starting material, $NaAlO_2$ was added to water glass.

SiO_2 gel was synthesized from tetraethyl orthosilicate (Nacalai tesque, EP-grade, once distilled) by hydrolysis in a water-ethanol mixture at boiling point followed by calcination at 773 K for 5 h in a dry air stream.[34] Before calcination, a dried sample was ground to powder under 100 mesh. No crystalline phases of SiO_2 were detected by XRD analysis.

Other silicas used were Japan Reference Catalyst (JRC-SIO-5, JRC-SIO-7), supplied by the Committee on Reference Catalyst, Catalysis Society of Japan. JRC-SIO-5 contains 134 ppm Na, 122 ppm Al, 40 ppm Ca, 57 ppm Fe, and 100 ppm Mg. JRC-SIO-7 contains 135 ppm Na, 195 ppm Al, 36 ppm Ca, 72 ppm Fe, and 117 ppm Mg. The BET specific surface area of JRC-SIO-5 and JRC-SIO-7 is 192 and 86 $m^2\ g^{-1}$, respectively. They were precalcined in dry air at 773 K for 3 h.

Reference catalysts used for α-pinene isomerization were HZSM-5 (JRC-Z5-25H, -70H, -1000H; Si/Al atomic ratio are 12.3, 40.0, 623, respectively), NaY (JRC-Z-1), γ-Al_2O_3 (JRC-ALO-4), ZrO_2 (JRC-ZRO-1), TiO_2 (JRC-TIO-4), $Mg(OH)_2$ (Rare Metallic Co., 99%), $Ca(OH)_2$ (Nacalai, GR), $Nb_2O_5{\cdot}nH_2O$ (CBMM) and $NiSO_4{\cdot}nH_2O$ (Nacalai, GR).

Characterization

NH_3-TPD measurements were carried out by a quadrupole-type mass spectrometer at a heating rate of 5 K min^{-1}. Before TPD measurements, each 100 mg of sample was evacuated at 673 K for 0.5 h and calcined under 6.66 kPa of O_2 for 1 h, followed by evacuation at the same temperature for 1 h. The sample was exposed to 500 μmol of NH_3 at room temperature for 0.5 h followed by evacuation at the same temperature for 1 h. The amount of desorbed gases (NH_3; m/e = 16) was normalized with that of introduced Ar (m/e = 40) as an internal standard.

FTIR spectra were recorded with a Perkin-Elmer Paragon 1000 spectrometer in a transmission mode at room temperature. IR spectra of adsorbed pyridine were recorded with a resolution of 4 cm^{-1}. Each sample (20-80 mg) was pressed into a self-supporting wafer (20 mm in diameter) with a pressure of 100 kg cm^{-2} for 10 s, and was mounted in an *in situ* IR cell equipped with BaF_2 windows. The wafer was pretreated in the same way as that for NH_3-TPD measurements and exposed to 27 Pa of pyridine vapor at 423 K for 5 min followed by evacuation at the same temperature for 1 h. The other spectra were recorded with a resolution of 2 cm^{-1}.

Thermogravimetric analysis was carried out with Rigaku Thermoflex TG 8110 in a dry N_2 stream at a heating rate of 5 K min^{-1}.

X-ray diffraction patterns of samples were obtained with a Rigaku Geigerflux diffractometer using Ni-filtered Cu Kα radiation (1.5418 Å).

The acid strength of catalysts was measured by various Hammett indicators. The indicators used for the titration method were 0.1 wt % benzene solution of methylred (H_0 = +4.8), *p*-dimethylaminoazobenzene (+3.3), benzenazodiphenylamine (+1.5), dicinnamal-acetone (-3.0) and benzalacetophenone (-5.6).

Catalysis

But-1-ene isomerization was carried out in a closed circulation system (dead volume, 200 cm^3). Prior to each run, 50 mg of FSM-16 was evacuated at a prescribed temperature for 0.5 h and calcined under 6.66 kPa of O_2 for 1 h, followed by evacuation at the same temperature for 1 h. The amount of substrate was 400 μmol, and the reaction temperature was 323 K.

α-Pinene isomerization was carried out under dry N_2 atmosphere using a stirred batch reactor at 303 or 353 K. The pretreatment procedure was the same as mentioned above. In a typical experiment, the reactor was loaded with 2 mL (12.6 mmol) of α-pinene (Nacalai, EP, 99.8%) and 50 mg of catalyst.

Products were analyzed by GC and GC-MS (Shimadzu, GCMS-QP5050).

Results and Discussion

Elemental Analysis

Table 1 summarizes elemental analysis of prepared catalysts. Although the Si/Al atomic ratio of water glass was 1463, that of synthesized FSM-16 was 735. This result shows that Al was slightly concentrated but the concentration was still quite low. Results of FSM-1173H and FSM-1373H show that no treatment changes the original elemental composition except for Na. Because $H_2Si_2O_5$ was treated with water of pH = 1.2 during synthesis, almost all of the trace elements were extracted off. SiO_2 gel contained little other elements.

Acidic Property

Figure 1 shows initial rates for but-1-ene isomerization over FSM-16 pretreated at various temperatures and BET specific surface areas of the FSM-16 samples. The initial rate strongly depended on the pretreatment temperature. Samples pretreated at temperatures from 473 through 673 K showed similar initial rates. Once pretreatments were performed at temperatures higher than 873 K, the initial rate drastically decreased although BET specific

TABLE 1: Elemental Analysis of Catalysts[a]

Catalyst	Elements (mass%)						Si/Al atomic ratio
	Na	Al	Ca	Fe	Mg	Ti	
FSM-16	0.008	0.061	0.012	0.023	0.003	0.032	735
FSM-1173H[b]	0.017	0.062	0.012	0.021	0.003	0.029	723
FSM-1373H[c]	0.021	0.071	0.014	0.031	0.004	0.035	631
FSM-16[d]	0.01	0.14		0.02			320
$H_2Si_2O_5$	0.005	0.008	0.006	0.002	0.001	0.007	5612
SiO_2 gel	0.002	<0.001	0.001	<0.001	<0.001	<0.001	-

a Analyzed by ICP (inductively coupled plasma) and atomic absorption spectroscopy.

b Hydrated at 353 K for 4h followed by calcination at 773 K for 5 h. Before hydration, FSM-16 was calcined in a dry air stream at 1173 K for 2 h.

c Hydrated at 353 K for 4 h followed by calcination at 773 K for 5 h. Before hydration, FSM-16 was calcined in a dry air stream at 1373 K for 2 h.

d Supplied by Toyota Central R&D Labs., Inc. (Lot No. NG78-550).

TABLE 2: Results of α-Pinene Isomerization at 303 K[a]

Catalyst	Pretreatment Temperature / K	Conversion (%)	Selectivity[b] (%)							
			1	2	3	4	5	6	7	8
FSM-16	373	16.0	1	42	6	42	6	1	1	1
	473	27.1	1	40	5	44	7	1	1	1
	673	44.6	tr	40	4	43	9	2	2	tr
	873	29.5	tr	39	3	48	7	1	1	1
	1073	6.6	1	37	3	48	7	2	2	1
	1273	1.5	4	37	3	46	7	1	2	tr
FSM-16[c]	673	52.9	tr	39	4	43	8	2	2	tr

a α-pinene, 2 mL; catalyst, 50 mg; reaction time, 0.5 h.

b 1, β-pinene; 2, camphene; 3, α-fenchene; 4, limonene; 5, terpinolene; 6, α-terpinene; 7, γ-terpinene; 8, others.

c Supplied by Toyota Central Lab., Inc. (lot no. NG78-550).

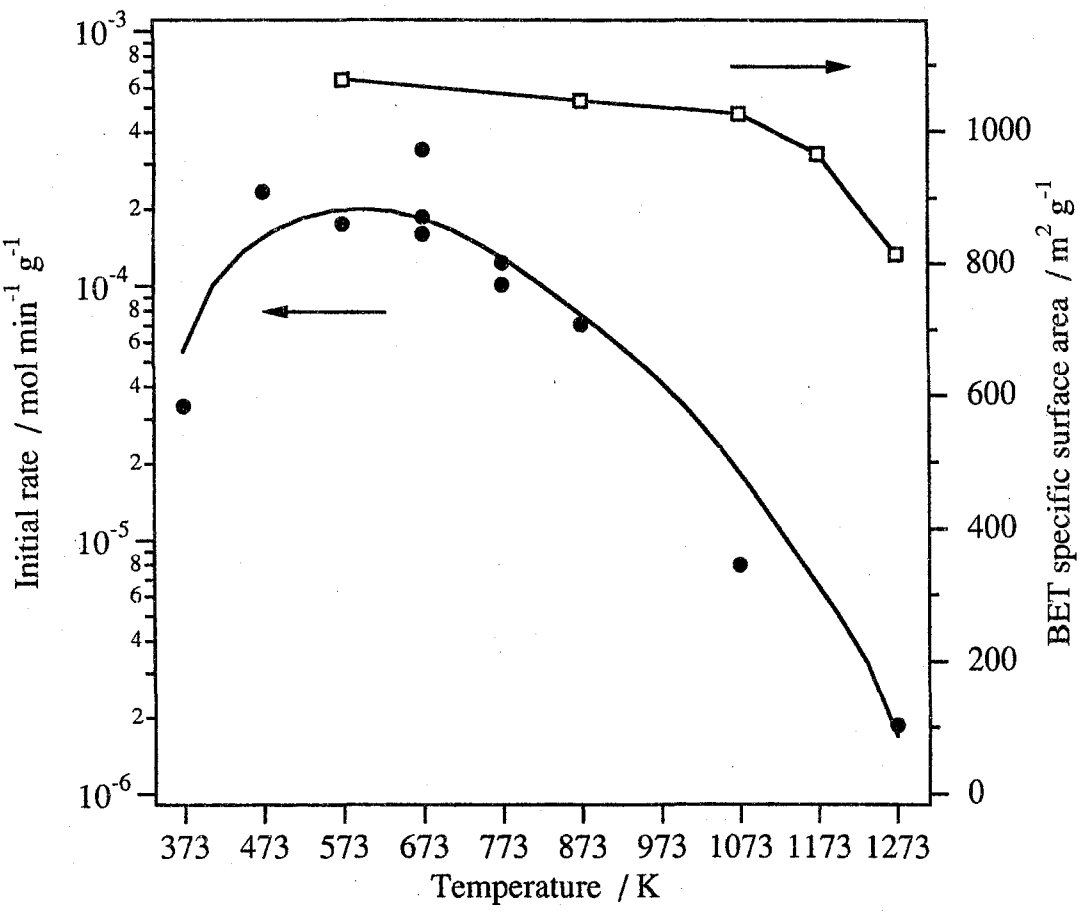

Figure 1. Plots of initial rates for but-1-ene isomerization over FSM-16 and BET specific surface area vs. pretreatment temperatures. Dead volume, 200 cm^3; catalyst, 50 mg; but-1-ene, 400 μmol; reaction temperature, 323 K.

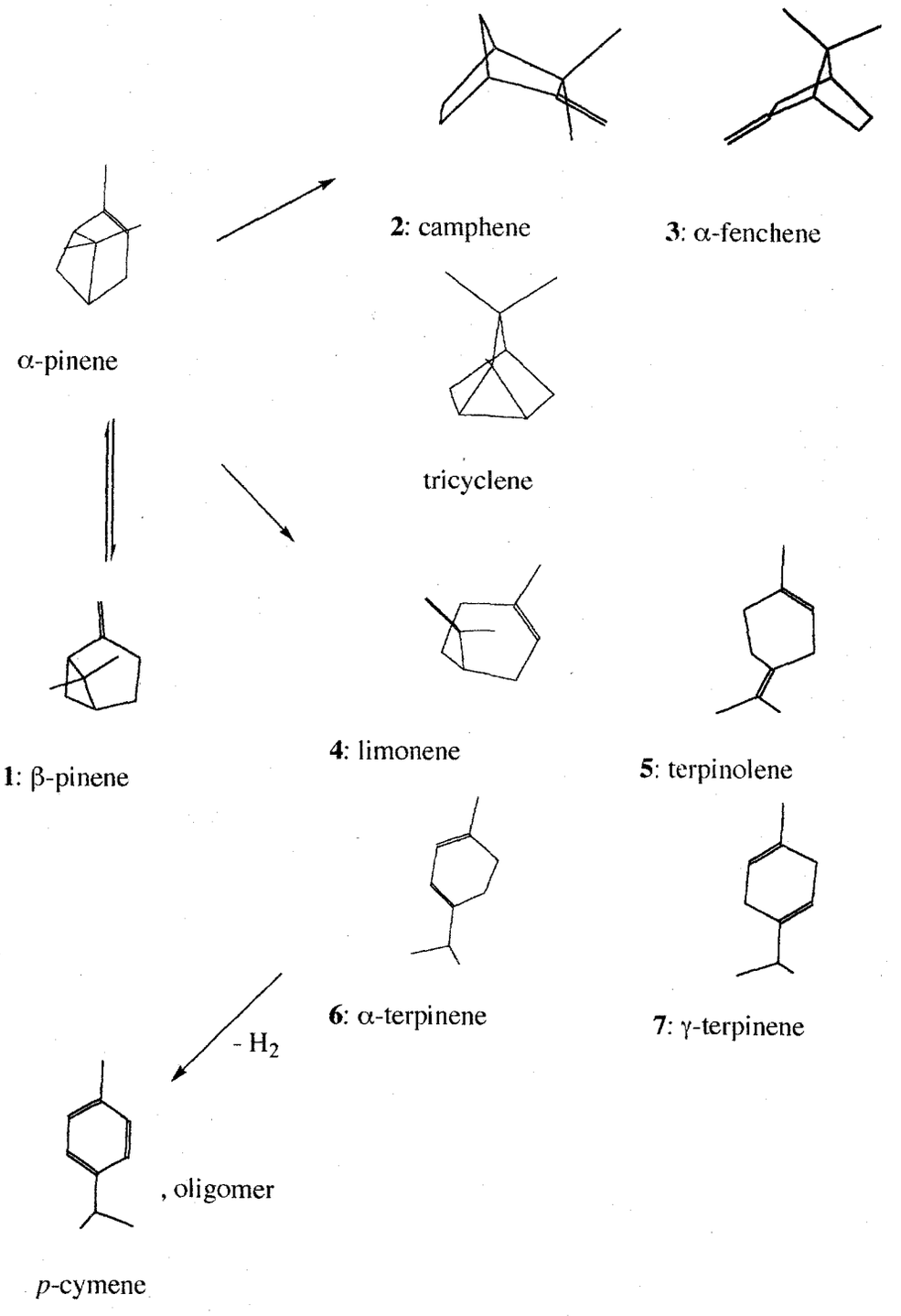

Figure 2. Scheme of α-pinene isomerization.

surface areas remained high. No correlation between initial rates and surface areas was observed. For example, only a 5% difference in surface area was observed for the samples pretreated at 873 and 1073 K, but the initial rates differed by 1.5 orders of magnitude. In all cases, the ratios of the cis-isomer to the trans-isomer in produced but-2-enes were 1.4 - 1.7, indicating that this reaction was catalyzed by acids. No reaction proceeded over SiO_2 gel pretreated at 673 K.

A similar catalytic behavior was exhibited in isomerization of α-pinene (Figure 2), as summarized in Table 2. It should be noted that the selectivity did not change at all, whereas the catalytic activity was drastically changed depending upon pretreatment temperature. Main products were camphene and limonene, and the selectivity to these two products was around 40%. Products of α-pinene isomerization can be classified into three groups. The first group is β-pinene. Over solid base catalysts, only equilibrium between α-pinene and β-pinene would be observed.[26] The second group consists of bicyclic (camphene, α-fenchene, etc.) and tricyclic (tricyclene, etc.) products. The last group is composed of monocyclic products (limonene, terpinolene, α-terpinene, γ-terpinene, etc.). One remarkable result of the present study is that the formation of β-pinene was negligible over FSM-16. This result also revealed that few basic sites existed on FSM-16, and this reaction was catalyzed by acids. It was reported that monocyclic products were formed more preferentially than bi- or tricyclic products over strong acid catalysts.[24] The independence of selectivity for this reaction indicates that the maximum acid strengths were not changed by pretreatment temperatures.

As shown in Table 3, over SiO_2 gel, δ-$Na_2Si_2O_5$, $H_2Si_2O_5$, JRC-SIO-5, and JRC-SIO-7, α-pinene isomerization hardly took place even at 353 K. As-calcined $H_2Si_2O_5$ pretreated at 373 and 473 K, which remained as a crystal structure, was also inactive. The result of JRC-SIO-7 shows that silica containing 195 ppm of Al is not enough to catalog this reaction at the temperature of 353 K. Furthermore, Al-doped $H_2Si_2O_5$ showed very low activity. Typical acid catalysts were also tested (Table 3). γ-Al_2O_3, TiO_2, $Nb_2O_5 \cdot nH_2O$, and $NiSO_4 \cdot nH_2O$ were active for this reaction at 353 K, but activities were quite low compared to that of FSM-16. In the case of $NiSO_4 \cdot nH_2O$, a selectivity for bi- or tricyclic products was particularly high, 88%, which coincides with the previous reports.[24] It is very intriguing that HZSM-5, the Si/Al atomic ratio of which was 12.3, known as a strong acid catalyst, was less active than FSM-16 at least at a temperature of 303 K. It may be due to its small pore size. Although FSM-16 has a large mesopore of 28 Å, the MFI type zeolite has a micropore in which the three-dimensional channel system has straight 10-ring 5.2 x 5.7 Å channels connected by a zigzag structure like 5.3 x 5.6 Å channels. In the case of HZSM-5, a diffusion of substrates or products was suppressed especially at a low temperature of 303 K. These results indicate that the effective surface area of MFI type zeolite for α-pinene isomerization is much lower than that of FSM-16. FSM-16 could provide a reaction field for large molecules such as α-pinene. In addition, HZSM-5 of Si/Al = 623 was almost inactive at 303 K and showed low activity even at 353 K, although the Si/Al atomic ratios of the HZSM-5 and FSM-16 were almost the same.

TABLE 3: Results of α-Pinene Isomerization at 353 K[a]

Catalyst	Pretreatment Temp/K	Conversion (%)	Selectivity[b] (%) 1	2	3	4	5	6	7	8
FSM-16 [c]	673	77.8	0	41	4	41	9	2	2	1
SiO_2 gel	673	0.0								
	1073	0.0								
δ-$Na_2Si_2O_5$	673	0.0								
Al-doped $Na_2Si_2O_5$[d]	673	0.0								
$H_2Si_2O_5$	673	0.0								
Al-doped $H_2Si_2O_5$[d]	673	1.7	4	38	4	43	6	1	2	2
JRC-SIO-5	673	<0.1								
JRC-SIO-7	673	<0.1								
γ-Al_2O_3	673	3.4	33	44	2	17	2	1	1	tr
TiO_2	673	0.6	31	43	2	13	3	1	3	4
ZrO_2	673	0.0								
HZSM-5 (12.3)[c]	673	18.8	1	36	28	25	2	2	1	5
HZSM-5 (40.0)[c]	673	6.1	2	35	19	33	3	2	2	4
HZSM-5 (623)	673	18.0	2	33	24	28	2	3	2	6
[c]	673	0.2								
NaY	673	21.1	1	24	2	55	9	3	5	1
$Nb_2O_5 \cdot nH_2O$	373	6.5	5	52	5	26	5	2	2	3
$NiSO_4 \cdot nH_2O$	673	54.5	tr	77	3	7	2	1	tr	10[e]
MgO[f]	873	2.1	100	tr						tr
CaO[f]	873	2.2	95							5

a α-Pinene, 2 mL; catalyst, 100 mg; reaction time,3 h.

b 1,β-pinene; 2, camphene; 3, α-fenchene; 4, limonene; 5, terpinolene; 6, α-terpinene; 7, γ-terpinene; 8, others.

c Catalyst: 50 mg; reaction temperature, 303 K.

d Si/Al atomic ratio was 16.1 as a starting material.

e Tricyclene: 8%.

f Catalyst: 300 mg as $M(OH)_2$ (M = Mg, Ca).

TABLE 4: Results of β-Pinene Isomerization[a]

Catalyst	FSM-16	MgO	CaO
Pretreatment Temperature /K	673	873	873
Reaction Temperature /K	353	423	423
Weight /mg	50	300[b]	300[b]
Time /h	0.5	3	3
Conversion (%)	20.8	3.5	9.3
Selectivity (%)			
α-Pinene	11	98	99
Camphene	27	2	1
Limonene	36		
Terpinolene	9		
Others	17	tr	tr

a β-Pinene: 2 mL.

b As $M(OH)_2$, (M = Mg, Ca).

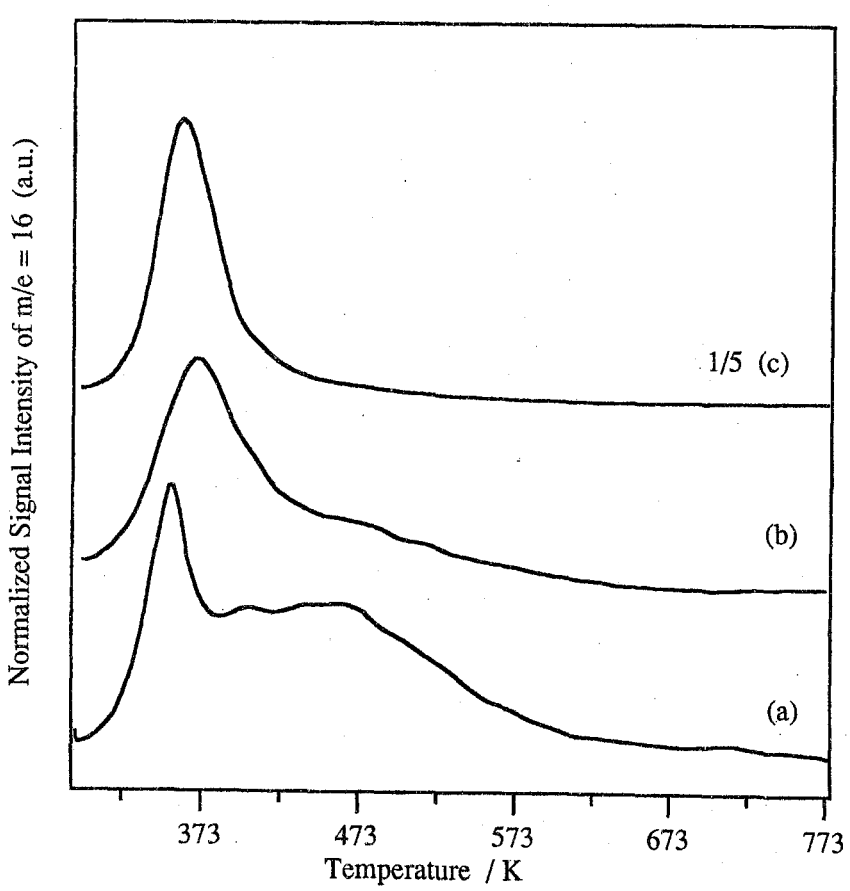

Figure 3. NH_3-TPD profiles of FSM-16 (a), SiO_2 (b), and $H_2Si_2O_5$ (c) pretreated at 673 K.

The second intriguing point is that the selectivity for formation of α-fenchene was particularly high. It results from restricted transition state selectivity. Another HZSM-5 of different Si/Al atomic ratio also showed high selectivity for α-fenchene formation. In the small pore of the MFI type zeolite, it is difficult for α-pinene isomerization to bulky transition states to produce terpinolene, α-terpinene, γ-terpinene, and so forth, compared to that of limonene. In contrast, the FAU type zeolite has larger supercages of 13 Å, and this restriction was no longer observed. It was reported that NaY had acid sites, the maximum acid strength of which range from H_0 = +1.5 to +4.0.[35] Although NaY is a very weak acid in nature, its specific surface area was estimated to be 973 $m^2\ g^{-1}$ by Langmuir plot. The high activity of NaY was due to the large surface area in comparison with other catalysts. Furthermore, over Brønsted acid catalysts, catalytic activity was strongly related to the mobility of protons. From IR experiments, Ward observed the delocalization of protons on HY in the range 473 - 700 K.[36] Baba et al. observed changes of the line width of the ^1H MAS NMR signal of acidic OH groups of HZSM-5 with temperature and found a relation between line widths and catalytic activities.[37] They discussed that the mobility of protons depended on temperature and the same amounts of protons would not necessarily exhibit the same activities.

MgO and CaO were also active for α-pinene isomerization. The selectivities for β-pinene formation were almost 100%, while they exhibited low conversion at 353 K (Table 3). The selective isomerization between α-pinene and β-pinene is one of the characteristics of solid base catalyst, and the low conversions were due to the low equilibrium constant of β-pinene to α-pinene.[26] Table 4 summarizes isomerization of β-pinene over FSM-16, MgO, and CaO. Over solid base catalysts, only transformation between β-pinene and α-pinene was selectively catalyzed, and formation of other products was negligible. In contrast, the reaction continuously proceeded via α-pinene, and many kinds of secondary products were observed over FSM-16. The result of β-pinene isomerization also strongly suggests that not basic but acidic sites were the main active sites on FSM-16. The lack of basic sites over FSM-16 was supported by the result of but-1-ene isomerization discussed above. In general, solid base catalyzes but-1-ene and the cis/trans ratio of produced but-2-ene is very large.[38] In the case of FSM-16, however, that ratio was between 1.4 and 1.7.

Figure 3 shows NH_3-TPD profiles of FSM-16, SiO_2 gel, and $H_2Si_2O_5$ pretreated at 673 K. SiO_2 gel and $H_2Si_2O_5$ exhibited a single peak around at 370 and 360 K respectively. The profile of FSM-16 shows a peak above 400 K besides a peak around 355 K; however the peak around at 473 K is not due to strong acid sites.[39] It clearly shows that the acid sites of FSM-16 pretreated at 673 K are different from those of the others. This was supported by IR spectra. Figure 4 shows IR spectra of adsorbed pyridine on SiO_2 gel and FSM-16 pretreated at 673 K. Assignment of pyridine adsorption peaks was as follows.[40] Peaks due to hydrogen-bonded pyridine were 1448 and 1598 cm^{-1}, those due to pyridine adsorbed on Brønsted acid sites were 1546 and 1638 cm^{-1}, and those on Lewis acid sites were 1456 and 1624 cm^{-1}.

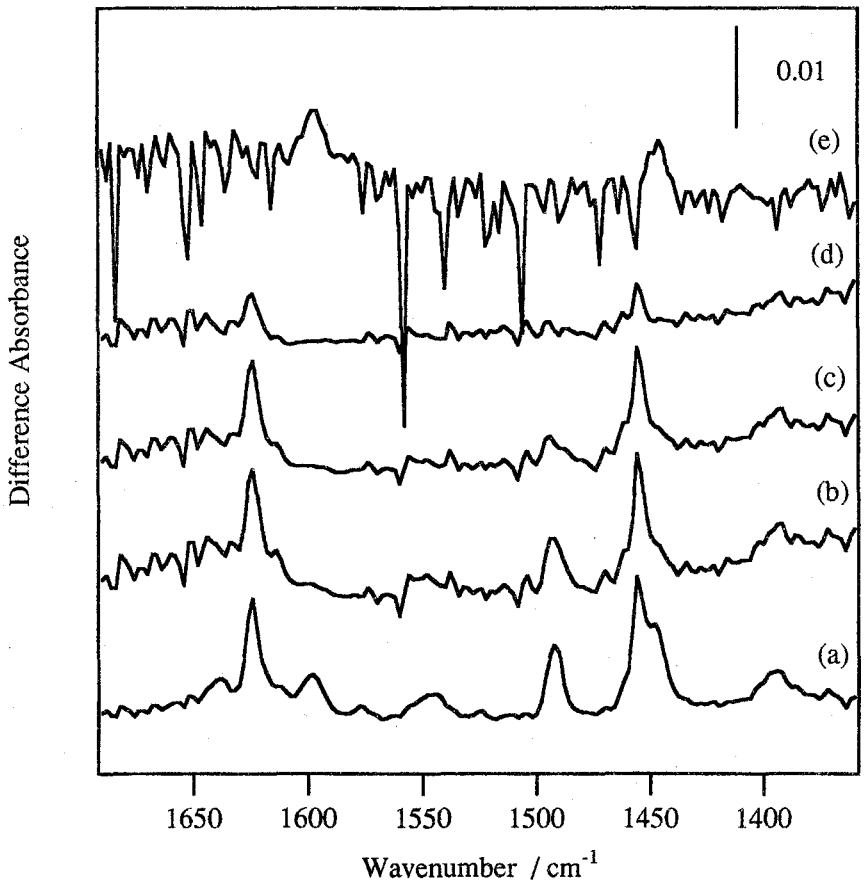

Figure 4. FTIR spectra of adsorbed pyridine at 423 K. FSM-16 (21 mg) evacuated at 423 K (a), 473 K (b), 573 K (c), and 673 K (d) and SiO_2 gel (80 mg) evacuated at 423 K (e).

A peak at 1493 cm^{-1} was due to pyridine adsorbed on both Brønsted and Lewis acid sites. SiO_2 gel possessed only hydrogen-bonded sites, whereas FSM-16 possessed both Brønsted and Lewis acid sites besides hydrogen-bonded sites. When FSM-16 adsorbing pyridine was evacuated at 473 K, hydrogen bonded pyridine and pyridine adsorbed on Brønsted sites were desorbed. Almost all of the pyridine was desorbed at 673 K with increasing evacuation temperature. IR spectra of pyridine adsorbed on Al-containing MCM-41 were measured by many researchers.[9-11,41] Although Corma et al. observed Brønsted acid sites on MCM-41 of Si/Al = 100,[9] Jentys et al. observed only Lewis acid sites on the same Si/Al ratio's material.[11] Further, Jentys et al. and Mokaya et al.[10] observed only hydrogen-bonded species on pure siliceous MCM-41. While the Si/Al atomic ratio of synthesized FSM-16 was 735, both Lewis and Brønsted acid sites were observed on FSM-16. The spectrum was quite similar to those of Al-MCM-41 (Si/Al = 100). Although we have not compared directly the acidic property between FSM-16 and MCM-41, IR spectra of adsorbed pyridine suggest that the acidic property of FSM-16 is higher than, or at least equal to, those of MCM-41. Zhao et al. performed pyridine TPD of siliceous MCM-41 and observed two desorption peaks in the temperature range 323 - 523 K.[42] They claimed that two peaks were due to desorbed pyridine from hydrogen-bonded SiOH and free SiOH groups, and both activation energies of desorption sites were similar to those of amorphous silica. In fact, the reported pyridine desorption profile for silica gel (Kieselgel 60; Merk NV) was quite similar.[43] The pyridine desorption profile for MCM-41 was also quite similar to the NH_3 desorption profile for FSM-16, although it is very difficult to compare with the results of pyridine and NH_3-TPD experiment. Because the NH_3-TPD profile for SiO_2 gel was different from that for FSM-16, it could be possible that the property of siliceous MCM-41 is similar to that of FSM-16 demonstrated in the present work.

Contribution of Aluminum to Acidic Property

FSM-16 employed in the present work contains a trace amount of Al (Si/Al = 320, 735), which might be associated with the acid sites. Van Roosmalen *et al.* reported the catalysis of but-1-ene isomerization over silica gel.[44] They concluded that activities of silica gel were directly proportional to the concentration of Al being present as a trace impurity at 600 - 700 K. In their report, silica gel (Rhône-Progil; Spherosil XOA-400, 361 $m^2\ g^{-1}$, Si/Al = 100 - 1000) showed a rate constant of 31 nmol $m^{-2}\ s^{-1}$ at 600 K and 1.1 x 10^5 Pa for but-1-ene, whereas in the case of FSM-16, the activity comparable to that reported was exhibited at a low temperature of 323 K and a low pressure of 4.7 x 10^3 Pa for but-1-ene. Furthermore, we confirmed that the amorphous silica prepared from the same water glass was inactive. West et al. reported that many reactions catalyzed by silica gel took place at impurity sites.[45] They observed improvement of activity more than 100 times for hex-1-ene isomerization over $Al(NO_3)_3$ added to silica gel (120 ppm as Al) than the original silica gel. However, the original silica gel (Davison Grade 59 or Grade 70) contains 0.1% Al_2O_3, 0.01% Fe_2O_3, 0.02% TiO_2,

0.07% CaO, 0.06% Na_2O, and 0.03% ZrO_2, and the rate of hex-1-ene isomerization was reported to be 0.2 mmol h^{-1} g^{-1} at 373 K.[45] This value was about 60 times smaller than the rate of but-1-ene isomerization over FSM-16 at 323 K. Although it is hard to compare them, we should suppose that the acidity of FSM-16 is much higher than that of silica gel containing 0.1% Al_2O_3.

In the case of ZSM-5, it was reported that catalytic activities of many reactions were directly proportional to the concentration of Al and the proportional relations were applicable down to 10 ppm.[46] The reported reactions were propylene polymerization,[47] *n*-hexane cracking,[48-50] hex-1-ene isomerizations,[49] and so forth. However, all reactions were performed over 700 K. On the other hand, isomerization of but-1-ene and α-pinene proceeds over FSM-16 even at 323 K. There have been no reports that butene isomerization proceeds at ambient temperature on silica including such a trace amount of impurity at measurable rates. In α-pinene isomerization, activities of FSM-16 whose Si/Al atomic ratio was 320 and 735 were almost the same. We emphasize again that the acidity of FSM-16 exhibited by the present sample is not due to Al impurity.

Dehydroxylation

As shown in Figure 1 and Table 2, FSM-16 pretreated at 673 K showed maximum catalytic activity. The activity was drastically reduced when FSM-16 was pretreated at higher than 873 K. Sintering or the change of surface property is thought to be the reason for deactivation. The possibility that sintering causes deactivation can be excluded from the result of BET measurements. Therefore, the change of surface property should be the main reason for deactivation. Dehydration and condensation of SiOH groups should relate closely to the change of specific property.

Figure 5 shows a thermogravimetric analysis and H_2O-TPD profile of FSM-16. The weight loss completely corresponded to desorption of H_2O. Since large part of physisorbed H_2O was eliminated below 373 K, a TPD experiment was performed after preevacuation at 373 K for 1 h. Because FSM-16 was once calcined at 823 K in a synthesis step, the signal intensity of $m/e = 18$ below 773 K was small. Dehydroxylation continuously proceeded over 773 K. A large quantity of H_2O evolution over 773 K was due to dehydroxylation of a silanol group to form a siloxane bridge,[51] and catalytic activities were drastically lowered in this region.

IR spectra of FSM-16 showed similar behavior, as shown in Figure 6. With increasing evacuation temperature, a very broad band around 3500 cm^{-1} gradually decreased and a new window around 900 cm^{-1} appeared. The band around 3500 cm^{-1} is due to strongly hydrogen bonded silanol groups. Figure 6b shows spectra of isolated silanol groups. In the case where the evacuation temperature was below 773 K, positions of the peak maximum were 3742 cm^{-1}. As evacuation temperature increases, the peak position was shifted to higher frequency. When FSM-16 was evacuated at 1073 K, the peak position was finally reached at 3745 cm^{-1}.

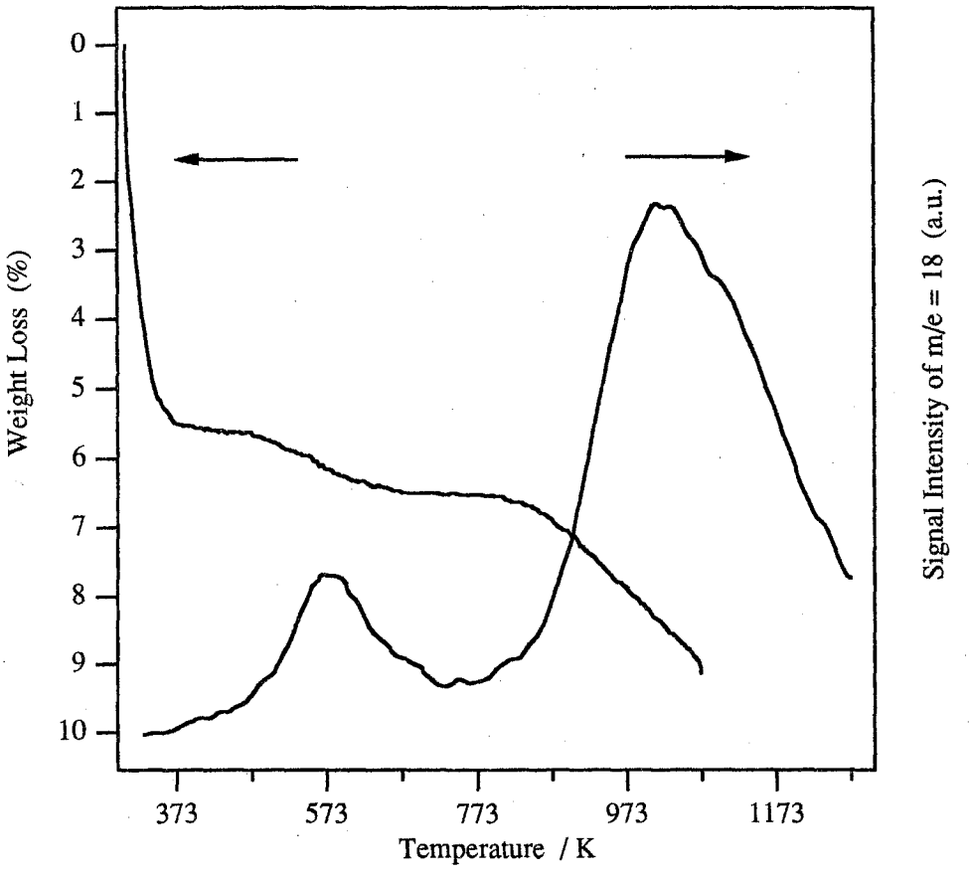

Figure 5. Thermogravimetric analysis and H_2O-TPD profile of FSM-16. Prior to TPD measurement, 20 mg of FSM-16 was evacuated at 373 K for 1 h.

Morrow et al. reported that observed bands of isolated silanol groups were a combination of two species.[52] One was truly isolated silanol (ν(SiO-H) of species I: 3750 cm^{-1}), and the other was weakly perturbed vicinal pairs of silanols (ν(SiO-H) of species II: 3740 cm^{-1}). Morrow et al. also reported that fumed silica and precipitated silica have different peak frequencies and bandwidths of isolated silanol because different preparation methods caused the ratio of the two isolated silanols to differ. If the concentration of weakly perturbed vicinal pairs of silanol is high, the peak position should be near 3740 cm^{-1}. On the contrary, if the concentration of truly isolated silanol is high, the peak position should be near 3750 cm^{-1}. From the band position of FSM-16, we conclude that isolated silanol groups on FSM-16 are rich in species II (weakly perturbed vicinal pairs of silanol). Ishikawa et al. observed a silanol band at 3740 cm^{-1} over FSM-16 and estimated the surface concentration.[53] The wavenumber also indicates that almost all the silanol groups are weakly perturbed, although their concentration was lower than that of ordinary silica gel. Over siliceous MCM-41, the band due to isolated silanol groups was confirmed at 3738 cm^{-1}, which was also close to the band of species II.[42]

When FSM-16 was evacuated at above 773 K, weakly perturbed vicinal pairs of silanol (species II) were selectively dehydroxylated to form truly isolated silanol (species I). The blue shift of the isolated silanol band on FSM-16 was due to a change of their ratio. These phenomena were more clearly shown in difference spectra, as shown in Figure 7. Below 673 K, broad bands of strongly hydrogen bonded silanol groups were mainly weakened. The difference spectrum between 573 and 673 K has the largest band area. It corresponded to the first peak of the H_2O-TPD profile and a gravimetric decrease (Figure 5). Above 773 K, the position of the weakened band was shifted to higher frequency. The most typical case was the difference spectra between 873 and 1073 K. The positions of weakened and strengthened peaks were 3741 and 3748 cm^{-1}, respectively. In this region, elimination of silanol groups occurred. We observed a new band generation around 892 cm^{-1} in accordance with blue shift of isolated silanol bands (Figure 6c). Morrow et al. observed generation of new two bands at 908 and 888 cm^{-1} on fumed silica. New bands appeared when silica was evacuated at temperatures higher than 873 K, and these intensities reached a maximum at 1473 K.[54-56] They assigned these peaks to a reactive strained siloxane bridge formed by condensation of isolated silanol groups. Further, Bunker *et al.* assigned them to an edge-shared silicate tetrahedral ring.[57] In the second derivative of the IR spectrum, a trace peak and a distinct peak were observed on FSM-16 at 912 and 892 cm^{-1}, respectively. IR behavior exhibited by FSM-16 resembles that previously reported on fumed silica, although the new band on FSM-16 was almost single. The IR result suggests that weakly perturbed vicinal pairs of silanols on FSM-16 condensed to produce siloxane bridges, similar to those on fumed silica and silica gel.[51] Therefore the dehydroxylation of surface silanol groups of FSM-16 was responsible for the deactivation. The temperature of 673 K is the point where catalytic activity of FSM-16 decreased. Matsumura et al. reported that silica gel pretreated above 1000 K was active for selective ethanol dehydrogenation and the active site was an active siloxane bridge formed by the dehydration of

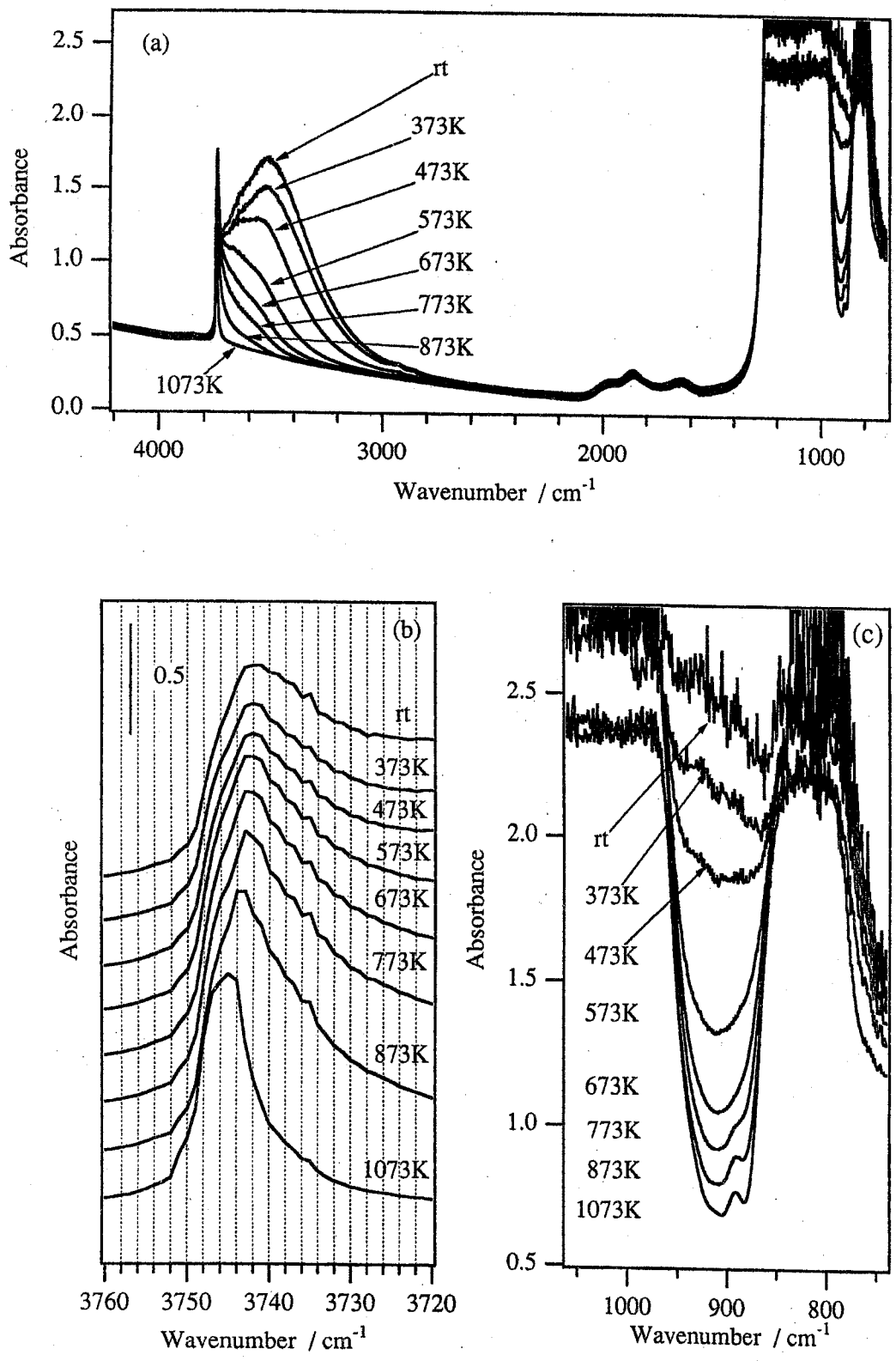

Figure 6. FTIR spectra of FSM-16 evacuated at various temperatures.

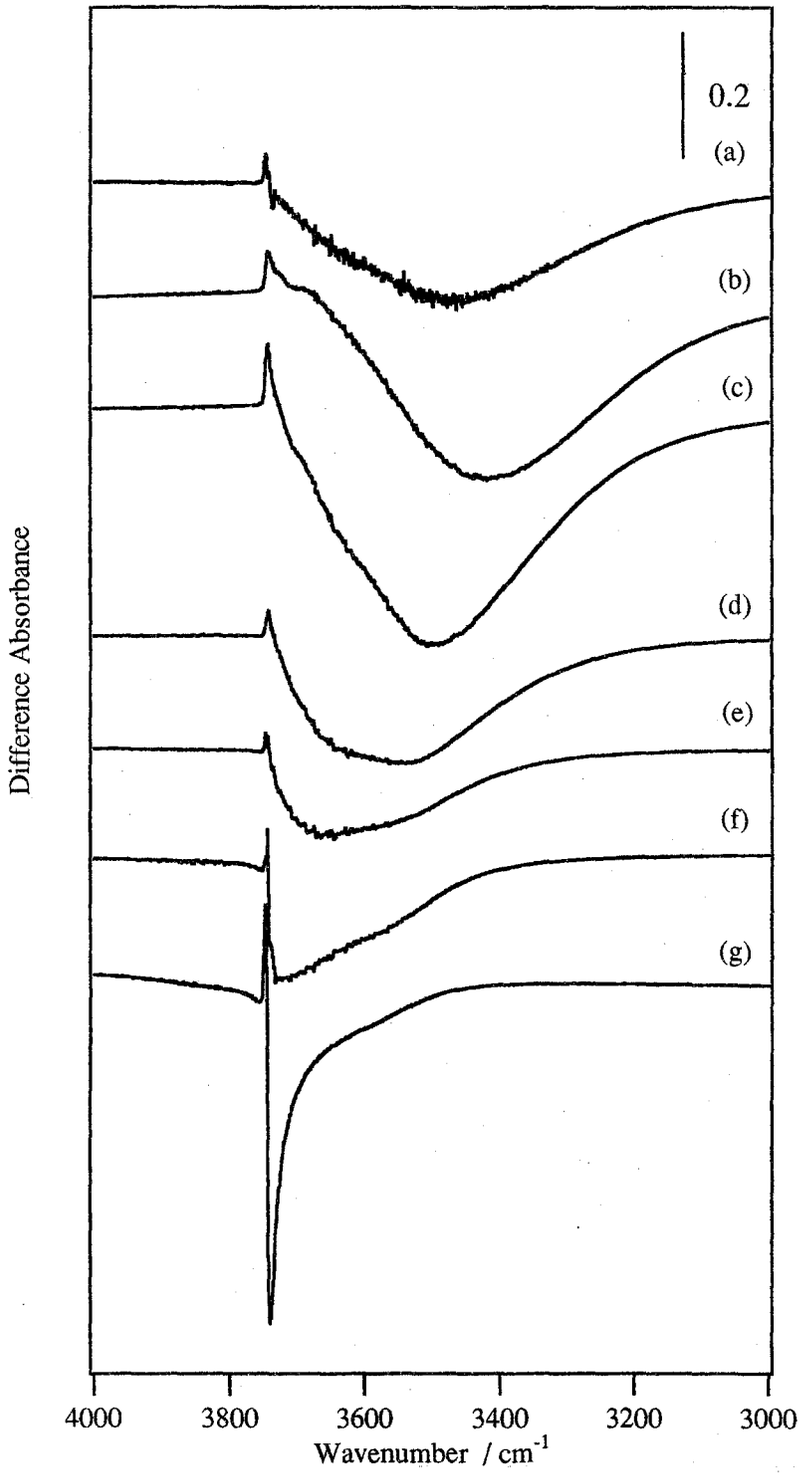

Figure 7. Difference IR spectra of FSM-16 evacuated at various temperatures: between 373 K and room temperature (a), 473 and 573 K (b), 573 and 673 K (c), 673 and 773 K (d), 773 and 873 K (e), and 873 and 1073 K (f).

silanol groups.[58,59] In contrast, the siloxane bridge on FSM-16 did not concern the isomerization because no increase in activity was observed for FSM-16 evacuated at higher temperatures. The isolated silanol band observed on FSM-16 was only one and the wavenumber was around 3742 cm^{-1}, so called neutral. We conclude that the active sites were surface silanol groups of species II themselves and/or silanol-related sites, although they were not so called acidic silanol bands around 3600 cm^{-1}. This presumably results from the synthesis method and the crystal structure of FSM-16, on which the silanol groups were supposed to be regularly arrayed. There are very few reports in which neutral silanol groups are active sites for any reactions. Sato et al. claimed that Beckmann rearrangement of cyclohexanone oxime was catalyzed by neutral silanol groups, whose wavenumber was 3740 cm^{-1}, on the external surface of highly siliceous MFI type zeolites.[60] Although they did not discuss the silanol groups in detail, we suspect that the silanol groups should be weakly perturbed vicinal pairs.

Regeneration of Acid Sites

In the previous section, we mentioned that catalytic activity of the highest FSM-16 was exhibited by pretreatment at 673 K and deactivation was due to dehydroxylation of silanol groups. To examine whether silanol groups of FSM-16 participate in acidic property or not, we prepared calcined and rehydrated FSM-16. If only silanol groups were the active sites, rehydrated FSM-16 should exhibit the same activity as fresh catalyst. Table 5 summarizes results of α-pinene isomerization over variously treated FSM-16. Pretreatments were performed at 673 K in all cases. The catalyst noted simply as FSM-16 in Table 5 was the fresh catalyst, which was the same catalyst as listed in Table 2. FSM-16 calcined at 1173 K (FSM-1173) was less active than the fresh catalyst, but the activity was slightly higher than that pretreated at 1073 K. As expected, the activity of the less active catalyst was completely restored by hydration of the catalyst at 353 K followed by calcination at 773 K (FSM-1173H). The selectivity was not changed. These results indicate that hydration to restore silanol groups on FSM-16 regenerates acidic sites. The reason FSM-1173 was more active than FSM-16 pretreated at 1073 K was explained as follows. By moisture in atmospheric air, partial rehydration proceeded on FSM-1173 during the storage. Rehydrated FSM-16 having been calcined at 1373 K (FSM-1373H) did not catalyze isomerization of α-pinene, in contrast to the result of FSM-1173H. This indicates that FSM-1373H no longer had the same properties as fresh FSM-16. The reason for the difference of catalytic activity between FSM-1173H and FSM-1373H is considered as follows. The possible first reason may be that the active elements such as Al and Ti on FSM-16 were lost during various treatments. The first reason can be excluded because no change of elemental composition was found (Table 1). The second is the fundamental structural change of FSM-16. This is only sintering.

TABLE 5: Change of the Activity of α-Pinene Isomerization over FSM-16[a]

Catalyst	Pretreatment Temp. /K	Conversion (%)	Selectivity[b] (%) 1	2	3	4	5	6	7	8
FSM-16	673	44.6	tr	40	4	43	9	2	2	tr
FSM-1173	673	8.8	1	36	4	46	8	2	2	1
FSM-1173H	673	48.1	tr	42	4	43	7	2	1	1
FSM-1373H	673	<0.1								

a α-Pinene: 2 mL. catalyst: 50 mg. reaction temperature: 303 K. reaction time: 0.5 h.

b 1, β-Pinene; 2, camphene; 3, α-fenchene; 4, limonene; 5, terpinolene; 6, α-terpinene; 7, γ-terpinene; 8, others.

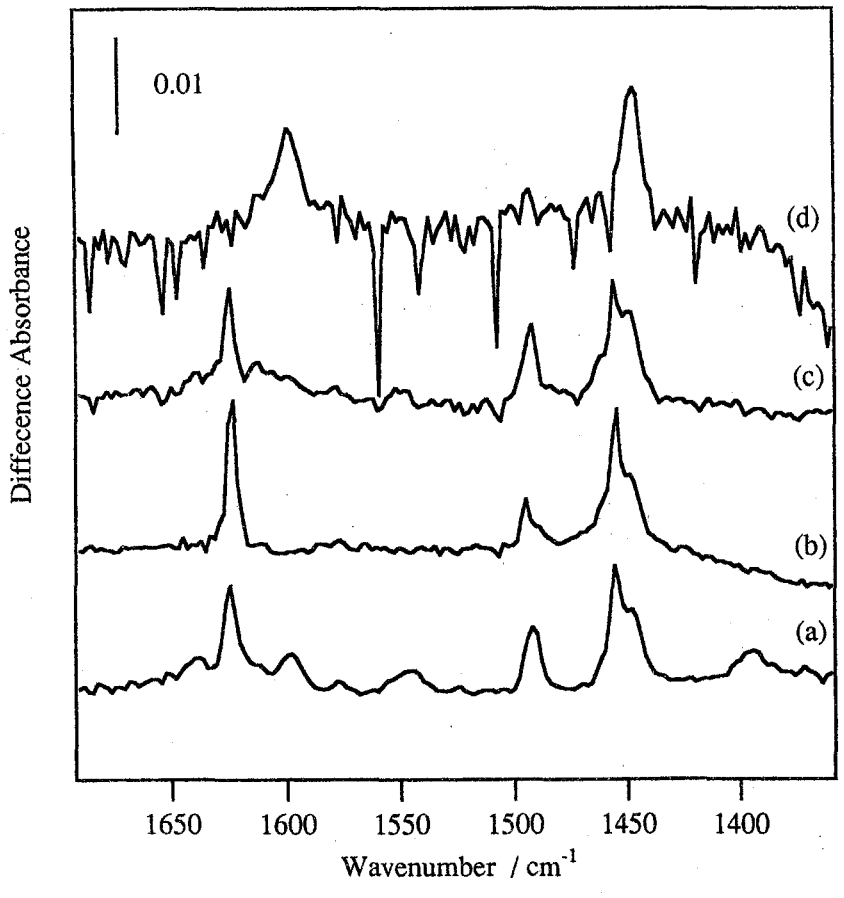

Figure 8. FTIR spectra of adsorbed pyridine at 423 K: fresh FSM-16 (21 mg) (a), FSM-1073pre (20 mg) (b), FSM-1173H (30 mg) (c), and FSM-1373H (80 mg) (d).

To investigate the difference of acidic properties more in detail, IR spectra of adsorbed pyridine were recorded. Figure 8 shows those of four typical variously treated FSM-16. The four catalysts are the fresh one, FSM-16 pretreated at 1073 K (FSM-1073pre), FSM-1173H, and FSM-1373H. Brønsted pyridine was observed on the fresh FSM-16, while not on FSM-1073pre. Although as many Lewis acid sites existed on the surface as on fresh FSM-16, FSM-1073pre was inactive for but-1-ene and α-pinene isomerization. The band around 1492 cm^{-1} was assigned to overlapping 19a bands of both Lewis and Brønsted pyridine. The intensity ratio of the band at 1492 cm^{-1} to a 19b band of Lewis pyridine at 1456 cm^{-1} was quite different from fresh FSM-16 and FSM-1073pre. The ratio of Lewis and Brønsted acid sites ([L]/[B] ratio) can be calculated from the band area of adsorbed pyridine at 1455 and 1492 cm^{-1}.[63] The calculated [L]/[B] ratio of fresh FSM-16 was 2.6, and that of FSM-1073pre was 5.6. This suggests that the fraction of Brønsted sites was decreased by pretreatment at 1073 K. The majority of acid sites were Lewis acid; however, Lewis acid sites are inactive for the catalysis of the isomerization of α-pinene and but-1-ene. The IR spectrum of adsorbed pyridine on FSM-1173H was quite similar to that on fresh FSM-16, and the [L]/[B] ratio of FSM-1173H was 2.6. This is in good accordance with the results of the catalysis. In other words, the surface property of FSM-1173H was the same as that of fresh FSM-16. On the other hand, FSM-1373H was quite different. Only hydrogen-bonded pyridine was observed in the IR spectrum of adsorbed pyridine on FSM-1373H, and it was quite similar to that of SiO_2 gel (Figure 4). This strongly suggests that FSM-1373H was fundamentally different from that of fresh FSM-16 and FSM-1173H. From the results of catalytic activities and IR spectra, we conclude that the surface property of FSM-1373H is similar to that of ordinary silica gel rather than that of FSM-16.

To clarify the difference of each structure, we measured the XRD pattern of these samples. Figure 9 shows those of variously treated FSM-16 listed in Table 5. The XRD pattern of fresh FSM-16 exhibited four peaks, and the primary *d* spacing was 38 Å. This profile is identical with that reported previously.[30] All peaks observed on FSM-1173 were shifted to higher degree. This was due to shrinkage of the lattice, and the shrunk primary *d* spacing was 32 Å. FSM-1173 and FSM-1173H still kept the structure of FSM-16, although the fourth peak disappeared. The result of XRD measurements shows that a series of rehydration procedures scarcely influenced the structure of FSM-1173. In the case of FSM-16 calcined at 1373 K, peaks below 10 degrees completely disappeared and no peaks were observed in all regions. This clearly shows that FSM-1373H became amorphous. From XRD results, we conclude that acidic properties appeared on only the crystal FSM-16. This result strongly suggests that the active site of FSM-16 was not due to impurity.

Over FAU type zeolites, Severino et al. reported that the change of the [L]/[B] ratio around 1.0 caused an abrupt change of selectivity to camphene in α-pinene isomerization.[64] They concluded that the reaction rate catalyzed by Brønsted sites was higher than that by Lewis sites and that Lewis sites preferentially catalyzed to produce bicyclic products such as

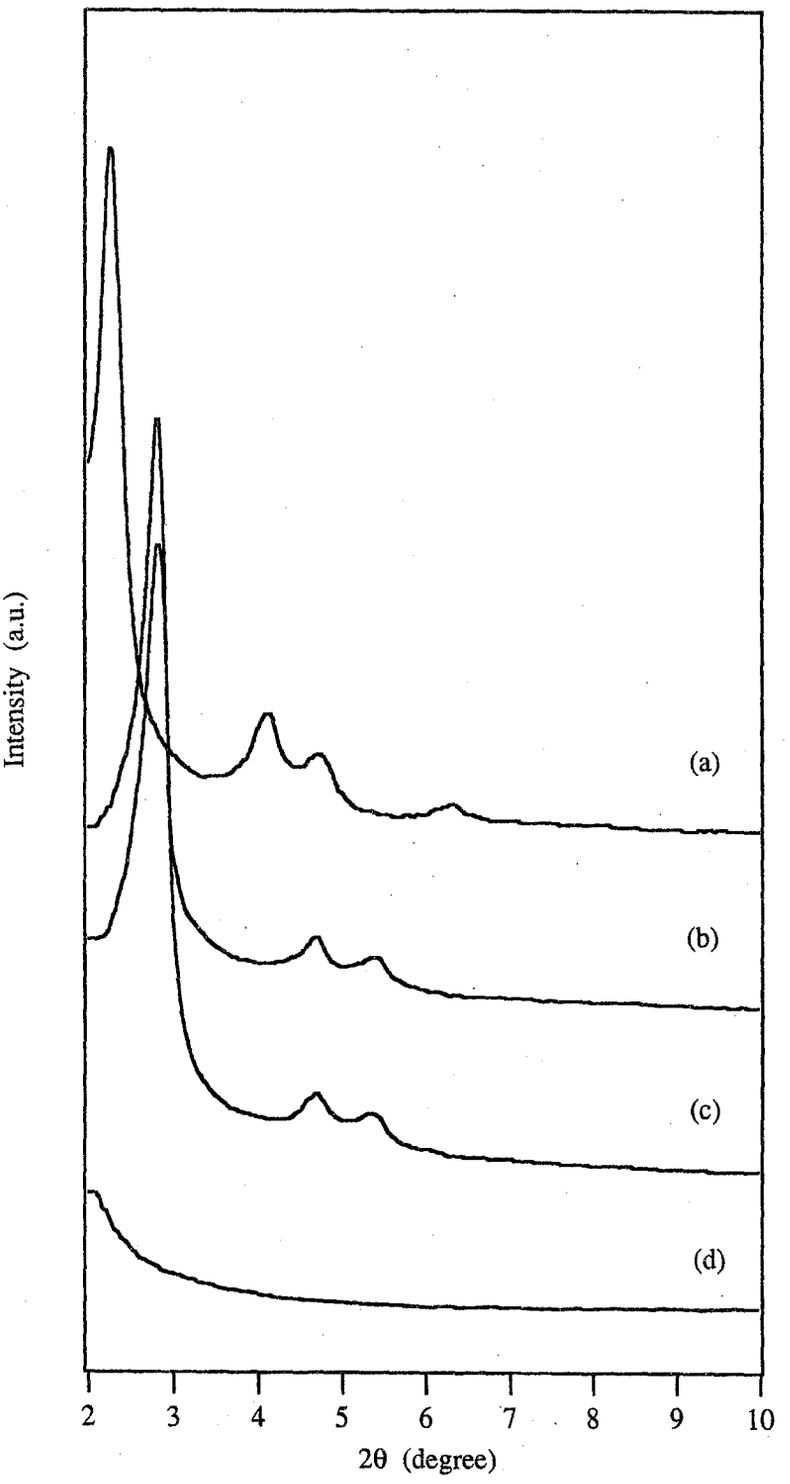

Figure 9. Cu Kα XRD patterns of fresh FSM-16 (a), FSM-1173 (b), FSM-1173H (c), and FSM-1373 (d).

camphene. In the case of FSM-16, selectivity for camphene was independent of pretreatment temperature. Further, low-temperature-treated niobic acid, known to be a typical Brønsted acid, gave a high selectivity for camphene. The suggestion by Severino et al. was not applicable to our experiments. The majority of acid sites on FSM-16 were Lewis sites, but Lewis sites did not participate in the catalysis of both but-1-ene and α-pinene isomerization. Therefore, we concluded that Brønsted acid sites were active sites for both reactions and that the sites were weakly perturbed vicinal pairs of silanol groups (species II).

Survey of Catalyst Property

It was reported that reversible dehydroxylation of silanols occurred below 673 K and irreversible dehydroxylation of isolated silanols occurred above 923 K.[51] On the other hand, silanol groups of FSM-1173 were completely restored by rehydration procedures. This was supported by results of α-pinene isomerization, as shown in Table 5. The difference between our experiments and reported results was due to rehydration processes. The rehydration has been attempted at ambient temperature with 100% relative humidity,[61,62] whereas FSM-16 was rehydrated in water at 353 K. To investigate the property of catalysts further, we measured the maximum of acid strength of catalysts by Hammett indicators. Table 6 summarizes maximum acid strength and BET specific surface area. Once SiO_2 gel (BET specific surface area was 650 $m^2\ g^{-1}$) was calcined at 1173 K, the surface area was reduced to 445 $m^2\ g^{-1}$. Even if calcined silica gel was rehydrated in water at 353 K, complete regeneration of silanol groups was impossible because of its sintering. In contrast, the surface area of FSM-1173 was maintained at 965 $m^2\ g^{-1}$. FSM-16 was stable at temperatures up to 1273 K and possessed high surface area even for a rehydrated sample calcined at 1173 K (Table 6). The rigid structure of FSM-16 made it possible to complete reversible dehydroxylation of isolated silanols.

FSM-16 pretreated at 673 and 1073 K exhibited medium acid strength of $H_0 = -3.0$. This value is almost the same as those for SiO_2-MgO [65,66] and $NiSO_4 \cdot nH_2O$,[67] but much weaker than that of SiO_2-Al_2O_3 which is stronger than $H_0 = -8.2$.[65,66] FSM-16, with Si/Al atomic ratios of both 735 and 320, showed the same value of maximum acid strength. The maximum acid strengths of SiO_2 gel were much weaker than those for FSM-16. Werner et al. reported that crystalline silicates have much stronger acid sites than those of silica gel. For example, $H_2Si_2O_5$ and $H_2Si_{14}O_{29} \cdot 5H_2O$ exhibited a maximum acid strength of $H_0 = +2.3$ to +3.3 and -5 to -3, respectively.[68] They discussed that the high acidity resulted from regular and extended hydrogen-bonding systems including the surface water molecules. The maximum acid strength of synthesized $H_2Si_2O_5$ was the same as the reported value of $H_0 = +3.0$, although calcined $H_2Si_2O_5$ became amorphous. From elemental analysis, The Al concentration of $H_2Si_2O_5$ was estimated to be only 80 ppm (Table 1); however, its maximum acid strength of $H_0 = +3.3$ was higher than that of SiO_2 gel of +4.8. These results show that almost pure siliceous materials have the possibility to exhibit acidic properties. Thus, we conclude that but-

TABLE 6: Maximum Acid Strength and BET Specific Surface Area

Catalyst	Pretreatment Temp. /K	Surface Area /$m^2\ g^{-1}$	H_0 max
FSM-16	473		-3.0 [c]
	673	1078	-3.0
	873	1045	
	1073	1026	-3.0
	1273	815	-5.6
FSM-16 [a]	673	965	-3.0
FSM-1173H	673	874	-3.0
FSM-1373H	673	37	-3.0 [c]
FSM-16 [b]	673	960	-3.0
SiO_2	673	650	+4.8
	1073	490	+3.3
$H_2Si_2O_5$	673	144	+3.3 [c]

a Calcined in a dry air stream at 1173 K for 2 h.

b Supplied by TOYOTA Central R & D Labs., Inc. (lot no. NG78-550).

c Hammet indicator was faintly colored.

1-ene and α-pinene isomerizations were catalyzed by Brønsted acid sites with an acidic strength of $H_0 < +3.3$. In the case of FSM-16, the selectivity of α-pinene isomerization and the maximum acid strength were independent of the pretreatment temperature. This result indicates that the change of catalytic activity of FSM-16 does not depend on the change of the acid strength but on the number of acid sites. IR and H_2O desorption experiments showed that active sites on FSM-16 were blocked by hydrogen-bonded adsorbed water when FSM-16 was pretreated at below 673 K. This was supported by the result that addition of water to pretreated FSM-16 drastically lowered catalytic activity. Although FSM-16 pretreated at 1273 K showed the maximum acid strength of $H_0 = -5.6$, the number of the strongest acid sites was quite small because no change of selectivity for α-pinene isomerization was observed and activities for α-pinene and but-1-ene isomerization were quite low. Although FSM-1373H was amorphous, it still possessed a small number of acid sites whose $H_{0\ max}$ was -3.0. As shown in Table 5, the activities of FSM-1373H and fresh FSM-16 were different from each other by over 400 times. On the other hand, the BET specific surface area of FSM-1373H was about 3% of the fresh one. The reduction of catalytic activity was far from that of the surface area. Therefore, the possibility that sintering was the main reason for deactivation is excluded. The structure of FSM-16 is indispensable to acidic property, although the mechanism of generation of acid sites is not clear. This is supported by the fact that FSM-16 having became amorphous, could not regenerate the acidic property by the rehydration process.

We suppose that the structure of FSM-16 is indispensable to acidic property, especially to its thin wall and regularly arrayed silanol groups.

Conclusion

FSM-16 catalyzes but-1-ene isomerization at 323 K and α-pinene isomerization at 303 K in the liquid phase. Catalytic activity of FSM-16 was dependent upon pretreatment temperatures and showed a maximum at 673 K. The activity of FSM-16 calcined at higher than 773 K was much reduced, but it could be restored by rehydration procedures as long as the samples maintained the crystal structure. The active sites were weakly perturbed silanol groups and a trace amount of Al of FSM-16 did not effect acidic property. Maximum acid strength was invariably $H_0 = -3.0$, independent of pretreatment temperatures. These properties are related to the regular structure of FSM-16.

References

1 Inagaki, S; Fukushima, Y; Kuroda, K. *J. Chem. Soc., Chem. Commun.* **1993**, 680.

2 Kresge, C. T.; Lenowicz, M. E.; Roth, W. J.; Vartuli, J. C.; Beck, J. S. *Nature* **1992**, *359*, 710.

3 Beck, J. S.; Vartuli, J. C.; Roth, W. J.; Lenowicz, M. E.; Kresge, C. T.; Schmitt, K. D.; Chu, C. T.-W.; Olson, D. H.; Sheppard, E. W.; McCullen, S. B.; Higgis, J. B.; Schlenker, J. L. *J. Am. Chem. Soc.* **1992**, *114*, 10834.

4 Tanev, P. T.; Chibwe, M.; Pinnavaia, T. J. *Nature* **1994**, *368*, 321.

5 Zhang, W.; Fröba, M.; Wang, J.; Tanev, P. T.; Wong, J.; Pinnavaia, T. J. *J. Am. Chem. Soc.* **1996**, *118*, 9164.

6 Monnier, A.; Schüth, F.; Huo, Q.; Kumar, D.; Margolese, D.; Maxwell, R. S.; Stucky, G. D.; Krishnamuty, M.; Petroff, P.; Firouzi, A.; Janicke, M.; Chmelka, B. F. *Science* **1993**, *261*, 1299.

7 O'Brien, S.; Francis, R. J.; Price, S. J.; O'Hare, D.; Clark, S. M.; Okazaki, N.; Kuroda, K. *J. Chem. Soc., Chem. Commun.* **1995**, 2423.

8 Tanabe, K.; Misono, M.; Ono, Y.; Hattori, H. *New Solid Acids and Bases*; Kodansha, Elsevier, Tokyo, 1989; pp 91-105.

9 Corma, A.; Fornes, V.; Navarro, M. T.; Pérez-Pariente, J. *J. Catal.* **1994**, *148*, 569.

10 Mokaya, R.; Jones, W.; Luan, Z.; Alba, M. D; Klinowski, J. *Catal. Lett.* **1996**, *37*, 113.

11 Jentys, A.; Pham, N. H.; Vinek. H. *J. Chem. Soc., Faraday Trans.* **1996**, *92*, 3287.

12 Inagaki, S.; Fukushima, Y.; Okada, A.; Kurauchi, T.; Kuroda, K.; Kato, C. *Proc. 9th Int. Zeolite Conf., I* **1992**, 305.

13 Inagaki, S.; Yamada, Y.; Fukushima, Y. *Stud. Surf. Sci. Catal.* **1996**, 105, 109.

14 Tanev, P. T.; Chibwe, M.; Pinnavaia, T. J. *Science* **1994**, *368*, 321.

15 Corma, A.; Navarro, M. T.; Pérez Pariente, J. *J. Chem. Soc., Chem. Commun.* **1994**, 147.

16 Rhee, C. H.; Lee, J. S. *Catal. Lett.* **1996**, *40*, 261.

17 Ryoo, R.; Ko, C. H.; Kim, J. M.; Howe, R. *Catal. Lett.* **1996**, *37*, 29.

18 Junges, U.; Jacobs, W.; Voigt-Martin, I.; Krutzsch, B.; Schüth, F. *J. Chem. Soc., Chem. Commun.* **1995**, 2283.

19 Shinoda, T.; Izumi, Y.; Onaka, M. *J. Chem. Soc., Chem. Commun.* **1995**, 1801.

20 Huber, C.; Moller, K.; Bein, T. *J. Chem. Soc., Chem. Commun.* **1994**, 2619.

21 Maschmeyer, T.; Rey, F.; Sanker, G.; Thomas, M. *Nature* **1995**, *378*, 159.

22 Macquarrie, D. J.; Jackson, D. B. *Chem. Commun.* **1997**, 1781.

23 Liu, C.-J.; Li, S.-G.; Pang, W.-Q.; Che, C.-M. *Chem. Commun.* **1997**, 65.

24 Ohnishi, R.; Tanabe, K.; Morikawa, S.; Nishizaki, T. *Bull. Chem. Soc. Jpn.* **1974**, *47*, 571.

25 Tanaka, T.; Iatagaki, A.; Zhang, G.; Hattori, H.; Tanabe, K. *J. Catal.* **1990**, *122*, 384.

26 Ohnishi, R.; Tanabe, K. *Chem. Lett.* **1974**, 207.

27 Galarneau, A.; Barodawalla, A.; Pinnavaia, T. J. *Chem. Commun.* **1997**, 1661.

28 Hamaguchi, K.; Hattori, H. *React. Kinet. Catal. Lett.* **1997**, *61*, 13.
29 Yoshida, H.; Kimura, K.; Inaki, Y.; Hattori, T. *Chem. Commun.* **1997**, 129.
30 Inagaki, S.; Koiwai, A.; Suzuki, N.; Fukushima, Y.; Kuroda, K. *Bull. Chem. Soc. Jpn.* **1996**, *69*, 1449.
31 Branston, P. J.; Kaneko, K.; Setoyama, N.; Sing, K. S.; Inagaki, S.; Fukushima, Y. *Langmuir* **1996**, *12*, 599.
32 Beneke, K.; Lagaly, G. *Am. Mineral.* **1977**, 62, 763.
33 Lagaly, G. *Adv. Colloid. Interface Sci.* **1979**, *11*, 105.
34 Yoshida, S.; Matsuzaki, T.; Kashiwazaki, T.; Mori, K.; Tarama, K. *Bull. Chem. Soc. Jpn.* **1974**, *47*, 1564.
35 Klading, W. *J. Phys. Chem.* **1976**, *80*, 262.
36 Ward, J. W. *J. Catal.* **1970**, *16*, 386.
37 Baba, T.; Inoue, Y.; Ono, Y. *J. Catal.* **1996**, *159*, 230.
38 Tanabe, K.; Misono, M.; Ono, Y.; Hattori, H. *New Solid Acids and Bases*; Kodansha, Elsevier, Tokyo, 1989; pp 215-220.
39 Niwa, M.; Iwamoto, M.; Segawa, K. *Bull. Chem. Soc. Jpn.* **1986**, *59*, 3735.
40 Parry, E. R.*J. Catal.* **1963**, *2*, 371.
41 Climent, M. J.; Corma, A.; Iborra, S.; Navarro, M. C.; Primo, J. *J. Catal.* **1996**, *161*, 783.
42 Zhao, X. S.; Lu, G. Q.; Whittaker, A. K.; Millar, G. J.; Zhu, H. Y. *J. Phys. Chem. B* **1997**, *101*, 6525.
43 Gillis-D'Hamers, I; Cornelissens, I; Vrancken, K. C.; Van Der Voort, P; Vansant, E. F. *J. Chem. Soc., Faraday Trans.* **1992**, *88*, 723.
44 Van Roosmalen, A. J.; Hartmann, M. C.; Mol, J. C. *J. Catal.* **1980**, *66*, 112.
45 West, P. B.; Haller, G. L.; Burwell, R. L., Jr, *J. Catal.* **1973**, *29*, 486.
46 Haag, W. O. *Stud. Surf. Sci. Catal.* **1994**, *84*, 1375.
47 Weisz, P. B. *Ind. Eng. Chem. Fundam.* **1986**, *25*, 53.
48 Olsen, D. H.; Haag, W. O.; Lago, R. M. *J. Catal.* **1980**, *61*, 390.
49 Haag, W. O.; Lago, R. M.; Weisz, P. W. *Nature* **1984**, *309*, 589.
50 Derouane, E. G.; Baltusis, L.; Dessau, R. M.; Schmitt, K. D. *Stud. Surf. Sci. Catal.* **1985**, *20*, 135.
51 Chuang, I-S.; Maciel, G. E. *J. Phys. Chem. B* **1997**, *101*, 3052, and references theirin.
52 Morrow, B. A.; McFarlan, A. J. *J. Phys. Chem.* **1992**, *96*, 1395.
53 Ishikawa, T; Matsuda, M; Yasukawa, A; Kandori, K; Inagaki, S; Fukushima, Y; Kondo, S. *J. Chem. Soc., Faraday Trans.* **1996**, *92*, 1985.
54 Morrow, B. A.; Devi, A. *J. Chem. Soc., Faraday Trans. I* **1972**, *68*, 403.
55 Morrow, B. A.; Cody, I. A. *J. Phys. Chem.* **1975**, *79*, 761.
56 Morrow, B. A.; Cody, I. A. *J. Phys. Chem.* **1976**, *80*, 1995.

57 Bunker, B. C.; Haaland, D. M.; Ward, K. J.; Michalske, T. A.; Binkley, J. S.; Melius, C. F.; Malfe, C. A. *Surf. Sci.* **1989**, *210*, 406.

58 Matsumura, Y.; Hashimoto, K.; Yoshida, S. *J. Chem. Soc., Chem. Commun.* **1987**, 1559.

59 Matsumura, Y.; Hashimoto, K.; Yoshida, S. *J. Catal.* **1989**, *117*, 135.

60 Sato, H.; Hirose, K.; Nakamura, Y. *Chem. Lett.* **1993**, 1987.

61 Brinker, C. J.; Kirkpatrick, R. J.; Tallant, D. R.; Bunker, B. C.; Montez, B. *J. Non-Cryst. Solids* **1988**, *99*, 418.

62 Léonardelli, S.; Facchini, L.; Fretigny, C.; Tougne, P.; Legrand, A. P. *J. Am. Chem. Soc.* **1992**, *114*, 6412.

63 Anderson, M. W.; Klinowsky, J. *Zeolites* **1986**, *6*, 455.

64 Severino, A.; Esculcas, A.; Rocha, J.; Vital, J.; Lobo, L. S. *Appl. Catal. A General* **1996**, *142*, 255.

65 Benesi, H. A. *J. Am. Chem. Soc.* **1956**, *78*, 5490.

66 Benesi, H. A. *J. Phys. Chem.* **1957**, *61*, 970.

67 Tanabe, K.; Takeshita, T. *Adv. Catal.* **1967**, *17*, 315.

68 Werner, Von H.-J.; Beneke, K.; Lagaly, G. *Z. Anorg. Allg. Chem.* **1980**, *470*, 118.

Chapter 2

Generation of Lewis Acid Sites on FSM-16

Abstract

Catalysis over Lewis acid sites on siliceous mesoporous FSM-16 was confirmed. Acidic property of FSM-16 was studied by pyridine-TPD measurements and catalyses of α-pinene isomerization and methylamine synthesis. FSM-16 posses both Brønsted and Lewis acid sites, and another Lewis acid site formed on FSM-16 when a catalyst was pretreated above 873 K. α-Pinene isomerization was catalyzed over Brønsted acid sites, the activity of which is the highest when FSM-16 is pretreated at 673 K. Lewis acid sites on FSM-16 catalyze methylamine synthesis and the initial rates enhanced with increasing pretreatment temperature up to 1273 K. The structure of FSM-16 was completely retained throughout a pretreatment at 1273 K and a reaction procedure for methylamine synthesis at 673 K.

Introduction

Since the discovery of highly ordered mesoporous silica,[1, 2] mesoporous silica such as MCM-41,[2, 3] HMS [4, 5] and FSM-16 [6] have been investigated extensively.[7] All the three materials exhibit a similar structure to each other, and posses high surface area, narrow pore size distributions, and high pore volume. Because siliceous mesoporous materials have been believed to be catalytically inert, preparation of Al-containing mesoporous materials has been attempted for the application to solid-acid catalysis. Most commonly, Al-source was added into the starting materials before synthesis of mesoporous materials.[7-10] Impregnation methods of $AlCl_3$ [11, 12] or $Al(O^iPr)_3$ [13, 14] to synthesized mesoporous silica were also performed. In another way, preparation of heteropoly acid introduced MCM-41 was reported.[15]

In contrast to the efforts, catalyses of acid-catalyzed reaction over siliceous mesoporous materials were reported by some researchers in 1997.[13, 16] However, they did not pay attention to catalyses by mesoporous silicas. In their reports, results over siliceous mesoporous silicas were dealt with one of the reference catalysts or blank test. Sakata found thermal degradation of polyethylene proceeds over siliceous FSM-16 as fast as silica-alumina.[17] The yield of liquid products over FSM-16 was higher than that for silica-alumina. They concluded that the mesopore surrounded by silica sheets act as a radical flask.

We have first reported the acid property of mesoporous silica in detail. FSM-16 catalyzes but-1-ene isomerization and α-pinene isomerization at 323 and 303 K, respectively.[18] Subsequently our results were confirmed and supported by a report of the catalyses over siliceous MCM-41 about acetalization of aldehydes and ketones.[19] The activities of FSM-16 depend on pretreatment temperatures and exhibit the highest when the catalyst was pretreated at 673 K. The acidity of FSM-16 is much reduced by calcination temperature at higher temperature, but restores by water treatment at 353 K as long as the FSM-16 retaines its structure. We have concluded from IR characterizations that the active sites for the two reactions are weakly perturbed silanol groups which act as Brønsted acid sites. However, FTIR characterization of adsorbed pyridine on FSM-16 revealed that majority of the acid sites was Lewis acid sites. Furthermore, the peak intensity assigned to 8a mode of Lewis pyridine (1624 cm^{-1}) on FSM-16 pretreated at 1073 K was stronger much more than that on FSM-16 pretreated at 673 K.[18] In the previous work, no evidence was obtained about catalyses over Lewis acids.

In the present study, we focused on the Lewis acid property of FSM-16. The property was evaluated with pyridine-TPD measurement and a catalysis for methylamine synthesis. Methylamine synthesis from methanol and ammonia is known to typical acid-catalyzed reaction, which proceeds over many solid acid catalysts having Lewis and/or Brønsted acid sites.[20] Segawa et al. reported that γ-Al_2O_3 (JRC-ALO-4) catalyzes methylamine synthesis from methanol and ammonia, and the initial rate was higher than those of amorphous silica-alumina (JRC-SAL-2; Al_2O_3 = 13 wt%) and HZSM-5 (Si/Al = 12.5).[21] It has been concluded from IR

spectra of adsorbed pyridine that the acid site of γ-Al_2O_3 is only Lewis acid sites.[22-24] Therefore, the reaction catalyzed over γ-Al_2O_3 is considered to be a Lewis acid promoted reaction, and is expected to proceed over FSM-16 pretreated above 1073 K.

Experimental

Materials

FSM-16 was synthesized according to the literature,[25] and the procedure was previously reported in detail.[18] The grade of water glass used for FSM-16 synthesis is as follows; Fuji Silysia Co., LTD: SiO_2 = 15.3 wt%, Na_2O = 6.1 wt%, Al = 0.6 ppm, Fe = 0.4 ppm; Osaka Keiso Co., LTD: SiO_2 = 31.93 wt%, Na_2O = 15.37 wt%, Al = 98 ppm, Fe = 28 ppm. The Cu-Kα XRD pattern of synthesized FSM-16 exhibits typical *d100*, *d110*, *d200* and *d210* reflections at 2θ = 2.3, 4.1, 4.7 and 6.3°, respectively.

SiO_2 gel was synthesized from tetraethyl orthosilicate (Nacalai tesque, EP-grade, singly distilled) by hydrolysis in a water-ethanol mixture at boiling point, followed by calcination at 773 K for 5 h.[25]

Precipitated silica was prepared from silicic acid, by calcination at 773 K for 5 h. Silicic acid was obtained by mixing of water glass (Fuji Silysia Co. LTD) and 2 M HCl at room temperature, followed by washing with 0.2 M HNO_3 until Cl^- was free based on $AgNO_3$ test.

Reference catalysts used were Japan Reference Catalyst (JRC-ALO-4, JRC-SAL-2), supplied by the Committee on Reference Catalyst, Catalysis Society of Japan. JRC-ALO-4 is γ-Al_2O_3 which contains 0.01% of Fe_2O_3, SiO_2 and Na_2O. JRC-SAL-2 is amorphous silica-alumina which contains 0.02% Fe, 0.012% Na_2O, 0.33% SO_4, and 13.75% Al_2O_3. The BET specific surface areas of JRC-ALO-4 and JRC-SAL-2 are 177 and 560 $m^2\ g^{-1}$, respectively.

Characterization

Elemental analysis was carried out by inductively coupled plasma (ICP) with Shimadzu ICPS-2000, and the results are shown in Table 1. The N_2 adsorption-desorption isotherm measurement was carried out with BELSORP 28SA (BEL JAPAN, Inc.) at 77 K. The specific surface area was calculated by BET method. The pore sized distribution was estimated by the Clanston-Inkley method. The pore volume and outer surface area were estimated by *t*-plot using a N_2 adsorption isotherm of non-porous silica as a standard.[27]

Pyridine temperature-programmed desorption (TPD) experiments were performed at a heating rate of 10 K min^{-1} and quadrupole-type mass spectrometer (MASSMATE-100, ULVAC) was used as a detector.[28] Before TPD measurements, each 100 mg of sample was pre-evacuated at 673 K for 0.5 h and calcined under 6.66 kPa of O_2 for 1 h, followed by evacuation at the same temperature for 1 h. The pretreated sample was exposed to 80 μmol of

pyridine at 373 or 423 K for 10 min, followed by evacuation at the same temperature for 1 h. The amount of desorbed pyridine was normalized to that of introduced Ar (m/z = 40) as an internal standard. Because the most intense signal for pyridine-mass spectrum was that of m/z = 52, we adopted profiles of m/z = 52 for acid properties of catalyst.

FTIR spectra were recorded using a Perkin-Elmer Paragon 1000 spectrometer with a resolution of 2 cm^{-1}. The 20 mg of FSM-16 was pressed into a self supporting wafer (20 mm in diameter) with a pressure of 100 kg cm^{-2} for 10 s, and was mounted in an in situ IR cell equipped with BaF_2 windows. A wafer was evacuated at 673 or 1073 K for 1 h. After cooling to room temperature, each spectrum was recorded in a transmission mode.

Catalysis

α-Pinene isomerization was carried out under dry N_2 atmosphere using a stirred batch reactor at 303 or 353 K.[18] Methylamine synthesis was carried out with a closed circulation system (dead volume, 200 cm^3) at 673 K. The pretreatment procedure for both reactions was the same as TPD experiment. In a typical experiment for α-pinene isomerization, the reactor was loaded with 2 mL (12.6 mmol) of α-pinene (Nacalai, EP, 99.8%) and 50 mg of catalyst. The amounts of substrates used for methylamine synthesis were 200 or 800 μmol of ammonia and 400 μmol of methanol. Products were analyzed by FID gas-chromatography (GC-14A, Shimadzu) with a CBP20-M25-025 capillary column (Shimadzu) for α-pinene isomerization, and by GC-8A (Shimadzu) with an Unicarbon B-2000 column (GL Sciences, 2.6 ϕ x 2 m) for methylamine synthesis.

Results and Discussion

Catalysis over Brønsted Acid Sites

From FTIR characterization, we have concluded that the active sites for but-1-ene and α-pinene isomerizations are Brønsted acid sites of weakly perturbed silanol groups. The 19b mode of Brønsted pyridine (1546 cm^{-1}) was observed on FSM-16 pretreated at 673 K, whereas not on FSM-16 pretreated at 1073 K.[18] A trace amount of Al of FSM-16 did not affect the acidic property at all. To confirm this conclusion again, α-pinene isomerization was carried out with two kinds of FSM-16 which contain different concentration of Al. Results of catalytic test are summarized in Table 2. The selectivity was independent on Al concentrations as well, and camphene (ca. 39%) and limonene (ca. 43%) were produced. A rate for successive isomerization of limonene was low over FSM-16 even at 353 K. If Al-related sites on FSM-16 participate in the acidity, obvious difference in the activity should have been observed between sample No. 1 and No. 2. As shown in Table 2, any evident relations between the catalytic

TABLE 1: Elemental Analysis of Catalysts

Sample No.	Catalyst	Elements (mass%) Na	Al	Ca	Fe	Mg	Ti	Si/Al [a]
1	FSM-16	0.008	0.061	0.012	0.023	0.003	0.032	735
2	FSM-16	0.013	0.110	0.009	0.012	0.007	<0.001	408
3	SiO_2-gel	0.002	<0.001	0.001	<0.001	<0.001	<0.001	-
4	*p*-Silica [b]	0.003	0.004	<0.001	<0.001	<0.001	<0.001	11226

[a] Atomic ratio

[b] Precipitated silica

TABLE 2: Results of α-Pinene Isomerization [a]

No.	Catalyst	Reaction temperature/K	Conversion (%)	Selectivity [b] (%) 1	2	3	4	5	6	7	8
1	FSM-16 [c]	303	44.6	tr.	40	4	43	9	2	2	tr.
1	FSM-16 [d]	353	97.4	tr.	43	4	33	10	4	2	4
1	FSM-16 [c,e]	303	6.6	1	37	3	48	7	2	2	1
2	FSM-16	303	38.7	tr.	38	4	44	8	2	2	2
3	SiO_2-gel [c,d]	353	0.0								
4	*p*-Silica	353	0.0								
	γ-Al_2O_3 [c,d]	353	3.4	33	44	2	17	2	1	1	tr.
	silica-alumina	303	99.8	tr.	43	3	26	14	6	4	4

[a] α-Pinene: 2 mL (12.6 mmol). Catalyst: 50 mg. Reaction time: 0.5 h. Pretreatment temperature: 673 K.

[b] 1, β-pinene; 2, camphene; 3, α-fenchene; 4, limonene; 5, terpinolene; 6, α-terpinene; 7, γ-terpinene; 8, others.

[c] Taken from reference (18).

[d] Catalyst: 100 mg. Reaction time: 3 h.

[e] Pretreatment temperature: 1073 K.

activity and Al concentration in FSM-16 were not observed. It strongly suggests that the acid property of FSM-16 is not due to contamination of Al.

Over silica-alumina of strong solid acid, consecutive isomerization of limonene proceeded and dehydrogenate product (*p*-cymene) and polymerized products were observed even at 303 K for 30 min. Effective acid strength for α-pinene isomerization was proposed to $H_0 \leq +3.3$.[18, 29] Although γ-Al_2O_3 possesses certain amounts of strong Lewis acid sites (580 μmol g^{-1}), the maximum strength of which is over $pKa \leq -5.6$,[23, 30] the activity was much less than that of FSM-16. It was proposed the reaction rate for α-pinene isomerization over Lewis acid site is lower than that over Brønsted acid site.[31] Low activity of γ-Al_2O_3 is due to scarce existence of Brønsted acid sites. Other silicas were inert for α-pinene isomerization at 353 K.

Temperature Programmed Desorption Measurements of Pyridine

To clarify a change of acidic property of FSM upon thermal treatment, pyridine TPD experiment was carried out. It was reported that strained siloxane bridge was formed on silica evacuated above 673 K. The site reacts with NH_3 to produce $SiNH_2$ and SiOH even at room temperature, whereas the sites do not react with pyridine.[32, 33] Therefore, we adopted pyridine as a base molecule to evaluate the acidic property. The results of pyridine TPD experiments, each adsorption temperature of which was 373 K, are shown in Figure 1. TPD profiles of FSM-16 pretreated at 673 K exhibited a large desorption peak around 473 K and a faint peak around 800 K. With increasing pretreatment temperatures, the peak intensity around 473 K drastically reduced, whereas that around 800 K was almost constant. In the desorption profiles of FSM-16 pretreated at 1073 and 1273 K, a new desorption peak appeared around 510 K. The behavior of the desorption peak around 473 K upon pretreatment temperature is consistent with that of catalytic activities for but-1-ene and α-pinene isomerization. This pyridine adsorption site may be conjectured to be the active sites of FSM-16, which have been proposed to Brønsted acid. However, a pyridine TPD profile of SiO_2 gel pretreated at 673 K, which was inert for the two reactions, exhibited a large desorption peak around 473 K. When pyridine-adsorption procedure was carried out at 373 K, a large amount of hydrogen bonded pyridine adsorbed onto residual water molecules of both the catalysts. Therefore, the peak observed around 473 K is desorption pyridine from both hydrogen-bonded and Brønsted acid sites.

To reduce the effect of hydrogen-bonded pyridine in TPD experiments, pyridine adsorption procedure was then performed at 423 K. The TPD profiles are shown in Figure 2. The TPD profile of FSM-16 pretreated at 673 K exhibited a small broad desorption peak around 600 K and a shoulder over 773 K. With increasing pretreatment temperature, a new desorption peak grew around 550 K. It is obvious that somewhat new acid sites generate, the amount of which increased on FSM-16 by thermal treatment. When pyridine was adsorbed at 373 K,

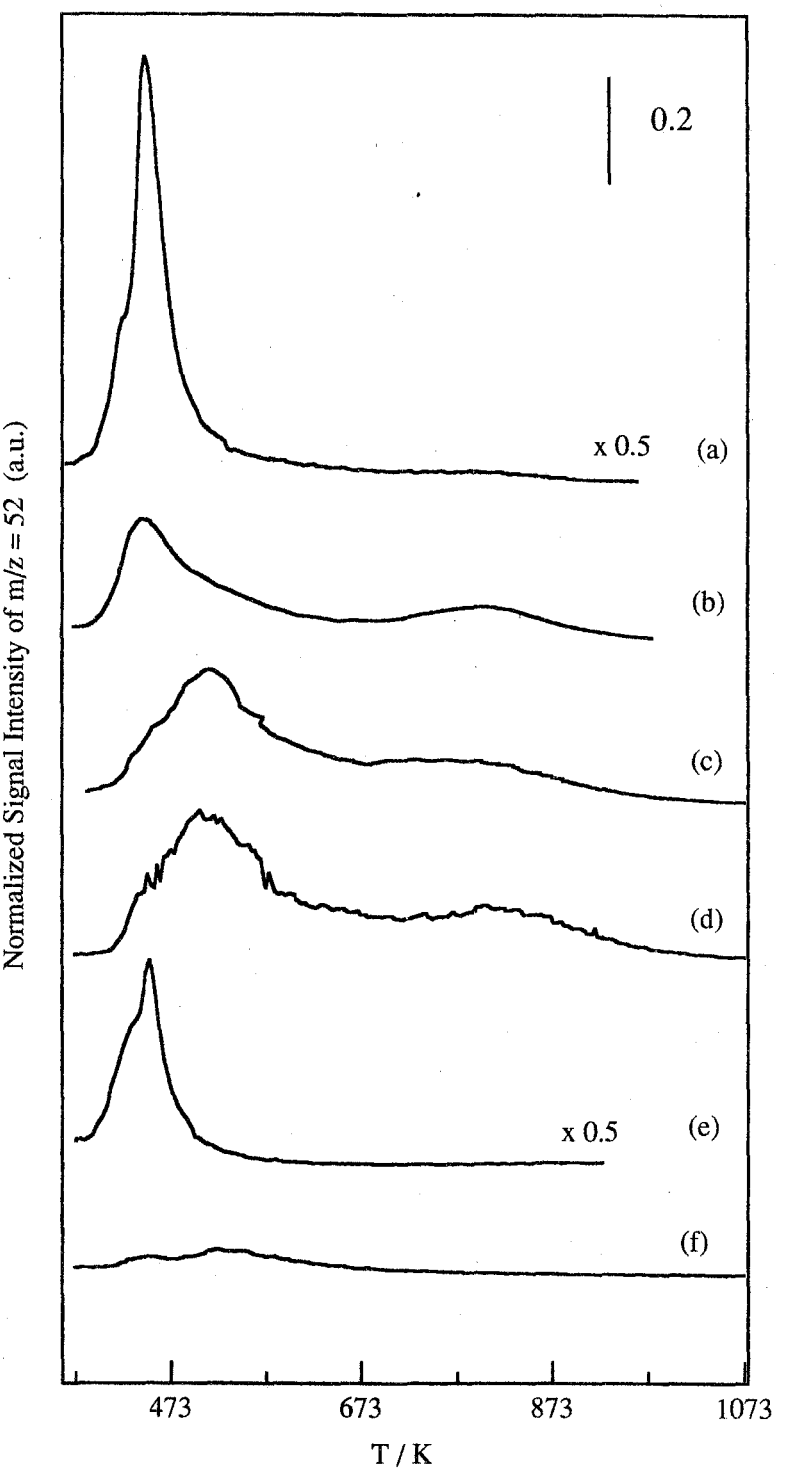

Figure 1. Pyridine TPD profiles of FSM-16 pretreated at 673 K (a), 873 K (b), 1073 K (c) and 1273 K (d), and SiO_2 gel pretreated at 673 K (e) and 1073 K (f). Adsorption temperature: 373 K. Rate: 10 K min^{-1}.

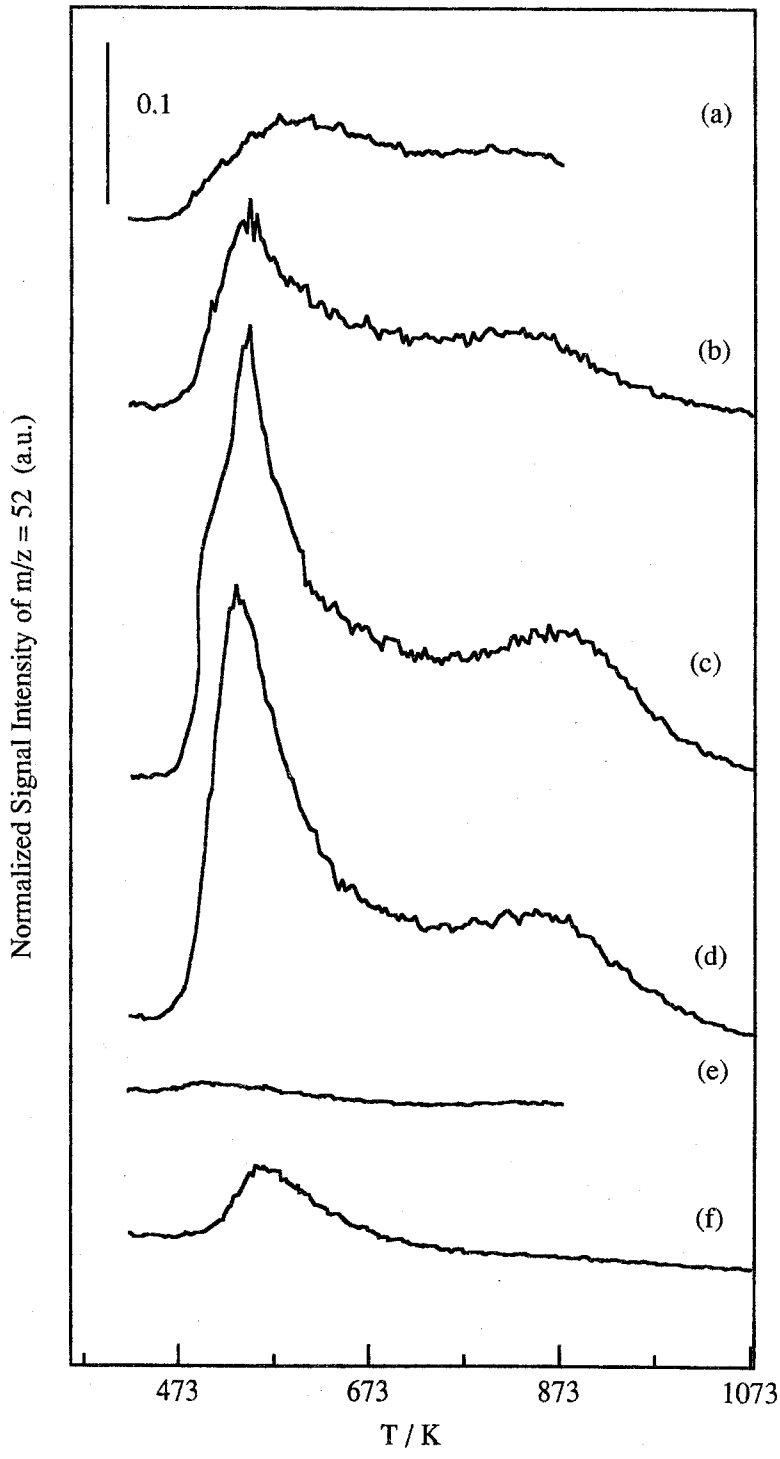

Figure 2. Pyridine TPD profiles of FSM-16 pretreated at 673 K (a), 873 K (b), 1073 K (c) and 1273 K (d), and SiO_2 gel pretreated at 673 K (e) and 1073 K (f). Adsorption temperature: 423 K. Rate: 10 K min^{-1}.

FSM-16 pretreated at 673 K desorbed the largest amounts of pyridine. In contrast, FSM-16 pretreated at 1273 K desorbed the largest amounts when pyridine was adsorbed at 423 K. Similar phenomena were observed in pyridine TPD profiles of SiO_2 gel adsorbed at 423 K. Little pyridine adsorbed on SiO_2 gel pretreated at 673 K. A new desorption peak was observed in that of SiO_2 pretreated at 1073 K as well, however, the intensity was much smaller than that of FSM-16. No desorption peaks were observed in those of SiO_2 gel above 673 K, in contrast to those of FSM-16.

When FSM-16 was pretreated above 1073 K, desorbed amounts of pyridine from FSM-16 were almost the same among the two different adsorption temperatures. IR spectra indicated that hydrogen-bonded silanol groups were absent on the surface of FSM-16 evacuated at 1073 K.[18] As a result, hydrogen-bonded pyridine was absent on FSM-16 pretreated above 1073 K, and differences of TPD profiles were not observed among different adsorption temperatures. Pyridine TPD experiment of siliceous MCM-41 pretreated at 573 K was performed by Zhao.[34] Unfortunately, because the adsorption temperature on MCM-41 was 325 K, the difference of acidic property between FSM-16 and MCM-41 is not able to compare with. In conclusions, another kind of acid sites generate on FSM-16 pretreated above 873 K, and effects of hydrogen-bonded pyridine are free if pyridine adsorption was carried out at 423 K.

Generation of Lewis Acid Sites

We have measured IR spectra of adsorbed pyridine on FSM-16, and estimated the ratio of Lewis and Brønsted acid sites ([L]/[B] ratio). Total amount of Lewis acid sites was much more than that of Brønsted acid sites. The [L]/[B] ratio of FSM-16 pretreated at 673 K was estimated to 2.9, and that of FSM-16 pretreated at 1073 K was 5.6.[18] In these spectra, the peak intensity assigned to 8a mode of Lewis pyridine (1624 cm^{-1}) enhanced by high-temperature pretreatment. The peak area on FSM-16 pretreated at 1073 K was 1.4 times as large as that on FSM-16 pretreated at 673 K. In cases of TPD experiments, cumulated amounts of desorbed pyridine in the range of 423-873 K differed by 2.2 times between the two FSM-16 samples of different evacuation temperatures. The tendency of pyridine TPD profile adsorbed at 423 K is consistent with the results of IR spectra.

Figure 3 shows IR spectra of FSM-16 evacuated at 673 and 1073 K. In the range around 900 cm^{-1}, a new peak appeared at 892 cm^{-1} when FSM-16 was treated at 1073 K. In the second derivative spectra, an additional peak was confirmed at 912 cm^{-1}. On the other hand, any peaks were not present in the IR spectrum of FSM-16 treated at 673 K. This phenomena observed on FSM-16 are quite similar to those for amorphous silica. It is well known that isolated surface silanol groups of silica are dehydroxylated to form strained siloxane bridge over 900 K.[35] Such the dehydroxylated silica, two defect bands are observed at 888 and 908 cm-1 in the range of 800-1000 cm^{-1} which were assigned to edge-shared disiloxane ring.[32, 33, 35-38] They are produced by dehydroxylation of isolated silanol groups, and can

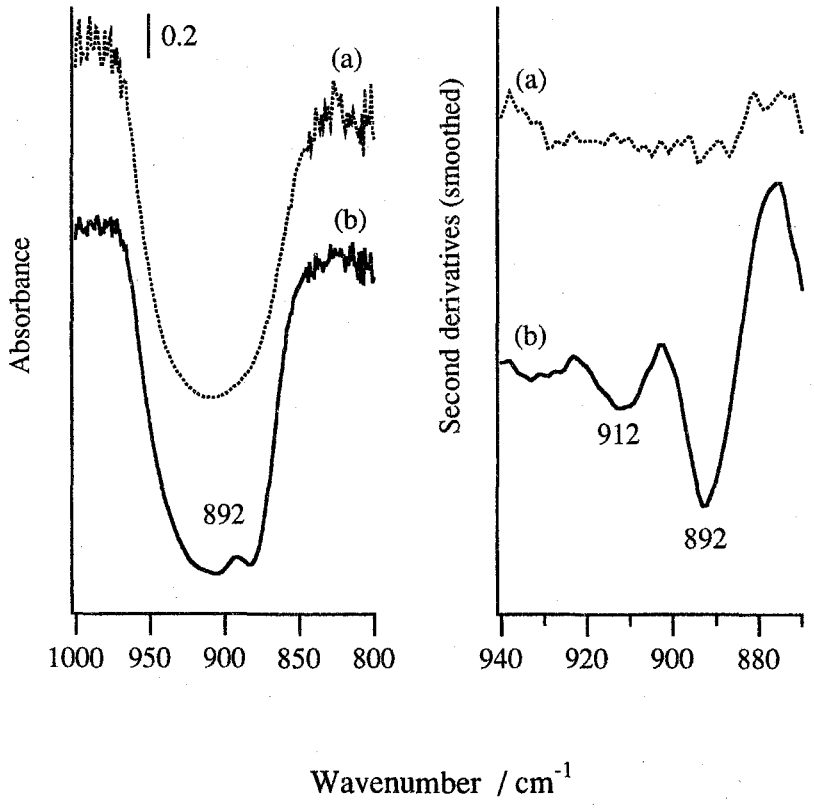

Figure 3. FTIR spectra of FSM-16 evacuated at 673 K (a) and 1073 K (b), and their second derivatives.

be classified to be Lewis acid.[38] In fact, dehydrogenation of ethanol was catalyzed over highly dehydrated silica, the active site of which was proposed to be Si-O-Si oxygen bridge.[39] However, the acid strength of SiO_2 pretreated at 1073 K was not very strong, so that only hydrogen bonded pyridine was detected with FTIR spectroscopy.[40] The newly formed acid sites on FSM-16 pretreated above 873 K are possibly due to silicon atoms of strained siloxane bridge as well as amorphous silica. If one of the silicon-oxygen bond of siloxane bridge was prolonged, the silicon atom could be regarded as pseudo-coordination unsaturated site and strength of the Lewis acidity remarkably should be enhanced. We speculate that such the pseudo-coordination unsaturated silicon species formed on FSM-16 pretreated at higher temperature. The rigid structure of FSM-16 permits the existence such unstable species like them. This might be the reason for the difference in acidity between FSM-16 and SiO_2 gel

Catalysis over Lewis Acid Sites

As shown in Figure 2, amounts of Lewis acid sites on FSM-16 increase with raising pretreatment temperatures. As a test reaction for Lewis acid sites on FSM-16, methylamine synthesis was examined. If the Lewis acid sites on FSM-16 are effective for this reaction, the catalytic activity should be enhanced with increasing pretreatment temperatures.

Figure 4 shows a time course of methylamine synthesis over FSM-16. As expected, the initial rate for methanol conversion exhibited the highest when FSM-16 was pretreated at 1273 K. Figure 4b shows the selectivity for methylamine synthesis over 1273 K pretreated FSM-16. At the initial step, a selectivity to monomethylamine (MMA) was 90% and that for trimethylamine (TMA) was 10%. Formation of dimethylether was not observed. Ammonia was rapidly methylated to MMA over FSM-16, however, a rate for consecutive methylated was very slow. The amount of dimethylamine (DMA) formation was very small even when reaction time was 180 minutes. The selectivities to each methylamine unchanged by pretreatment temperatures, and no induction periods were observed in all cases. Figure 5 summarizes initial rates for methylamine synthesis and activities of α-pinene isomerization over FSM-16 versus pretreatment temperature. Catalytic activity for α-pinene isomerization was dependent upon heat treatment and reached maximum at 673 K, and the activity was drastically reduced when FSM-16 was pretreated above 1073 K. In contrast, methylamine synthesis was catalyzed by FSM-16 pretreated at 1273 K, the activity of which was higher than that of FSM-16 pretreated at 673 K. It clearly shows that methylamine synthesis proceeds over Lewis acid sites on FSM-16. These two reactions should be catalyzed by the different active sites on FSM-16.

Lewis acid sites on FSM-16 might change to Brønsted acid sites with water which formed by dehydration among methanol and ammonia. Hence, it is doubtful whether Lewis acid sites really participate in a catalysis for methylamine synthesis. If Brønsted acid sites were active sites, which were converted from the Lewis acid sites, induction period should have been observed. Furthermore, the reaction rate over FSM-16 pretreated at 1273 K should never

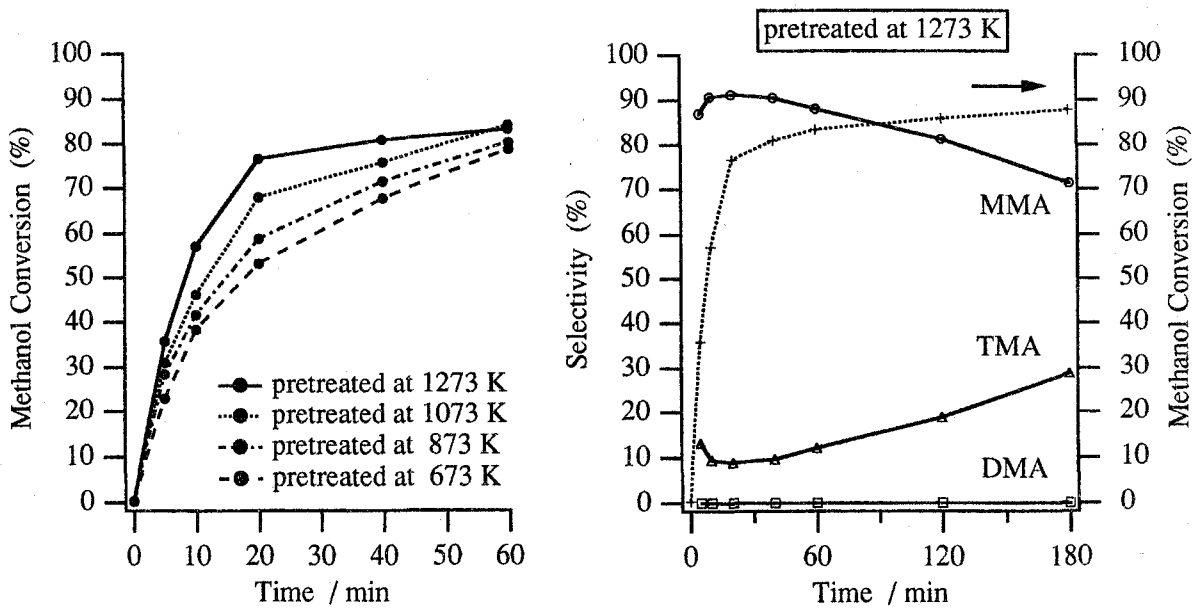

Figure 4. Time course of methylamine synthesis over FSM-16 pretreated at various temperatures. Methanol: 400 μmol. Ammonia: 200 μmol. Catalyst: 100 mg. Reaction temperature: 673 K. Dead volume: 200 cc.

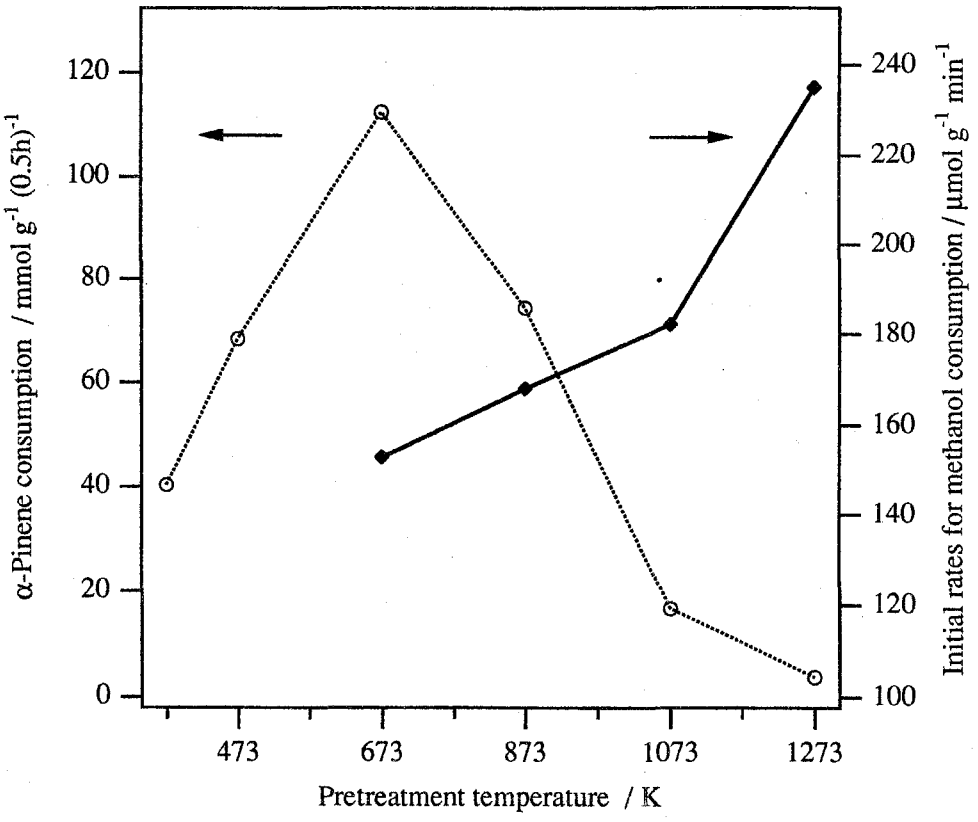

Figure 5. Effects of pretreatment temperature on catalytic properties of FSM-16. Dotted line: α-Pinene isomerization at 303 K. Reproduced from reference (18). Solid line: Methylamine synthesis at 673 K. N/C = 0.5.

exceed one over FSM-16 pretreated at 673 K. However, present results of catalysis did not agree with these postulates. Therefore, it is obvious that the Lewis acid sites formed on FSM-16 acts as active sites.

From the results that H-type MFI, Y and Mordenite zeolites exhibit higher activities for methylamine synthesis than those of each Na-type zeolite,[21, 41] not only Lewis but also Brønsted acid sites catalyze this reaction. In addition, reaction mechanisms catalyzed by Brønsted acid sites have been proposed.[20] We cannot conclude whether the active sites of FSM-16 for methylamine synthesis were Brønsted and/or Lewis acid sites. However, we say again that Lewis acid sites on FSM-16 participate in this catalysis.

When the reaction was carried out with 400 μmol of methanol and 200 μmol of NH_3, evident difference in initial rates was observed on FSM-16 pretreated various temperatures. In contrast, the differences in activities to pretreatment temperatures were small when the reaction was performed with 400 μmol of methanol and 800 μmol of NH_3. The reaction rates for methanol conversion were not so different by N/C (ammonia to methanol) ratios, however, the rate of TMA formation increased in a case N/C = 2. FSM-16 catalyzed methylamine synthesis to produce MMA readily, but the rate of consecutive methanation was relatively slow in all reaction conditions. As a result, reaction rates for methanol consumption were not influenced by the reaction condition of different N/C ratios.

To compare the catalytic activity of FSM-16 with other catalysts, methylamine synthesis was carried out with various reference catalysts. No products other than methylamines were formed in all cases. The time courses of methanol consumption are shown in Figure 6. Activities of silica-alumina and γ-Al_2O_3 were higher by one order of magnitude than that of FSM-16. γ-Al_2O_3 exhibited the largest initial rates in the catalysts. SiO_2 gel pretreated at 1073 K were not active for this reaction at all. The activity of FSM-16 (sample no. 1) was slightly lower than that of FSM-16 (sample no. 2). The amounts of contained Al were 610 ppm for FSM-16 (sample no. 1) and 1100 ppm for FSM-16 (sample no. 2). The difference of catalytic activities between FSM-16 (no. 1) and FSM-16 (no. 2) was much less than that of contained amounts of Al impurities. Although FSM-16 were less active than silica-alumina and γ-Al_2O_3, the point we emphasize is that not only Brønsted but also Lewis acid sites on FSM-16 participate in certain kinds of catalyses.

The results of methylamine synthesis are summarized in Table 3. Consecutive methylation over FSM-16 was accelerated in a reaction condition of N/C = 2 more than N/C = 0.5. The equilibrium concentrations of methylamines (MMA/DMA/TMA) are 5/25/70 for N/C = 0.5, and 31/38/31 for N/C = 2 at 673 K.[20] It suggests that FSM-16 possesses the acid sites to catalyze methylation of ammonia, the acid strength of which is not sufficient to reach the equilibrium of methylamines rapidly. In an initial period of methylamine synthesis over γ-Al_2O_3, MMA was selectively produced and the formation of TMA was scarce. In contrast, TMA was produced in an initial step over silica-alumina of strong solid acid.

TABLE 3: Results of Methylamine Synthesis at 673 K [a]

Catalyst	Pretreatment Temperature / K	N/C [b]	Conversion [c] (%)	Selectivity (%) MMA	DMA	TMA
FSM-16 [d]	673	0.5	78.7	88	-	12
	873	0.5	80.3	88	-	12
	1073	0.5	84.2	87	-	13
	1273	0.5	83.4	88	-	12
FSM-16 [e]	673	2	84.1	58	4	38
	1073	2	83.8	62	4	34
	1273	2	86.9	69	3	28
FSM-16 [d]	1073	2	74.3	71	3	26
SiO_2 gel	1073	2	1.3			
γ-Al_2O_3 [f]	673	2	83.5 [g]	90	5	5
		2	91.7	51	21	28
silica-alumina [f]	673	2	81.3 [h]	68	6	26
		2	95.3	50	8	42

[a] Catalyst, 100 mg; Methanol, 400 μmol; Ammonia, 200 or 800 μmol.

[b] Molar ratio of ammonia to methanol.

[c] Reaction time, 1 h.

[d] Sample No. 1.

[e] Sample No. 2.

[f] Catalyst, 10 mg.

[g] Reaction time, 10 min.

[h] Reaction time, 20 min.

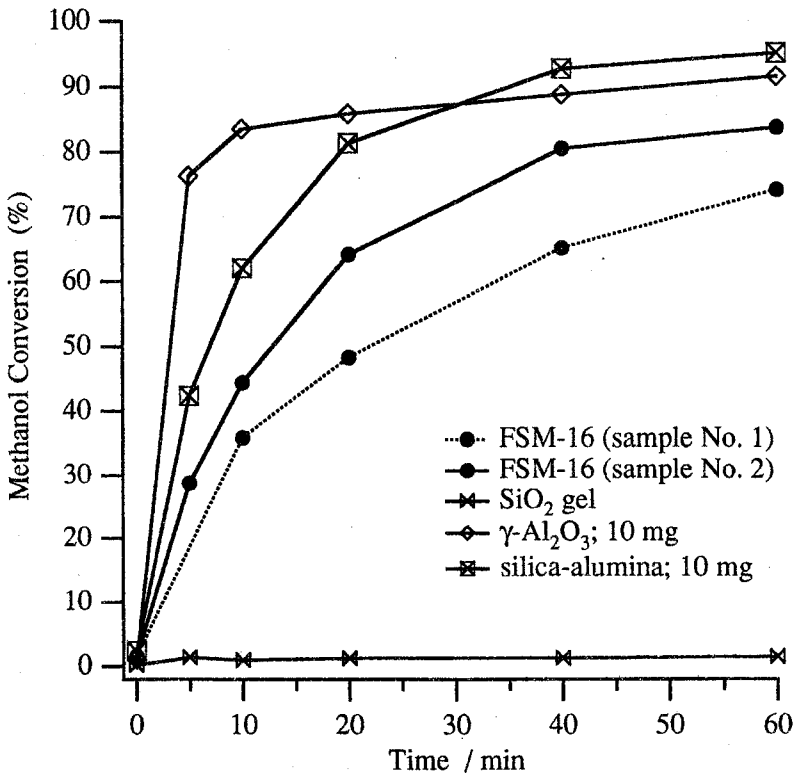

Figure 6. Time course of methylamine synthesis over FSM-16 and reference catalysts. Methanol: 400 μmol. Ammonia: 800 μmol. Catalyst: 100 mg. Reaction temperature: 673 K. Dead volume: 200 cc.

We have estimated the maximum acid strength of catalysts with Hammet indicators. When pretreatment procedure was performed below 1073 K, FSM-16 exhibits medium acid strength of H_0 = -3.0. In a case that FSM-16 was pretreated at 1273 K, the maximum acid strength was estimated to H_0 = -5.6.[18] When FSM-16 was pretreated above 1073 K, catalytic activities for but-1-ene and α-pinene isomerization drastically reduced, in spite of the results that FSM-16 still exhibited solid acidity of medium acid strength. Therefore, we conclude that Lewis acid site on FSM-16 possesses medium acid strength of H_0 max = -3.0 to -5.6, which little catalyze but-1-ene and α-pinene isomerization at 323 K.

Thermal and Hydrothermal Stability of FSM-16

To examine the structural change of FSM-16 throughout a reaction, N_2 adsorption isotherms of fresh and reacted samples were measured. The reacted sample measured was FSM-16 (sample no. 2) which was pretreated at 1273 K and the reaction was carried out at 673 K for 3 h (N/C = 2). Prior to measurement, reacted FSM-16 was calcined at 873 K for 2 h in a dry air, followed by evacuation at 673 K for 3 h. Figure 7 shows adsorption/desorption isotherms (a), *t*-plots (b) and pore size distribution curves (c) of fresh and reacted FSM-16. The estimated pore parameters are summarized in Table 4. The shape of *t*-plot and estimated parameters for fresh FSM-16 are quite similar to those of FSM-16,[42] and that of MCM-41.[43, 44]

TABLE 4: Surface Area and Porosity of Samples

Sample No.	Catalyst	S_{BET} [a] /$m^2\ g^{-1}$	V_p [b] /$cm^3\ g^{-1}$	S_t [c] /$m^2\ g^{-1}$	S_{out} [d] /$m^2\ g^{-1}$	D [e] /nm
1	FSM-16	1059	0.721	1012	102	2.76
2	FSM-16	1068	0.762	948	97	2.76
2	FSM-16 [f]	924	0.642	888	94	2.76
3	SiO_2 gel	637	0.683	582	59	4.26
4	*p*-Silica [g]	464	0.266	477	14	(3.76)

[a] BET specific surface area.

[b] Pore volume estimated by *t*-plot.

[c] Total surface area estimated by *t*-plot.

[d] Outer surface area estimated by *t*-plot.

[e] Tentative pore diameter estimated by Clanston-Inkley method.

[f] After methylamine synthesis at 673 K for 3h. The catalyst was pretreated at 1273 K.

[g] Precipitated silica.

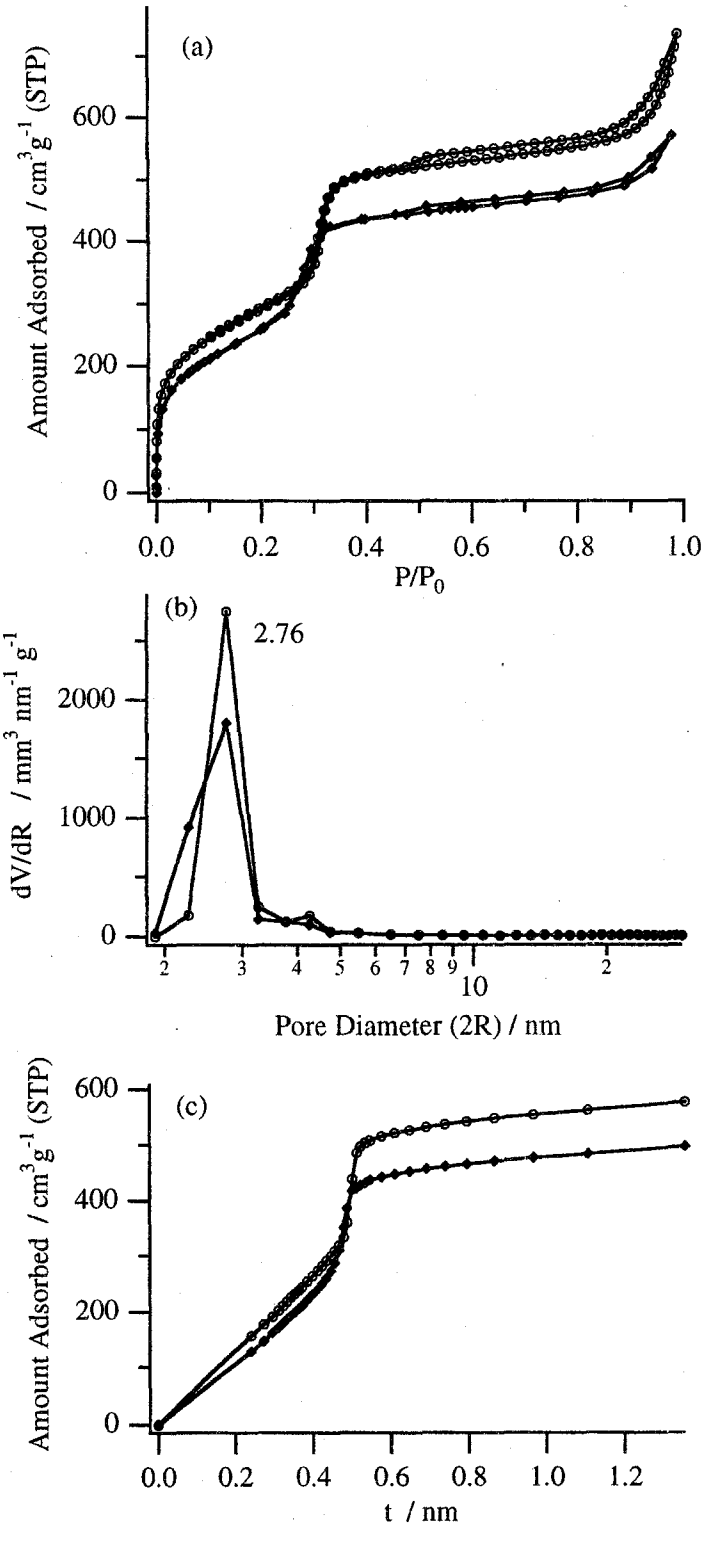

Figure 7. Results of N_2 adsorption/desorption isotherm measurements at 77 K: Adsorption/desorption isotherms (a), pore size distribution curves (b) and *t*-plots (c). Circle: Fresh FSM-16 (sample No. 2). Square: Reacted FSM-16, which was pretreated at 1273 K and used for methylamine synthesis at 673 K for 3 h (N/C = 2).

Reacted FSM-16 retained 85% of BET specific surface area (924 $m^2 g^{-1}$) and total pore volume (0.642 mL g^{-1}), comparing to those of fresh ones. The shape of N_2 adsorption/desorption isotherm of reacted FSM-16 was retained to that of fresh one. The ranges of capillary condensation were observed among P/P_0 = 0.29 - 0.34 and 0.25 - 0.32, respectively. In the case of reacted FSM-16, the range of pore filling was slightly shifted to lower P/P_0 due to shrinkage of the lattice, however, its decay was almost the same as that of fresh FSM-16. It clearly shows that the crystallinity and pore-uniformity of FSM-16 retained in the pretreated and reacted sample. It was supported by the pore size distribution curves.

Under reaction condition of a methylamine synthesis, H_2O is produced by dehydrative condensation among methanol and ammonia. As a result, catalysts were exposed to saturated water vapor at 673 K. Nevertheless, scarce reduction of the crystallinity occurred and no increase of outer surface area was observed throughout the reaction. Furthermore, FSM-16 has been pretreated at a high temperature of 1273 K prior to the reaction. The N_2 adsorption/ desorption isotherm measuring experiments strongly demonstrate the excellent thermal and hydrothermal stability of FSM-16. It was consistent with the result that FSM-16 soaking into 353 K of water for 5 h retained the original structure, without reducing its crystallinity at all.[18]

Conclusion

Lewis acid site formed on siliceous FSM-16 when a catalyst was pretreated above 873 K. Lewis acid sites on FSM-16 catalyzed methylamine synthesis at 673 K. The activity was enhanced with increasing pretreatment temperature up to 1273 K. The structure of FSM-16 was retained throughout a pretreatment at 1273 K and a reaction at 673 K. When FSM-16 was pretreated at 673 K, reactions catalyzed over Brønsted acid sites exhibit the highest rates. The rates of Lewis acid-catalyzed reactions were enhanced with increasing pretreatment temperature up to 1273 K.

References

1 Yanagisawa, T.; Shimizu, T.; Kuroda, K.; Kato, C. *Bull. Chem. Soc. Jpn.* **1990**, *63*, 988.

2 Kresge, C. T.; Lenowicz, M. E.; Roth, W. J.; Vartuli, J. C.; Beck, J. S. *Nature* **1992**, *359*, 710.

3 Beck, J. S.; Vartuli, J. C.; Roth, W. J.; Lenowicz, M. E.; Kresge, C. T.; Schmitt, K. D.; Chu, C. T-W.; Olson, D. H.; Sheppard, E. W.; McCullen, S. B.; Higgis, J. B.; Schlenker, J. L. *J. Am. Chem. Soc.* **1992**, *114*, 10834.

4 Tanev, P. T.; Chibwe, M.; Pinnavaia, T. J., *Nature* **1994**, *368*, 321.

5 Tanev, P. T.; Pinnavaia, T. J. *Science* **1995**, *267*, 865.
6 Inagaki, S.; Fukushima, Y.; Kuroda, K. *J. Chem. Soc., Chem. Commun.* **1993**, 680.
7 Biz, S.; Occelli, M. L. *Catal. Rev.-Sci. Eng.* **1998**, *40*, 329, and references therein.
8 Chen, C.-Y.; Li, H.-X.; Davis, M. E. *Microporous Mater.* **1993**, *2*, 17.
9 Corma, A.; Fornes, V.; Navarro, M. T.; Pérez-Pariente, J. *J. Catal.* **1994**, *148*, 569.
10 Inagaki, S.; Yamada, Y.; Fukushima, Y. *Stud. Surf. Sci. Catal.* **1996**, *105*, 109.
11 Inagaki, S.; Fukushima, Y.; Okada, A.; Kurauchi, T.; Kuroda, K.; Kato, C. *Proc. 9th. International Zeolite Conf.*, **1992**, *I*, 305.
12 Ryoo, R.; Jun, S.; Kim, J. M.; Kim, M. J.; *Chem. Commun.* **1997**, 2225.
13 Hamaguchi, K.; Hattori, H. *React. Kinet. Catal. Lett.* **1997**, *61*, 13.
14 Mokaya, R.; Jones, W. *Chem. Commun.* **1997**, 2185.
15 Kozhevnikov, I. V.; Kloestra, K. R.; Sinnema, A.; Zandbergen, H. W.; van Bekkum, H. *J. Mol. Catal. A* **1996**, *114*, 287.
16 Galarneau, A.; Barodawalla, A.; Pinnavaia, T. J. *Chem. Commun.* **1997**, 1661.
17 Sakata, Y.; Uddin, M. A.; Muto, A.; Koizumi, K.; Kanada, Y.; Murata, K. *J. Anal. Appl. Pyrolysis* **1997**, *43*, 15.
18 Yamamoto, T.; Tanaka, T.; Funabiki, T.; Yoshida, S. *J. Phys. Chem. B* **1998**, *102*, 5830.
19 Tanaka, Y; Sawamura, N; Iwamoto, M. *Tetrahedron Lett.* **1998**, *39*, 9457.
20 Corbin, D. R.; Schwarz, S.; Sonnichsen, G. C. *Catal. Today* **1997**, *37*, 71, and references therein.
21 Segawa, K.; Sugiyama, A.; Sakaguchi, N.; Sakurai, K. *Acid-Base Catalysis*; Tanabe, K.; Hattori H.; Yamaguchi, T.; Tanaka, T.; eds., Kodansha: Tokyo, 1989, 53.
22 Connell, G.; Dumesic, J. A. *J. Catal.* **1986**, *102*, 216.
23 Tanabe, K.; Misono, M.; Ono, Y.; Hattori, H. *New Solid Acids and Bases*; Kodansha: Tokyo, 1989, pp. 78-91
24 Take, J.; Yoneda, Y. *Shokubai* **1980**, *22*, 120. (Data-JRC-0006; in Japanese).
25 Inagaki, S.; Koiwai, A.; Suzuki, N.; Fukushima, Y.; Kuroda, K. *Bull. Chem. Soc. Jpn.* **1996**, *69*, 1449.
26 Yoshida, S.; Matsuzaki, T.; Kashiwazaki, T.; Mori, K.; Tarama, K. *Bull. Chem. Soc. Jpn.* **1974**, *47*, 1564.
27 Lippens, B. C.; de Boer, J. H. *J. Catal.* **1965**, *4*, 319, and references therein.
28 Yamamoto, T.; Matsuyama, T.; Tanaka, T.; Funabiki, T.; Yoshida, S. *J. Mol. Catal. A*, in press
29 Tanabe, K. *Solid Acids and Bases*; Kodansha, Tokyo, 1970, pp. 119-125
30 Yamaguchi, H.; Tsutsumi, K.; Takahashi, H. *Shokubai* **1980**, *22*, 118. Data-JRC-0004; in Japanese).
31 Severino, A.; Esculcas, A.; Rocha, J.; Vital, J.; Lobo, L. S. *Appl. Catal. A General* **1996**, *142*, 255.

32 Mollow, B. A.; Cody, I. A. *J. Phys. Chem.* **1976**, *80*, 1995.

33 Mollow, B. A.; Cody, I. A. *J. Phys. Chem.* **1976**, *80*, 1998.

34 Zhao, X. S.; Lu, G. Q.; Whittaker, A. K.; Millar, G. J.; Zhu, H. Y. *J. Phys. Chem. B* **1997**, *101*, 6525.

35 Chuang, I.-S.; Maciel, G. E. *J. Phys. Chem. B* **1997**, *101*, 3052, and references therein.

36 Morrow, B. A; Devi, A. *J. Chem. Soc., Faraday Trans. I* **1972**, *68*, 403.

37 Bunker, B. C.; Haaland, D. M.; Ward, K. J.; Michalske, T. A.; Binkley, J. S.; Melius, C. F.; Malfe, C. A. *Surf. Sci.* **1989**, *210*, 406.

38 Bunker, B. C.; Haaland, D. M.; Michalske, T. A; Smith, W. L. *Surf. Sci.* **1989**, *222*, 95.

39 Matsumura, Y.; Hashimoto, K.; Yoshida, S. *J. Catal.* **1989**, *117*, 135.

40 Yamamoto, T.; Matsuyama, T.; Tanaka, T.; Funabiki, T.; Yoshida, S. *Phys. Chem. Chem. Phys.* **1999**, *1*, 2841.

41 Segawa, K.; Tachibana, H. *J. Catal.* **1991**, *131*, 482.

42 Branston, P. J.; Kaneko, K.; Setoyama, N.; Sing, K. S. W.; Inagaki, S.; Fukushima, Y. *Langmuir* **1996**, *12*, 599.

43 Branston, P. J.; Hall, P. G.; Sing, S. W. *J. Chem. Soc., Chem. Commun.* **1993**, 1257.

44 Zhu, H. Y.; Zhao, X. S.; Lu, G. Q.; Do, D. D. *Langmuir* **1996**, *12*, 6513.

Part II

Acidic Property and their Structural Characterization of Silica-Supported Rare Earth Oxide Catalysts

Introduction of Part II

Supported Rare Earth Oxide Catalysts

Rare earth oxides themselves are well-known solid base catalysts, and enhance certain kinds of reactions, which are catalyzed by alkali earth oxides.[1-4] Rare earth oxides possess not only base sites but also acid sites. In fact, Lewis acid sites are observed on La_2O_3,[5,6] CeO_2 [6] and Yb_2O_3 [7] evidenced by IR spectra of adsorbed pyridine. Aurox carried out microcalorimetric study of acidity and basicity of rare-earth oxide.[8,9] In dehydration of secondary alcohols, it was reported that both acid and base sites on CeO_2 act simultaneously to give olefins of E1cB selectivity (Hofmann orientation).[9,10] Such an acid-base pair was proposed on La_2O_3, and the pair activates methane to form methyl radicals in an oxidative coupling of methane.[11]

Investigations for catalysis by supported rare earth oxides are very scarce. According to the hypothesis for acidity prediction proposed by Tanabe *et al.*, binary oxides of La_2O_3-SiO_2 and Y_2O_3-SiO_2 are expected to exhibit solid acidity.[12,13] In fact, the maximum acid strengths estimated with Hammet indicators were H_0 = -5.6 for SiO_2-Y_2O_3 and H_0 = -4.4 for La_2O_3-SiO_2.[2,14,15] Recently, catalysis of monoethanolamine synthesis over SiO_2-Y_2O_3 was reported.[16] To the author's knowledge, this is the only one case for acid catalyzed reactions over supported rare earth oxide catalysts.

In the Ln/γ-Al_2O_3 systems (Ln = La, Sm, Lu), Captián *et al.* observed a strong interaction between a supported phase and the Al_2O_3 support, which affects the vibration frequency of Al-O bonds, binding energy of the Ln(4d) levels, the white line intensities at Ln-L_{III} edge XANES spectra, and the d-orbital electron densities evaluated with ab initio calculations.[17] They proposed that the strong interaction causes a redistribution of the electron density over Al-O-Ln ensembles, which implies a modification of acid-base properties of the surface. On the other hand, Shen *et al.* investigated acid-base properties of silica- and alumina-supported europium oxide with spectroscopic and calorimetric methods. They found that alumina supported europium oxide possesses basic sites stronger than that of Eu_2O_3, and silica-supported europium oxide exhibits Lewis acid properties.[18] Connell and Dumesic observed both Lewis and Brønsted acid sites over Sc-loaded silica.[19] Nevertheless, no acid-base catalyzed reactions were not performed over those kinds of La/Al_2O_3, Eu/Al_2O_3 and Eu/SiO_2.

Soled *et al.* prepared various kinds of rare earth oxide modified silica-aluminas, and carried out model reactions to evaluate the acid strengths.[20] From the selectivity in 2-methylpent-2-ene isomerization, they concluded that acid strengths of rare-earth modified catalysts, which contain 5-20 wt% of rare earth oxides, were the same level as halide ion-treated aluminas of intermediate acid strength. However, their aim was to control the acidity of

silica-alumina catalysts themselves. The addition of weakly basic rare earth oxides in a well dispersed state poisons the stronger acid sites of amorphous silica-alumina. As a result, the acid strength of silica-alumina was lowered.

Vannice *et al.* reported that dispersed La_2O_3 on alumina exhibits higher activity for selective reduction of NO to N_2 with CH_4 in the presence of oxygen at 973 K than unsupported La_2O_3 and Co/ZSM-5, while the catalytic activity of La/SiO_2 was quite lower than that of La_2O_3.[21-23] They found the activity was dependent upon the La_2O_3 precursor used, the pretreatment, and the loading amounts. The most active catalyst was that prepared with γ-Al_2O_3 and lanthanum acetate, and calcined at 1023 K. The optimum loading amount was 40 %, which corresponds to 1.5 theoretical monolayers of La_2O_3 on alumina. They concluded that the precursor of lanthanum salt affects the dispersion on alumina, and speculated that the low catalytic ability of La/SiO_2 relates to its water sensitivity to form lanthana-silicate. Capitán *et al.* investigated Sm_2O_3/Al_2O_3 catalyst focusing correlations between catalysis for oxidative coupling of methane and the surface Sm-Al-O phases.[24] They concluded that oxide-like structure shows better selectivity toward C_2 species than the $SmAlO_3$ phase. When Sm/Al_2O_3 catalyst was calcined at 873 K, samarium species present as oxide-like structure over alumina surface. If the catalyst was calcined at 1173 K, samarium species formed perovskite-like phase on the surface. The phase transition of samarium species on alumina, which affects the catalytic performance, is quite similar to that for La/Al_2O_3 proposed by Bettman.[25]

As mentioned above, the study of the supported lanthanides from the view point of acid-base catalysis has just begun and we need more accumulation of the knowledge. In the present part, acid-base properties of silica-supported rare-earth oxides are described on the basis of investigation with various spectroscopic methods and α-pinene isomerization as an acid-base model reaction. The effects of loading elements and amounts, and thermal treatments on their catalytic properties are discussed. Accompanied by structural characterizations, the structures of acid sites on silica-supported rare-earth oxide catalysts were proposed. In Chapter 3, physicochemical properties of silica-supported ytterbium oxide catalysts are reported. The effects of loading amounts and pretreatment temperature on the catalytic activity are discussed. The structure of active species is also proposed. In Chapter 4, XAFS investigation for characterization of Yb/SiO_2 catalysts is reported. Differences in the local structure around Yb between Yb/SiO_2 catalysts and Yb_2O_3, and coordination environments around Yb are discussed. In Chapter 5, differences in acid properties of silica-supported rare-earth oxides among supported elements are described. Relations among catalytic properties and the structural environment of each Ln/SiO_2 catalyst are discussed.

References

1 Rosynek, M. P. *Catal. Rev.-Sci. Eng.*, **1977**, *16*, 111.
2 Tanabe, K.; Misono, M.; Ono, Y.; Hattori, H. *New Solid Acids and Bases*, Kondansha, Tokyo, 1989, pp. 41-47.
3 Amenomiya, Y.; Birss, V. I.; Goledzinowski, M.; Galuszka, J.; Sanger, A. R. *Catal. Rev.-Sci. Eng.*, **1990**, *32*, 163.
4 Inumaru, K.; Misono, M. *Shokubai*, **1995**, *37*, 198.
5 Hussein, G. A. M.; Gates, B. C. *J. Chem. Soc., Faraday Trans.*, **1996**, *92*, 2425.
6 Zaki, M. I.; Hussein, G. A. M.; Mansour, S. A. A.; El-Ammawy, H. A. *J. Mol. Catal.*, **1989**, *51*, 209.
7 Yamamoto, T.; Matsuyama, T.; Tanaka, T.; Funabiki, T.; Yoshida, S. *Phys. Chem. Chem. Phys.*, **1999**, *1*, 2841.
8 Auroux, A.; Gervasini, A. *J. Phys. Chem.*, **1990**, *94*, 6371.
9 Auroux, A.; Aritzzu, P.; Ferino, I.; Monaci, R.; Rombi, E.; Solinas, V.; Pertini, G. *J. Chem. Soc., Faraday Trans.*, **1996**, *92*, 2619.
10 Thomke, K. *Proc. 6th. Int. Congr. Catal.*, London, **1977**, *1*, 303.
11 Choudhary, V. R.; Rane, V. H. *J. Catal.*, **1991**, *130*, 411.
12 Tanabe, K.; Sumiyoshi, T.; Shibata, K.; Kiyoura, T.; Kitagawa, J. *Bull. Chem. Soc. Jpn.*, **1974**, *47*, 1064.
13 Tanabe, K.; Misono, M.; Ono, Y.; Hattori, H. *New Solid Acids and Bases*, Kodansha, Elsevier, Tokyo, 1989, pp. 108-114.
14 Kotsarenko, N. S.; Karakchiev, L. G.; Dzisko, V. A. *React. Katal.*, **1968**, *9*, 158.
15 Shibata, K.; Kiyoura, T.; Kitagawa, J.; Sumyoshi, T.; Tanabe, K. *Bull. Chem. Soc. Jpn.*, B, *46*, 2985.
16 Moriya, A.; Tsuneki, H. US 5599999, **1997**; Tsuneki, H. *Shokubai*, **1998**, *40*, 304.
17 Capitán, M. J.; Centeno, M. A.; Malet, P.; Carrizosa, I.; Odriozola, J. A.; Muñoz-Páez, A.; Fernández, J. *J. Phys. Chem.*, **1995**, *99*, 4655.
18 Shen, J.; Lochhead, M. J.; Bray, K. L.; Chen, Y.; Dumesic, J. A. *J. Phys. Chem.*, **1995**, *99*, 2384.
19 Connell, G.; Dumesic, J. A. *J. Catal.*, **1987**, *105*, 285.
20 Soled, S. L.; McVicker, G.; Miseo, S.; Gates, W.; Baumgartner, J. *Stud. Surf. Sci. Catal.*, **1996**, *101*, 563.
21 Zhang, X.; Walters, A. B.; Vannice, M. A. *J. Catal.*, **1995**, *155*, 290.
22 Shi, C.; Walters, A. B.; Vannice, M. A. *Appl. Catal. B:*, **1997**, *14*, 175.
23 Scheithauer, M.; Knözinger, H.; Vannice, M. A. *J. Catal.*, **1998**, *178*, 701.
24 Capitán, M. J.; Malet, P.; Centeno, M. A.; Muñoz-Páez, A.; Carrizosa, I.; Odriozola, J. A. *J. Phys. Chem.*, **1993**, *97*, 92333.
25 Bettman, M.; Chase, R. E.; Otto, K.; Weber, W. H. *J. Catal.*, **1989**, *117*, 447.

Chapter 3

Silica-Supported Ytterbium Oxide Characterized by Spectroscopic Methods and Acid-Catalyzed Reactions

Abstract

Acid-Base properties of silica-supported ytterbium oxide catalyst, loading amounts of which are 25 μ - 8.4 mmol Yb $g(SiO_2)^{-1}$, were investigated by TPD experiment and α-pinene isomerization. The relations among acid properties, structures, and catalytic properties are discussed. The catalytic activity depends on loading amounts of ytterbium and pretreatment temperatures, and reached the highest when loading amount were 3.4 mmol $g(SiO_2)^{-1}$ and pretreatment temperature 1073 K. No crystalline phase was detected with XRD technique. By XAFS spectroscopy, Yb atoms adjacent to Yb were found to be absent, but the presence of Si atoms adjacent to Yb was observed in all the catalysts. XRD and XAFS analyses revealed that Yb atoms are supported on SiO_2 in a highly dispersed form as YbO_6 octahedra. Solid acidity is concluded to be due to strong interaction between a YbO_6 octahedron and a SiO_4 tetrahedron, and the specific activity per Yb-Si unit was independent of loading amounts. When loading amounts of Yb were excess to form two-dimensional ytterbium oxide overlayer, the apparent turn over numbers drastically reduced.

Introduction

The catalysis of rare-earth oxide is well known, and many reactions have been reported.[1-3] Rare earth oxide is known as a solid base catalyst, but there are few reports about catalysis over supported rare earth compound. As a general use, rare earth elements are added to catalyst supports to enhance their thermal stability.[4] Binary oxides of SiO_2-La_2O_3 and SiO_2-Y_2O_3 were predicted to exhibit acidity, according to the hypothesis proposed by Tanabe.[5,6] Shen et al. investigated acid-base property of europium oxides supported on silica and alumina by microcalorimetry and IR spectra of adsorption of ammonia and carbon dioxide.[7] They observed a generation of base sites on alumina-supported europium oxide, whereas a generation of acid sites was observed on silica-supported europium oxide. Connell and Dumesic reported the generation of Lewis and Brønsted acid sites on Sc/SiO_2 with IR spectra of adsorbed pyridine.[8] However, catalytic reactions have not been performed in these works mentioned above. Recently, Soled et al. reported the catalysis by rare earth oxide loaded on silica-aluminas, acid strength of which was the same level as halide-treated aluminas.[9] However, their aim was to control the acidity of silica-alumina by reduction of acid strength. Therefore, the relations among acid-base properties, structures, and catalytic properties of supported rare earth oxides have left unclear.

In the series of rare earth elements, we paid attention to ytterbium. Kobayashi et al. reported that lanthanide trifluoromethanesulfonate acts as a water-tolerant Lewis acid, and the ytterbium triflate exhibited the highest activities in lanthanide triflates.[10] Imamura et al.[11-13] and Baba et al.[14-16] prepared various kinds of supported Yb amide complexes, which were prepared by impregnation of support-materials with a liquid ammonia solution of Yb metal, followed by evacuation. They reported that supported Yb(III)-amide complexes successively changed to Yb(II)-imide and finally to Yb(III)-nitride as ramping evacuation temperatures. The catalytic properties exhibited by these complexes were quite different from each other. In the case of Y-type zeolite supported Yb complex, Yb(II)-imide complex promoted base-catalyzed reactions.[14-16] In the case of Yb-dosed SiO_2, the atomic array of $\equiv$ Si-O-Yb-NH_2 was responsible for hydrogenation property.[12]

However, catalysis by supported ytterbium oxide has not been reported. We prepared silica-supported ytterbium oxide catalysts with various loading amounts of Yb by conventional impregnation method. In this work, we report acid-base property of silica-supported ytterbium oxide catalysts and the results of characterization of their structure. For a model reaction for the acid-base property, α-pinene isomerization was utilized.

Experimental

SiO_2 gel was synthesized from tetraethyl orthosilicate (Nacalai tesque, EP-grade, singly distilled) by hydrolysis in a water-ethanol mixture at the boiling point, followed by calcination at 773 K for 5 h. Before calcination, a dried sample was ground to a powder under 100 mesh. Silica supported ytterbium oxide catalyst was prepared by impregnation of SiO_2 gel with an aqueous solution of ytterbium nitrate (Mitsuwa Co., 99.9%) at 353 K. The sample was dried at 363 K for 12 h, followed by calcination at 773 K for 5 h. These samples are referred to as *x* mmol Yb/SiO_2 (*x* stands for loading amounts of Yb atom per one gram of SiO_2). Ytterbium oxide was prepared by thermal decomposition of ytterbium nitrate at 773 or 1273 K for 5 h. They were identified by XRD patterns in comparison with Yb_2O_3 of C-rare earth structure (JCPDS file No. 18-1463).

α- Pinene isomerization was carried out under dry a N_2 atmosphere using a stirred batch reactor at 323 K. Before reaction, each sample was evacuated at 1073 K for 0.5 h and calcined under 6.66 kPa of O_2 for 1 h, followed by evacuation at the same temperature for 1 h. In a typical experiment, the reactor was loaded with 2 mL (12.6 mmol) of α-pinene (Nacalai, EP, 99.8%) and 50 mg of catalyst. Products were analyzed by GC and GC-Mass (Shimadzu, GCMS-QP5050).

The BET specific surface area measurements were carried out with N_2 adsorption isotherms at 77 K. Each sample was pretreated in the same way as α-pinene isomerization.

Temperature-programmed desorption (TPD) experiment was used as a detector for quadrupole-type mass spectrometer. NH_3 and CO_2 TPD measurements were performed at a heating rate of 5 K min^{-1}, and TPD measurement of pyridine was performed at a heating rate of 10 K min^{-1}. The pretreatment procedure was the same as mentioned above. The sample (100 mg) was exposed to 500 μmol of CO_2 or NH_3 at 373 K for 30 min, or 80 μmol of pyridine at 423 K for 10 min, followed by evacuation at the same temperature for 1 h. The amounts of desorbed gases (CO_2; m/e = 44, NH_3; m/e = 16, pyridine; m/e = 52) were normalized to that of introduced Ar (m/e = 40) as an internal standard. Because the most intense signal for pyridine-mass spectrum was that of m/e = 52, we adopted the profiles of m/e = 52 for acid properties of the catalyst.

X-ray diffraction patterns of samples were obtained with a Rigaku Geigerflux diffractometer using Ni-filtered Cu Kα radiation (1.5418 Å).

Yb-L_{III} edge X-ray absorption experiments were carried out at BL10B, Photon Factory in High Energy Accelerator Research Organization (KEK-PF; Tsukuba, Japan) with a ring energy of 2.5 GeV and a stored current, 250 - 280 mA. The X-ray absorption spectra were recorded by the EXAFS facilities installed on the BL10B in transmission mode at room temperature with a Si(311) two-crystal monochromator. X-ray was detected with ion chambers filled with 100% N_2, which are flowing at atmospheric pressure. The lengths of the ion chamber for incident and transmitted X-ray detection were 17 and 31 cm, respectively.

Data reduction was performed using a FACOM M1800 computer of Kyoto University Data Processing Center. The normalization method has been previously reported in detail.[17] To curve-fitting analysis, the following EXAFS formula was applied.

$$(1) \quad k^3\chi(k) = \Sigma_j (k^2 N_j / R_j^2) A_j(k) \exp(-2\sigma_j^2 k^2) \sin(2kR_j + \delta_j(k))$$

where k is the wavenumber of photoelectron, N_j the number of scattering atoms of the j th shell located at a distance of R_j from an Yb atom, A_j the envelope function which includes backscattering amplitude and damping factor caused by inelastic loss during electron traveling, σ_j the Debye-Waller factor and δ_j the phase shift. For an oxygen atom scatter, A_j and δ_j were extracted from L_{III} edge EXAFS spectrum of C-type Yb_2O_3 crystal, and hence σj corresponds to the relative Debye-Waller factor derivatived from that of the reference compound. In the extraction of these parameters, EXAFS spectrum of Yb_2O_3 prepared at 1273 K was used.

Results and Discussion

Catalysis

It is known that α-pinene isomerization was one of the excellent test reactions for acid-base catalyst,[18-20] and the products of α-pinene isomerization can be classified to three groups as shown in Scheme 1. The first group is ß-pinene. The second group consists of bicyclic products (camphene, α-fenchene, etc.). The last group is composed of monocyclic products (limonene, terpinolene, α-terpinene, γ-terpinene, etc.). Over solid base catalysts such as MgO and SrO, only equilibrium between α-pinene and ß-pinene should be observed.[21] In contrast, acid catalysts promote the reactions producing all the three groups, and the selectivities depend on the maximum acid strength. Table 1 shows results of α-pinene isomerization over silica-supported ytterbium oxide catalyst. Yb/SiO_2 catalysts exhibited high activity, however, SiO_2 and Yb_2O_3 were inactive for this reaction at 323 K. Catalytic activities were varied with Yb loading amounts. Catalytic activities per unit weight catalyst were enhanced as increasing Yb loading amounts and reached the highest when those were 3.4 through 5.8 mmol $g(SiO_2)^{-1}$. The selectivity was independent of loading amounts. The main products were limonene and camphene, selectivities of which were ca. 70% and 20%, respectively. A selective formation of ß-pinene from α-pinene occurs over solid bases, whereas ß-pinene was scarcely produced over Yb/SiO_2 catalysts. The selectivities of Yb/SiO_2 catalysts for α-pinene isomerization indicate that the generated active sites were acid sites. The independence of selectivities to loading amounts was revealed that the acid strength distributions of all Yb/SiO_2 catalysts resemble each other. A difference of the selectivity for 280 μmol Yb/SiO_2 catalyst against others was only due to its low conversion of 1.3%.

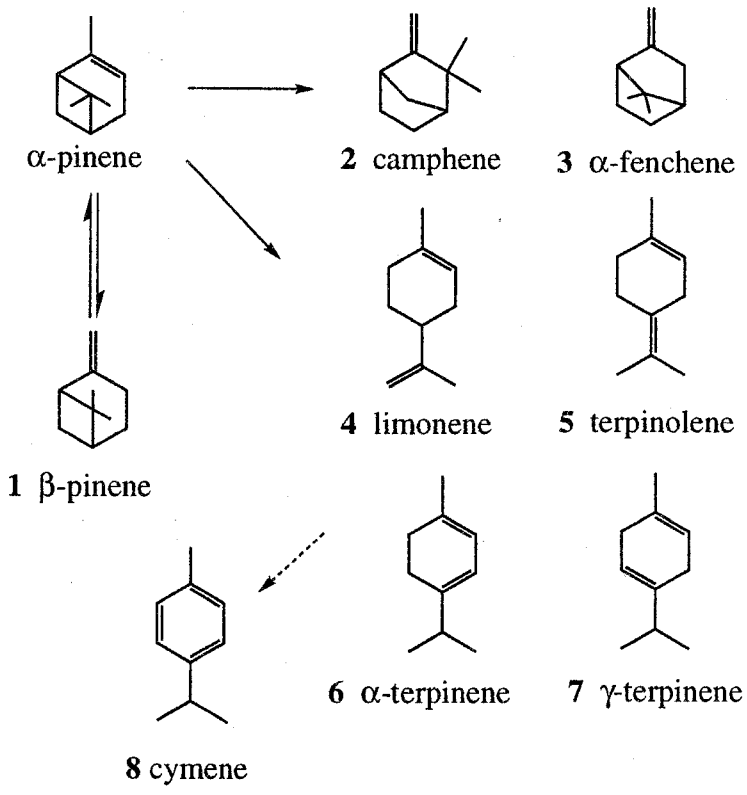

Scheme 1. α-Pinene isomerization.

TABLE 1: Results of α-pinene isomerization at 323 K [a]

Yb content / mmol $g_{(SiO_2)}^{-1}$	Yb content [wt%] [b]	Conversion (%)	Selectivity (%)[c] 1	2	3	4	5	6	7	8
SiO_2		0								
0.0258	0.5	tr								
0.280	5.2	1.3	5	20	3	55	6	3	4	7
1.7	24.9	12.5	tr	26	2	62	4	2	2	2
3.4	39.8	26.5	tr	23	2	67	4	2	2	tr
3.8	42.9	20.9	tr	20	2	67	5	2	2	2
5.8	53.4	30.8	tr	20	1	68	5	2	2	2
8.4	62.3	5.5	tr	17	1	67	6	2	3	4
Yb_2O_3		0								
MgO [d]		2.1	100							tr

[a] α-Pinene, 2 mL (12.6 mmol); catalyst, 50 mg; pretreatment temperature, 1073 K; reaction time, 3 h.

[b] As Yb_2O_3.

[c] 1: β-Pinene, 2: camphene, 3: α-fenchene, 4: limonene, 5: terpinolene, 6: α-terpinene, 7: γ-terpinene, 8: others.

[d] Catalyst: 300 mg as $Mg(OH)_2$, pretreatment temperature: 873 K, reaction temperature: 353 K.

To clarify the effect of loading amounts on catalytic activity, we estimated specific activities per an Yb atom from results of Table 1. The calculation is according to an assumption that all Yb-related sites on catalyst participate in the catalysis. As shown in Figure 1, estimated turn over numbers (TONs) per Yb atom are almost equal, except for 280 μmol and 8.4 mmol Yb/SiO_2 catalysts. This shows that each Yb-related site, loading amounts of which were among 1.7 and 5.8 mmol $g(SiO_2)^{-1}$, exhibits similar catalytic activities. The results, to which specific activity and the selectivity were quite similar, indicate that the structure of active sites resembles each other.

The effect of pretreatment temperature in α-pinene isomerization is shown in Figure 2. We selected 3.4 mmol Yb/SiO_2 catalyst as a representative of silica-supported ytterbium oxide catalysts because the catalyst exhibited the highest catalytic activity. Catalytic activity strongly depends on pretreatment temperature. The highest activity was exhibited when a catalyst was pretreated at 1073 K. When the pretreatment was carried out at 1273 K, the catalytic activity drastically reduced. To clarify the effect of pretreatment temperature to catalysis, concentrations of products versus that of α-pinene during reaction are plotted in Figure 3. Although pretreatment and reaction temperatures were variant for each plot, plots of all products concentrations, except for α-fenchene and cymene, versus that of α-pinene were on lines. The slope of the lines for each product represents the selectivity for α-pinene isomerization. Those of limonene and camphene were 0.62 and 0.19, respectively, and these were almost the same as the results found in Table 1. This shows that the products selectivities of α-pinene isomerization independent of pretreatment temperatures, and these compounds are the primary products. The concentration of cymene rapidly increased when α-pinene was almost consumed. This shows that cymene was the second products formed by dehydrogenation of monocyclic products such as limonene,[18] terpinolene and α-, γ-terpinene.[22]

The independence of selectivities to pretreatment temperatures also revealed that the acid strength distributions resemble each other, the same as effects of loading amounts. The same results were observed in the case of 1.7 mmol Yb/SiO_2 catalyst.

Temperature Programmed Desorption

To examine acid-base property of catalysts, CO_2 and NH_3-TPD were carried out and the profiles are shown in Figure 4. Much amount of CO_2 was desorbed from Yb_2O_3, whereas 3.4 mmol Yb/SiO_2 and SiO_2 did not desorb CO_2 at all. Basicity of ytterbium oxide completely disappeared in Yb/SiO_2 catalyst. In NH_3-TPD profiles, 3.4 mmol Yb/SiO_2 exhibited much larger peak around 473 K than those on Yb_2O_3 and SiO_2. It shows that new acid sites generate over Yb/SiO_2 catalyst. On the other hand, another desorption peak above 573 K was observed on both Yb_2O_3 and SiO_2. It has been reported that rare earth oxide possesses not only basic sites but also acid sites.[23,24] The NH_3-TPD profile of Yb_2O_3 had a desorption peak at 473 K and a shoulder peak at 723 K, and the tendency resembles that of previously reported.[25] The

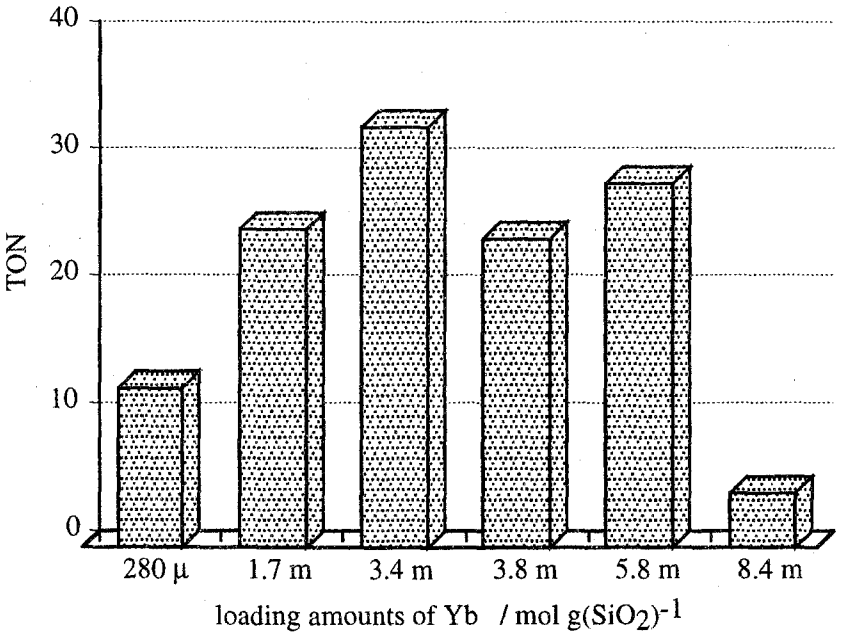

Figure 1. Turn over numbers (TONs) of catalysts in α-pinene isomerization. The TON per one Yb atom was calculated from results of TABLE 1.

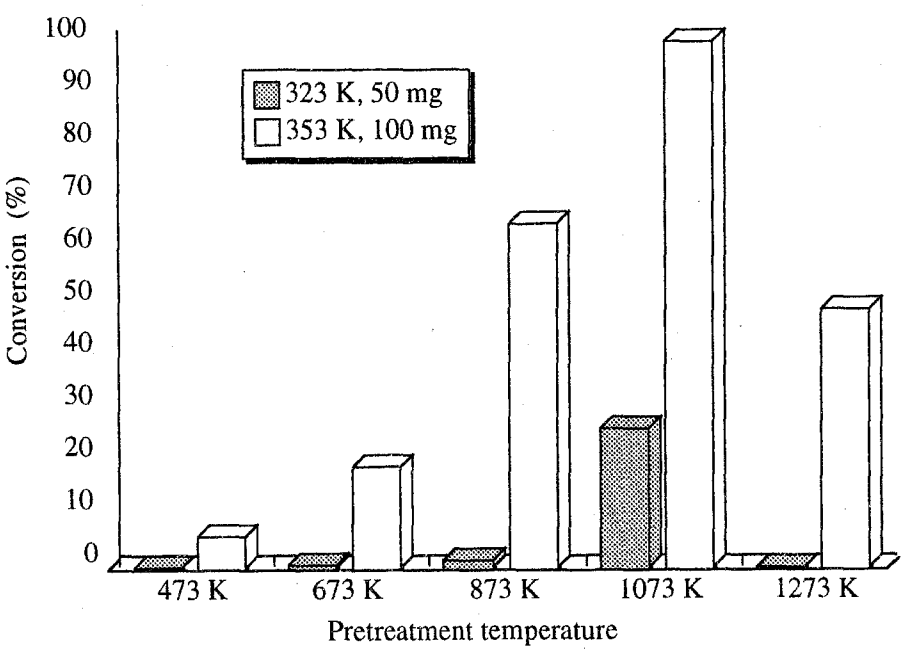

Figure 2. Dependence of pretreatment temperature in α-pinene isomerization. Catalyst: 3.4 mmol Yb/SiO_2, α-pinene: 2 mL, reaction time: 3 h.

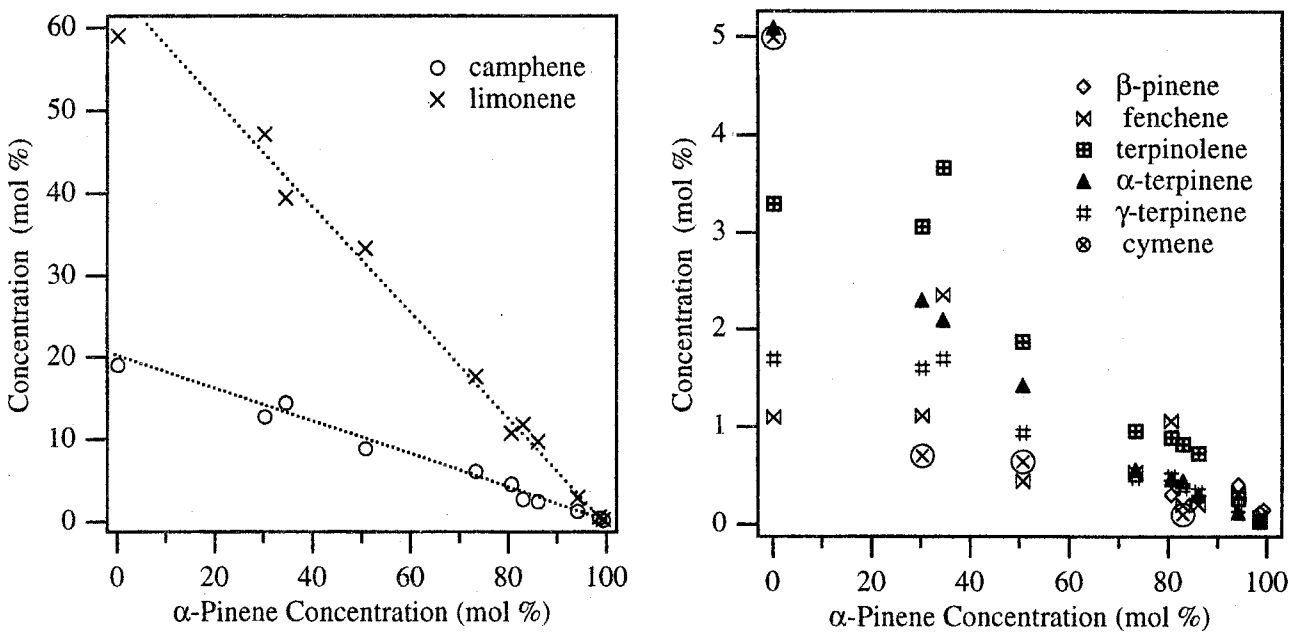

Figure 3. Concentration of products vs substrate in α-pinene isomerization. Plotted data are results of Figure 2. Catalyst: 3.4 mmol Yb/SiO_2. Pretreatment temperature: 473-1273 K. Reaction time: 323, 353 K.

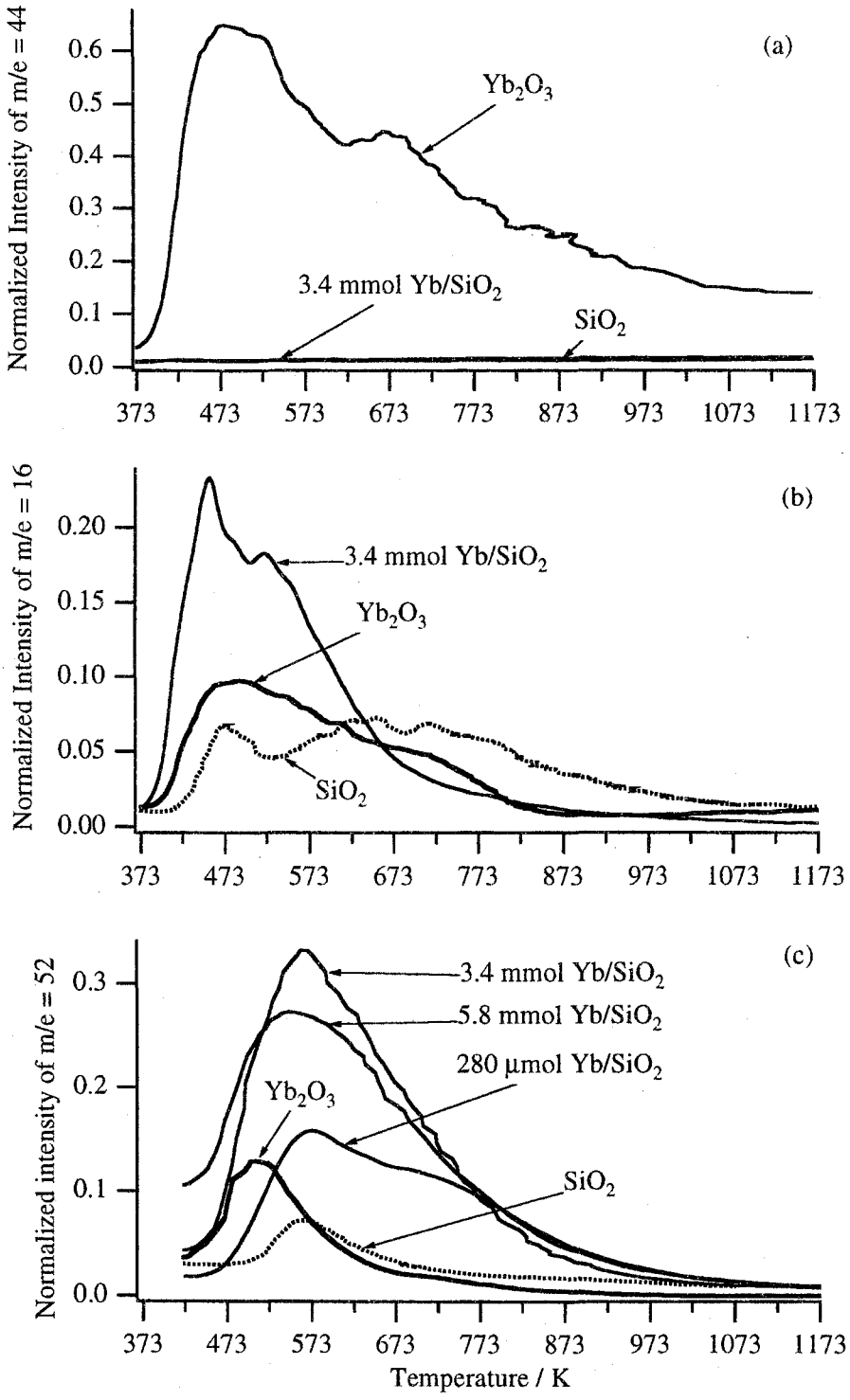

Figure 4. Temperature-programmed desorption profiles of CO_2 (a), NH_3 (b), and pyridine (c). Pretreatment procedure was performed at 1073 K.

NH_3-TPD profiles revealed that Yb_2O_3 possesses both acid and base sites; however Yb_2O_3 pretreated at 1073 K was inactive for α-pinene isomerization at 323 K.

From IR study, Morrow et al. reported that silica evacuated above 673 K has active siloxane bridge that reacts with NH_3 to produce $SiNH_2$ and SiOH at room temperature, whereas it did not react with pyridine.[26,27] In the present study, each the catalyst was pretreated at 1073 K, the temperature of which is enough to form such the active siloxane bridge. Therefore, the desorption peak around 623 K observed on silica was due to decomposition of surface $SiNH_2$ species. To clarify acidic property in more detail, pyridine TPD was also performed. Results were shown in Figure 4c. The 3.4 mmol Yb/SiO_2 catalyst exhibited the largest peak around 573 K in all the catalysts. The desorption peak of pyridine was observed on Yb_2O_3 and SiO_2, as the same as those of NH_3-TPD measurements. However the quantity of desorbed pyridine from Yb/SiO_2 catalysts extremely exceeded those of SiO_2 and Yb_2O_3. Results of pyridine TPD measurements corresponded to catalytic results. In our case, pyridine TPD measurement is more suitable method for an explanation of the acidic property of the catalysts pretreated at 1073 K than that of NH_3. In addition, the profile of SiO_2 exhibited only a single peak in contrast to that of NH_3. It is in agreement with IR study described above.[26,27]

X-ray Diffraction

Figure 5 shows Cu Kα XRD patterns of catalysts pretreated at 1073 K. Yb_2O_3 exhibited strong *d222* and *d400* reflections at 29.7 and 34.4°. SiO_2 gel exhibited only halo around 22 °. With increasing loading amounts of Yb, a new halo grew around 30 °. This halo was due to amorphous phase of Yb_2O_3 or ytterbium silicate. Any distinct peak was not observed over all the catalysts, although loading amounts of ytterbium as Yb_2O_3 went up to 5 - 60 wt%. This clearly shows that long-range ordering structures not formed. A trace peak was observed on 8.4 mmol Yb/SiO_2 at 29.8 °, which might be due to the *d222* reflection of Yb_2O_3. However, large parts of Yb atoms of 8.4 mmol Yb/SiO_2 were present on SiO_2 in an amorphous phase because this peak was very faint overlapping with large halo.

In the phase diagram of Yb_2O_3-SiO_2 system, it is reported that Yb_2O_3 and SiO_2 does not form solid solutions but form crystals of $Yb_2O_3 \cdot SiO_2$ and/or $Yb_2O_3 \cdot 2SiO_2$.[28] On the other hand, no crystalline phases were detected in all the catalysts. Therefore, it is concluded that ytterbium oxide on silica available for α-pinene isomerization is not in a crystal state but in an amorphous one.

X-ray Absorption Fine Structure

Figure 6 shows k^3-weighted EXAFS spectra and their Fourier transforms of Yb_2O_3. In the Fourier transform (FT) of EXAFS, peaks due to six O atoms and twelve Yb atoms were

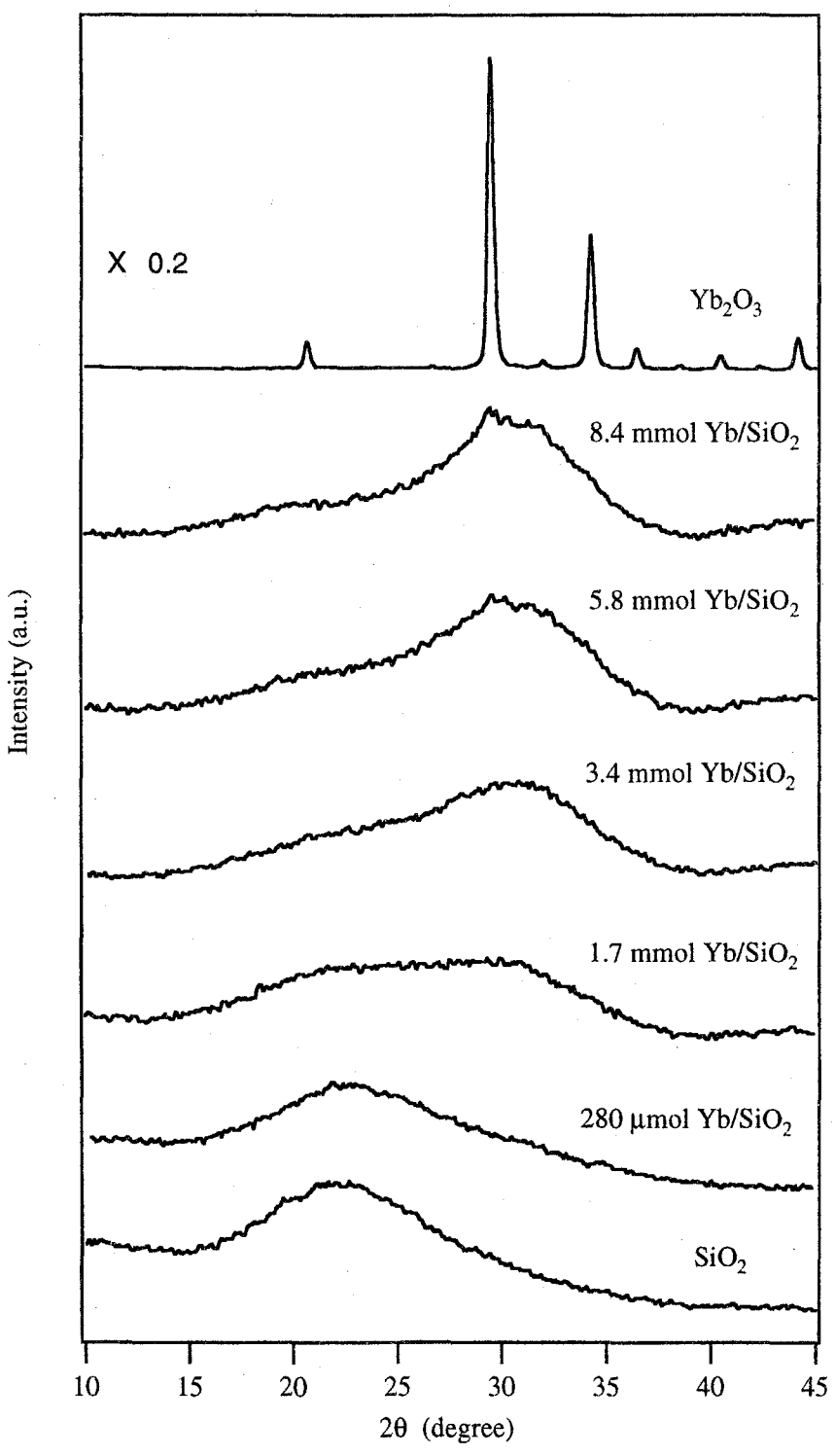

Figure 5. Cu-Kα XRD patterns of catalysts.

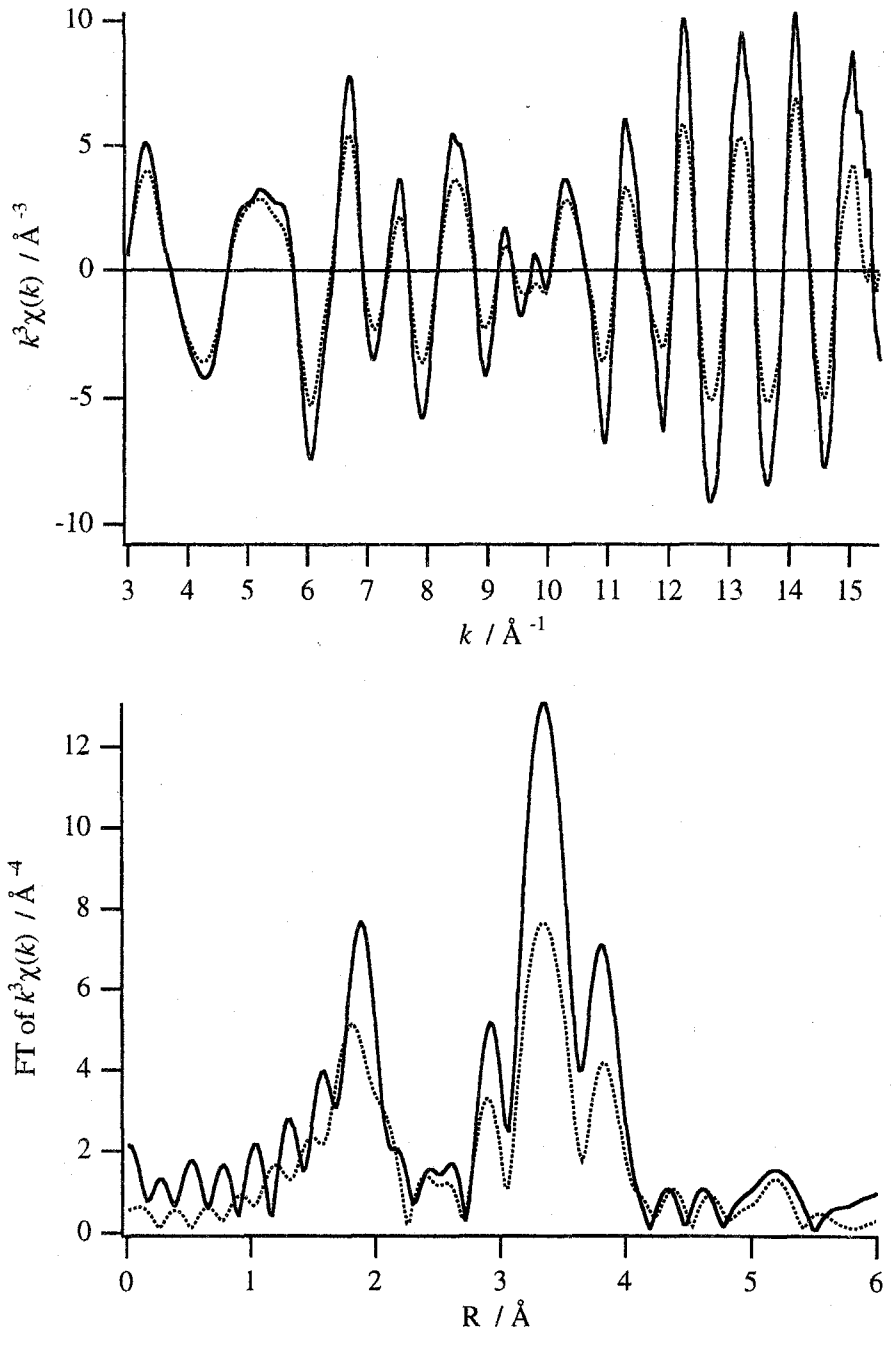

Figure 6. XAFS spectra of Yb_2O_3 prepared by calcination of ytterbium nitrate at 773 K (dotted curve), and 1273 K (solid curve).

observed at 1.9 and 3.3 Å, respectively. These calculated distances from crystallographic data (a_0 = 10.436 Å), are 2.259 Å for Yb-O, and 3.690 Å for Yb-(O)-Yb. The dotted curves in Figure 6 are the spectra of the sample that was prepared by thermal decomposition of ytterbium nitrate at 773 K. The k^3-weighted EXAFS spectrum was quite similar to that of Yb_2O_3 prepared at 1273 K, although the amplitude was lower. It shows that the temperature of 773 K is enough to decompose ytterbium nitrate salt to form Yb_2O_3 crystal, although the crystallinity was relatively low. Therefore, all Yb atoms of catalysts were present on SiO_2 as oxide.

Figure 7 shows Yb-L_{III} edge k^3-weighted EXAFS spectra of Yb/SiO_2 catalysts calcined at 773 K. The amplitudes and phases of all spectra were quite similar to each other. The amplitude decayed with k increasing, and no oscillations were observed beyond 12 Å^{-1}. The similarity of each EXAFS spectrum indicates that the local structures around Yb were almost the same. The oscillation frequencies of one EXAFS spectrum were not constant, and it shows that the EXAFS spectrum consists of some sine waves, as noted in EXAFS formula (1). It is clear that neighboring atoms of Yb were not a single kind. Teo et al. calculated that backscattering amplitude functions of lanthanides which have two peaks in low and high k region, and that of Yb has a large peak above 10 Å^{-1}.[29] On the other hand, those of light elements such as O and Si are monotonously decreasing with k, and become very small above 10 Å^{-1}. Because the amplitude of EXAFS spectra of catalysts monotonously decayed with k, it is concluded that any Yb atoms did not present around an Yb atom, in contrast to Yb_2O_3.

The k^3-weighted Fourier transformation was carried out against EXAFS of catalysts in the k range of 3.0 - 15.0 Å^{-1}, to obtain the radial structure function (RSF). The results are shown in Figure 8. In analogy with EXAFS spectra, all RSF were quite similar, and two peaks were observed around 1.8 and 2.9 Å. The peak around 1.8 Å was due to O atoms, the distance of which was similar to that of Yb_2O_3. The distance of second peak (indicated by an arrow) was much shorter than the peaks due to Yb atoms in Yb_2O_3 crystal. From the envelope functions of corresponding EXAFS spectra, it is obvious that the second peaks are not due to Yb atoms but due to light elements. As shown in Figure 6, ytterbium nitrate was decomposed to Yb_2O_3 crystal even at 773 K. Then, we assigned the second peaks due to Si atoms of supports. The distance was similar to previously reported ones between Si and transition metal atoms, such as Ti,[30] Ni,[31] and Nb.[32-35]

The curve-fitting results of catalysts and the crystallographic datum of Yb_2O_3 are summarized in Table 2. The first coordination spheres of all the catalysts could be fitted by one shell, and the estimated parameters were almost identical to each other. All the estimated parameters are consistent with those of Yb_2O_3 within an experimental error. The inter-atomic distances between Yb and O atoms strongly supported that Yb atoms of all the catalysts are in an octahedral coordination. From the results that no Yb-(O)-Yb contribution was observed and that of Yb-(O)-Si were observed, it is concluded that Yb atoms were supported on SiO_2 in a highly dispersed form as a YbO_6 octahedron, and a YbO_6 octahedron connected with SiO_4 tetrahedron through bridging oxygen. It is well known that coordination environments of

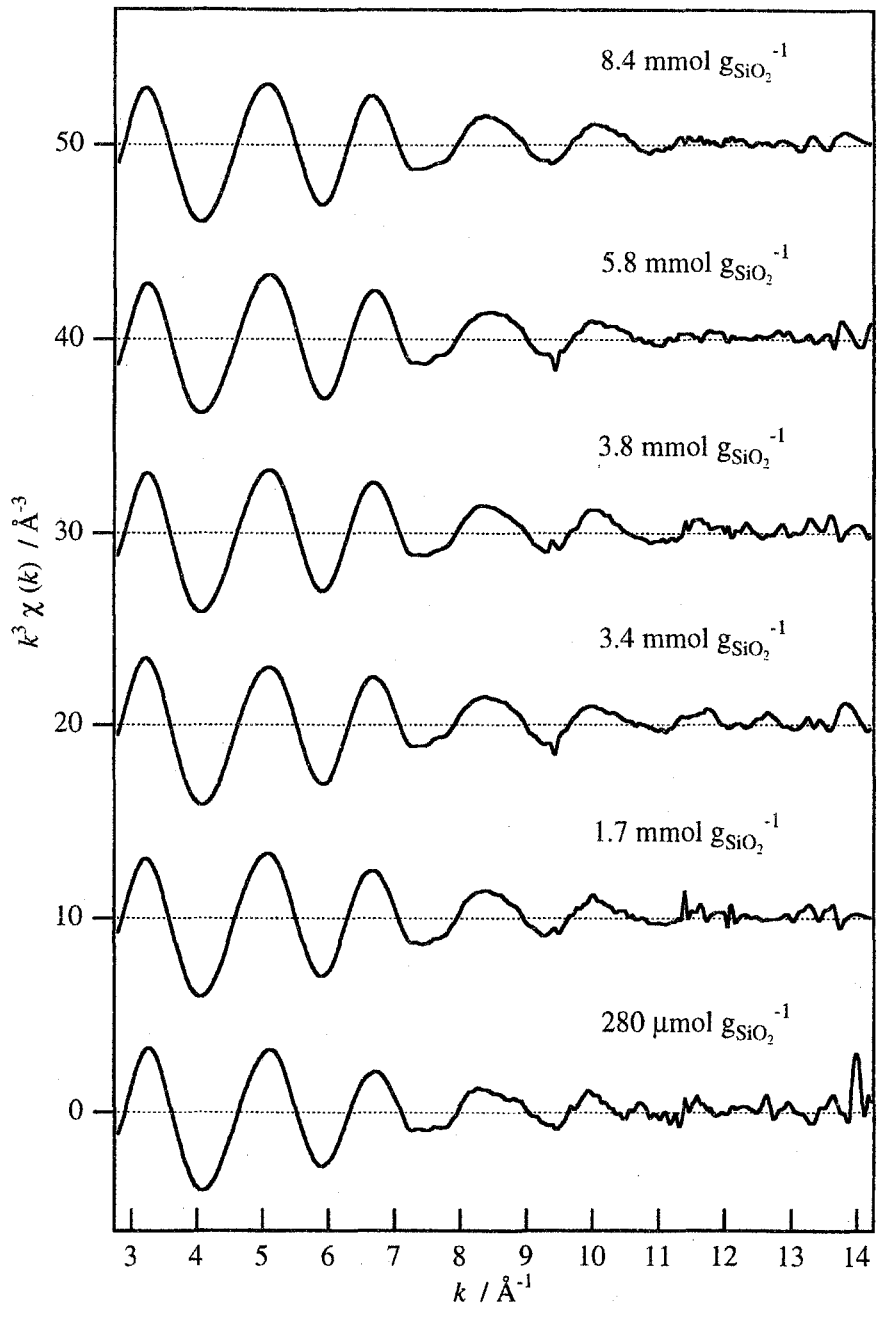

Figure 7. k^3-Weighted Yb-L_{III} edge EXAFS spectra of silica-supported ytterbium oxide.

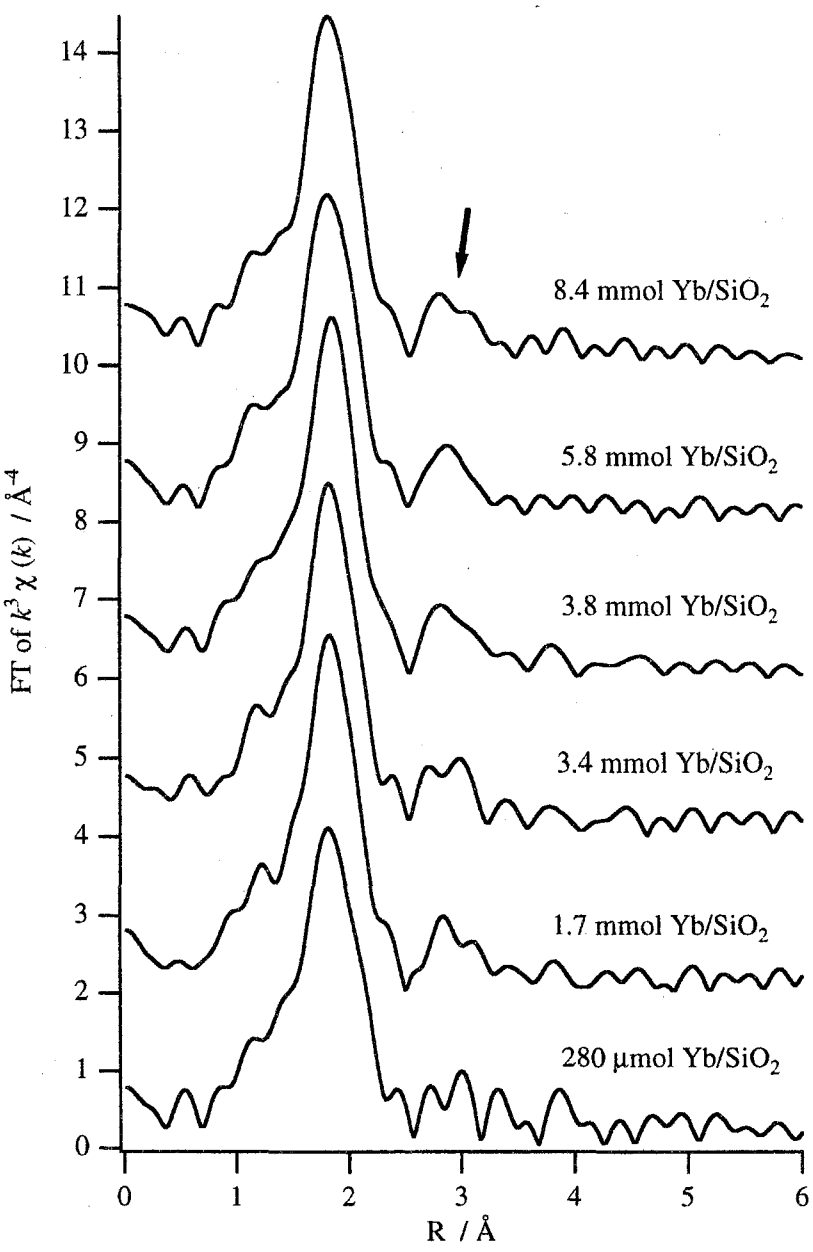

Figure 8. Fourier Transforms of k^3-weighted Yb-L_{III} edge EXAFS spectra of silica-supported ytterbium oxide.

TABLE 2: Structural Parameters for Yb-O Shells of Samples [a]

Sample	CN [b]	R / Å [c]	$\Delta\sigma^2$ / Å^2 [d]	Refinement (%) [e]
Yb_2O_3	6	2.259		
280 μmol Yb/SiO_2	6.2	2.29	0.0048	5.8
1.7 mmol Yb/SiO_2	6.2	2.29	0.0032	5.1
3.4 mmol Yb/SiO_2 [f]	6.0	2.29	0.0035	5.8
3.8 mmol Yb/SiO_2	5.7	2.29	0.0024	5.6
5.8 mmol Yb/SiO_2	5.9	2.28	0.0033	6.9
8.4 mmol Yb/SiO_2	6.1	2.29	0.0025	7.1

[a] Inverse-Fourier range, $\Delta R = 1.2 - 2.2$ Å; fitting range, $\Delta k = 4.0 - 12.0$ Å^{-1}.

[b] Coordination number.

[c] Distance between Yb and O atoms.

[d] Relative Debye-Waller factor against that of reference sample (Yb_2O_3).

[e] $\sqrt{\Sigma (k^3\chi_{obvious} - k^3\chi_{calculated})^2 / \Sigma (k^3\chi_{obvious})^2}$ x 100.

supported metal oxide often change by loading amounts and/or various treatments, and the changes of coordination cause the change of catalysis.[36,37] On the other hand, the coordination environments around Yb were independent of its loading amounts. This is the reason of the result of α-pinene isomerization that no changes of its selectivity was observed.

Structure of Active Sites

Table 3 summarized the estimated BET specific surface areas. The areas of catalysts include the SiO_2 carrier. The S_0 is a surface area $g(SiO_2)^{-1}$ carrier, which was calculated from BET specific surface area and Yb content. The $S_{occupied}$ is estimated occupied area by YbO_6 unit according to three assumptions described below. The first assumption is that all Yb atoms exist as a YbO_6 octahedron. The second is that all YbO_6 units have the same cross section. The third assumption is that the cross section is 16.0 $Å^2$ per YbO_6 unit, which is calculated by the following equation; 2.26 x 2.26 x π.

The BET specific surface area gradually decreased with increasing Yb loading amounts, and the surface area of carrier also decreased. In the case of 3.4 mmol Yb/SiO_2 catalyst, the surface area pretreated at 1073 K kept 85% of that pretreated at 673 K (fresh catalyst), whereas that pretreated at 1273 K was reduced to 50% of the original by sintering. This abrupt decrease of surface area between 1073 and 1273 K is one of the reasons for deactivation of catalyst, as shown in Figure 2. Because the extent of deactivation significantly exceeded that of sintering, another factor for deactivation should be considered although it is not clear now.

As shown in Figure 1, the high catalytic activities per Yb atom were demonstrated when loading amounts of Yb were among 1.7 and 5.8 mmol $g(SiO_2)^{-1}$. In cases of these loading amounts, the areas occupied by YbO_6 units ($S_{occupied}$) were calculated to 162 - 559 m^2 $g(SiO_2)^{-1}$. These values were comparable to the surface areas of $g(SiO_2)^{-1}$ carriers and the area of SiO_2 pretreated at 1073 K. It shows that two dimensional thin-layers of ytterbium oxide formed on SiO_2 surface, and local interaction between a YbO_6 octahedron and a SiO_4 tetrahedron generate solid acidity. In the case of 8.4 mmol Yb/SiO_2, the calculated $S_{occupied}$ is 812 m^2 $g(SiO_2)^{-1}$, which exceeds the area of carrier. The excess Yb atoms deposited on the thin-layer and blocked active sites, as the same as zirconium oxide deposited on TiO_2.[38] As a result, the estimated specific activity per Yb atom of 8.4 mmol Yb/SiO_2 was quite low. Because the highest activity was exhibited when pretreatment procedure was performed at 1073 K, we propose that the active sites are Lewis acid sites. It was reported that silica monolayer deposited on metal oxide exhibits weak Brønsted acidity,[39-42] and niobium oxide one-atom-layers on SiO_2 catalyzes dehydration of ethanol.[33] In the case of Yb/SiO_2 catalysts, it is concluded that the analogous two-dimensional ytterbium oxide overlayers were formed in 5.8 mmol Yb/SiO_2. The reason for no Yb-(O)-Yb configuration was observed in XAFS spectra is as follows; the distributions of distances among Yb atoms were wide and the Debye-Waller factor of Yb-Yb bonding due to static structural disorder was extremely large. In the case of 1.7 mmol Yb/SiO_2,

TABLE 3: Physical Properties of Samples

Yb content / mmol $g(SiO_2)^{-1}$	[wt%] [a]	Pretreatment Temp / K	Area [b] / $m^2\ g^{-1}$	S_0 [c] / m^2	$S_{occupied}$ [d] / $m^2\ g(SiO_2)^{-1}$
SiO_2		673	661	661	
		1073	601	601	
0.0258	0.5	1073	597	600	2.5
0.28	5.2	1073	501	528	27
1.7	24.9	1073	321	427	162
3.4	39.8	473	206	342	323
		673	212	352	323
		873	199	331	323
		1073	180	299	323
		1273	104	173	323
3.8	42.9	1073	145	253	368
5.8	53.4	1073	108	231	559
8.4	62.3	1073	50	132	812
Yb_2O_3 [e]		673	45		
		1073	16		

[a] As Yb_2O_3.

[b] BET specific surface area.

[c] Surface area of $g_{(SiO_2)}^{-1}$ carrier.

[d] Occupied area by assumed YbO_6 unit.

[e] Prepared by thermal decomposition of ytterbium nitrate at 773 K for 5 h.

the loading amount of Yb was much less than a formation of YbO_6 monolayer, but the specific activity per Yb atom was comparable to that of 5.8 mmol Yb/SiO_2. It shows that the formation of ytterbium oxide monolayer was not necessary for the generation of acid sites. It was concluded that the generation of solid acidity over Yb/SiO_2 catalyst was due to the strong interaction between a YbO_6 octahedron and a SiO_4 tetrahedron.

Conclusion

Silica supported ytterbium oxide catalyst exhibit solid acidity and catalyzes α-pinene isomerization at 323 K. The selectivity was independent of loading amounts and pretreatment temperature. The highest activity is exhibited when the pretreatment procedure was performed at 1073 K. Catalytic activity per Yb atom is constant when loading amounts are below 5.8 mmol $g(SiO_2)^{-1}$. Ytterbium atoms widely spread on SiO_2 surface as a YbO_6 octahedron, and the YbO_6 octahedron strongly interacts with SiO_4 tetrahedra. Local interaction between silica and ytterbium oxide generates solid acidity.

References

1 Rosynek, M. P. *Catal. Rev. -Sci. Eng.* **1977**,*16*, 111.

2 Tanabe, K.; Misono, M.; Ono, Y.; Hattori, H. *New Solid Acids and Bases*; Kodansha, Elsevier, Tokyo, 1989, pp 41-47.

3 Otsuka, K.; Jinno, K.; Morikawa, A. *J. Catal.* **1986**, *100*, 353.

4 Arai, H.; Machida, M. *App. Catal. A: General* **1996**, *138*, 161, and references therein.

5 Tanabe, K.; Sumiyoshi, T.; Shibata, K.; Kiyoura, T.; Kitajima, J. *Bull. Chem. Soc. Jpn.* **1974**, *47*, 1064.

6 Tanabe, K.; Misono, M.; Ono, Y.; Hattori, H. *New Solid Acids and Bases*; Kodansha, Elsevier, Tokyo, 1989, pp 108-11.

7 Shen, J.; Lochhead, M. J.; Bray, K. L.; Chen, Y.; Dumesic, J. A. *J. Phys. Chem.* **1995**, *99*, 2384.

8 Connell, G.; Dumesic, J. A. *J. Catal.* **1987**, *105*, 285.

9 Soled, S. L.; McVicker, G.; Miseo, S.; Gates, W.; Baumgartner, J. *Stud. Surf. Sci. Catal.* **1996**, *101*, 563.

10 Kobayashi, S.; Hachiya, I. *J. Org. Chem.* **1994**, *59*, 3590.

11 Imamura, H.; Yoshimochi, H.; Sakata, Y.; Tsuchiya, S. *J. Mol. Catal.* **1991**, *66*, L33.

12 Imamura, H.; Konishi, T.; Sakata, Y.; Tsuchiya, S. *J. Chem. Soc., Faraday Trans.* **1992**, *88*, 2251.

13 Imamura, H.; Konishi, T.; Suda, E.; Sakata, Y.; Tsuchiya, S. *Bull. Chem. Soc. Jpn.* **1996**, *69*, 77.
14 Baba, T.; Kim, G. J.; Ono, Y. *J. Chem. Soc., Faraday Trans.* **1992**, *88*, 891.
15 Tanaka, T.; Hanada, T.; Yoshida, S.; Baba, T.; Ono, Y. *Jpn. J. Appl. Phys.* **1993**, *32*, 481.
16 Baba, T.; Hikita, S.; Koide, R.; Ono, Y.; Hanada, T.; Tanaka, T.; Yoshida, S. *J. Chem. Soc., Faraday Trans.* **1993**, *89*, 89.
17 Tanaka, T.; Yamashita, H.; Tsuchitani, R.; Funabiki, T.; Yoshida, S. *J. Chem. Soc., Faraday Trans. I* **1988**, *84*, 2987.
18 Ohnishi, R.; Tanabe, K.; Morikawa, S.; Nishizaki, T. *Bull. Chem. Soc. Jpn.* **1974**, *47*, 571.
19 Corma, A.; García, H. *Catal. Today* **1997**, *38*, 257, and references therein.
20 Yamamoto, T.; Tanaka, T.; Funabiki, T.; Yoshida, S. *J. Phys. Chem. B* **1998**, *102*, 5830.
21 Ohnishi, R.; Tanabe, K. *Chem. Lett.* **1974**, 207.
22 Tanaka, T.; Itagaki, A.; Zhang, G.; Hattori, H.; Tanabe, K. *J. Catal.* **1990**, *122*, 384.
23 Choudhary, V. R.; Rane, V. H. *J. Catal.* **1991**, *130*, 411.
24 Hussein, G. A. M.; Gates, B. C. *J. Chem. Soc., Faraday Trans.* **1996**, *92*, 2425.
25 Choudhary, V. R.; Rane, V. H. *J. Catal.* **1991**, *130*, 411.
26 Morrow, B. A.; Cody, I. A. *J. Phys. Chem.* **1976**, *80*, 1995.
27 Morrow, B. A.; Cody, I. A. *J. Phys. Chem.* **1976**, *80*, 1998.
28 Levin, E. M.; Robbins, C. R.; McMurdie, H. F. *Phase Diagrams for Ceramists*; ed. The American Ceramic Society, Columbus: Ohio, 1969, p.108, Figure 2391.
29 Teo, B.-K.; Lee, P. A. *J. Am. Chem. Soc.* **1979**, *101*, 2815.
30 Yoshida, S.; Takenaka, S.; Tanaka, T.; Hirano, H.; Hayashi, H. *Stud. Surf. Sci. Catal.* **1996**, *101*, 871.
31 Carriat, J. Y.; Che, M.; Kermarec, M.; Verdaguer, M.; Michalowicz, A. *J. Am. Chem. Soc.* **1998**, *120*, 2059.
32 Nishimura, M.; Asakura, K.; Iwasawa, Y. *Proc. 9th. Int. Congr. Catal.*, Calgary, **1988**, 1842.
33 Asakura, K.; Iwasawa, Y. *J. Phys. Chem.* **1991**, *95*, 1711.
34 Ichikuni, N.; Iwasawa, Y. *Catal. Today* **1993**, *16*, 427.
35 Yoshida, H.; Tanaka, T.; Yoshida, T.; Funabiki, T.; Yoshida, S. *Catal. Today* **1996**, *28*, 79.
36 Yoshida, S.; Tanaka, T. *X-ray Absorption Fine Structure for Catalysts and Surfaces*: ed. Iwasawa, Y.; World Scientific, Danvers, 1996, pp 304-325.
37 Asakura, K.; Iwasawa, Y. *X-ray Absorption Fine Structure for Catalysts and Surfaces*: ed. Iwasawa, Y.; World Scientific, Danvers, 1996, pp 192-215.

38 Tanaka, T.; Salama, T. M.; Yamaguchi, T.; Tanabe, K. *J. Chem. Soc., Faraday Trans.* **1990**, *86*, 467.
39 Niwa, M.; Katada, N.; Murakami, Y. *J. Phys. Chem.* **1990**, *94*, 6441.
40 Niwa, M.; Katada, N.; Murakami, Y. *J. Catal.* **1992**, *134*, 340.
41 Katada, N.; Toyama, T.; Niwa, M. *J. Phys. Chem.* **1994**, *98*, 7647.
42 Sheng, T.-C.; Gay, I. D. *J. Catal.* **1994**, *145*, 10.

Chapter 4

Structural Analysis of Silica-Supported Ytterbium Oxide Catalyst by XAFS

Abstract

The structure of silica-supported ytterbium oxide catalyst (1.7, 3.4, 8.4 mmol Yb $g(SiO_2)^{-1}$) was characterized by X-ray diffraction and Yb L_{III}-edge XAFS. XANES and EXAFS spectra of all the catalysts were quite similar to each other but different from those of the Yb_2O_3 crystal. The local structure around Yb was not affected by the loading amounts of Yb and thermal treatment up to 8.4 mmol $g(SiO_2)^{-1}$ and 1273 K, respectively. In the second derivatives of the XANES spectra, Yb_2O_3 exhibited a doublet, while all the Yb/SiO_2 samples gave a singlet. The presence of Yb-O-Si linkage and the absence of Yb-O-Yb contributions were confirmed in all the Yb/SiO_2 catalysts. Yb atoms were supported on SiO_2 in a highly dispersed form as a YbO_6 octahedron, which strongly interacted with SiO_4 tetrahedra.

Introduction

The silica-supported ytterbium oxide catalyst (Yb/SiO_2) exhibits an acid property, although SiO_2 and Yb_2O_3 themselves are inactive for this reaction at 323 K.[1] The Yb/SiO_2 catalyst, loading amounts of which are in the rage of 280 μmol - 8.4 mmol $g(SiO_2)^{-1}$, catalyzes α-pinene isomerization to produce limonene selectively. The catalytic activity, which depends on loading amounts of ytterbium and pretreatment temperatures, reached its highest level at 3.4 mmol $g(SiO_2)^{-1}$ and 1073 K, respectively. It is known that the selectivity for α-pinene isomerization changes with acidity.[2] Loading amounts of Yb and pretreatment temperatures did not affect the selectivity, indicating that all the Yb/SiO_2 catalysts possess similar maximum acid strengths. Furthermore, specific activities per Yb atom were almost equal between 1.7 and 5.8 mmol $g(SiO_2)^{-1}$. This clearly shows that the structure of active sites have similar structure. In the present study, the local structures of Yb/SiO_2 catalyst samples around Yb are investigated by Yb L_{III}-edge XAFS.

Experimental

Silica supported ytterbium oxide catalyst (Yb/SiO_2) was prepared by impregnation of SiO_2 gel (637 $m^2\ g^{-1}$) with an aqueous solution of ytterbium nitrate at 353 K. The sample was dried at 363 K for 12 h, followed by calcination at 773 K for 5 h. These samples are referred to as *x* mmol Yb/SiO_2 (*x* stands for loading amounts of Yb atom per one gram of SiO_2). Pretreated samples were prepared as follows: each sample was evacuated at a prescribed temperature for 0.5 h and calcined under 6.66 kPa of O_2 for 1 h, followed by evacuation at the same temperature for 1 h. A post-reacted sample (3.4 mmol Yb/SiO_2 pretreated at 1073 K) was prepared.[3]

Yb_2O_3 of C-rare earth structure[4] was prepared by thermal decomposition of ytterbium nitrate at 1273 K for 5 h. $YbPO_4$ of xenotime structure[5] was prepared by calcination of precipitate at 1273 K for 5 h. The precipitate was obtained by addition of phosphoric acid solution (1.6 M) into an aqueous solution of ytterbium nitrate (0.1 M). $Yb_3Al_5O_{12}$ of garnet structure, which is the same structure as $Y_3Al_5O_{12}$,[6] was synthesized by the citric acid process. A mixture of ytterbium nitrate (3 mmol), aluminum nitrate (5 mmol) and citric acid (40 mmol) was dissolved at 348 K in 2 mL of water. The solution was stirred vigorously until it was solidified, followed by aging at 383 K for 48 h. The formed amber foam was precalcined at 623 K for 2 h, followed by calcination at 1273 K for 5 h. After calcination, it was quenched to a room temperature. Each ytterbium atom of $YbPO_4$ and $Yb_3Al_5O_{12}$ is surrounded by two kinds of oxygen shells and the total coordination number is eight. The crystalline phases were identified by XRD pattern measurements with JCPDS files (Yb_2O_3: 18-1463, $YbPO_4$: 26-998,

$Yb_3Al_5O_{12}$: 23-1476). The reference compound used was $YbNbO_4$ (Soekawa, Co. LTD: monoclinic distortion of the sheelite structure).[7]

Yb-L_{III} edge X-ray absorption experiments were carried out on the BL01B1 at SPring-8 (Hyogo, Japan) with a ring energy of 8 GeV and a stored current from 16 to 20 mA (proposal No. 1997B0100, 1998A0258). The X-ray absorption spectra were recorded in transmission mode at room temperature with a Si(111) two-crystal monochromator. The dispersive X-ray was collimated to be a parallel ray by a total reflection mirror, which locates at an upper stream 32.9 m from an X-ray source. The height of the X-ray size was 1.0 mm. X-ray absorption spectra were recorded every 0.3 eV in XANES region. Data reduction was performed using a FACOM M1800 computer at the Kyoto University Data Processing Center. The normalization method has been previously reported in detail.[8] For curve-fitting analysis, backscattering amplitude and phase shift functions for Yb-O pairs were obtained from k^3-weighted EXAFS spectrum of the Yb_2O_3 crystal.

Results and Discussion

X-ray Diffraction

The Cu-Kα XRD pattern of Yb_2O_3 exhibited strong d_{222} and d_{400} reflections at $2\theta =$ 29.7 and 34.4°. The pattern of SiO_2 gel exhibited only a single halo around 22 °. No distinct peaks were observed for any of the catalysts pretreated at 1073 K. With increasing loading amounts of Yb, a new halo grew on those of Yb/SiO_2 catalysts around 30 °. The origin of this amorphous phase could not be identified as both crystalline ytterbium silicates and Yb_2O_3, which exhibit typical reflections in this region.

XANES

Figure 1 shows the XANES spectra and second derivatives of Yb/SiO_2 catalysts and Yb_2O_3. Absorption edges of all the spectra were identical, indicating all the Yb/SiO_2 catalysts consist of Yb^{3+} species. Each XANES spectrum of the Yb/SiO_2 catalyst exhibited almost the same shape. This shows that the local structure around Yb is quite similar to each other for all the catalysts. A small peak around 8962 eV, which was tentatively ascribed to shake-up transition,[9] were observed on the spectrum of Yb_2O_3, but not on spectra of Yb/SiO_2. Normalized heights of the white line are 2.3 for that of Yb_2O_3, and about 3.0 for those of Yb/SiO_2. Yb-L_{III} edge XANES spectra could be deconvoluted with two curves: one is Lorentzian for $2p$-$5d$ transition; the other is an arctangent for the continuum absorption. Peak areas and FWHM for the Lorentzian curve of Yb_2O_3 are 56 a.u. and 6.5 eV, and those for 3.4 mmol Yb/SiO_2 pretreated at 1073 K are 71 a.u. and 5.3 eV, respectively.

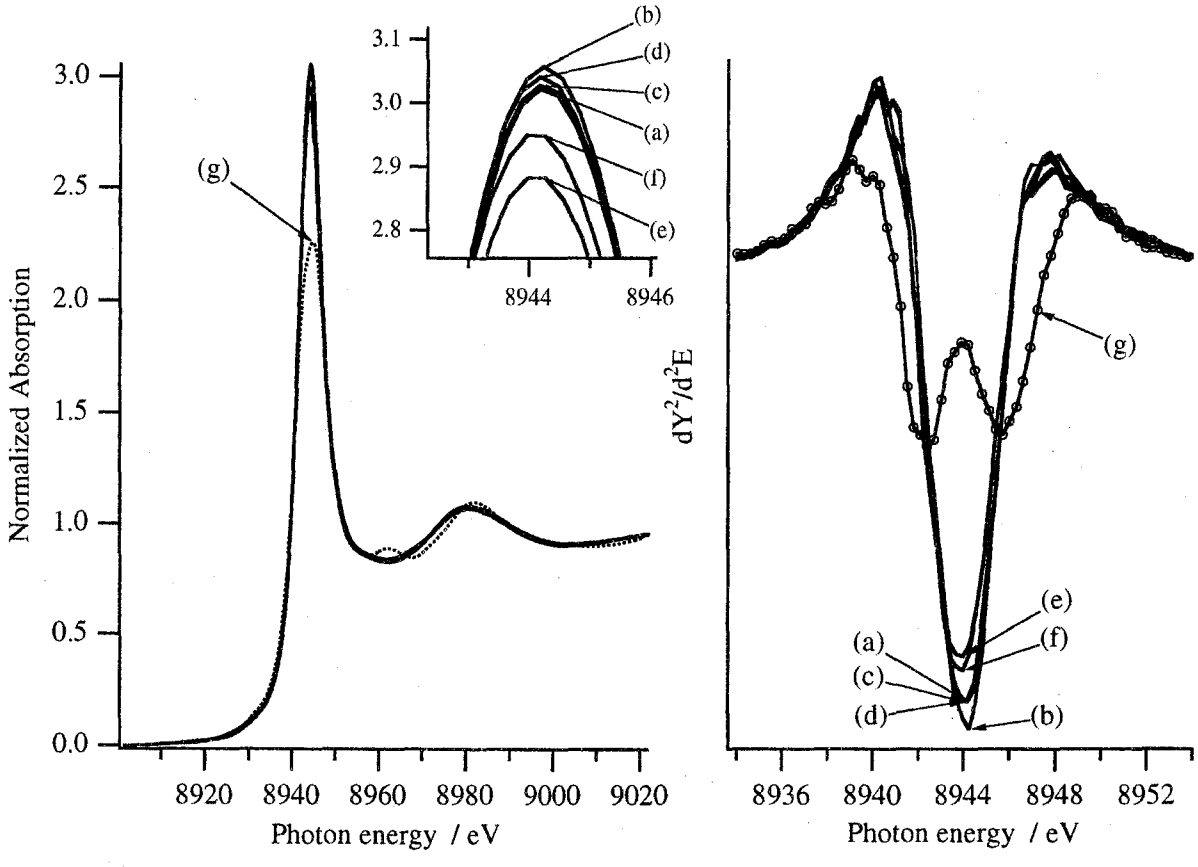

Figure 1. Yb-L_{III} edge XANES spectra and their second derivatives: (a) 1.7 mmol Yb/SiO_2; (b) 3.4 mmol Yb/SiO_2; (c) pretreated at 1073 K; (d) after reaction pretreated at 1073 K; (e) pretreated at 1273 K; (f) 8.4 mmol Yb/SiO_2 pretreated at 1073 K, and (g) Yb_2O_3.

The white line of Yb_2O_3 was a little broader and lower than those of Yb/SiO_2. To investigate white lines in more detail, we differentiated the XANES spectra. As shown in Figure 1, the second derivative of Yb_2O_3 split to a doublet, while all Yb/SiO_2 derivatives were singlets. Each doublet peak intensity of Yb_2O_3 was equivalent. One possible reason for this split is coexistence of Yb^{2+} and Yb^{3+} species; however, this could be excluded. In the Yb-L_{III} edge XANES spectra of Yb^{2+} and Yb^{3+} compounds, the peak positions of each white line differ by 7 eV.[10-12] In the present study, the energy difference for splitted peaks was only 3.3 eV. This splitting energy is close to the ordinary *d*-orbital splitting energy caused by the crystal field. The *5d* orbital of Yb^{3+} is vacant. If the *5d* orbital splits to two by a crystal field, the five *d*-orbitals would redistribute two kinds of energy levels, vacant sites of which are two to three. As the split peaks were equivalent in intensity, this split is not caused by the crystal field. The other possible reason is the crystal structure of Yb_2O_3. There are two kinds of distorted YbO_6 octahedra in Yb_2O_3 of C-rare earth structure. However, Lytle *et al.* observed a similar doublet structure on second derivatives of Ho_2O_3 and Eu_2O_3, but not on Nd_2O_3 and Lu_2O_3.[13] This splitting phenomenon does not arise from C-rare earth structure.

All Yb/SiO_2 catalyst samples are amorphous. To examine whether a split of white line results from the crystallinity or not, XANES spectra of other ytterbium oxide crystals were recorded. Figure 2 shows XANES spectra and their second derivatives of Yb_2O_3 (T_h^7; *Ia3*), $YbNbO_4$ (C_2^3; *C2*), $YbPO_4$ (D_{4h}^{19}; *Ia/amd*) and $Yb_3Al_5O_{12}$ (O_h^{10}; *Ia3d*). In the second derivative, the spectrum of $YbNbO_4$ was a triplet, and those of $YbPO_4$ and $Yb_3Al_5O_{12}$ were singlets. It may be questionable whether the second derivative of $YbNbO_4$ XANES exhibits a triplet, but obviously the second derivative is not a singlet. It shows that a split of white line is not related merely to the crystallinity. Although we do not know the origin of this splitting at the present stage, it can be concluded that local structures around Yb in Yb/SiO_2 catalysts are quite different from that of Yb_2O_3.

The characteristic peak in Yb-L_{III} XANES is a small peak at 8962 eV. The crystal system of $YbPO_4$ is tetragonal, the symmetry of which is the highest in reference compounds. Garnet crystallize of *Ia3d* is one of the most symmetric space groups of the cubic system.[14] $YbPO_4$ has not only the highest white line, but also the smallest peak intensity of 8962 eV. In the XANES spectra of all the Yb/SiO_2 catalysts, there are no peak around 8962 eV, and there are higher white lines than in spectra of $YbPO_4$ and $Yb_3Al_5O_{12}$. Therefore, it is possible that a YbO_n unit on SiO_2 is highly symmetric.

EXAFS

Figure 3 shows Yb-L_{III} edge k^3-weighted EXAFS spectra and their Fourier transforms. The amplitudes and phases of all the spectra of Yb/SiO_2 were quite similar, whereas each EXAFS oscillation does not consist of a single frequency. The similarity of each EXAFS spectrum indicates that each of the local structures around Yb was almost the same and

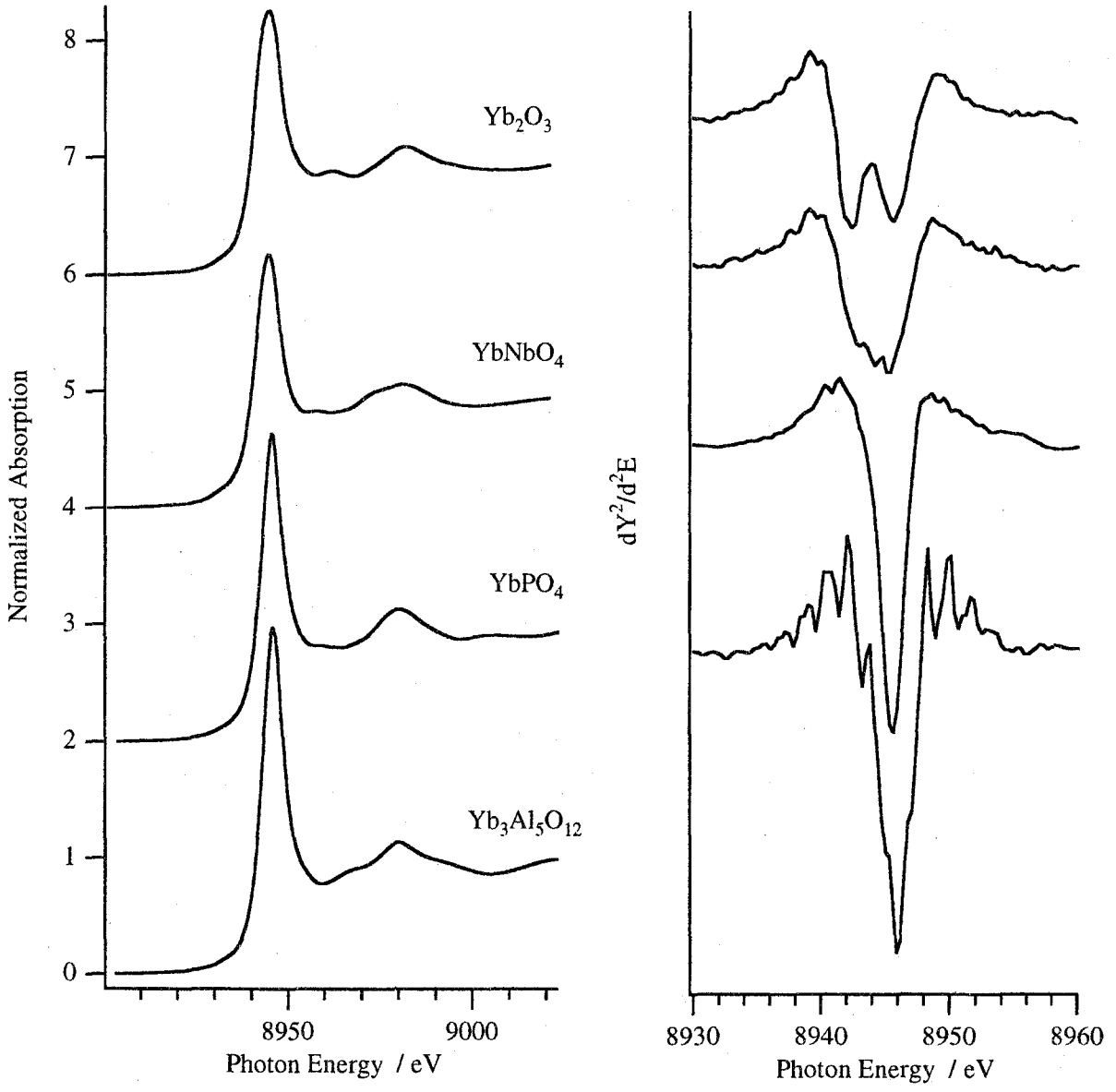

Figure 2. Yb-L_{III} edge XANES spectra and their second derivatives.

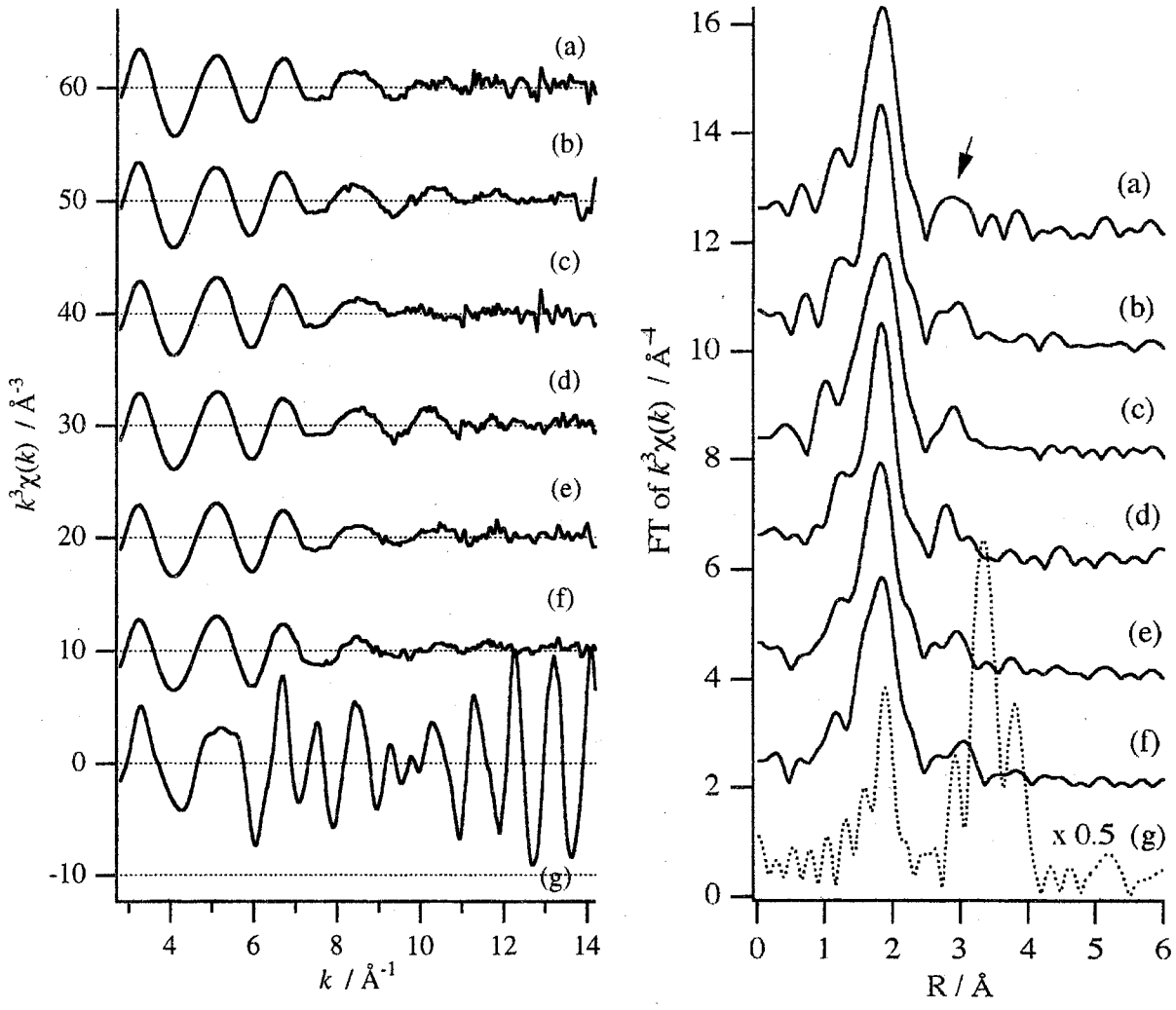

Figure 3. k^3-weighted Yb-L_{III} edge EXAFS spectra and their Fourier transform: (a) 1.7 mmol Yb/SiO_2; (b) 3.4 mmol Yb/SiO_2; (c) pretreated at 1073 K; (d) after reaction pretreated at 1073 K; (e) pretreated at 1273 K; (f) 8.4 mmol Yb/SiO_2 pretreated at 1073 K, and (g) Yb_2O_3.

that none of the treatments affected the structure. In contrast to that of Yb_2O_3, the amplitude of EXAFS functions decayed with increasing wavenumber and no oscillations were observed over 12 $Å^{-1}$ in the Yb/SiO_2 catalysts. The lack of oscillations above 12 $Å^{-1}$ indicates that the contributions of Yb-O-Yb pairs are not present in the Yb/SiO_2 catalyst. As in the EXAFS spectra, all radial structure functions (RSFs) were quite similar, and two peaks were observed around 1.8 and 2.9 Å in each spectrum. The distance of the second peak (indicated by an arrow) was much shorter than that of the peak due to Yb atoms of Yb_2O_3.

To clarify the structure of the Yb/SiO_2 catalyst around Yb, an inverse Fourier transformation of RSFs was performed against Yb_2O_3 and 3.4 mmol Yb/SiO_2 catalyst pretreated at 1073 K. Figure 4 shows the inverse Fourier transformed k^3-weighted EXAFS spectra and their envelope functions. The envelope function for the second shell of Yb_2O_3, which is due to Yb-Yb pairs, had two peaks around 7 and 13 $Å^{-1}$. In contrast, those for both the first and second shells of Yb/SiO_2 catalyst monotonically decreased with k. Then, we assigned the peak appeared in the RSFs at 2.9 Å due to not Yb, but Si atoms of support. This was supported by the results that the position of the second peak in the RSF of Yb/SiO_2 was quite different from that of Yb_2O_3, and that the envelope function has a similar tendency to the backscattering amplitude function for Si of theoretical calculations.[15] In each the RSF of Yb/SiO_2 sample, the magnitude of peaks due to Si was the same level in all the catalysts, regardless of loading amounts and pretreatment procedures. It shows that a strong interaction between Yb and Si atoms had formed in the sample preparation step.

The curve-fitting results are summarized in Table 1. Because all the samples are amorphous and the loading amounts of Yb are very large 25 - 62 wt% as in Yb_2O_3, it is presumed that the local structure of each Yb/SiO_2 catalyst sample around Yb should not be uniform. Then, we did not carry out a curve fitting analysis for the second peak, which appeared in the RSF around 2.9 Å.

The first coordination spheres of all the catalysts could be satisfactory fitted by a single shell. All the estimated parameters were within errors, and were similar to those of Yb_2O_3. The inter-atomic distances between Yb and O atoms strongly supported the hypothesis that Yb atoms of all the catalysts are in a six-fold coordination. The results, that no Yb-O-Yb contribution was observed and that contribution of Yb-O-Si were observed, indicate the presence of an isolated YbO_6 octahedron connected to SiO_4 tetrahedra with sharing oxygen atoms. However, all of an YbO_6 units are not always truly isolated. The distributions of distances among Yb atoms were broad, and the Debye-Waller factor due to static structural disorder was extremely large. Therefore, Yb-Yb contributions were not observed in all the spectra of Yb/SiO_2 catalysts. The interaction between a YbO_6 octahedron and SiO_4 tetrahedra is concluded to be much stronger than that of among the YbO_6 units.

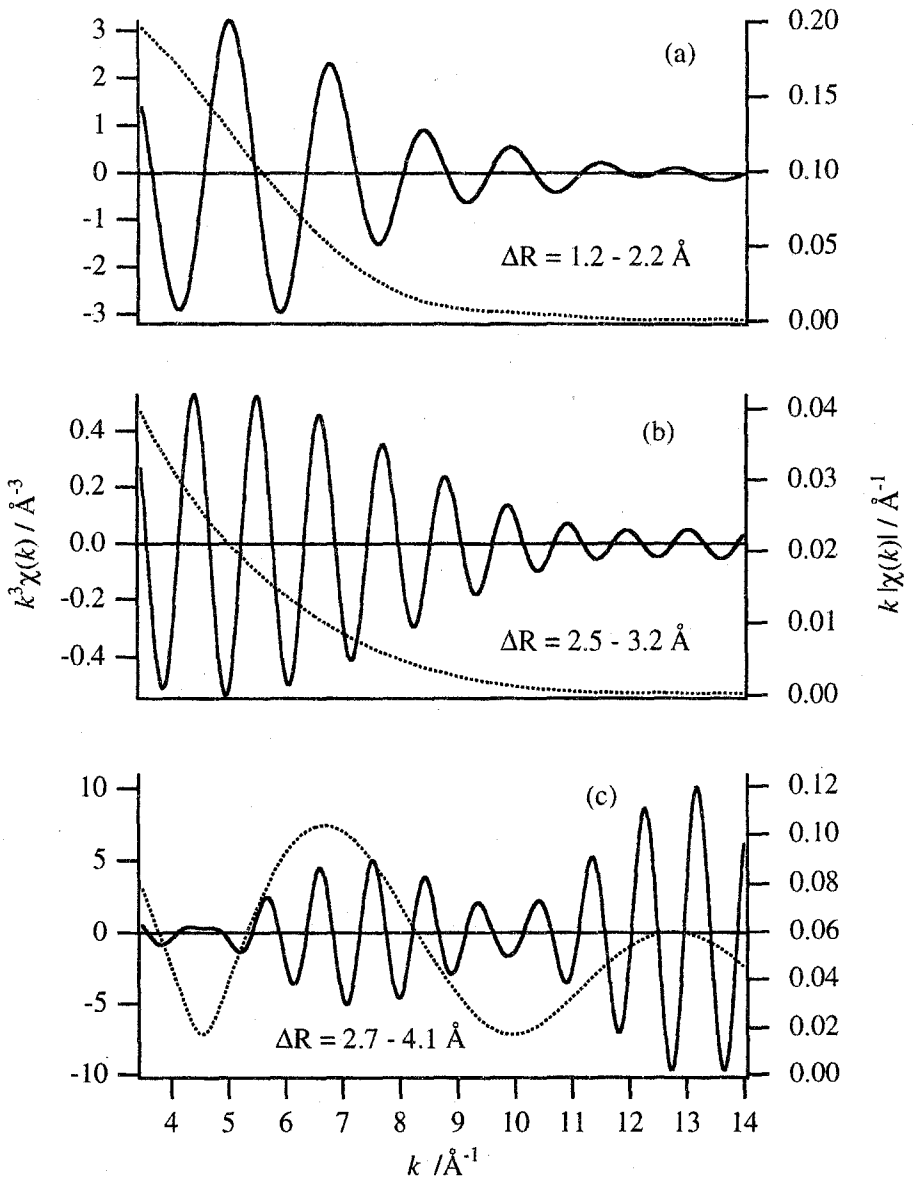

Figure 4. Inverse Fourier transformed EXAFS (solid curves) and their envelope functions (dotted curves); 3.4 mmol Yb/SiO_2 pretreated at 1073 K (a, b), and Yb_2O_3 (c).

TABLE 1: Structural Parameters for Yb-O Shells of Samples [a]

Sample	CN	R / Å	$\Delta\sigma^2$ / Å^2	Refinement (%) [b]
Yb_2O_3	6	2.259 [c]		
$YbPO_4$ [d]	3.7	2.29	-0.0064	10.2
	3.7	2.42	-0.0068	
1.7 mmol Yb/SiO_2	6.5	2.29	0.0044	7.3
3.4 mmol Yb/SiO_2				
fresh	6.0	2.28	0.0032	9.2
pretreated at 1073 K	6.0	2.27	0.0044	9.5
after reaction	5.3	2.27	0.0020	6.7
pretreated at 1273 K	5.7	2.27	0.0039	7.5
8.4 mmol Yb/SiO_2				
pretreated at 1073K	6.0	2.27	0.0044	12.2

[a] Inverse-Fourier range, ΔR = 1.2 - 2.2 Å; fitting range, Δk = 4.0 - 12.0 Å^{-1}.

[b] $\sqrt{\Sigma (k^3\chi_{obvious} - k^3\chi_{calculated})^2 / \Sigma (k^3\chi_{obvious})^2}$ x 100.

[c] Average interatomic distance, calculated from the crystallog datum (a_0 = 10.436 Å).

[d] Inverse-Fourier range, ΔR = 1.4 - 2.4 Å; fitting range, Δk = 4.0 - 12.0 Å^{-1}.

Conclusion

All the silica-supported ytterbium oxide catalysts (1.7, 3.4, 8.4 mmol Yb g$(SiO_2)^{-1}$) retained their amorphous state after thermal treatment at 1073 K. Neither the loading amounts of Yb nor thermal treatment affected on the local structure around Yb. The coordination sphere around Yb was quite similar to each Yb/SiO_2 catalyst. Yb atoms were supported on SiO_2 in a highly dispersed form as a YbO_6 octahedron. The YbO_6 octahedron strongly interacted with SiO_4 tetrahedra, rather than with other YbO_6 octahedra. A definitive difference between Yb_2O_3 crystal and ytterbium oxide supported on SiO_2 was observed in Yb-L_{III} edge XANES spectra.

References

1 Yamamoto, T.; Matsuyama, T.; Tanaka, T.; Funabiki, T.; Yoshida, S. *J. Mol. Catal. A* in press.

2 Ohnishi, R.; Tanabe, K.; Morikawa, S.; Nishizaki, T. *Bull. Chem. Soc. Jpn.* **1974**, *47*, 571.

3 α- Pinene isomerization was carried out under dry N_2 atmosphere at 323 K for 3 h using a stirred batch reactor, which was loaded with 5 mL of α-pinene (32 mmol) and 300 mg of pretreated catalyst. The 99.8% of α-pinene had converted to limonene and camphene, selectivities of which were 66% and 18%, respectively.

4 Wyckoff, R. W. G., *Crystal Structures 2nd ed.*, vol.2, pp. 2-6. Interscience Publishers. New York 1986.

5 Wyckoff, R. W. G., *Crystal Structures 2nd ed.*, vol.3, pp. 15-18. Interscience Publishers. New York 1986.

6 Wyckoff, R. W. G., *Crystal Structures 2nd ed.*, vol.3, pp. 222-225. Interscience Publishers. New York 1986.

7 Wyckoff, R. W. G., *Crystal Structures 2nd ed.*, vol.3, pp. 19-23. Interscience Publishers. New York 1986.

8 Tanaka, T.; Yamashita, H.; Tsuchitani, R.; Funabiki, T.; Yoshida, S. *J. Chem. Soc., Faraday Trans. I* **1988**, *84*, 2987.

9 Kutzler, F. W.; Hodgson, K. O.; Misemer, D. K.; Doniach, S. *Chem. Phys. Lett.* **1982**, *92*, 626.

10 Hatwa, T. K.; Nayak, R. M.; Padalia, B. D.; Ghatikar, M. N.; Sampathkumaran, E. V.; Gupta, L. C.; Vijayaraghavan, R. *Solid State Commun.* **1980**, *34*, 617.

11 Rao, C. N. R.; Sarma, D. D.; Sarode, P. R.; Sampathkumaran, E. V.; Gupta, L. C.; Vijayaraghavan, R. *Chem. Phys. Lett.* **1980**, *76*, 413.

12 Tanaka, T.; Hanada, T.; Yoshida, S.; Baba, T.; Ono, Y. *Jpn. J. Appl. Phys.* **1993**, *32*, 481.

13 Lytle, F. W.; van der Laan, G.; Greegor, R. B.; Larson, E. M.; Violet, C. E.; Won, J. *Phys. Rev. B* **1990**, *41*, 8955.

14 *International Tables for Crystallography*; D. Reidel Publishing Co.: Dordrecht, Boston, 1993; Vol. A, p. 706.

15 Rehr, J. J.; Mustre de Leon, J.; Zabinsky, S. I.; Albers, R. C. *J. Am. Chem. Soc.* **1991**, *113*, 5135.

Chapter 5

Generation of Acid Sites on Silica-Supported Rare Earth Oxide Catalysts: Structural Characterization and Catalysis for α-Pinene Isomerization

Abstract

Silica-supported rare earth oxide catalysts (Ln/SiO_2; Ln = La, Ce, Pr, Sm, Eu, Tb, Yb and Y), loading amounts of which were 3.4 mmol $g(support)^{-1}$, were characterized by α-pinene isomerization, and temperature-programmed desorption (TPD), Fourier transform infrared (FTIR), X-ray diffraction (XRD), X-ray absorption fine structure (XAFS), thermogravimetric-differential thermal analysis (TG-DTA) and Raman spectroscopy. In the lanthanoid series, the catalytic activity increased with atomic number from ^{57}La to ^{70}Yb, except for Ce. All the Ln/SiO_2 catalysts, except for Ce, were amorphous. On the surface of the catalyst, Ln-O-Si and Ln-O-Ln linkages formed, the ratio of which varied with the loaded element. The ratio of Ln-O-Si linkage increases with stronger affinity among LnO_n unit and SiO_4 tetrahedra, and the affinity depends on the size of Ln^{3+}. With increasing ratio of Ln-O-Si to Ln-O-Ln linkage, the catalytic activity increases. Silica-supported yttrium oxide catalyst, trivalent ion radius of which is quite similar to that of ytterbium, exhibited the same activity as that of Yb/SiO_2. Raman spectroscopic characterization revealed that excess loading of Yb atoms on SiO_2-support block Yb-O-Si linkage to form Yb_2O_3 fine particle. When Yb/SiO_2 was pretreated at 1273 K, fine ytterbium silicate crystallites formed. Ln-O-Si linkage without a long-ranged ordering structure was the active site for α-pinene isomerization.

Introduction

The addition of rare-earth elements to catalysts has been performed mainly to enhance thermal stability of the catalysts themselves.[1,2] In contrast, there are few studies concerning catalyses of supported rare earth oxides. Capitán *et al.* investigated the Sm_2O_3/Al_2O_3 catalyst for correlations between catalysis for oxidative coupling of methane and the surface Sm-Al-O phases.[3] They concluded that the oxide-like structure shows better selectivity toward C_2 species than the $SmAlO_3$ phase. Shi *et al.* reported that dispersed La_2O_3 on alumina exhibits higher activity for reduction of NO with CH_4 in the presence of oxygen than unsupported La_2O_3, while the catalytic activity of La/SiO_2 was significantly lower than that of La_2O_3.[4]

According to the hypothesis for acidity prediction proposed by Tanabe *et al.*, binary oxides among silica and rare-earth oxides, such as La_2O_3-SiO_2 and Y_2O_3-SiO_2 are expected to exhibit solid acidity.[5,6] Shen *et al.* investigated acid-base properties of silica- and alumina-supported europium oxide with spectroscopic methods. They found that alumina-supported europium oxide possesses basic sites stronger than that of Eu_2O_3, and silica-supported europium oxide exhibits Lewis acid properties.[7] To our knowledge, this report is the only study so far to investigate acid-base properties of supported rare earth oxides. Recently, the catalysis of monoethanolamine synthesis over SiO_2-Y_2O_3 was reported, while the precise acidity remained unknown.[8]

In a previous study, we reported that silica-supported ytterbium oxides exhibit solid acidity and catalyze α-pinene isomerization at 323 K.[9,10] The activity depends on the loading amounts of ytterbium and pretreatment temperatures. The maximum activity was exhibited when loading amount was 3.4 mmol Yb $g(SiO_2)^{-1}$, and was pretreated at 1073 K. From X-ray absorption fine structure (XAFS) characterization, we have concluded that Yb atoms are supported on silica in a highly dispersed form as a YbO_6 octahedron. A YbO_6 octahedron strongly interacts with SiO_4 tetrahedra, rather than other YbO_6 octahedra. The Yb-O-Si linkage was concluded to be the active sites for α-pinene isomerization.

Following on from this, we prepared several kinds of silica-supported rare earth oxide catalysts to elucidate the specific character of each rare earth element. Here, we will report on the catalytic properties of supported rare earth oxides and their structural characterization. As a model reaction of acid-base properties of each catalyst, α-pinene isomerization was adopted, as in our previous work.[9] It is known that the difference in acidity of each catalyst influences the catalysis for α-pinene isomerization concerning its selectivity.[11-15] Effective acid strength for α-pinene isomerization was proposed as $H_0 \leq +3.3$.[15, 16]

Experimental

Material

SiO_2 gel (661 $m^2\ g^{-1}$) was synthesized from tetraethyl orthosilicate (Nacalai, EP-grade, singly distilled) by hydrolysis in a water-ethanol mixture at the boiling point, followed by calcination at 773 K for 5 h in dry air stream.[17] Before calcination, a dried sample was grounded to a powder under 100 mesh. The silica-supported rare earth oxide catalyst was prepared by impregnation of SiO_2 gel with an aqueous solution of $Ln(NO_3)_3 \cdot xH_2O$ at 353 K. The elements used were La (Nacalai, 99.9%), Ce, Eu (Rare Metallic, 99.9%), Pr, Gd, Tb (Rare Metallic, 99.99%), Sm (Wako, 99.5%), Yb (Mitsuwa, 99.9%), and Y (Wako, 99.9%). The impregnated sample was dried at 363 K for 12 h, followed by calcination at 773 K for 5 h. Other supports used were γ-Al_2O_3 (JRC-ALO-4), $Mg(OH)_2$ (Rare Metallic, 99%), and $Zr(OH)_4$ (obtained by hydrolysis of $ZrOCl_2$ [18, 19]). The loading amount of Ln atom per one gram of support was 3.4 mmol in each catalyst.

Catalysis

α- Pinene isomerization was carried out under a dry N_2 atmosphere using a stirred batch reactor at 323 K. Prior to each reaction, the catalyst was evacuated at 1073 K for 0.5 h and calcined under 6.66 kPa of O_2 for 1 h, followed by evacuation at the same temperature for 1 h. For an each experiment, the reactor was loaded with 2 mL (12.6 mmol) of α-pinene (Nacalai, EP, 99.8%) and 50 mg of catalyst. Products were analyzed by FID gas chromatography (GC-14A; Shimadzu) with a CBP20-M25-025 capillary column (Shimadzu).

Characterization

The BET specific surface area measurement was carried out with BELSORP 28SA (BEL Japan, Inc.) using a N_2 adsorption isotherm at 77 K. Prior to the measurement, each sample was outgassed at 1073 K for 3 h. The analyzed results are summarized in Table 1.

X-ray diffraction (XRD) patterns were obtained with a Rigaku Geigerflux diffractometer using Ni filtered Cu-Kα radiation (averaged as 1.5418 Å).

FTIR spectra of adsorbed pyridine were recorded using a Perkin-Elmer Paragon 1000 spectrometer with the resolution of 4 cm^{-1}. Each sample (42-79 mg) was pressed into a self supporting wafer (20 mm in diameter), and was mounted in an *in situ* IR cell equipped with NaCl windows. A wafer was pretreated in the same way as for the catalytic reaction. The pretreated wafer was exposed to 1.0 kPa of pyridine vapor at 423 K for 5 min, followed by evacuation at the same temperature for 1 h. After cooling to room temperature, each spectrum was recorded in the transmission mode.

Pyridine temperature-programmed desorption (TPD) experiments were performed at a heating rate of 10 K min^{-1} and a quadrupole-type mass spectrometer (MASSMATE-100, ULVAC) was used as a detector. Prior to TPD measurement, 200 mg of sample was pretreated

TABLE 1: Specific Surface Area of Catalysts Pretreated at 1073 K

	SiO_2	3.4 mmol Ln / SiO_2							
		^{57}La	^{58}Ce	^{59}Pr	^{62}Sm	^{63}Eu	^{65}Tb	^{70}Yb	^{39}Y
wt% [a]	-	36	37 [b]	36	37	37	38	40	28
Area / $m^2\ g^{-1}$ [c]	601	159	301	216	179	164	210	180	246
S_0 / $m^2\ g^{-1}$ [d]	601	248	477	337	284	260	338	300	341

[a] As Ln_2O_3

[b] As CeO_2

[c] BET specific surface area estimated with a N_2 adsorption isotherm at 77 K.

[d] Surface area of $g(SiO_2)^{-1}$ carrier.[9]

in the same way as for α-pinene isomerization. The pretreated sample was exposed to 2.0 kPa of pyridine at 473 K for 10 min, followed by evacuation at the same temperature for 1 h. The amount of desorbed pyridine was normalized to that of introduced Ar (m/z = 40) as an internal standard.

Thermogravimetric-differential thermal analysis (TG-DTA) was carried out with a Rigaku Thermoflex TG 8110. Each profile was recorded under a dry N_2 stream (20 mL min^{-1}) at the heating rate of 5 K min^{-1}. α-Al_2O_3 crystal was utilized as the standard material for DTA analysis.

The laser Raman spectra were recorded with a JASCO NRS-2000 spectrometer using the 514.5 nm line of Ar^+ laser emission. The incident laser power was 20 mW at sample position, and scan time was 60 - 120 s for a single spectrum. The spectral resolution was 4 cm^{-1}.

X-ray absorption experiments were carried out on the BL01B1 at SPring-8 (Hyogo, Japan). The ring energy was 8 GeV, and the stored current was 17 - 20 mA. The X-ray absorption spectra were recorded in the transmission mode with a Si(111) two-crystal monochromator. Higher harmonics were eliminated with Rh-coated mirrors (1.5 mrad for Y-K edge, and 5 mrad for Ln-L_{III} edge XAFS measurements). The dispersive X-ray was collimated by a total reflection mirror, at an upper stream 32.9 m from an X-ray source as a parallel ray. The height of the X-ray size was 1.0 mm. X-ray absorption spectra were recorded every 0.3 eV in the XANES region of each L_{III} edge. Data reduction was performed using a FACOM M1800 computer at the Kyoto University Data Processing Center. The normalization method has been previously reported in detail.[20]

TABLE 2: Results of α-Pinene Isomerization over 3.4 mmol Ln/SiO_2 at 323 K [a]

Element	Conversion	Selectivity [b] (%)							
	(%)	1	2	3	4	5	6	7	8
La	0.4	10	22	1	50	5	5	3	4
	15.3 [c]	1	17	2	66	6	3	3	3
Ce	0								
	1.0 [c]	9	27	3	43	7	2	4	5
Pr	0.7	4	19	1	58	6	4	3	5
	30.1 [c]	tr	16	2	67	5	3	3	4
Sm	3.7	1	18	1	66	5	3	2	4
Eu	6.7	1	18	1	69	5	2	2	2
Tb	8.2	1	18	2	67	5	2	3	2
Yb	26.5	tr	23	2	67	4	2	2	tr
(SiO_2) [c]	0								
Y	28.3	tr	17	2	63	4	2	2	tr

[a] α-Pinene, 2 mL (12.6 mmol); Catalyst, 50 mg; Pretreatment temperature, 1073 K; Reaction time, 3 h.

[b] 1: ß-Pinene, 2: camphene, 3: α-fenchene, 4: limonene, 5: terpinolene, 6: α-terpinene, 7: γ-terpinene, 8: others.

[c] Catalyst, 100 mg; Reaction temperature, 353 K.

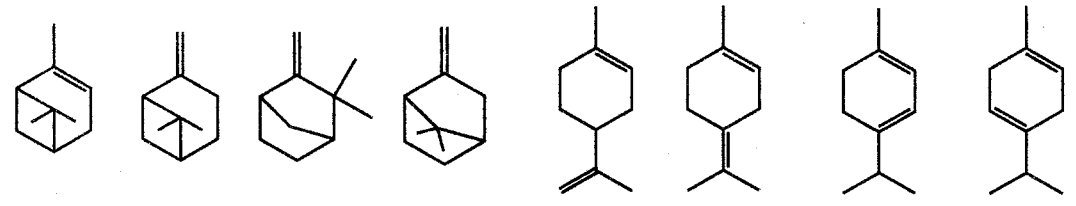

α-pinene β-pinene camphene α-fenchene limonene terpinolene α-terpinene γ-terpinene

Results

Catalysis

Table 2 shows results of α-pinene isomerization over 3.4 mmol Ln/SiO_2 catalysts pretreated at 1073 K. Only Ce/SiO_2 was inert for this reaction in the series of Ln/SiO_2 catalysts, and Yb/SiO_2 exhibited the highest activity. The activity of La/SiO_2 was much lower than that of Yb/SiO_2. With increasing atomic number from ^{57}La of light rare earth elements to ^{70}Yb of heavy rare earth elements, the activity increased except for Ce/SiO_2. In all the catalysts, α-pinene was selectively converted to limonene (*ca.* 68%) and camphene (*ca.* 20%) when the conversion was above 1%. Because La/SiO_2 and Pr/SiO_2 were poorly active at 323 K, the obtained selectivities were different from those of other catalysts. When the reaction was performed at 353 K, La/SiO_2 and Pr/SiO_2 gave identical selectivities to the others. Ce/SiO_2 exhibited quite low activity for α-pinene isomerization even at 353 K. Y/SiO_2 exhibited almost the same activity and selectivity as those of Yb/SiO_2, although yttrium is not a lanthanoid but an element of the sixth period.

The effect of support was examined with a supported ytterbium oxide catalyst. The supports used were SiO_2, γ-Al_2O_3, MgO and ZrO_2. The pretreatment temperature was 1073 K for each catalyst. As summarized in Table 3, only a silica-supported ytterbium oxide catalyst exhibited catalytic activity. No active sites catalyzing this reaction formed on the other supports.

TABLE 3: Results of α-Pinene Isomerization over Supported Ytterbium Oxides and the Physical Properties of Catalyst Samples Pretreated at 1073 K

Support [a]	Conversion (%) [b]	S_{BET} / $m^2\ g^{-1}$	Phase
SiO_2	26.5	180	amorphous
γ-Al_2O_3	tr	76	γ-Al_2O_3, Yb_2O_3
MgO	tr	39	MgO, Yb_2O_3
ZrO_2	tr	25	c-ZrO_2*ss* [c]
(Yb_2O_3)	tr	16	Yb_2O_3

[a] Loading amount of Yb; 3.4 mmol g(support)$^{-1}$.

[b] α-Pinene, 2 mL; Catalyst, 50 mg; Pretreatment temperature, 1073 K; Reaction temperature, 323 K; Reaction time; 3 h.

[c] Cubic-ZrO_2 solid solution.

XRD

Figure 1 shows Cu-Kα XRD patterns of 3.4 mmol Ln/SiO_2 catalysts and SiO_2 gel pretreated at 1073 K. SiO_2 gel exhibited only one halo around $2\theta = 22°$. The other catalysts possess a halo around $2\theta = 29\text{-}31°$ beside the halo due to amorphous silica. XRD characterization demonstrates that only Ce/SiO_2 crystallized to form CeO_2, and the other catalysts were amorphous. It shows that all of the other rare-earth oxides were supported on silica as an amorphous state. The origin of amorphous phases could not be identified, because both crystalline rare earth silicates and rare earth oxides exhibit typical reflections in this region where the new halo appeared. The 3.4 mmol Yb/SiO_2 sample pretreated at 1273 K, the catalytic activity of which was significantly lower than that of one pretreated at 1073 K,[9] was amorphous as well.

Ytterbium oxide and zirconium oxide forms a solid solution.[21] In the XRD pattern of 3.4 mmol Yb/ZrO_2 pretreated at 1073 K, only a cubic solid solution ZrO_2-Yb_2O_3 phase was detected. As shown in Table 3, the supported species crystallized on γ-Al_2O_3 and MgO to form Yb_2O_3 (JCPDS file No. 18-1463). Any binary oxides present were not detected in the XRD patterns of all of the supported ytterbium oxide samples.

FTIR

Figure 2 shows FTIR spectra of adsorbed pyridine on catalyst samples pretreated at 1073 K. The peak assignments were carried out based on studies by Connell and Dumesic.[22,23] On 3.4 mmol Yb/SiO_2, pyridine adsorption gave three distinct bands bonded to a Lewis site at 1448, 1492 and 1608 cm^{-1}. The spectrum on Yb_2O_3 displayed five bands at 1442, 1474, 1488, 1574 and 1602 cm^{-1}, and a similar spectrum of adsorbed pyridine was obtained on La_2O_3.[24] Bands at 1442, 1488 and 1602 were attributed to pyridine adsorbed on a Lewis acid site (L-pyridine). The residual two peaks at 1474 and 1574 were due to carboxylate species formed as cracking products.[24] In contrast, only hydrogen-bonded pyridine (H-pyridine) was observed on SiO_2 pretreated at 1073 K.

The 19b mode of L-pyridine on Yb/SiO_2 (1448 cm^{-1}) and 19b mode of H-pyridine on SiO_2 (1446 cm^{-1}) gave quite similar wavenumbers, and it is difficult to distinguish between H-pyridine and L-pyridine. However, the spectrum of SiO_2 had no peak around 1490 cm^{-1} (19a mode), and had the typical wavenumber of 8a mode below 1600 cm^{-1}. In addition, it was reported that SiO_2 gave H-pyridine at 1446 and 1598 cm^{-1}.[22] Therefore, we conclude that Yb/SiO_2 possesses Lewis acid sites, and pretreated SiO_2 has no acid sites to give L-pyridine. Yb_2O_3 possesses Lewis acid sites of almost as much as 3.4 mmol Yb/SiO_2, however, the acid sites do not catalyze α-pinene isomerization at 353 K.

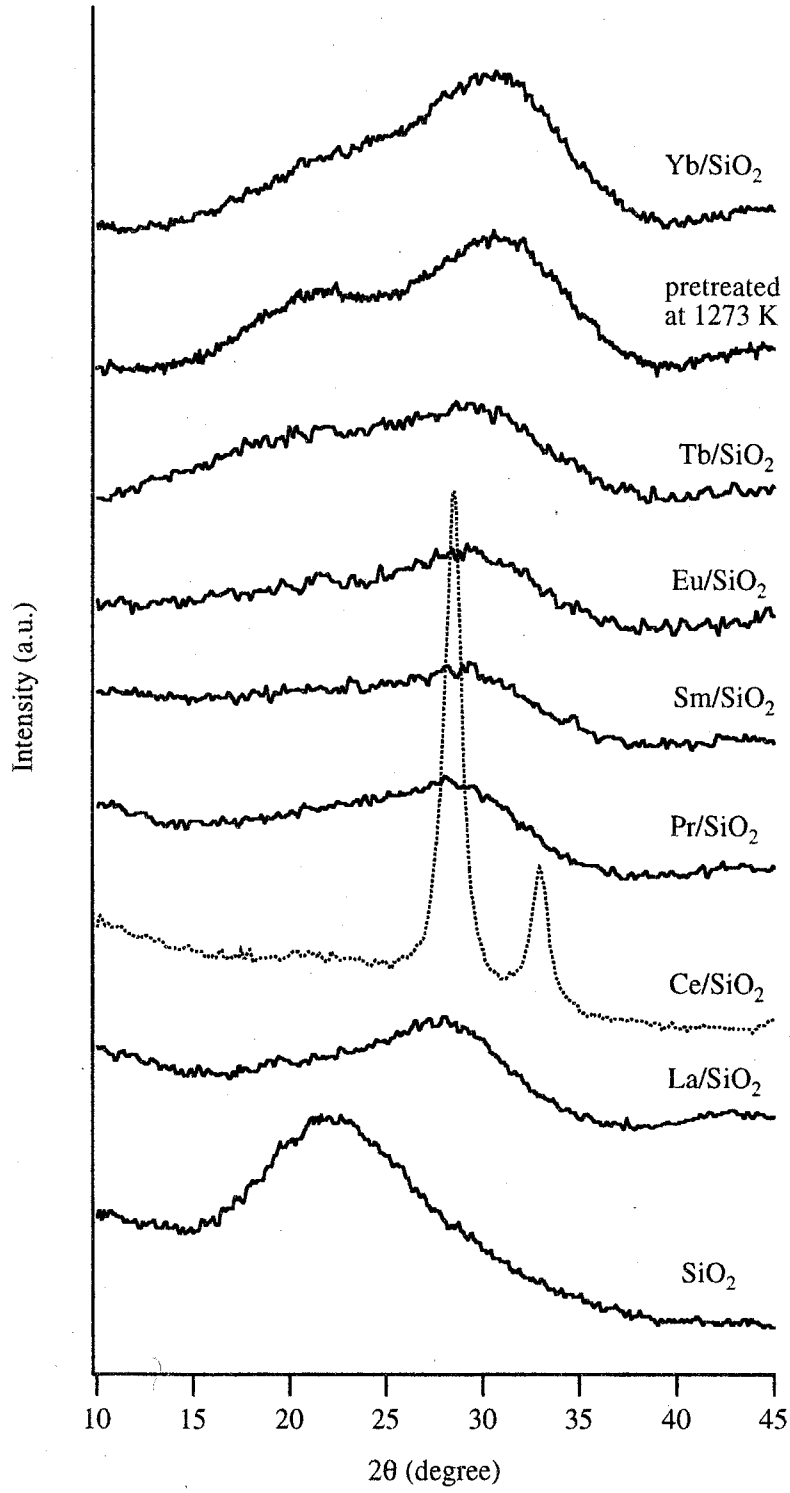

Figure 1. Cu-Kα XRD patterns of 3.4 mmol Ln/SiO_2 pretreated at 1073 K.

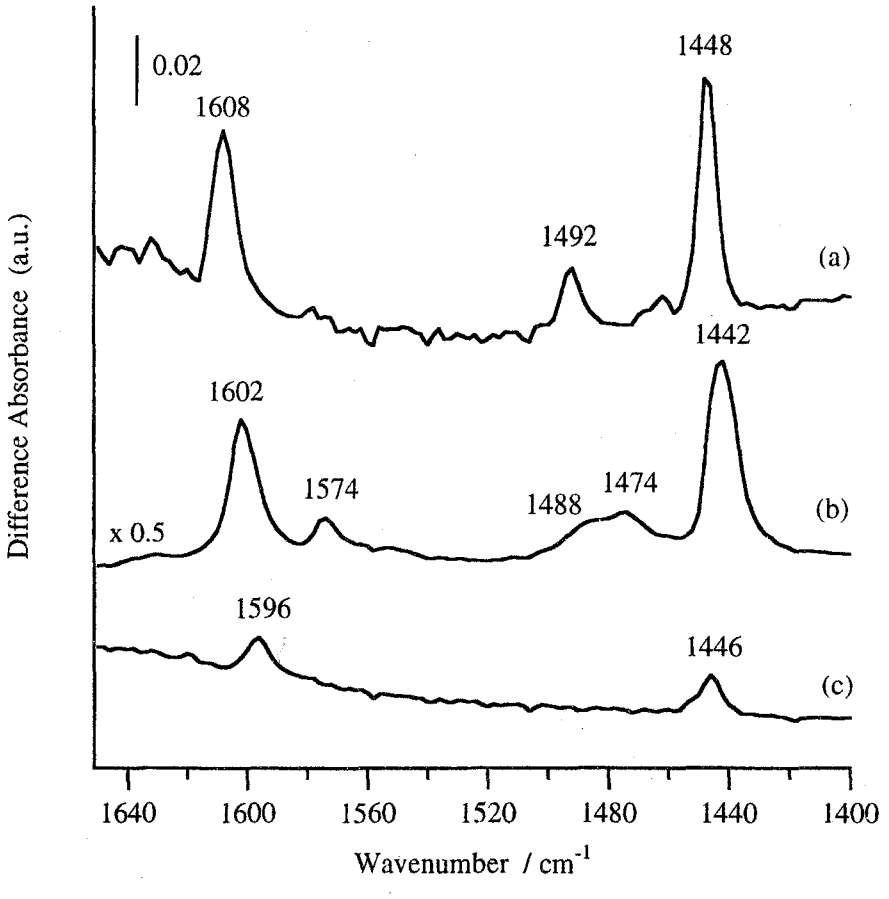

Figure 2. FTIR spectra of adsorbed pyridine at 423 K: 3.4 mmol Yb/SiO_2 (46 mg) (a), Yb_2O_3 (79 mg) (b), and SiO_2 (42 mg) (c) pretreated at 1073 K.

TPD

Figure 3 shows pyridine TPD profiles of catalysts pretreated at 1073 K. The pyridine adsorption procedure was carried out at 473 K to avoid effects of physisorption. SiO_2 seldom desorbed pyridine. The profiles of all Ln/SiO_2 catalysts possessed a single desorption peak around 600 K, indicating that certain amounts of acid sites exist on the surface of Ln/SiO_2. In contrast to the catalytic activity for α-pinene isomerization, the difference in each TPD profile among the supported rare earth elements was relatively small.

The profiles of Yb/SiO_2 and Tb/SiO_2 were quite similar to each other, the tailing of which ranged to slightly higher temperatures than those of the other Ln/SiO_2. Although catalytic activities of La/SiO_2 and Eu/SiO_2 differed by one order of magnitude, their TPD profiles exhibited identical features above 700 K. The total desorbed amount of pyridine from La/SiO_2 was 1.5 times larger than that of Pr/SiO_2. Furthermore, the Ce/SiO_2 catalyst desorbed about half as much pyridine as the Yb/SiO_2 catalyst. It was reported that CeO_2 possesses Lewis acid sites, which was confirmed by the IR spectra of adsorbed pyridine[25] and adsorption microcalorimetry of ammonia.[26] A large part of desorbed pyridine from the Ce/SiO_2 was due to CeO_2 crystal. An evident difference in acidic properties of Ln/SiO_2 was not found from TPD experiments. It clearly shows that part of the pyridine adsorption sites catalyze α-pinene isomerization, the ratio to total amounts of which were not able to estimate.

XANES

Figure 4 shows X-ray absorption near-edge structure (XANES) spectra of rare earth oxides and 3.4 mmol Ln/SiO_2 catalysts pretreated at 1073 K. In the L_{III}-edge XANES spectra, a strong white line due to the atomic like transition of $2p$-$5d$ appeared. XANES spectra of CeO_2 and Tb_4O_7 exhibit doublet white lines due to the coexistence of Ln^{3+} and Ln^{4+}.[27] The ground state of CeO_2 should be described by a mixing of two electron configurations $4f^0$ and $4f^1\underline{L}$, where $\underline{L}$ indicates a hole in the oxygen $2p$ valence bond,[28] the same spectrum was recorded by other research groups.[27-29] Those of the other rare earth oxides exhibit a single white line. A double white line was observed for that of Ce/SiO_2, which was identical to that of CeO_2. In contrast, single white lines were observed for those of other Ln/SiO_2 samples. The single white lines and the photon energies of the Ln/SiO_2 catalysts indicate that all Ln species supported on SiO_2 were trivalent. Terbium atoms supported on silica were trivalent only, although the average composition of terbium oxide obtained by calcination of terbium salts at 1073 K is $Tb_2^{3+}Tb_2^{4+}O_7$.[30] The height of the white line for each supported rare earth oxide is higher than that of each rare earth oxide crystal, as well as in the case of Yb/SiO_2,[10] Ln/Al_2O_3 (Ln = La, Sm, Lu),[31,32] and $Si:Er_2O_3$.[33] Furthermore, the shapes of Y-K edge XANES spectra of Y_2O_3 and Y/SiO_2 are different from each other. If Y atom (Y^{3+}; $4d^0$) was supported on silica

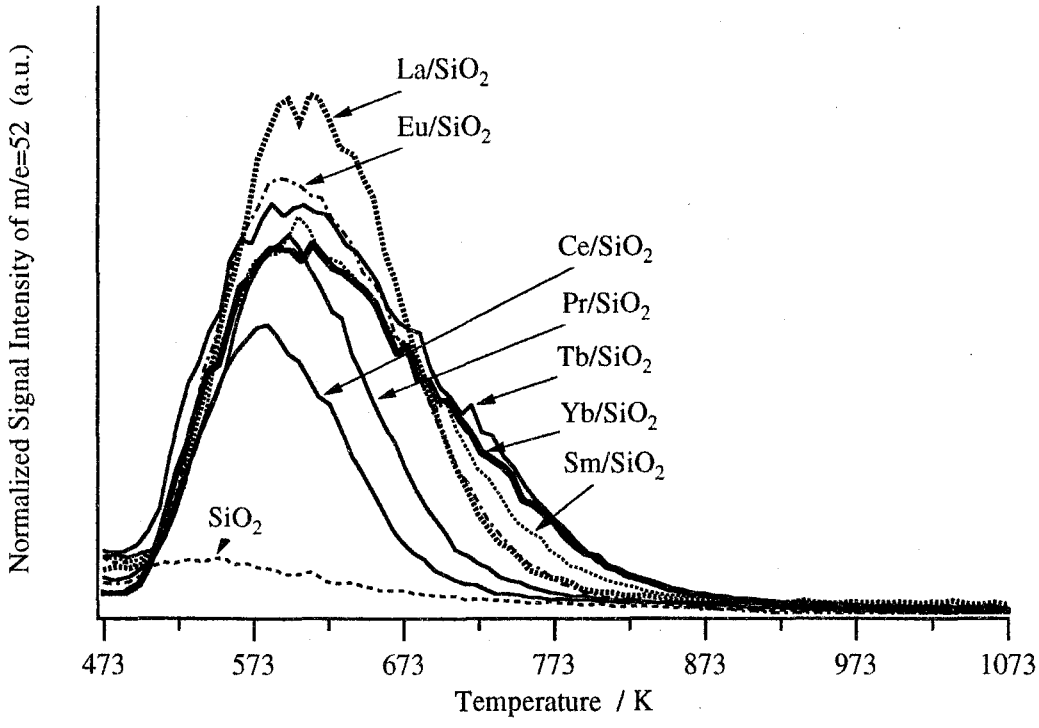

Figure 3. Pyridine TPD profiles of 3.4 mmol Ln/SiO_2 and SiO_2 pretreated at 1073 K.

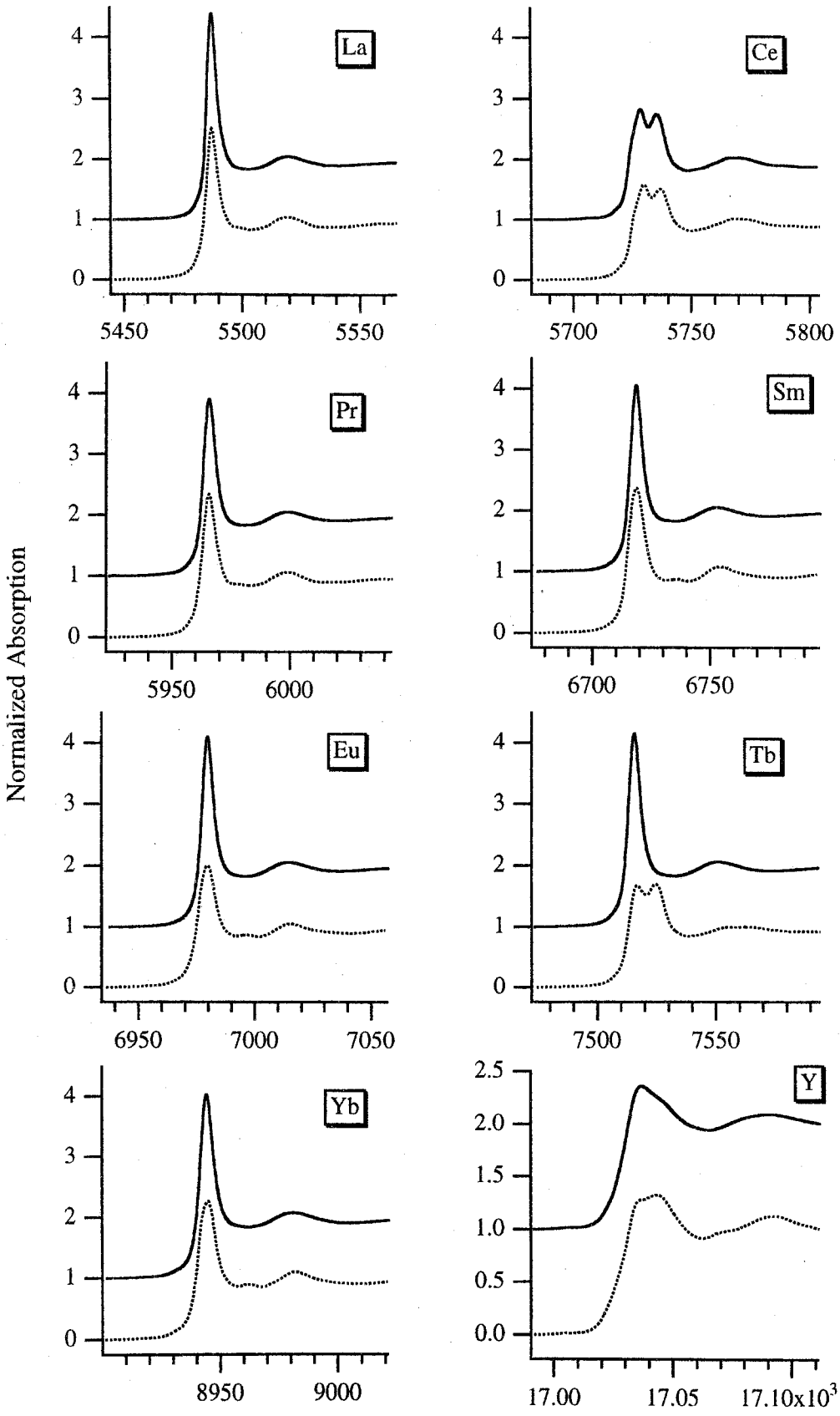

Figure 4. XANES spectra of 3.4 mmol Ln/SiO_2 pretreated at 1073 K (solid curves) and rare earth oxide crystal (broken curves).

in a tetrahedral coordination, a pre-edge or shoulder peak due to the 1*s*-4*d* transition should be observed, as in the case for Nb[34,35] and Mo.[36,37] In the Y-K edge XANES spectra of the catalyst, no pre-edge and/or shoulder peaks were observed. The coordination sphere around Y on silica is concluded not to be tetrahedral. These results indicate that the geometry and electric configuration of each supported rare earth oxide is different from that of the rare earth oxide itself.

EXAFS

The extraction of the Ce-L_{III} edge EXAFS function of Ce/SiO_2 was not carried out because Ce species on silica consist of tri- and tetravalent cations with different threshold energy, and the formation of a crystalline CeO_2 phase has already been confirmed by XRD characterization. Figure 5 shows k^3-weighted EXAFS spectra of 3.4 mmol Ln/SiO_2 pretreated at 1073 K. Yb-L_{III} and Y-K edge EXAFS spectra of the catalysts were quite similar to each other. Because the phase shift of the K and L_{III} edge EXAFS function is differed by π radian,[38] those of Y/SiO_2 and Yb/SiO_2 are fundamentally the same. This result indicates that local structures around the Y and Yb atoms of supported catalysts are similar to each other. The Tb-L_{III} edge EXAFS spectrum of the Tb/SiO_2 catalyst was quite similar to that of Yb/SiO_2, while the oscillation amplitude of Tb/SiO_2 below $k = 5$ Å^{-1} was slightly smaller than that of Yb/SiO_2. With decreasing atomic number from ^{70}Yb to ^{57}La, the complicated oscillations of each EXAFS spectrum of the catalyst changed. Furthermore, each amplitude decreased as well. One possible reason for the decrease in the amplitude is that many kinds of scatters with different bond length counteract the EXAFS oscillations.

The radial structure functions (RSFs) obtained by Fourier transformation of k^3-weighted EXAFS functions are shown in Figure 6. The Fourier-filtered range of each EXAFS spectrum differs by the element because of the different limitation of each L_{II}-absorption edge. In the RSFs of Y/SiO_2, Yb/SiO_2 and Tb/SiO_2, distinct two peaks were observed around 1.8 and 2.8 Å. In the Yb/SiO_2 catalysts, loading amounts of which were 280 μmol - 8.4 mmol $g(SiO_2)^{-1}$, we have assigned the peak around 1.8 Å due to oxygen, and that around 2.8 Å due to Si atoms of the supports.[9,10] Analogous with Yb/SiO_2, Ln-O-Si linkage are present on Tb/SiO_2 and Y/SiO_2. On the other hand, another peak was observed above 3 Å in the RSFs of Eu/SiO_2, Sm/SiO_2, Pr/SiO_2, and La/SiO_2. These distances were similar to the second peaks observed in the RSFs of rare earth oxide itself. We assigned the peaks observed in RSFs of the catalysts above 3 Å due to Ln-O-Ln linkages. Therefore, the coexistence of Ln-O-Ln and Ln-O-Si linkages with different bond length was concluded, especially in light rare earth oxides supported on silica.

All the samples remained in the amorphous state and each loading amount of the rare earth element was very large, 30 - 40 wt% as Ln_2O_3. The complicated EXAFS spectra of Ln/SiO_2 catalysts show that the coordination sphere around each Ln atom does not always

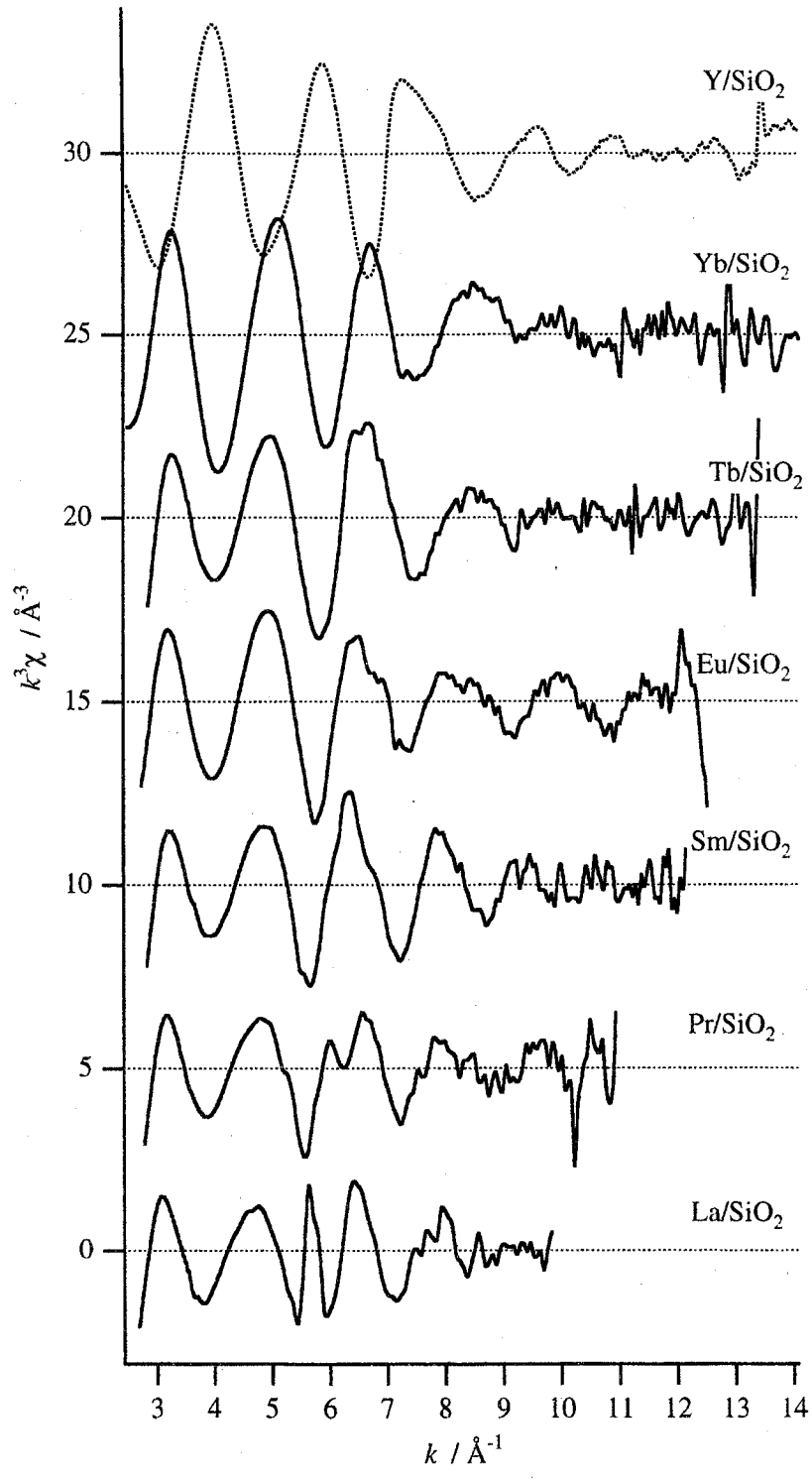

Figure 5. k^3-weighted EXAFS spectra of 3.4 mmol Ln/SiO_2 pretreated at 1073 K.

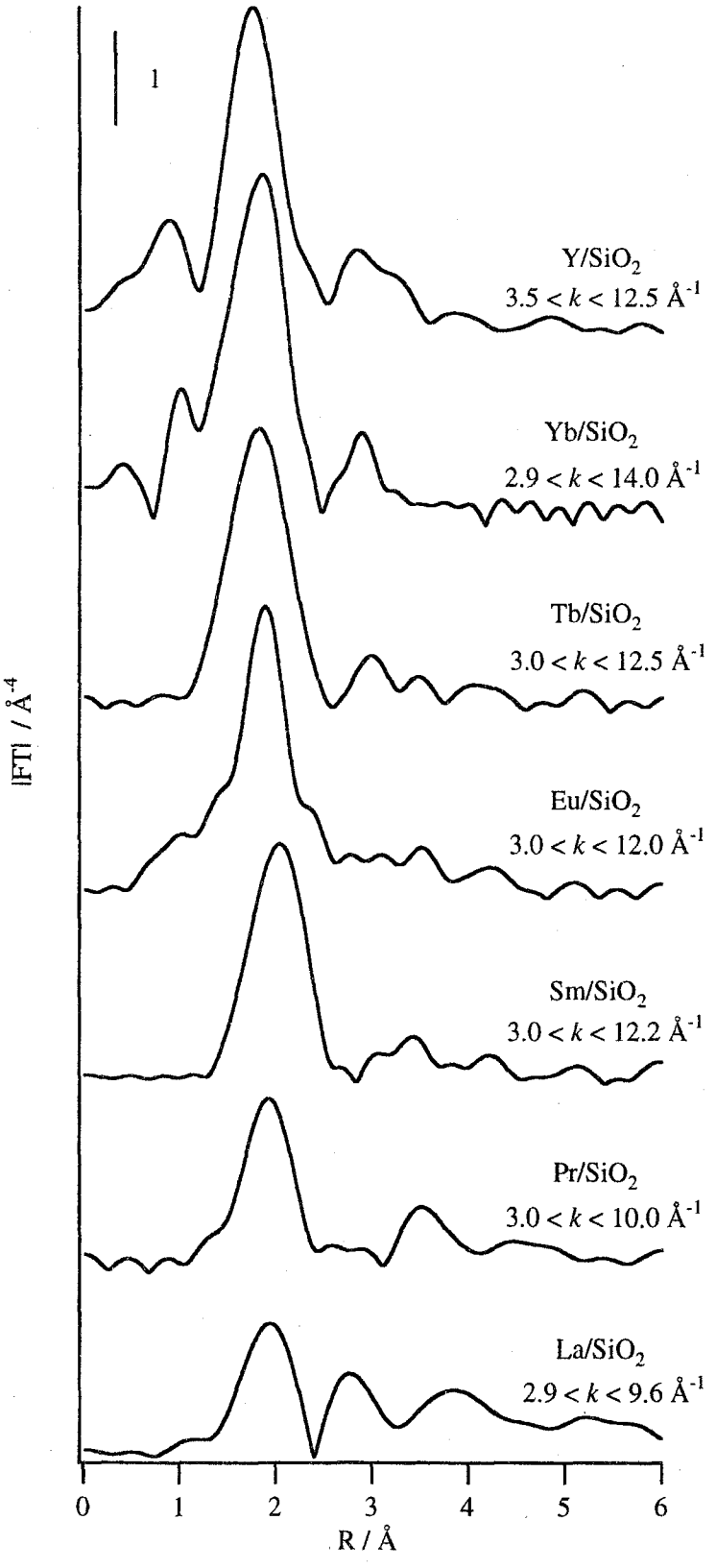

Figure 6. Fourier Transforms for k^3-weighted EXAFS spectra of 3.4 mmol Ln/SiO_2 pretreated at 1073 K.

consist of a single component. Therefore, we did not carry out curve fitting analyses for these Ln/SiO_2 catalysts.

Thermogravimetric-Differential Thermal Analysis (TG-DTA)

The preparation of each catalyst was carried out accompanied by calcination of the $Ln(NO_3)_3$-SiO_2 precursor at 773 K. We have concluded from XAFS analysis that a strong interaction between Yb and Si atoms, which are the active sites for α-pinene isomerization, had formed in the sample preparation step.[10] The transformation of each precursor upon thermal decomposition was examined with TG-DTA up to 1200 K. If some crystalline phase formed or phase transition was brought about upon thermal treatment, exothermic or endothermic heat flow should be observed. Figure 7 shows TG-DTA profiles of $Yb(NO_3)_3 \cdot xH_2O$, non-calcined 3.4 mmol Yb/SiO_2, SiO_2 and $Si(OH)_4$. $Yb(NO_3)_3 \cdot xH_2O$ decomposed to Yb_2O_3 over many steps, including ytterbium hydroxide nitrate salts.[39] SiO_2 and $Si(OH)_4$ desorbed a large amount of water below 373 K, and then continuously released water with ramping temperatures. The exothermic peak was not observed in the DTA profile of SiO_2, indicating crystallization did not occur below 1200 K. The TG-DTA profile of non-calcined Yb/SiO_2 was quite different from those of $Yb(NO_3)_3 \cdot xH_2O$, $Si(OH)_4$ and SiO_2. In contrast to the confusing DTA profile of $Yb(NO_3)_3 \cdot xH_2O$, that of the non-calcined sample was uncomplicated in the temperature range of 473 - 773 K. This result shows that the decomposition mechanism of the ytterbium nitrate salt on silica was different from the nitrate salt only. Any significant heat flow was not observed in the profile of Yb/SiO_2 sample up to 1200 K. The DTA characterization suggests that some ytterbium species, which are different from Yb_2O_3 crystal, had formed during the catalyst sample preparation step. In addition, excess loading amounts of non-calcined sample (15 mmol Yb loading $g(SiO_2)^{-1}$) exhibited a similar DTA profile to that of the $Yb(NO_3)_3$ salt.

Raman Spectra

To clarify the structure of each catalyst in more detail, Raman spectroscopy was applied to the Yb/SiO_2 catalysts. Figure 8 shows laser Raman spectra of SiO_2, Yb_2O_3, 3.4 mmol Yb/SiO_2 and 8.4 mmol Yb/SiO_2. The spectrum of Yb_2O_3 exhibited strong Raman bands at 360 and 612 cm^{-1}, and a small band at 310 cm^{-1}. That of SiO_2 gel exhibits characteristic Raman bands at 490 and 605 cm^{-1}.[40,41] The band at 977 cm^{-1} is due to silanol groups.[42] The Raman spectrum of 3.4 mmol Yb/SiO_2 was quite similar to that of SiO_2 gel, and exhibited no other bands except for those due to SiO_2. The lack of characteristic Raman bands due to crystalline oxides indicates that the metal oxides were well dispersed and any crystallites did not formed on the support.[43] Raman spectroscopic characterization shows that the crystalline phase of Yb_2O_3 was not present on 3.4 mmol Yb/SiO_2. In the spectrum of 8.4 mmol Yb/SiO_2, a tiny

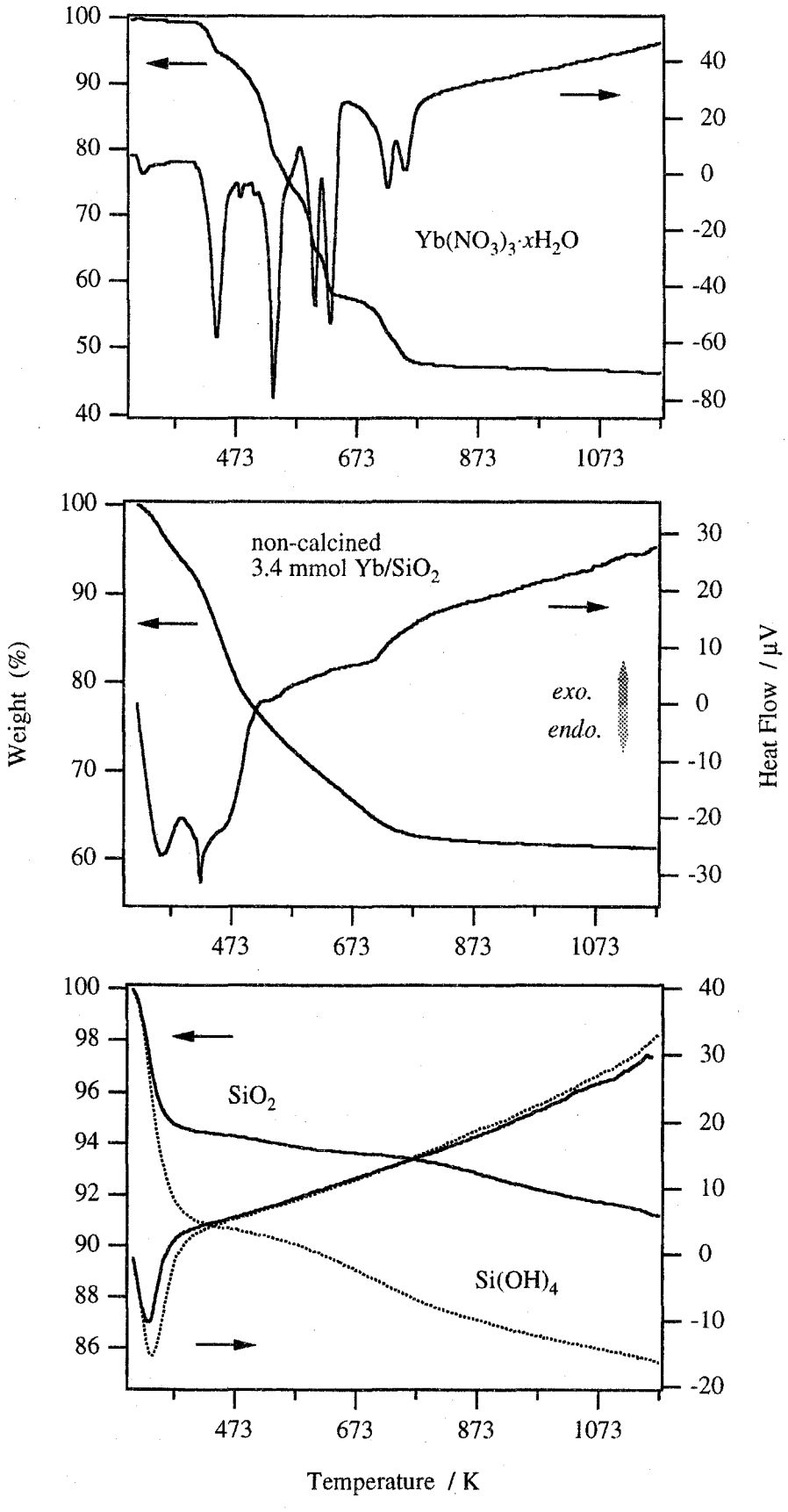

Figure 7. TG-DTA profiles of $Yb(NO_3)_3 \cdot xH_2O$, non-calcined 3.4 mmol Yb/SiO_2, $Si(OH)_4$, and SiO_2.

but distinct peak appeared at 364 cm^{-1} marked by an arrow, besides the peaks due to SiO_2. This tiny peak was assigned to Yb_2O_3 crystal. Although the Yb-L_{III} edge EXAFS spectrum of 8.4 mmol Yb/SiO_2 did not indicate any presence of Yb-O-Yb bonding,[9] quite a small part of the Yb species on 8.4 mmol Yb/SiO_2 form the Yb_2O_3 phase. The loading amount of Yb on 8.4 mmol Yb/SiO_2 is very high, 62 wt% Yb_2O_3. Because EXAFS characterization gave the averaged information against a target element, trace amounts of fine Yb_2O_3 crystallite could not be detected by EXAFS analysis. We have proposed that a large part of the Yb species in 8.4 mmol Yb/SiO_2 constitute Yb-O-Si linkages, and the trace residues deposit over Yb-O-Si linkages to reduce the catalytic activity.[9] The deposited excess Yb species, which were YbO_6, formed a fine Yb_2O_3 crystallite and was detected with Raman spectroscopy.

To examine the structural transformation of catalysts upon pretreatment temperature, *in-situ* Raman spectra of 3.4 mmol Yb/SiO_2 pretreated at various temperatures were recorded. The results are shown in Figure 9. The sample pretreated below 1073 K exhibited an identical spectrum to that of SiO_2 gel, while many Raman bands appeared on the sample pretreated at 1273 K. The new band positions were quite different from those of the Yb_2O_3 crystal. One possible assignment of them is due to formation of crystalline SiO_2 polymorphism. In the temperature range 1140 - 1743 K, the stable phase of SiO_2 is tridymite.[44] It is well known that the phase transition of SiO_2 polymorphism occurs rapidly and reversibly.[44] We did not quench the sample immediately after the pretreatment procedure, and we measured the Raman spectra at room temperature. If this was the case, the observed crystalline phase of SiO_2, should be α-quartz. However, there were only two observed Raman bands for α-quartz (Nacalai, GR) at 206 and 464 cm^{-1} in the range 200 - 1000 cm^{-1}. It was concluded that crystalline SiO_2 polymorphism had not formed on Yb/SiO_2 pretreated at 1273 K. The other possible assignment of the new Raman bands is due to the formation of crystalline ytterbium silicates. As shown in the phase diagram of the Yb_2O_3-SiO_2 system, $Yb_2O_3 \cdot SiO_2$ and $Yb_2O_3 \cdot 2SiO_2$ are stable binary oxides.[45] Although we have not prepared ytterbium silicate crystals and do not have any information about their Raman spectra, we presume that fine crystalline particle of $Yb_2O_3 \cdot 2SiO_2$ and/or $Yb_2O_3 \cdot SiO_2$ formed on 3.4 mmol Yb/SiO_2 pretreated at 1273 K. The size and proportion of Yb-silicate crystallite to the total contents of Yb were too small to detect by XRD and EXAFS measurements.

Discussion

In a series of lanthanoid oxides supported on silica, Yb/SiO_2 exhibited the highest activity for α-pinene isomerization. The catalytic activities of Yb/SiO_2 and La/SiO_2 were quite different from each other by fifty times. The activities changed by the loaded elements in the order of atomic number, but the selectivities were almost the same for all the catalysts. It is very interesting that Yb/SiO_2 and Y/SiO_2 exhibited not only the similar catalytic activities but also

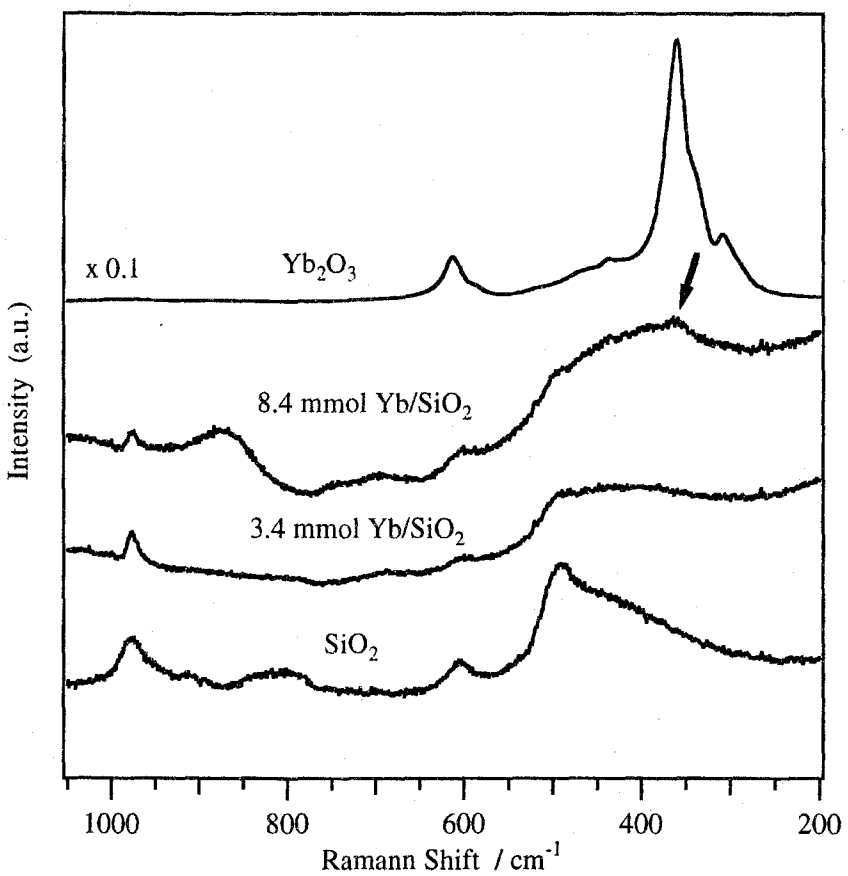

Figure 8. Raman spectra of Yb_2O_3, 8.4 mmol Yb/SiO_2, 3.4 mmol Yb/SiO_2 and SiO_2.

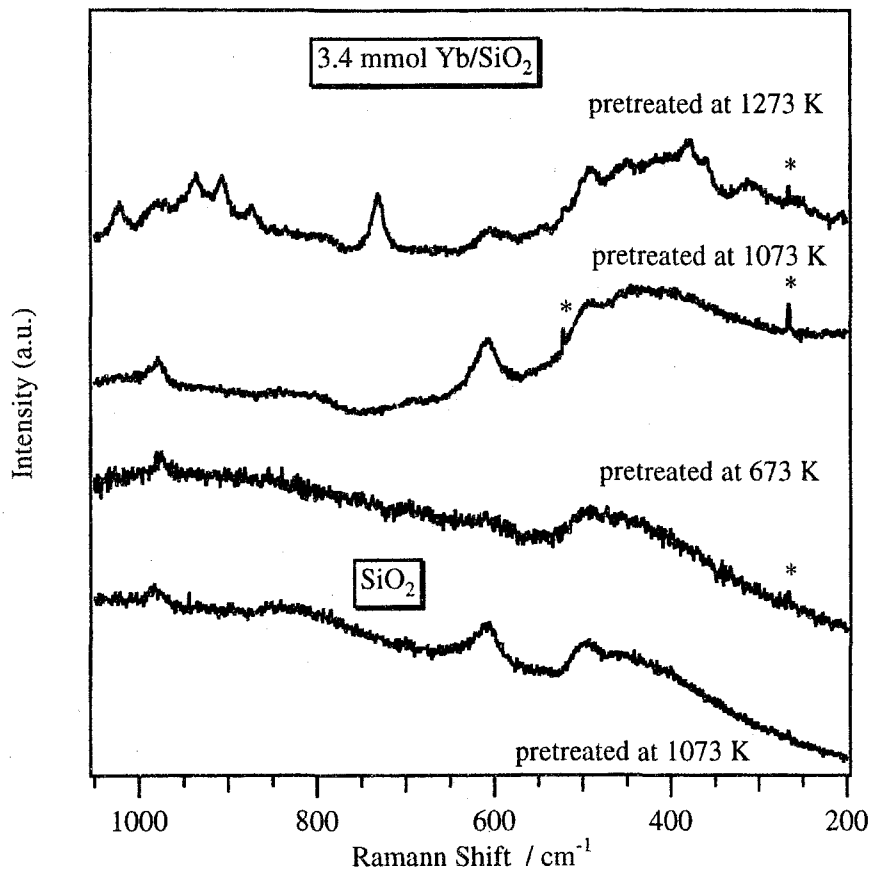

Figure 9. Raman spectra of 3.4 mmol Yb/SiO_2 and SiO_2 pretreated at various temperatures. *; laser plasma lines.

similar selectivities. The selectivity for ß-pinene was relatively high over La/SiO_2 and Pr/SiO_2 catalysts when the reaction was carried out at 323 K. The selective isomerization of α-pinene toward ß-pinene is one of the characteristic base-catalyzed reactions and other compounds hardly formed a over solid base.[46] However, the formation of ß-pinene is catalyzed by both acids and bases.[15,46,47] The equilibrium constant of β-pinene to α-pinene is quite low and produced β-pinene converting to α-pinene again. The selectivity of ß-pinene decreased with decreasing total concentration of α-pinene in the reaction system. The high selectivity for ß-pinene observed in the cases of La/SiO_2 and Pr/SiO_2 was due to the low conversion. In fact, identical selectivity was obtained over La/SiO_2 and Pr/SiO_2 when each reaction was performed at 353 K. The similarity of each selectivity indicates that the property and structure of active sites is similar among all of the Ln/SiO_2 catalysts.

Pyridine and/or ammonia adsorption experiments are general methods to characterize acid properties of catalysts. As shown in Figures 2 and 3, however, no distinct difference in acid properties of Ln/SiO_2 catalysts was obtained by characterization with pyridine. Ce/SiO_2 and Yb_2O_3 did not catalyze α-pinene isomerization very effectively. On the other hand, IR spectra of adsorbed pyridine showed that Yb_2O_3 possesses certain amounts of Lewis acid sites as much as 3.4 mmol Yb/SiO_2 catalysts. The difference in TPD profile among supported rare earth elements was small, and the existence of acid sites on Ce/SiO_2 was demonstrated. The pyridine TPD profiles and IR spectra of adsorbed pyridine gave information not only about the real active sites, but also pyridine adsorption sites which did not participate in catalyses. It is impossible to distinguish them. Pyridine desorption sites do not always directly reflect on the real active sites for catalyses. From TPD measurements, we could not find out the effective difference in acid strengths and the amounts among Ln/SiO_2 catalysts.

XRD characterization shows that all of the Ln/SiO_2 catalysts are amorphous, except for Ce/SiO_2. It was reported that the monolayer structures of transition metal oxides hardly formed on SiO_2 with a simple impregnation method, and the oxides were easily crystallized.[43,48] However, we could prepare amorphous silica supported rare earth oxides by impregnation with nitrate aqueous solutions, followed by calcination. There are some reports that X-ray amorphous rare earth oxides supported on silica are prepared with the same preparation methods, such as 22 wt% La_2O_3/SiO_2[49] and 31 wt% Eu_2O_3/SiO_2.[7] Rare earth oxides easily spread on the SiO_2 surface, in contrast to other transition metal oxides. Only ceria hardly spread on silica, and the crystalline phase was detected even at a low loading amount of 5.8 wt%.[50]

In the Yb/SiO_2 system, the loading amount of which ranged from 280 μmol - 8.4 mmol Yb atom $g(SiO_2)^{-1}$, each Yb-L_{III} edge EXAFS spectra were identical and no Yb-O-Yb contributions were observed.[9] We have concluded that ytterbium atoms were widely spread on the SiO_2 surface as a YbO_6 octahedron. Each YbO_6 octahedron strongly interacted with SiO_4 tetrahedra, rather than with other YbO_6 octahedra. The Yb-O-Si species exhibit solid acidity to catalyze α-pinene isomerization.[9,10] In a series of Ln/SiO_2 catalysts, the selectivity for various

products from α-pinene was similar to each other. The difference in acidity of each catalyst influences the selectivity of the produced compounds from α-pinene. Thus, we propose that the structures of active sites of all the Ln/SiO_2 catalysts are Ln-O-Si species with similar acidity.

In the cases of other Ln/SiO_2 catalysts, EXAFS spectra indicate that a contribution of Ln-O-Ln appeared, besides that of Ln-O-Si. Especially in case of the light rare earth elements, Ln-O-Si contribution was small. The decrease of Ln-O-Si contribution and the increase of Ln-O-Ln contribution directly related to the catalytic performance. The LnO_n polyhedron connected with other SiO_4 tetrahedra and/or LnO_n polyhedra. In the case of the heavy rare earth element of Yb, almost all of the YbO_6 units strongly connected with SiO_4 tetrahedra only. In the case of the light rare earth element of La, LaO_n units connected with other LaO_n and SiO_4 units. The fraction differed in order of atomic number of each element. In the case of CeO_2, the interaction among SiO_4 tetrahedra and CeO_n polyhedra are particularly weak. We conclude that the Ce/SiO_2 catalyst is the mixture of CeO_2 and SiO_2. The low affinity among ceria and SiO_2 might be due to the high redox ability of CeO_2. It was reported that Ce silicate formed only if the Ce/SiO_2 was reduced by hydrogen at 1073 K in the presence of Rh.[51] As a result, Ce/SiO_2 catalyst was inert for the acid catalyzed reaction, and the specific surface area was much larger than the others, especially in the surface area of $g(SiO_2)^{-1}$ carrier.

Quite similar EXAFS spectra were observed at the Y-K and Yb-L_{III} edge. As shown in Figure 6, Y-O-Si contributions were present in the Y/SiO_2 catalyst, whereas Y-O-Y contributions were absent. The similarity of the Y-K edge EXAFS spectrum of Y/SiO_2 to that of Yb/SiO_2 revealed that all of Y atoms located at a center of oxygen-octahedron connected with SiO_4 tetrahedra in sharing oxygen.

Two reasons why the catalysis for α-pinene isomerization changes continually with atomic number are considered. The first possible reason is concerning electronegativity. Tanabe *et al.* found the correlation between maximum acid strengths of binary metal oxides and the averaged electronegativities of each ion.[6,52] Maximum acid strengths of La_2O_3-SiO_2 and Y_2O_3-SiO_2 have been estimated to $H_0 \leq -4.0$ and $H_0 \leq -5.6$, respectively.[6,52] The acid strength of 3.4 mmol Yb/SiO_2 was evaluated with Hammet indicators to $-3.0 \geq H_0$ max > -5.6. Various definitions of electronegativity have been proposed, such as Pauling, Mulliken, Allred & Rochow, Sanderson, and so on. Because all electronegativities of the rare earth elements are quite similar to each other, the continuum and drastic change in the catalytic activity could not be explained by electronegativity effects. This was supported by the result that each selectivity of produced compounds from α-pinene was independent of the supported elements.

The other possible reason for this continuum change in catalyses is the effects of ion radius. It is well known that the ion radius of lanthanides continually decrease with atomic number from ^{57}La to ^{71}Lu. The largest ion radius of the lanthanoid ion employed in this work is 1.061 Å for La^{3+}, and the smallest one is 0.858 Å for Yb^{3+}.[53] The second smallest lanthanide ion used in the present study is 0.923 Å for Tb^{3+}. The size of Y^{3+} is 0.88 Å, which is close to that of Yb^{3+}. It clearly shows that a close relationship between the ion radius of

Ln^{3+} and the catalytic activity exists. It is obvious that the size of the LnO_n unit would change with the center element. We propose that a suitable size of LnO_n unit strongly interacts with SiO_4 units rather than the other LnO_n units. As a result, remarkable catalytic activity for α-pinene isomerization was exhibited over Yb/SiO_2 and Y/SiO_2 catalysts. Catalytic activity depends on the number of effective Ln-O-Si linkages present on the surface.

We have proposed that YbO_6 units form on the surface of SiO_2 by sharing oxygen atoms regardless of the loading amounts. From results of surface area measurements, the deactivation of the 8.4 mmol Yb/SiO_2 catalyst was due to the blockage of active sites with excess YbO_6 units.[9] As shown in Figure 8, Raman spectroscopy detected the formation of Yb_2O_3 fine crystallites over 8.4 mmol Yb/SiO_2, the activity of which (conversion 5.5%) was much lower than that of 3.4 mmol Yb/SiO_2 (conversion 26.5%). When the loading amounts exceed the amounts needed to form the YbO_6 monolayer over a SiO_2 surface, the apparent turn over frequency per one ytterbium atom decreases due to the decrease of effective active sites on the surface.

When 3.4 mmol Yb/SiO_2 was pretreated at 1273 K, α-pinene isomerization was scarcely catalyzed under the same conditions as shown in Table 2 (conversion < 0.1%). The BET specific surface areas of 3.4 mmol Yb/SiO_2 pretreated at 1073 and 1273 K were 180 and 104 $m^2\ g^{-1}$, respectively. Therefore, sintering of the catalyst was not the main reason for deactivation. As shown in Figure 9, many new Raman bands appeared only on the deactivated sample. We presume that fine crystalline particles of $Yb_2O_3 \cdot 2SiO_2$ and/or $Yb_2O_3 \cdot SiO_2$ formed on the catalyst. It indicates that crystallites of ytterbium silicates do not exhibit catalytic activity for α-pinene isomerization, and partial crystallization corresponds to deactivation. From spectroscopic characterization and catalysis for α-pinene isomerization, the site corresponding to solid acidity is the local Yb-O-Si network without having long-range ordering structure.

Conclusion

Silica-supported rare earth oxides exhibit solid acidity for catalysis of α-pinene isomerization, and the activities strongly depend on the supported element. In the lanthanoid series (La, Pr, Sm, Eu, Tb, and Yb), the activity increased continuously with atomic number from La to Yb. Ce/SiO_2 was inert for this reaction, and crystalline CeO_2 formed. Y/SiO_2 exhibited the same activity as Yb/SiO_2. All the Ln/SiO_2 catalysts, except for Ce/SiO_2, are amorphous, and form Ln-O-Si and/or Ln-O-Ln linkages with different compositions in each catalyst. The affinity among the LnO_n unit and SiO_4 tetrahedra depends on the size of Ln^{3+}. With increasing ratio of Ln-O-Si to Ln-O-Ln linkages, the catalytic activity increases.

Excess loading of Yb atoms to SiO_2 blocks the Yb-O-Si linkages of the active site to form Yb_2O_3 fine particles. When Yb/SiO_2 was pretreated at 1273 K, fine ytterbium silicate crystallites formed and the crystalline ytterbium silicate did not exhibit catalysis. The Ln-O-Si

linkage in Ln/SiO_2 having no long-ranged ordering structure is the active site for α-pinene isomerization.

References

1 Schaper, H.; Doesburg E. B. M.; van Reijen, L. L. *Appl. Catal.*, **1983**, *7*, 211.

2 Arai, H.; Machida, M. *Appl. Catal. A* **1996**, *138*, 161.

3 Capitán, M. J.; Malet, P.; Centeno, M. A.; Muñoz-Páez, A.; Carrizosa, I.; Odriozola, J. A. *J. Phys. Chem.* **1993**, *97*, 92333.

4 Shi, C.; Wlters, A. B; Vannice, M. A. *Appl. Catal. B* **1997**, *14*, 175.

5 Tanabe, K.; Sumiyoshi, T.; Shibata, K.; Kiyoura, T.; Kitagawa, J. *Bull. Chem. Soc. Jpn.* **1974**, *47*, 1064.

6 Tanabe, K.; Misono, M.; Ono, Y.; Hattori, H. *New Solid Acids and Bases*, Kodansha, Elsevier, Tokyo, **1989**, pp. 108-114.

7 Shen,J.; Lochhead, M. J.; Bray, K. L.; Chen, Y.; Dumesic, J. A. *J. Phys. Chem.* **1995**, *99*, 2384.

8 (a) Moriya, A.; Tsuneki, H. US 5599999, **1997**, (b) Tsuneki, H. *Shokubai* **1998**, *40*, 304.

9 Yamamoto, T.; Matsuyama, T.; Tanaka, T.; Funabiki, T.; Yoshida, S. *J. Mol. Catal. A* in press.

10 Yamamoto, T.; Tanaka, T.; Matsuyama, T.; Funabiki, T.; Yoshida, S. *Solid State Commun.*, in press.

11 Stanislaus, A.; Yeddanapalli, L. M. *Can. J. Chem.* **1972**, *50*, 61.

12 Ohnishi, R.; Tanabe, K.; Morikawa, S.; Nishizaki, T. *Bull. Chem. Soc. Jpn.* **1974**, *47*, 571.

13 Corma, A.; García, H. *Catal. Today* **1997**, *38*, 257, and references therein.

14 Severino, A.; Esculcas, A.; Rocha, J.; Vital, J.; Lobo, L. S. *Appl. Catal. A* **1996**, *142*, 255.

15 Yamamoto, T.; Tanaka, T.; Funabiki, T.; Yoshida, S. *J. Phys. Chem. B* **1998**, *102*, 5830.

16 Tanabe, K. *Solid Acids and Bases*; Kodansha, Tokyo, **1970**, pp. 119-125.

17 Yoshida, S.; Matsuzaki, T.; Kashiwazaki, T.; Mori, K.; Tarama, K. *Bull. Chem. Soc. Jpn.* **1974**, *47*, 1564.

18 Kohno, Y.; Tanaka, T.; Funabiki, T.; Yoshida, S. *Chem. Commun.* **1997**, 841.

19 Kohno, Y.; Tanaka, T.; Funabiki, T.; Yoshida, S. *J. Chem. Soc., Faraday Trans.* **1998**, *94*, 1875.

20 Tanaka, T.; Yamashita, H.; Tsuchitani, R.; Funabiki, T.; Yoshida, S. *J. Chem. Soc., Faraday Trans. I* **1988**, *84*, 2987.

21 Roth, R. S.; Negas, T.; Cook, L. P. *Phase Diagrams for Ceramists,* American Ceramic Society, Columbus, Ohio, 1981, vol. 4, p. 143, Figure 5257.

22 Connell, G.; Dumesic, J. A. *J. Catal.* **1986**, *101*, 103.

23 Connell, G.; Dumesic, J. A. *J. Catal.* **1987**, *105*, 285.

24 Hussein, G. A. M.; Gates, B. C. *J. Chem. Soc., Faraday Trans.* **1996**, *92*, 2425.

25 Zaki, M. I.; Hussein, G. A. M.; Mansour, S. A. A.; El-Ammawy, H. A. *J. Mol. Catal.* **1989**, *51*, 209.

26 Auroux, A.; Artzzu, P.; Ferino, I.; Monaci, R.; Rombi, E.; Solinas, V.; Petrini, G. *J. Chem. Soc., Faraday Trans.* **1996**, *92*, 2619.

27 (a) Karnatak, R. C.; Esteva, J.-M.; Dexpert, H.; Gasnier, M.; Caro, P. E.; Albert, L. *Phys. Rev. B* **1987**, *36*, 1745; (b)Dexpert, H.; Karnatak, R. C.; Esteva, J.-M.; Connerade, J. P.; Gasgnier, M.; Caro, P. E.; Albert, L. *Phys. Rev. B* **1987**, *36*, 1750.

28 Bianconi, A.; Marcelli, A.; Dexpert, H.; Karnatak, R.; Kotani, A.; Jo, T.; Petiau, J. *Phys. Rev. B* **1987**, *35*, 806.

29 Lytle, F. W.; van der Laan, G.; Greegor, R. B.; Larson, E. M.; Violet, C. E.; Wong, J. *Phys. Rev. B* **1990**, *41*, 8955.

30 Topp, N. E. *Chemistry of the Rare-Earth Elements*, Elsevier, Amsterdam, 1965.

31 Capitán, M. J.; Centeno, M. A.; Malet, P.; Carrizosa, I.; Odriozola, J. A.; Márquez, A.; Fernández Sanz, J. *J. Phys. Chem.* **1995**, *99*, 4655.

32 Hatsui, T.; Tanaka, T.; Funabiki, T.; Yoshida, S. unpublished results.

33 Ishii, M.; Komuro, S.; Morikawa, T.; Aoyagi, Y.; Ishikawa, T.; Ueki, T. *Jpn. J. Appl. Phys.* in press.

34 Yoshida, S.; Tanaka, T.; Hanada, T.; Hiraiwa, T.; Kanai, H.; Funabiki, T. *Catal. Lett.* **1992**, *12*, 277.

35 Yoshida, H.; Tanaka, T.; Yoshida, T.; Funabiki, T.; Yoshida, S. *Catal. Today* **1996**, *28*, 79.

36 Aritani, H.; Tanaka, T.; Funabiki, T.; Yoshida, S.; Kudo, M.; Hasegawa, S. *J. Phys. Chem.* **1996**, *100*, 5440.

37 Takenaka, S.; Tanaka, T.; Funabiki, T.; Yoshida, S. *J. Phys. Chem. B* **1998**, *102*, 2960.

38 Teo, B.-K. *EXAFS: Basic Principles and Data Analysis*, Springer-Verlag, Berlin, 1986, pp. 24-31.

39 Haschke, J. M. *Inorg. Chem.* **1974**, *13*, 1812.

40 Shibata, N.; Horigudhi, M.; Edahiro, T. *J. Non-Cryst. Solids* **1981**, *45*, 115.

41 Brinker, C. J.; Tallant, D. R.; Roth, E. P.; Ashley, C. S. *J. Non-Cryst. Solids* **1986**, *82*, 117.

42 Wallence, S.; West, J. K.; Hench, L. L. *J. Non-Cryst. Solids* **1993**, *152*, 101.

43 Wachs, I. E.; Hardcastle, F. D. *Proc. 9th. Int. Congr. Catal.*, Calgary, 1988, 1449.

44 Levin, E. M.; McMurdie, H. F.; Hall, F. P.; Reser, M. K. *Phase Diagrams for Ceramists*; American Ceramic Society, Columbus, Ohio, 1956.

45 Levin, E. M.; Robbins, C. R.; McMurdie, H. F. *Phase Diagrams for Ceramists*; American Ceramic Society, Columbus, Ohio, vol. 2, 1969, p. 108, Figure 2391.

46 Ohnishi, R.; Tanabe, K. *Chem. Lett.* **1974**, 207.

47 Tanaka, T.; Kumagai, H.; Hattori, H.; Kudo, M.; Hasegawa, S. *J. Catal.* **1991**, *127*, 221.

48 Asakura, K.; Iwasawa, Y. *J. Phys. Chem.* **1991**, *95*, 1711.

49 Craciun, R.; Dulamita, N. *Catal. Lett.* **1997**, *46*, 229.

50 Trovarelli, A.; de Leitenburg, C.; Dolcetti, G.; LLorca, J. *J. Catal.* **1995**, *151*, 111.

51 Krause, K. R.; Schabes-Retchkiman, P.; Schmidt, L. D. *J. Catal.* **1992**, *134*, 204.

52 Shibata, K.; Kiyoura, T.; Kitagawa, J.; Sumyoshi, T.; Tanabe, K. *Bull. Chem. Soc. Jpn.* **1973**, *46*, 2985.

53 Moeller, T. *The Chemistry of the Lanthanides*, Reinhold, New York, 1963.

Part III

Characterization of Iron- and Manganese-Promoted Sulfated Zirconia

Introduction of Part III

Sulfated Zirconia and Promoted Sulfated Zirconia

In 1976, Tanabe *et al.* found that addition of $(NH4)2SO4$ to TiO_2 causes an increase of the activity for but-1-ene isomerization by two orders of magnitude.[1] Any superacidic characters, however, were not confirmed at that time. In 1979, Arata and Hino found that SO_4^{2-}/ZrO_2 catalyzes *n*-butane skeletal isomerization at room temperature.[2] The catalytic activity depends on calcination temperatures of $SO_4^{2-}/Zr(OH)_4$, and the maximum activity was exhibited when $SO_4^{2-}/Zr(OH)_4$ was calcined at 848-923 K. The maximum acid strength was estimated to be $-16.04 \geq H_0$ using Hammet indicators.[3] Besides SO_4^{2-}/ZrO_2, they found many sulfated oxides such as SO_4^{2-}/TiO_2 and SO_4^{2-}/Fe_2O_3 catalyze *n*-butane skeletal isomerization, which is usually employed as a test reaction for super acids.[4,5]

In a series of sulfated metal oxides, SO_4^{2-}/ZrO_2 exhibits the strongest acidity and is prepared by good reproducibility. Both Brønsted and Lewis acid sites are confirmed on SO_4^{2-}/ZrO_2 with IR spectra of adsorbed pyridine, and the Lewis and Brønsted sites are easily inter changeable by adsorption or desorption of water.[5] A recent ^{1}H-NMR study [6] and quantum chemistry calculations [7] indicate that Brønsted acidity of sulfated zirconia is not so strong as estimated by Hino but comparable to that of H_2SO_4 ($H_0 = -11.93$). Based on changes in ^{1}H-NMR and FTIR parameters caused by adsorption of acetonitrile, Sachatler claims that the acid strength of Brønsted acid sites of SO_4^{2-}/ZrO_2 and Fe-, Mn-SO_4^{2-}/ZrO_2 is similar to that of HY, but weaker than that of HZSM-5.[8] On the other hand, it is well known that amorphous silica-alumina, H-MOR and H-MFI, maximum acid strengths of which are comparable to that of H_2SO_4, never catalyze *n*-butane skeletal isomerization at around room temperature. In fact, it was reported that SO_4^{2-}/ZrO_2 was more active than H-MOR by two orders of magnitude for pentane isomerization at 308 K.[9] Strictly to say, sulfated zirconia might not be super acid judging from H_0 function criteria. However, it is newly established that sulfated zirconia catalyzes super acidic reactions.

Main disadvantage of SO_4^{2-}/ZrO_2 is the rapid deactivation against alkane skeletal isomerization. In 1988, Hosoi found that the addition of platinum to sulfated zirconia (Pt-SO_4^{2-}/ZrO_2) enhances catalytic activity in the skeletal isomerization of alkanes without deactivation when the reaction was carried out in the presence of hydrogen.[10] In 1990s, Hsu discovered iron- and manganese-prompted sulfated zirconia (Fe-, Mn-SO_4^{2-}/ZrO_2) exhibits higher activity for *n*-butane isomerization by three orders of magnitude than sulfated zirconia.[11] Tábora found that SO_4^{2-}/ZrO_2 and Fe-, Mn-SO_4^{2-}/ZrO_2 exhibit a steady activity for *n*-butane isomerization at 323 K, although the rate over Fe-, Mn-SO_4^{2-}/ZrO_2 drastically reduced after a characteristic induction period.[12] So far, plenty of reviews have been published about sulfated zirconia and promoted sulfated zirconia.[5,13-19] Nowadays, $SO_4^{2-}/Zr(OH)_4$, which is a

precursor of SO_4^{2-}/ZrO_2, is commercially supplied by Magnesium Elektron, Inc. The $SO_4^{2-}/Zr(OH)_4$ was prepared commonly with impregnation of $Zr(OH)_4$ with a dilute sulfuric acid or an ammonium sulfate aqueous solution.

The activity of non-promoted SO_4^{2-}/ZrO_2 decreases as the reaction proceeds, which is generally interpreted to be due to coke deposition. To avoid coke formation, promoted catalysts on which a small amount of Pt, Ni etc. was added, were developed. Over a Pt-SO_4^{2-}/ZrO_2 catalyst, no deactivation was observed for more than 1000 h in the skeletal isomerization of *n*-pentane at 423 K under hydrogen atmosphere.[10] In a *n*-butane isomerization without hydrogen, however, Tábora and R. J. Davis found that Pt-SO_4^{2-}/ZrO_2 exhibits stable activity at 323 K for 10 h.[12] The optimal loading amount of Pt on SO_4^{2-}/ZrO_2 was found to be 0.5-0.7 wt%. They proposed that higher loadings result in metal agglomeration and suppression of the activity.[12] These results show that role of platinum on SO_4^{2-}/ZrO_2 is not only to remove coke-deposits. On the other hand, Parera proposed that deactivation of SO_4^{2-}/ZrO_2 results from a decrease in the oxidation state of sulfur in the surface complex.[20] Recently, Stair applied UV-Raman spectroscopy to clarify the deactivation mechanism of SO_4^{2-}/ZrO_2.[21] They concluded that the surface phase of SO_4^{2-}/ZrO_2 is reconstructed from tetragonal to monoclinic phase during the deactivation process, while the bulk remains in the tetragonal phase. It should be noted that Raman spectra bring forth more information from the surface layers of a sample than that from the bulk, the partial phase transformation in the surface region could be detected with the Raman characterization.

Ebitani found that CO is scarcely adsorbed on Pt-SO_4^{2-}/ZrO_2,[22] and propene hydrogenation ability of Pt-SO_4^{2-}/ZrO_2 at 323 K is lower by two orders than that of Pt/ZrO_2 at 273 K.[23] The amount of uptaken hydrogen by Pt-SO_4^{2-}/ZrO_2 is fifty times larger than the equivalent to Pt-content in the catalyst,[24] and Lewis acid site on Pt-SO_4^{2-}/ZrO_2 is reversibly converted to Brønsted acid sites by heating under hydrogen atmosphere.[25] Remarkable promotive effects of hydrogen on Pt-SO_4^{2-}/ZrO_2 were found on pentane isomerization at 523 K [23] and cumene cracking at 423 and 473 K.[26] On the basis of hydrogen effects, Hattori and coworkers proposed a mechanism accompanied by a molecular hydrogen-originated protonic acid site formation on Pt-SO_4^{2-}/ZrO_2.[18,23,27,28]

The state of platinum on SO_4^{2-}/ZrO_2 has been examined by means of mainly TPR, XPS, and XAFS. Ebitani reported that Pt is supported on SO_4^{2-}/ZrO_2 mainly in an oxidized state with some metallic phase inside.[22,29,30] Paál [31] and Iglesia [32] claimed that Pt is supported as sulfied one on the activated catalyst. Sayari and coworkers proposed that Pt is metallic, even after calcination in air.[33,34] In the studies mentioned above, loading amounts of Pt (5-7 wt%) were ten times as much as those of practically used catalysts (ca. 0.5 wt%). Tábora and R. J. Davis measured XANES spectrum of Pt (0.74 wt%)/SO_4^{2-}/ZrO_2 and concluded that platinum is present as PtO_2.[12] On the other hand, Tanaka and Shishido measured XAFS spectra of 0.5 wt% Pt-SO_4^{2-}/ZrO_2 in a oxidized and reduced state. They found that state of platinum in Pt-SO_4^{2-}/ZrO_2 is the mixture of metallic platinum and platinum

oxide in both cases, and metallic platinum particles are covered with the thin layer of platinum oxide.[35,36]

The transition metal doping of Zn, Ni, Co, Fe, Mn, W, Ir, Pt, Rh, Ru, Os has been found to promote greatly *n*-alkane rearrangement.[15,37] Besides Pt in metal-promoted sulfated zirconia, iron- and manganese-promoted sulfated zirconia (Fe-, Mn-SO_4^{2-}/ZrO_2) has been a subject of the most recent attention for alkane conversion.[19] In 1990's, Hsu and coworkers discovered Fe-, Mn-SO_4^{2-}/ZrO_2, the activity of which for *n*-butane isomerization at room temperature was higher by three orders of magnitude than that of conventional SO_4^{2-}/ZrO_2.[11,38] During *n*-butane isomerization, Fe-, Mn-SO_4^{2-}/ZrO_2 exhibits an induction period followed by a fast deactivation.[39,40] The deactivation of Fe-, Mn-SO_4^{2-}/ZrO_2 for skeletal isomerization was somewhat suppressed even in the absence of hydrogen. Tábora observed a steady activity for *n*-butane isomerization at 323 K over Fe-, Mn-SO_4^{2-}/ZrO_2 after 5 h, although the activity was quarter as much as the maximum activity at the initial period.[12] Phenomenon occurring in the induction period is interpreted as a formation and/or accumulation of unsaturated species such as butenes.[12,41-44] The *n*-butane isomerization over Fe-, Mn-SO_4^{2-}/ZrO_2 was proposed to proceed predominantly via oligomeric intermediates of C_8 species, as well as over SO_4^{2-}/ZrO_2.[45-47] The formed butenes induce the skeletal isomerization of bimolecular mechanism by reacting with C_4 carbenium ions, but their accumulation on the surface leads to a formation of coke precursors. In fact, Alvarez found over Fe-, Mn-SO_4^{2-}/ZrO_2 that the activity under continuous flow operation was much higher than that obtained in the pulse mode.[43,48] They proposed that the intermediates are desorbed or decomposed under He stream without *n*-butane at 423 K, while at 373 K they retain. In the case that the reaction was carried out at 423 K, the activity started from a very low value and a new induction period was observed whenever *n*-butane flow was stopped. By contrast, the induction period was only observed during the first cycle, when the experiment was performed at 373 K. The similar results were obtained in case over Ni-SO_4^{2-}/ZrO_2.[49]

In cases of ethane and propane isomerizations above 473 K, the product distributions show that reactions over Fe-, Mn-SO_4^{2-}/ZrO_2 are consistent with chemistry analogous to that in superacidic solutions.[50-52] Based on results of the catalyses, Gates concluded Fe-, Mn-SO_4^{2-}/ZrO_2 is a stronger acid than SO_4^{2-}/ZrO_2, USY and HZSM-5.[50,52] From benzene-TPD characterizations, Lin and Hsu reported that catalytic activity deeply depends on the SO_4^{2-} content, and acid sites on Fe-, Mn-SO_4^{2-}/ZrO_2 are stronger than those on SO_4^{2-}/ZrO_2.[38] Morterra measured IR spectra of adsorbed CO over Fe-, Mn-SO_4^{2-}/ZrO_2, Fe-SO_4^{2-}/ZrO_2 and Mn-SO_4^{2-}/ZrO_2. They confirmed one peak at 2200 cm^{-1} and a shoulder at 2170 cm^{-1} on Fe-, Mn-SO_4^{2-}/ZrO_2 and Fe-SO_4^{2-}/ZrO_2, while only one peak at 2200 cm^{-1} on Mn-SO_4^{2-}/ZrO_2.[53] The peak at 2200 cm^{-1} was assigned to CO adsorbed onto coordinately unsaturated (CUS) Zr^{4+}. They assigned the shoulder at 2170 cm^{-1} to those onto CUS surface Fe^{n+} sites, where *n* is between 2 and 3. M. E. Davis reported that Fe-, Mn-SO_4^{2-}/ZrO_2 is much more active for *n*-butane isomerization than Fe-SO_4^{2-}/ZrO_2 and Mn-SO_4^{2-}/ZrO_2; and Mn-SO_4^{2-}

/ZrO_2 scarcely catalyzes the reaction at 308 K.[39] However, they pointed out the possibility that differences of activities among them merely depend on the sulfur content. Benzene TPD characterization did not give any informations about differences of the acidities.[39] In fact, Gates reported that addition of manganese increases the activity by two or three orders of magnitude.[37] From CO-FTIR and ^{1}H-NMR characterizations, Sachtler insisted that both Lewis and Brønsted acidities on SO_4^{2-}/ZrO_2 and Fe-, Mn-SO_4^{2-}/ZrO_2 are as such within experimental errors.[8] Tábora gave the same CO-FTIR spectra of SO_4^{2-}/ZrO_2 and Fe-, Mn-SO_4^{2-}/ZrO_2, indicating that Lewis acidities of the both are the same level,[40] in contrast to the work by Morterra.[53] At the present stage, clear differences in acidity among SO_4^{2-}/ZrO_2, Mn-SO_4^{2-}/ZrO_2 and Fe-, Mn-SO_4^{2-}/ZrO_2 are not obtained.

Tábora and R. J. Davis proposed that the role of Fe and Mn promoters in SO_4^{2-}/ZrO_2 is to increase the surface concentration of intermediate butenes which subsequently react to form isobutane. They concluded that Fe-, Mn- promoted catalyst forms butene not catalytically whereas the Pt-promoted sample forms butene catalytically.[12] Wan found an effect of calcination and He-purge pretreatment temperature on the activity of Fe-, Mn-SO_4^{2-}/ZrO_2.[47] With increasing calcination temperature in air, catalytic activity for *n*-butane isomerization increases. On the other hand, with increasing He-purge temperature of pre-calcined catalyst, the activity decreases at a temperature above 523 K. They speculated that high-valent iron oxy species such as tetrahedral Fe^{4+} species forms on Fe-, Mn-SO_4^{2-}/ZrO_2 during calcination in air, and these sites are responsible for the oxidative dehydrogenation of *n*-butane to butene.

Only a few works were performed to investigate the states of Fe and Mn atoms on Fe-, Mn-SO_4^{2-}/ZrO_2, because Fe-, Mn-SO_4^{2-}/ZrO_2 contains very small amounts of Fe (ca. 1.5 wt%) and Mn (ca. 0.5 wt%). Tábora *et al.* measured Fe K-edge EXAFS spectrum of Fe-, Mn-SO_4^{2-}/ZrO_2 and no contributions from Fe-Zr and/or Fe-Fe pairs were confirmed in the radial structure functions. They concluded that the Fe atoms are not substituted isomorphously into bulk tetragonal zirconia but instead exist in nanometer-size oxide clusters or rafts which located on the surface or at defects inside the bulk.[40] However, the quality of the datum and method of datum reduction for the EXAFS spectrum were not adequate. It is quite difficult to obtain the information from the spectrum about the local structure abound Fe. From the fact that a pre-edge peak was not present in the Mn-K edge XANES spectrum, they commented that Mn atom in Fe-, Mn-SO_4^{2-}/ZrO_2 is not tetrahedral coordination. Milbum carried out in-situ XPS characterization of Fe-, Mn-SO_4^{2-}/ZrO_2.[54] They reported that both Fe and Mn atoms were supported on sulfated zirconia in an oxidized state after hydrogen treatment at 423 K. Unfortunately, their X-ray photoelectron spectra of Fe$2p$, Mn$2p$, and S$2s$ were too noisy to determine the accurate binding energies. Knözinger, Gates and coworkers carried out precise characterization of Fe-, Mn-SO_4^{2-}/ZrO_2 with UV-vis, ESR, Raman, XPS and XRF.[55] The UV-vis and Raman characterizations show that iron was present in an aggregated form and not as atomically isolated species, although the ESR spectrum shows the presence of isolated Fe^{3+} ions. Manganese in Fe-, Mn-SO_4^{2-}/ZrO_2 and Mn-SO_4^{2-}/ZrO_2 was identified by the ESR

spectra of Mn^{2+}, with the resolved hyperfine structure. Based on the spectroscopic characterizations, they concluded that Fe atoms are present as small Fe_2O_3 particles (1-2 nm) with some isolated Fe^{3+} ions, and Mn atoms are present as divalent ions in a highly dispersed form.

As mentioned above, property of SO_4^{2-}/ZrO_2 and SO_4^{2-}/ZrO_2-based catalysts have been uncovered gradually. However, the physicochemical properties of Fe-, Mn-SO_4^{2-}/ZrO_2, the most promising catalyst in practice, is still full of controversy. The present part, although it contains only one chapter, is devoted to the clarification of the states of Fe and Mn in Fe-, Mn-SO_4^{2-}/ZrO_2 catalysts. The use of the XAFS and the other techniques firstly elucidated the states of Fe, Mn precisely and the role of these elements is discussed.

References

1 Tanabe, K.; Itoh, M.; Morishige, K.; Hattori, H. *Stud. Surf. Sci. Catal.*, **1976**, *1*, 65.

2 Hino, M.; Kobayashi, S.; Arata, K. *J. Am. Chem. Soc.* **1979**, *101*, 6439.

3 Hino, M.; Arata, K. *J. Chem. Soc., Chem. Commun.*, **1980**, 851.

4 Hino, M.; Arata, K.*Chem. Lett.*, **1979**, 1259.

5 Arata, K. *Adv. Catal.*, **1990**, *37*, 165.

6 Semmer, V.; Batamack, P.; Dorémieux-Morin, C.; Vincent, R.; Fraissard, J. *J. Catal.*, **1996**, *161*, 186.

7 Babou, F.; Bigot, B.; Coudurier, G.; Sautet, P.; Védrine, J. C. *Stud. Surf. Sci. Catal.*, **1994**,*90*, 519.

8 Adeeva, V., de Haan, J. W.; Jänchen, J.; Lei, G. D.; Schünemann, V.; van de Ven, L. J. M.; Sachtler, W. M. H.; van Santen, R. A. *J. Catal.*, **1995**, *151*, 364.

9 Gao, Z.; Chen, J.-M.; Hua, W.-M.; Tang, Y. *Stud. Surf. Sci. Catal.*, **1994**,*90*, 507.

10 Hosoi, T.; Shimadzu, T.; Ito, S.; Baba, S.; Takaoka, H.; Imai, T.; Yokoyama, N. *Prepr. Symp. Div. Petr. Chem. Am. Chem. Soc.*, **1988**, 562.

11 Hsu, C.-Y.; Heimbuch, C. R.; Armes, C. T.; Gates, B. C. *J. Chem. Soc., Chem. Commun.*, **1992**, 1645.

12 Tábora, J. E.; Davis, R. J. *J. Catal.*, **1996**, *162*, 125.

13 Tanabe, K.; Misono, M.; Ono, Y.; Hattori, H. *New Solid Acids and Bases*, Kodansha, Tokyo, **1989**, pp. 199-206.

14 Yamaguchi, T. *Appl. Catal.*, **1990**, *61*, 1, and references therein

15 Corma, A. *Chem. Rev.*, **1995**, *95*, 559.

16 Corma, A.; García, H. *Catal. Today*, **1997**, *38*, 257, and references therein

17 Song, X.; Sayari, A. *Catal. Rev.-Sci. Eng.*, **1996**, *38*, 329.

18 Hattori, H.; Shishido, T. *Catal. Survey Jpn.*, **1997**, *1*, 205.

19 Cheung, T.-K.; Gates, B. C. *Top. Catal.*, **1998**, *6*, 41, and references therein
20 Yori, J. C.; Luy, J. C.; Parera, J. M. *Appl. Catal.*, **1989**, *46*, 103.
21 Li, C.; Stair, P. C. *Catal. Lett.*, **1996**, *36*, 119.
22 Ebitani, K.; Konno, H.; Tanaka, T.; Hattori, H. *J. Catal.*, **1992**, *135*, 60.
23 Ebitani, K.; Konishi, J.; Hattori, H. *J. Catal.*, **1991**, *130*, 257.
24 Ebitani, K.; Konno, H.; Tanaka, T.; Hattori, H. *J. Catal.*, **1993**, *143*, 322.
25 Ebitani, K.; Tsuji, J.; Hattori, H.; Kita, H. *J. Catal.*, **1992**, *135*, 609.
26 Shishido, T.; Hattori, H. *J. Catal.*, **1996**, *161*, 194.
27 Hattori, H. *Stud. Surf. Sci. Catal.*, **1993**, *77*, 69.
28 Hattori, H.; Shishido, T.; Tsuji, J.; Nagase, T.; Kita, H. *Stud. Surf. Sci. Catal.*, **1995**, *92*, 93.
29 Ebitani, K.; Konno, H.; Tanaka, T.; Hattori, H. *J. Catal.*, **1992**, *143*, 322.
30 Ebitani, K.; Tanaka, T.; Hattori, H. *Appl. Catal. A*, **1993**, *102*, 79.
31 Paál, M.; Muhler, M.; Schröl, R. *J. Catal.*, **1993**, *143*, 318.
32 Iglesia, E.; Doled, S. L.; Kramer, G. M. *J. Catal.*, **1993**, *144*, 238.
33 Sayari, A.; Dicko, A. *J. Catal.*, **1994**, *145*, 561.
34 Dicko, A.; Song, X.; Adnot, A.; Sayari, A. *J. Catal.*, **1994**, *145*, 561.
35 Tanaka, T.; Shihidi, T.; Hattori, H.; Ebitani, K.; Yoshida, S. *Physica B* **1995**, *208/209*, 649.
36 Shishido, T.; Tanaka, T.; Hattori, H. *J. Catal.*, **1997**, *172*, 24.
37 Lange, F. C.; Cheung, T.-K.; Gates, B. C. *Catal. Lett.*, **1996**, *41*, 95.
38 Lin, C.-H.; Hsu, C.-Y. *J. Chem. Soc., Chem. Commun.*, **1992**, 1479.
39 Jatia, A.; Chang, C.; MacLeod, J. D.; Okubo, T.; Davis, M. E. *Catal. Lett.*, **1994**, *25*, 21.
40 Tábora, J. E.; Davis, R. J. *J. Chem. Soc., Faraday Trans*, **1995**, *91*, 1825.
41 Adeeva, V.; Lei,G. D.; Sachtler, W. M. H. *Catal. Lett.*, **1995**, *33*, 135.
42 Coelho, M. A.; Resasco, D. E.; Sikabwe, E. C.; White, R. C. *Catal. Lett.*, **1995**, *32*, 253.
43 Coelho, M. A.; Alvarez, W. E.; Sikabwe, E. C.; White, R. C.; Resasco, D. E. *Catal. Today*, **1995**, *28*, 415.
44 Chao, K.-J.; Wu, H.-C.; Leu, L.-J. *J. Catal.*, **1995**, *157*, 289.
45 Adeeva, V.; Lei, G. D., Sachtler, W. M. H. *Appl. Catal. A*, **1994**, *118*, L11.
46 Cheung, T.-K.; d'Itri, J. L.; Gates, B. C. *J. Catal*, **1995**, *151*, 464.
47 Wan, K. T.; Khouw, C. B.; Davis, M. E. *J. Catal.*, **1996**, *158*, 311.
48 Alvarez,W. E.; Liu, H.; Resasco, D. E. *Appl. Catal. A*, **1997**, *162*, 103.
49 Alvarez, W. E.; Liu, H.; Garcia, E. A.; Rueda, E. H.; Rouco, A. J.; Resasco, D. E. *Stud. Surf. Sci. Catal.*, **1996**,*101*, 553.
50 Cheung, T.-K.; Lange, F. C.; Gates, B. C. *J. Catal*, **1996**, *159*, 99.
51 Cheung, T.-K.; Gates, B. C. *Chem. Commun.*, **1996**, 1937.

52 Cheung, T.-K.; Gates, B. C. *J. Catal*, **1997**, *168*, 522.

53 Morterra, C.; Cerrato, G.; Ciero, S. D.; Signoretto, M.; Minesso, A.; Pinna, F.; Strukul, G. *Catal. Lett.*, **1997**, *49*, 25.

54 Milbum, D. R.; Keogh, R. A.; Sparks, D. E.; Davis, B. H. *Appl. Surf. Sci*,, **1998**, *126*, 11.

55 Scheithauer, M.; Bosch, E.; Schubert, U.; Knözinger, H.; Cheung, T.-K.; Jentoft, F. C.; Gates, B. C.; Tesche, B. *J. Catal.*, **1998**, *177*, 137.

Chapter 6

Structural Analysis of Iron and Manganese Species in Iron- and Manganese-Promoted Sulfated Zirconia

Abstract

The structural analyses of Fe, Mn-SO_4^{2-}/ZrO_2 (FMSZ), Fe-SO_4^{2-}/ZrO_2 (FSZ), Mn-SO_4^{2-}/ZrO_2 (MSZ), and Fe-Mn/ZrO_2 (FMZ) were carried out by means of XAFS, XRD and Raman spectroscopy. Local structure around Fe and Mn of each catalyst, which were at a working state for *n*-butane isomerization and in vacuo, were studied by in-situ XAFS. The valence of the Fe atom of all the catalysts was invariantly trivalent. Coordination environment around Fe of all the catalysts was quite similar to each other. Fe atoms are present inside the bulk phase of ZrO_2, the system of which forms interstitial-type solid solution and located at the center of distorted oxygen octahedra. Reaction gas does not directly make contact with Fe atoms, because the introduction of reaction gas did not cause any change of coordination environment and the valence. Mn species on FMSZ and MSZ were present as $MnSO_4$, and their coordination environment was reversibly affected by exposure to *n*-butane. Without sulfate ions, Mn species are present on the catalyst as α-Mn_2O_3.

Introduction

Since Arata et al. discovered SO_4^{2-}/ZrO_2 (SZ) which catalyzes *n*-butane skeletal isomerization at room temperature,[1] SZ and promoted SZ have been investigated extensively.[2-4] As a promoter, various transition metals have been added to SZ. In the 1990s, Hsu et al. discovered sulfated Fe-Mn-Zr oxide (FMSZ), the activity of which for *n*-butane isomerization at room temperature was higher by 3 orders of magnitude than that of conventional SO_4^{2-}/ZrO_2.[5] Furthermore, the deactivation of FMSZ for skeletal isomerization was much suppressed even in the absence of hydrogen.[6] Therefore, much attention has been paid to this new solid acid catalyst.[7] However, the distinct difference in physical property except for catalysis between SZ and FMSZ has not been clarified.[8,9] Further, the role and structure of promoted elements on FMSZ remained unclear, in contrast to the case of $Pt\text{-}SO_4^{2-}/ZrO_2$.[3, 10] Only a few studies were performed to investigate the states of Fe and Mn atoms on FMSZ because FMSZ contains no more than very small amounts of Fe (*ca.* 1.5 wt %) and Mn (*ca.* 0.5 wt %).

Tábora et al. measured Zr-K edge EXAFS spectrum of FMSZ, and concluded that the phase of ZrO_2 was tetragonal.[11] They also measured Fe K-edge EXAFS spectrum and reported that Fe atoms were supported on ZrO_2 as small clusters or rafts of Fe_2O_3. However, its quality and the method of datum reduction of the Fe K-edge EXAFS were not adequate, and it is difficult to obtain the information about the local structure abound Fe. From XPS investigation, Milbum et al. reported that both Fe and Mn atoms were supported on sulfated zirconia in an oxidized state.[12] Unfortunately, their recorded X-ray pohotoelectron spectra of Fe_{2p}, Mn_{2p}, and S_{2s} were too noisy to determine the accurate binding energies. More recently, Gates and co-workers investigated the structure of FMSZ with various spectroscopic methods. From XPS, ESR, UV-VIS, and Raman characterizations, they concluded that Fe atoms are present as small Fe_2O_3 particles with some isolated Fe^{3+} ions, and Mn atoms are present as divalent ions.[13] In contrast, Wan et al. speculated that high-valent iron oxy species such as tetrahedral Fe^{4+} species had formed on FMSZ, and these sites are responsible for the oxidative dehydrogenation of *n*-butane to butene.[14]

If Fe^{4+} species had formed on FMSZ, Fe ions would have been reduced by exposure of butane and some change of the coordination environment should have occurred. In the present study, we carried out in-situ XAFS measurements to investigate the local structures around Fe and Mn atoms, and studied their changes during *n*-butane isomerization.[15] There are no studies investigating coordination environment of Fe and Mn species at a working state.

Experimental

Material

Fe- and Mn- promoted sulfated zirconia (Fe, Mn-SO_4^{2-}/ZrO_2; FMSZ) was prepared according to Cheung's method.[16] The sulfate ion-treated $Zr(OH)_4$ ($SO_4^{2-}/Zr(OH)_4$) was prepared by the impregnation of $Zr(OH)_4$ with 1 M $(NH_4)_2SO_4$ aqueous solution at room temperature for 0.5 h with stirring followed by filtration and drying at 383 K for 6 h. The $Zr(OH)_4$ was obtained by hydrolysis of $ZrOCl_2 \cdot 8H_2O$ with 25 mass % NH_3 aqueous solution at room temperature followed by filtration. The final value of pH was 8.0, and the aging time was 2 h. The obtained gel was washed with distilled water repeatedly until Cl^- was free on the basis of the $AgNO_3$ test. Fe and Mn ions were supported on $SO_4^{2-}/Zr(OH)_4$ by stepwise equilibrium adsorption of 0.2 M $Fe(NO_3)_3 \cdot 6H_2O$ and 0.043 M $Mn(NO_3)_2 \cdot 9H_2O$ aqueous solutions. Each equilibrium adsorption was performed at room temperature for 0.5 h with stirring followed by filtration. After drying at 383 K for 6 h, it was then calcined at 873 K for 3 h.

Fe-SO_4^{2-}/ZrO_2 (FSZ), Mn-SO_4^{2-}/ZrO_2 (MSZ) and Fe-Mn/ZrO_2 (FMZ) were prepared the same as FMSZ was prepared, by omitting each step.

Elemental composition was determined by X-ray fluorescence (XRF) with a RIGAKU 3270 spectrometer. The BET specific surface area measurement was carried out with BELSORP 28SA using a N_2 adsorption isotherm at 77 K. Results of elemental analysis and surface area measurements are summarized in Table 1.

TABLE 1: BET Specific Surface Area and Chemical Composition

Catalyst	Surface Area	Elements (wt%)		
	/ $m^2\ g^{-1}$	S	Fe	Mn
ZrO_2	33	-	-	-
SO_4^{2-}/ZrO_2	98	0.88	-	-
Fe-, Mn-SO_4^{2-}/ZrO_2	124	0.81	1.7	0.25
Fe-SO_4^{2-}/ZrO_2	107	0.96	1.1	-
Mn-SO_4^{2-}/ZrO_2	101	1.5	-	0.27
Fe, Mn/ZrO_2	110	-	1.9	0.42

X-ray Diffractions (XRD)

X-ray diffraction patterns of samples were obtained with a RIGAKU RINT 1300 diffractometer using Ni-filtered Cu Kα radiation (averaged as 1.5418 Å).

Raman Spectra

The laser Raman spectra were recorded with a JASCO NRS-2000 spectrometer using the 514.5 nm line of an Ar^+ laser emission. An incident laser power was 0.5 - 5 mW at sample position, and the scan time was 60 - 180 s for a single spectrum. The spectral resolution was 4 cm^{-1}. All spectra were recorded under ambient conditions at room temperature.

In Situ XAFS Measurements

Fe and Mn K-edge X-ray absorption experiments were carried out on the BL7C and BL12C at Photon Factory in High Energy Accelerator Research Organization (KEK-PF; Tsukuba, Japan) with a ring energy of 2.5 GeV and a stored current of 250 - 400 mA (Proposal No. 97G041). The X-ray absorption spectra of catalysts were recorded in a fluorescent mode, and those of reference compounds were recorded in a transmission mode with a Si(111) two-crystal monochromator. The energy was calibrated by the preedge peak position of Cu foil (8980.3 eV).

Data reduction was performed using a FACOM M1800 computer of Kyoto University Data Processing Center. The normalization method has been previously reported in detail.[17] For curve-fitting analysis, the following EXAFS formula was applied.

$$k^3\chi(k) = \Sigma_j (k^2 N_j / R_j^2) A_j(k) \exp(-2\sigma_j^2 k^2) \sin(2kR_j + \delta_j(k))$$

where k is the wavenumber of photoelectron, N_j the number of the scattering atoms of the j th shell located at a distance of R_j from a central atom, A_j the envelope function which includes the backscattering amplitude and damping factor caused by inelastic loss during electron traveling, σ_j the Debye-Waller factor and δ_j the phase shift. For curve-fitting analysis, the backscattering amplitude and phase shift functions of Fe-O pair were obtained from a k^3-weighted EXAFS spectrum of the CoO crystal (Rock salt type, a_0 = 4.260 Å). For Zr atom scatterers, they were estimated with FEFF (6.0).[18] EXAFS analysis for Mn K-edge could not be performed because the *S/N* ratio of each spectrum was too bad to obtain useful information.

Each catalyst was charged in an in-situ XAFS cell with a Kapton window to prevent exposure to the air. The recorded XAFS spectra of each catalyst were pretreated ones (1), ones

at a working state for *n*-butane isomerization (2), and ones evacuated after a reaction (3). XAFS experiments and *n*-butane isomerization were carried out at the same time.

Catalysis

The isomerization of *n*-butane was performed with an in-situ XAFS cell under static conditions at 293 K, at the same time as the XAFS measurement. The cell was made of Pyrex glass and was connected with a glass balloon filled with *n*-butane (54.1 mmol). Total dead volume of the cell was 1,300 cm^3. The catalyst of FMSZ (700 mg) was evacuated at 673 K for 1 h, followed by contact with *n*-butane at 293 K. After 24 h in a static condition, Fe and Mn K-edge XAFS spectra were recorded at a working state. Then reaction gases were evacuated at room temperature for 10 min, followed by measurement of Fe and Mn K-edge XAFS spectra. The evacuated gas was stored in another vessel, and the composition was analyzed with TCD gas chromatography.

In the cases of FSZ, MSZ, and FMZ, XAFS measurements and *n*-butane isomerization were carried out in a manner similar to mentioned above. For these three catalysts, another type of in-situ XAFS cell, the dead volume of which was 60 cm^3, was used. The amounts of catalyst and substrate were 200 mg and 99 μmol, respectively. Catalysis over SO_4^{2-}/ZrO_2 (SZ) was performed under the same reaction conditions, using a closed reaction vessel (60 cm^3). In all cases, reaction time and temperature were 24 h and 293 K, respectively.

Results

Catalysis

After 24 h at 293 K under static conditions, 12.5 % of the *n*-butane had converted to *iso*-butane over FMSZ. The amount of reacted *n*-butane was 6.76 mmol. Formation of C_3 and C_5 species was negligible. The amounts of Fe and Mn contained in 700 mg of FMSZ were 213 and 32 μmol, respectively. The apparent turn over numbers per one Fe and Mn atoms were 32 and 211, respectively.

Over FSZ and MSZ, 25 % and 7.3 % of *n*-butane were converted to *iso*-butane, respectively. The conversion over SZ was 5.8 %. FMZ was inert for *n*-butane isomerization. In the case of FSZ, the amount of reacted *n*-butane was 24.8 μmol and the amount containing an Fe atom was 39 μmol. In the case of MSZ, the amount of reacted *n*-butane was 7.2 μmol and the amount containing a Mn atom was 9.8 μmol.

Because the reaction vessels for the FMSZ catalyst and for the others are different, we cannot directly compare the activity between them. But it is obvious that the activity for FMSZ is the highest. FSZ exhibited higher activity than SZ. Lange et al. observed Mn increases the

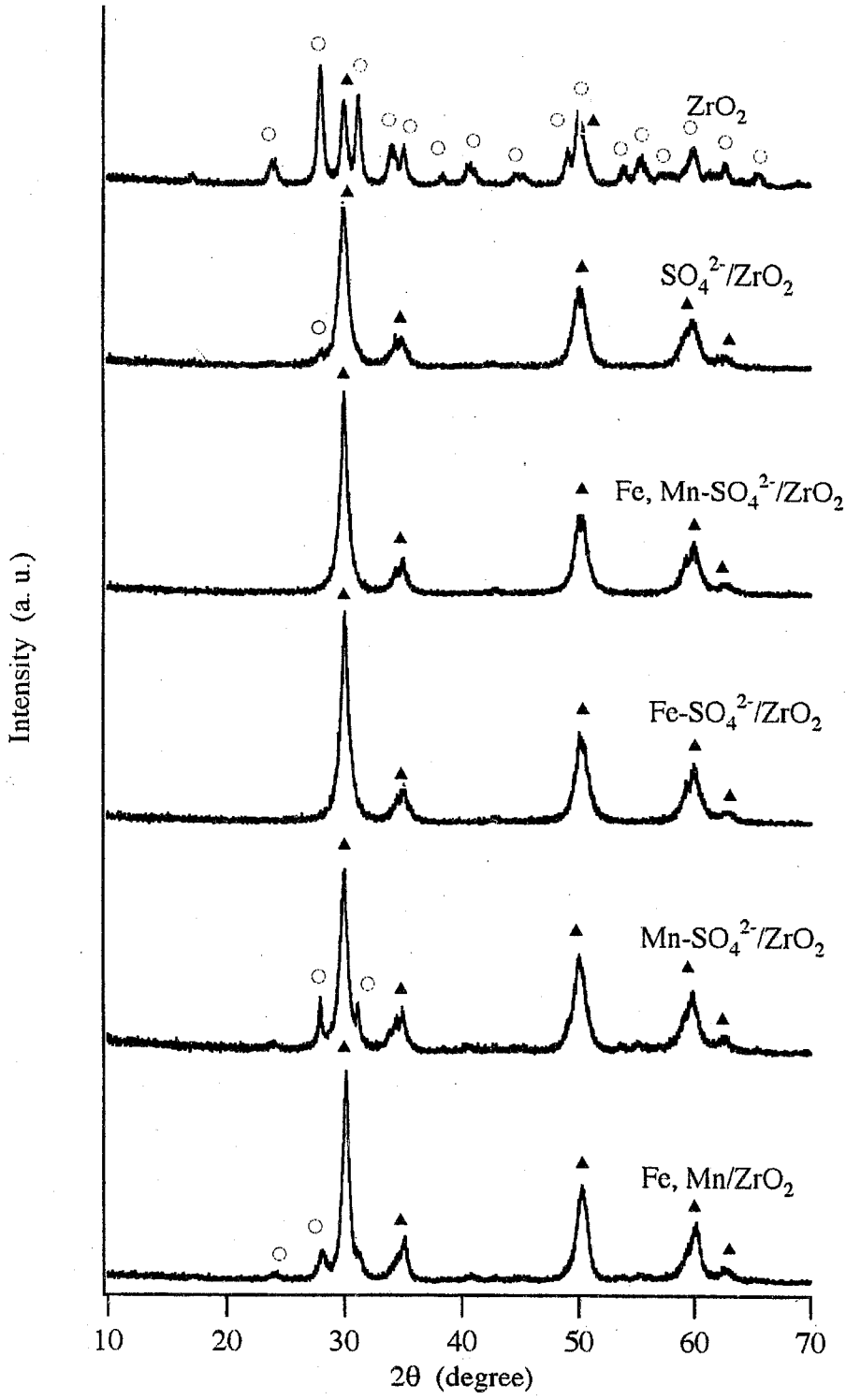

Figure 1. Cu Kα XRD patterns of samples calcined at 873 K: ○; monoclinic phase, ▲; tetragonal phase.

activity by 2 or 3 orders of magnitude.[19] Whereas in our case, Mn addition to SZ is not very effective, the same as in the previous report.[8]

XRD

Figure 1 shows XRD patterns of catalysts calcined at 873 K. ZrO_2 consists of a mixture of monoclinic and tetragonal phases. SZ, FMSZ, and FSZ consist of only tetragonal ZrO_2 of metastable phase. The ZrO_2 phases of FMZ and MSZ are mainly tetragonal. Any peaks, other than ZrO_2 phases, were not observed in all the XRD patterns.

Raman Spectra

It has been reported that the tetragonal phase of ZrO_2 exhibits typical Raman bands at 148, 263, 325, 472, 608, and 640 cm^{-1},[19] and that the Raman spectrum of SO_4^{2-}/ZrO_2 is identical to that of tetragonal ZrO_2.[13,21,22] Raman spectra of the catalysts are shown in Figure 2. Although the XRD pattern of ZrO_2 shows that ZrO_2 consists of both monoclinic and tetragonal phases, the Raman spectrum of ZrO_2 calcined at 873 K is identical to the reported spectrum of 100 % monoclinic ZrO_2.[20] The positions of the observed Raman bands were 96, 140, 173, 185, 216, 260, 301, 328, 342, 378, 471, 499, 533, 553, 610, 632, and 752 cm^{-1}. Two tiny peaks at 140 and 260 cm^{-1} were due to the tetragonal phase, and the others were due to the monoclinic phase. It shows that the surface region of ZrO_2 calcined at 873 K consists of the monoclinic phase only, whereas the bulk is a mixture of two phases. The Raman spectrum of SZ shows that the surface phase of is mainly the tetragonal ZrO_2 phase with a trace amount of monoclinic phase. The surface ZrO_2 phases of FMSZ, FSZ and MSZ consist mainly of the tetragonal phase as well, corresponding to the results of XRD measurements. The positions of the Raman bands assigned to the tetragonal ZrO_2 phase were 140, 261, 310, 450 and 635 cm^{-1}. Scheithauer et al. measured the Raman spectra of SZ, FSZ, FMSZ and MSZ. They confirmed that ZrO_2 phases of all the catalysts were tetragonal only, and also observed the characteristic Raman bands of α-Fe_2O_3 on the spectrum of FMSZ.[13] In contrast, we did not observe any bands due to α-Fe_2O_3 (210, 272, 386, 579 cm^{-1}) on all the spectra. α-Mn_2O_3 and ß-MnO_2 exhibit no Raman bands in this region.[23]

Characteristic hydrated sulfate groups were observed on SZ, FMSZ, FSZ and MSZ at 1029 - 1031 cm^{-1}, as well as Scheithauer's results. In the range of 950 - 1050 cm^{-1}, sulfate groups of reference compounds exhibit characteristic Raman bands at 1016 cm^{-1} for $MnSO_4$, 973 cm^{-1} for $FeSO_4$, and 1010, 1029, 1034 sh, and 1047 cm^{-1} for $Fe_2(SO_4)_3$, as shown in Figure 3. These Raman bands of metal sulfates appeared in a region similar to those of the sulfate group of SZ. In addition, Tábora et al. measured IR spectra of activated FMSZ and SZ without exposure to air.[11] In the sulfate region, IR spectra of both SZ and FMSZ exhibited strong two peaks at 1010 and 1043 cm^{-1}. Both wavenumbers are similar to those of

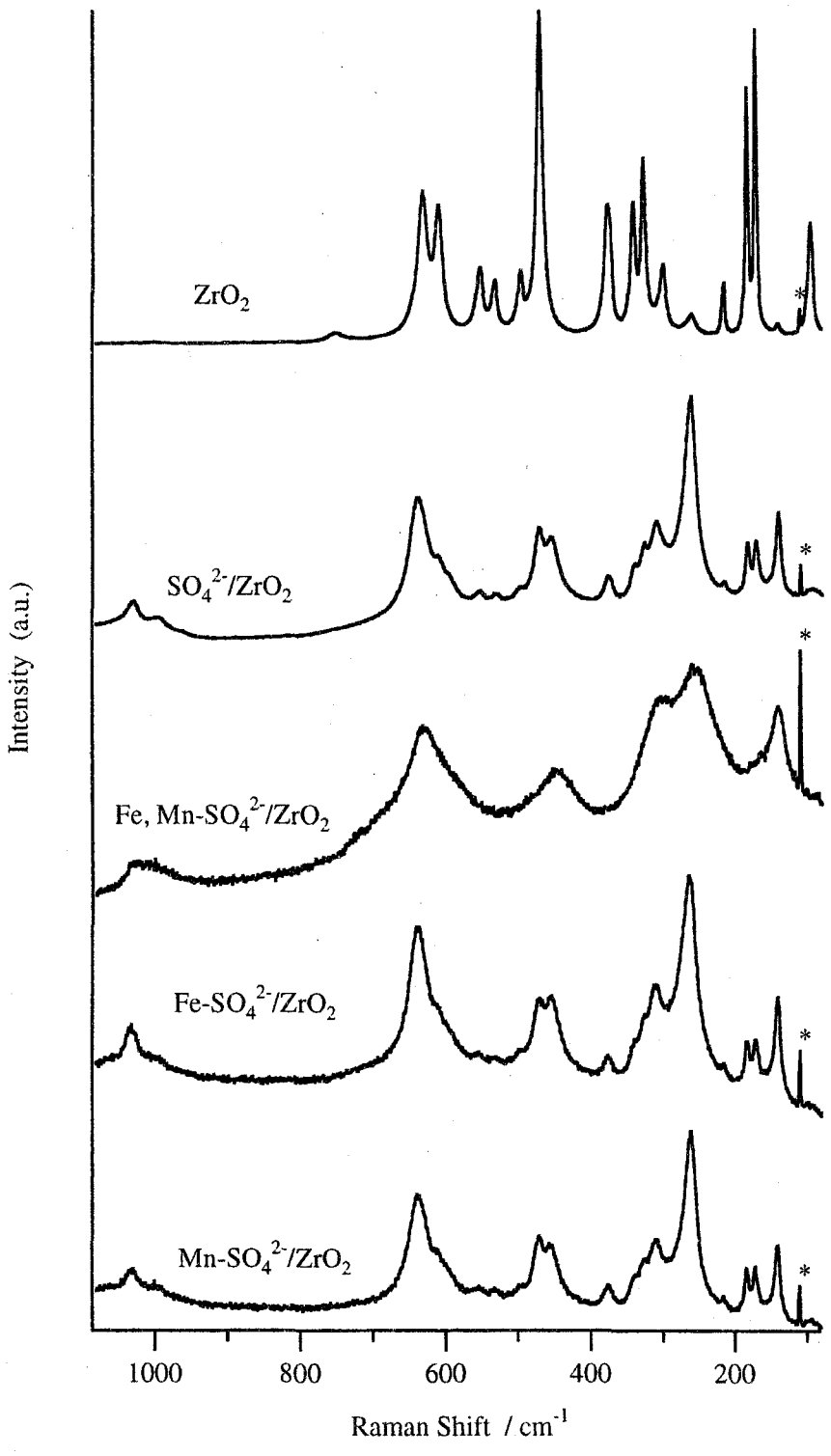

Figure 2. Raman spectra of catalysts: (*) plasma lines.

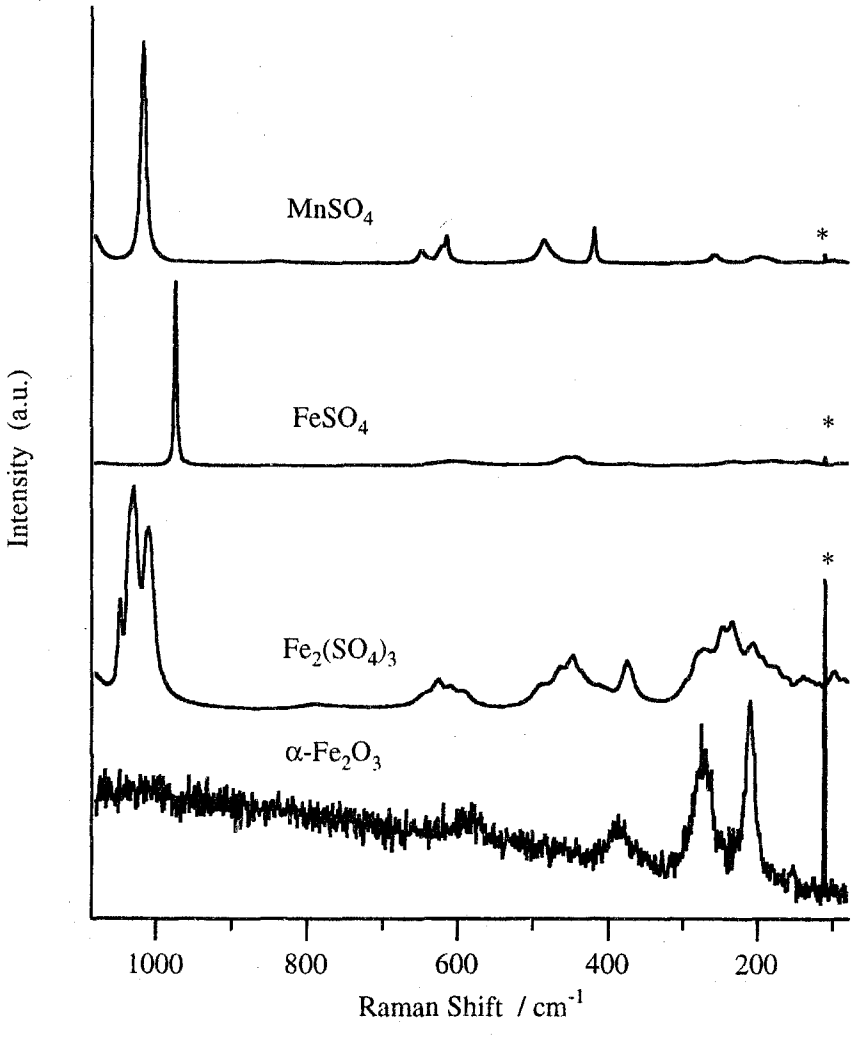

Figure 3. Raman spectra of reference compounds: (*) plasma lines.

characteristic Raman bands of $MnSO_4$ (1016 cm^{-1}) and $Fe_2(SO_4)_3$ (1010, 1028, 1047 cm^{-1}). With Raman and IR spectroscopy, it is very difficult to prove the presence of $MnSO_4$ and to determine the origin of sulfate groups of catalysts.

Fe K-edge XANES

Figure 4 shows Fe K-edge XANES spectra and the first derivatives of reference compounds. The chemical shift between Fe^{2+} and Fe^{3+} was observed in the edge position of each spectrum. XANES spectra show that $Fe_2(SO_4)_3$ had transformed to α-Fe_2O_3 when it was calcined at 873 K. As for the Fe^{3+} species, the preedge peak of α-Fe_2O_3 was split but that of γ-Fe_2O_3 was not.

Fe K-edge XANES spectra and their first derivatives of the samples are shown in Figure 5. It is very interesting that XANES spectra of all the catalysts, including the feature and the height of preedge peaks, the edge positions, and the shapes of all spectra, were almost the same as each other. The edge energy shows that Fe atoms of the three catalysts were in the trivalent state. However, XANES spectra of all the catalysts were quite different from those of reference compounds. It shows that Fe atoms on sulfated zirconia are not present as compounds such as the reference samples shown in Figure 4. Furthermore, the local structure around Fe of all the catalysts is not affected by the presence of sulfate nor Mn ions. As pointed out in the case of FMSZ previously,[15] reaction gas did not affect the edge energy nor the shape of XANES spectra. Similar phenomena were observed in XANES spectra of FSZ and FMZ. Redox of Fe atoms on all the catalysts did not take place under a reaction conditions. Evacuation of reacted gas did not cause any change of XANES spectra of the catalyst samples as well.

The preedge peak of Fe K-edge XANES is assigned to the *1s-3d* transition which is formally dipole-forbidden. The peak intensity is closely related to the symmetry around Fe atoms, and this peak becomes more intense as the symmetry is distorted from a regular octahedron.[24,25] Each preedge peak area of all the catalyst samples was a little larger than that of octahedral Fe^{3+} compounds such as α-Fe_2O_3 and did not change during *n*-butane isomerization. However, the preedge peak area was smaller than those of Fe-MFI and $FePO_4$, whose local structure around Fe is an FeO_4 tetrahedron.[26] It shows that the local symmetry around Fe was not tetrahedral, but distorted more than that of α-Fe_2O_3. The symmetrical environment around Fe of each sample was not affected by reaction gas. In addition, the differential XANES spectrum of α-Fe_2O_3 exhibits a doublet preedge peak; however, those of FMSZ have only singlet curves. These results strongly suggest the local structure around Fe is quite different from that of α-Fe_2O_3. We propose that Fe atoms are located at a center of a highly distorted octahedron. Because the reacted amounts of *n*-butane much exceeded those of Fe atoms contained in FMSZ, it could be concluded that *n*-butane does not affect the structure or the valence of Fe as well. If any chemical reaction and/or change of coordination

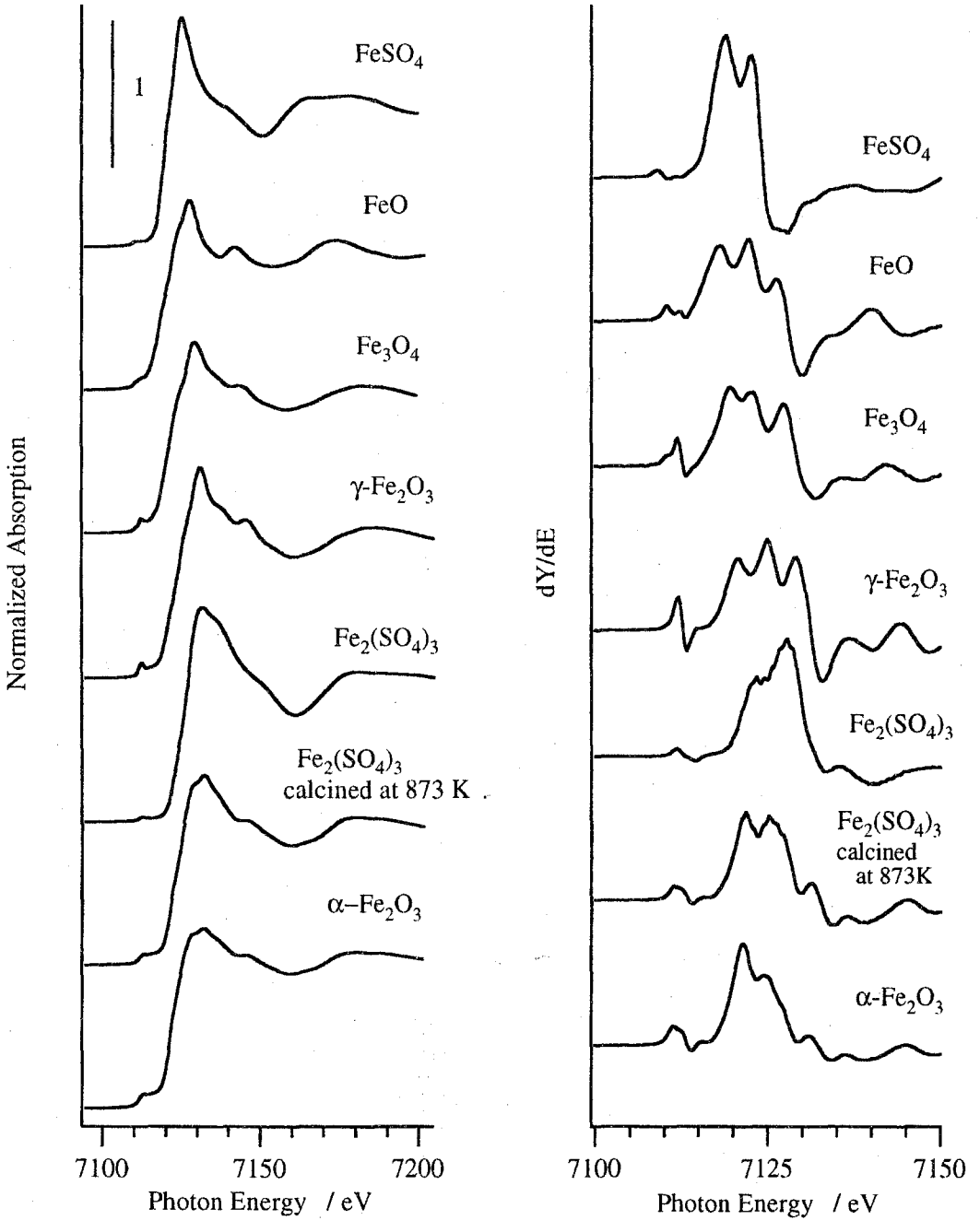

Figure 4. Fe K-edge XANES spectra of reference compounds and their first derivatives. Spectra of FeO, Fe_3O_4, γ-Fe_2O_3 were recorded on the BL10B at KEK-PF with a Si(311) channel-cut monochromator. The others were recorded on the BL7C at KEK-PF with a Si(111) two-crystal monochromator.

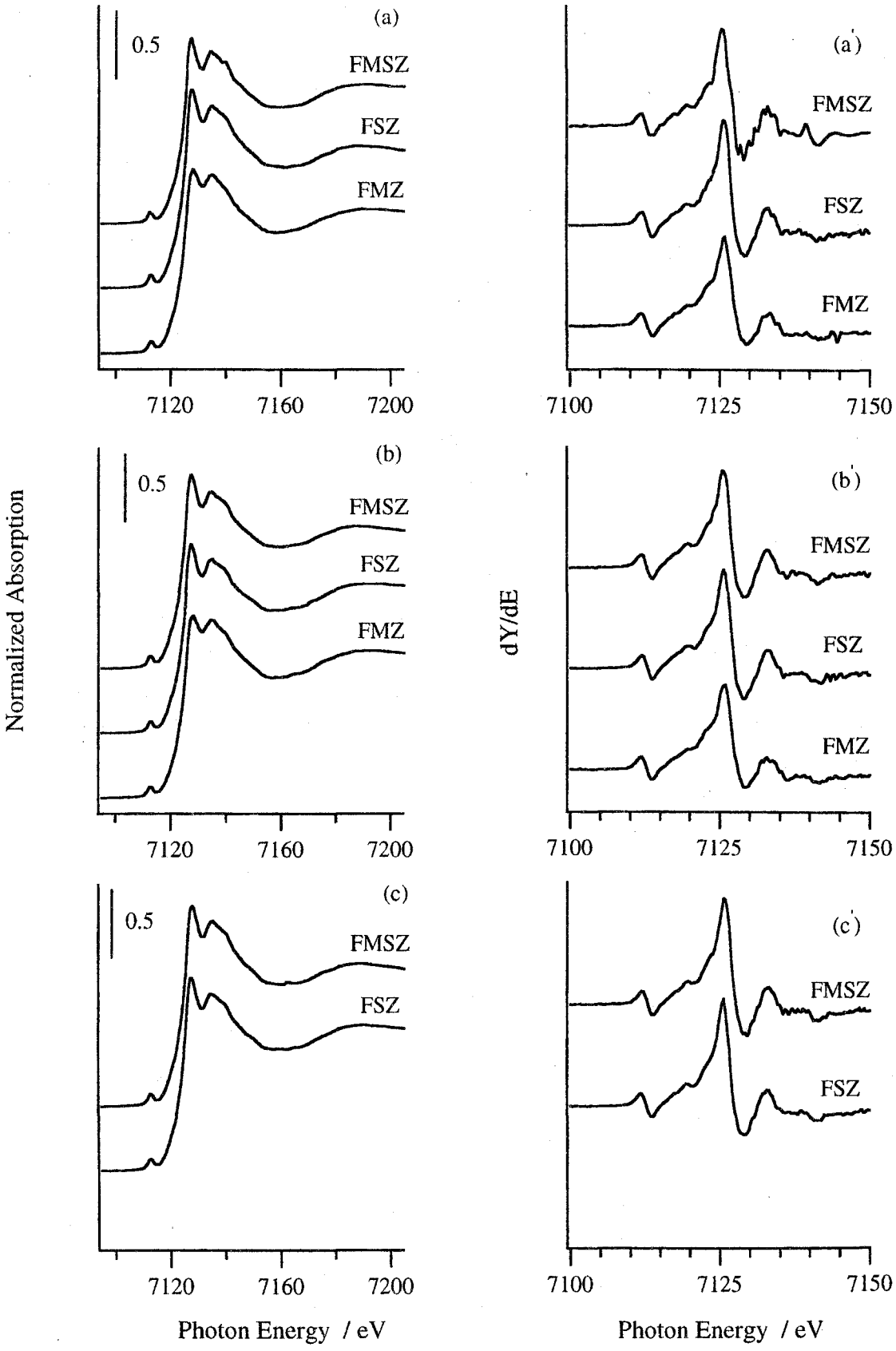

Figure 5. XANES spectra and their first derivatives of catalysts evacuated at 673 K (a), at a working state (b), and evacuated at room temperature after reaction (c).

environment had occurred on Fe species, some changes would have been observed in XANES spectra of catalyst samples.

Mn K-edge XANES

Figure 6 shows the Mn K-edge XANES spectra of reference compounds and their first derivatives. As previously reported,[27] the edge positions of manganese oxides shift to higher energy with increasing the oxidation number. The divalent compounds of MnO and $MnSO_4$ exhibit quite similar edge energies in XANES spectra.

Figure 7 shows the Mn K-edge XANES spectra and their first derivatives of catalyst samples. The edge positions of MSZ and FMSZ evacuated at 673 K indicate that Mn atoms were present as a divalent form. The shapes of these two XANES spectra are quite similar to that of $MnSO_4$. In contrast, the Mn K-edge XANES spectrum of FMZ exhibits the identical edge position of the trivalent. The shapes of its XANES spectrum and the first derivative resemble those of α-Mn_2O_3. Although they were noisy because of the low concentration of Mn species, the similarity of XANES spectra between FMZ and α-Mn_2O_3 especially support this deduction. These results indicate that Mn atoms are present as $MnSO_4$ on sulfated ZrO_2, whereas Mn atoms are present as α-Mn_2O_3 on sulfate-free ZrO_2.

At a working state, the postedge peak of the Mn K-edge XANES of FMSZ was sharpened, but the edge position did not change. After evacuation, the shape of the postedge peak had turned back to the original state. This reversible change of XANES spectra corresponds to the change of the coordination environment around Mn. It indicates that the Mn atom is present on the surface and directly makes contact with *n*-butane. A similar phenomenon was observed in XANES spectra of MSZ. No change was observed on those of FMZ.

Fe K-edge EXAFS

Figure 8 shows k^3-weighted Fe K-edge EXAFS spectra of Fe^{3+} reference compounds and their Fourier transforms in the k -range of 3 - 14 $Å^{-1}$. An EXAFS spectrum of $Fe_2(SO_4)_3$ calcined at 873 K and its Fourier transforms are identical to those of α-Fe_2O_3. Even if supported Fe species on sulfated zirconia had formed $Fe_2(SO_4)_3$, it might be decomposed in the calcination step at 873 K.

Figure 9 shows k^3-weighted Fe K-edge EXAFS spectra of the catalyst samples. EXAFS spectra of FMSZ, FSZ, and FMZ, which were pretreated, are similar to each other. All spectra of the catalyst samples are quite different from those of reference compounds. Although *S/N* ratios of EXAFS spectra are not good, we conclude that the three EXAFS spectra of the catalyst samples are identical. These results suggest that short-range structure around Fe was not affected by any additives such as manganese and/or sulfate ions. In the case of FMSZ, the three variously treated EXAFS spectra are also quite similar to each other. It clearly shows that the

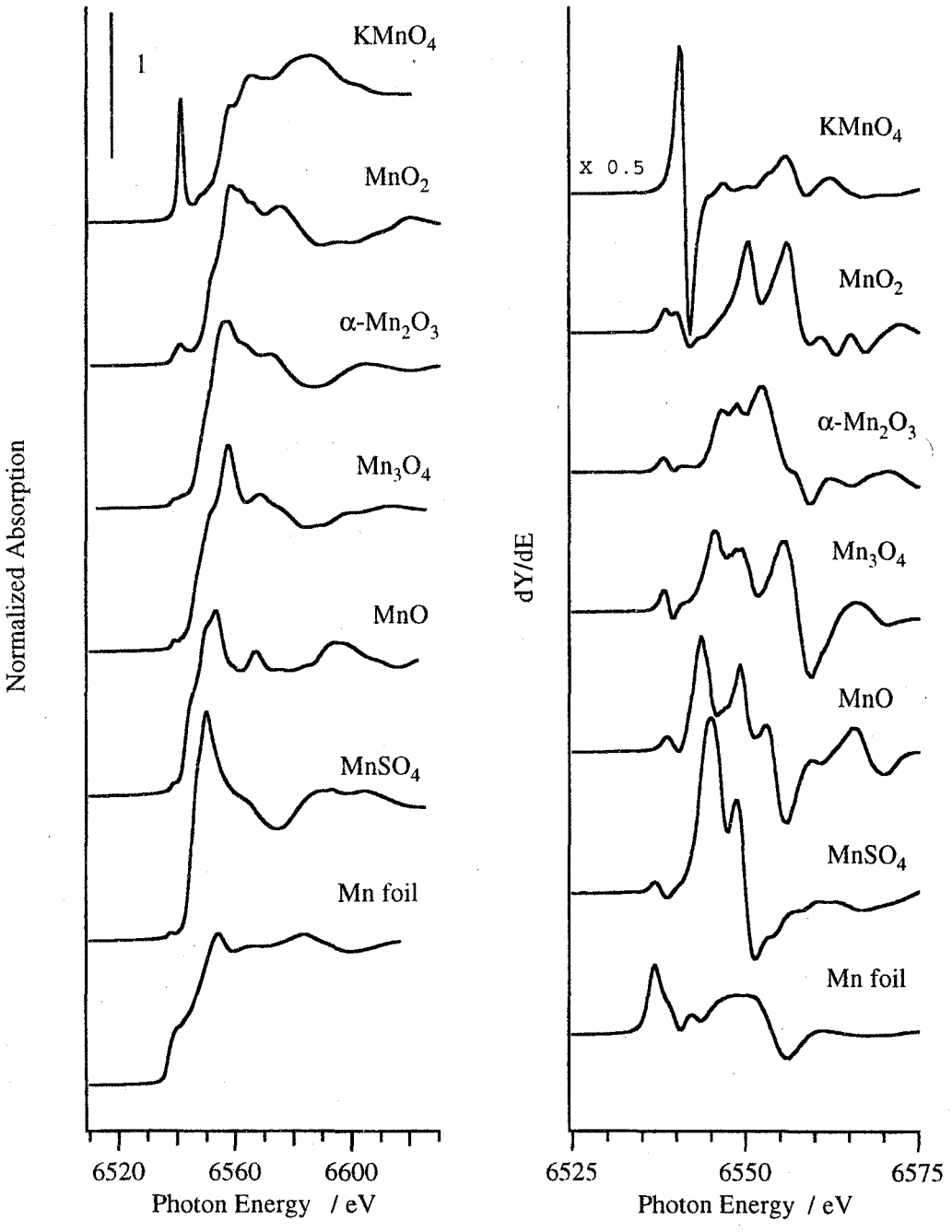

Figure 6. Mn K-edge XANES spectra and their first derivatives of reference compounds.

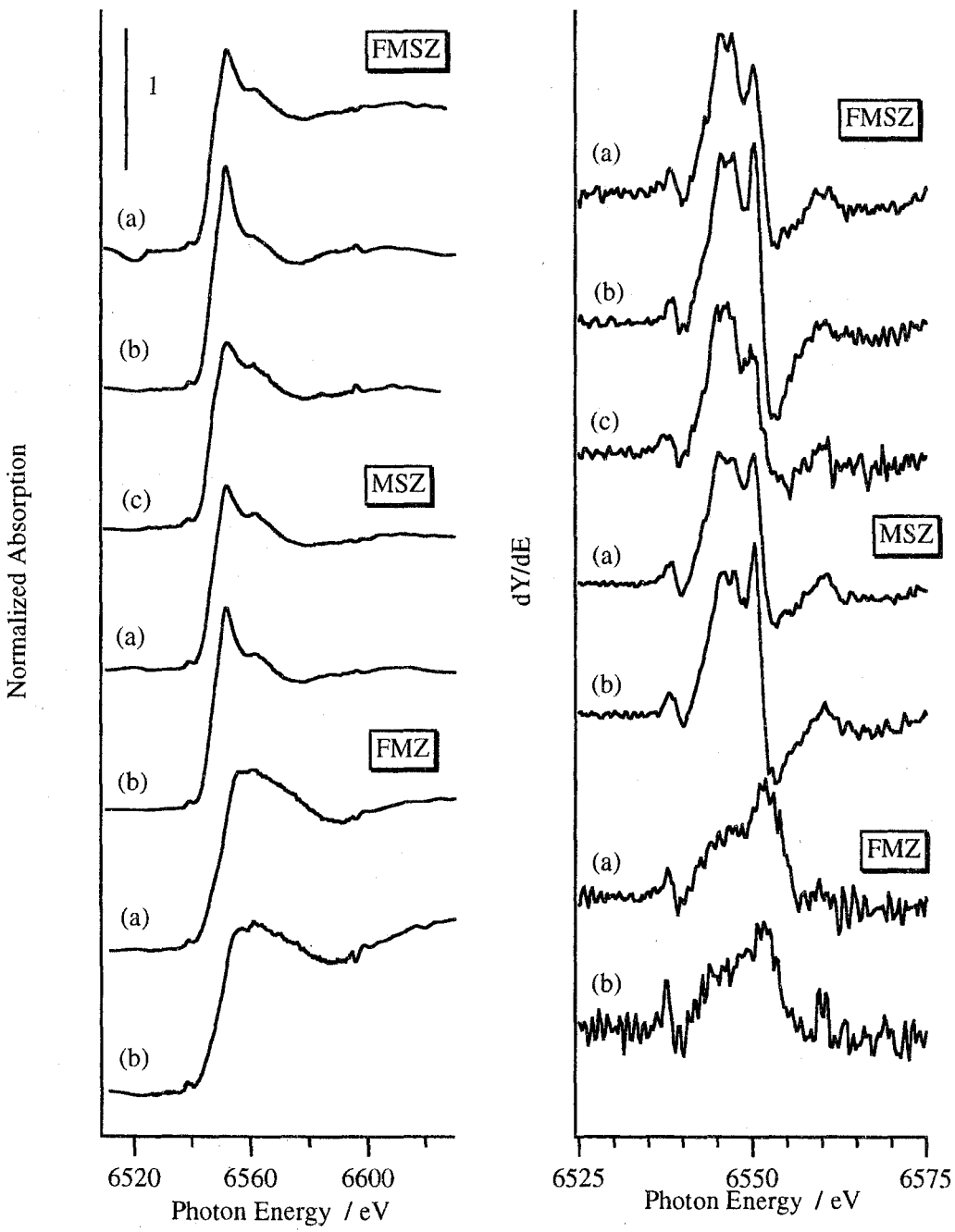

Figure 7. Mn K-edge XANES spectra and their first derivatives of catalysts: evacuated at 673 K (a), at a working state (b), and evacuated at room temperature after reaction (c).

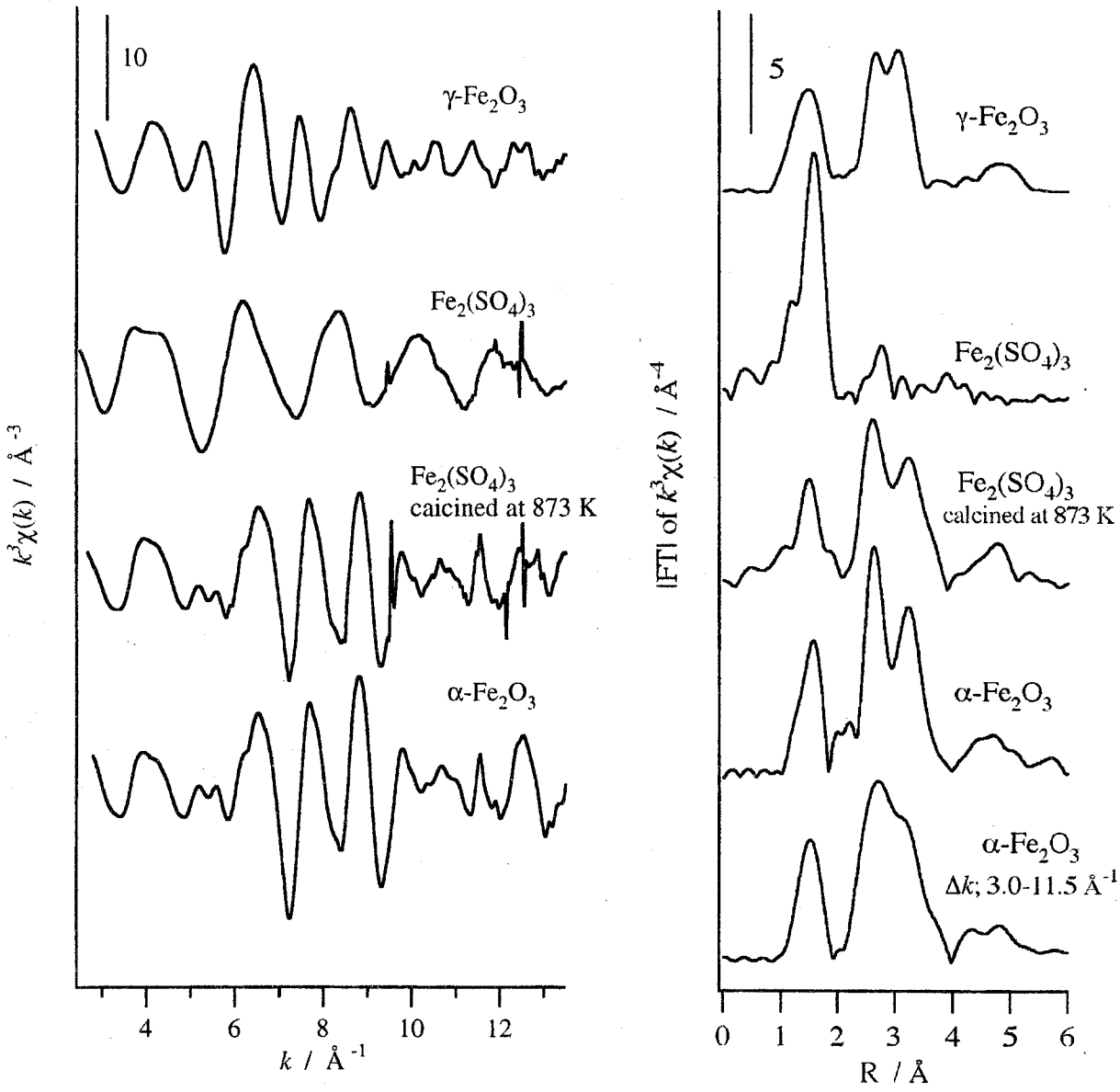

Figure 8. Fe K-edge EXAFS spectra and their Fourier transforms of reference Fe^{3+} compounds.

short-range structure of FMSZ around Fe was not affected by *n*-butane at all. The exposure to *n*-butane also did not affect on the local structure of FSZ and FMZ around Fe as well.

Figure 10 shows Fourier transforms of Fe K-edge k^3-weighted EXAFS spectra of the catalyst samples. Because the noise level of each spectrum is different, Fourier filtered ranges of EXAFS spectra are not regular. The transformed ranges of pretreated FMSZs and the other two spectra are 3 - 13 and 3 - 14 $Å^{-1}$, respectively. The ranges of all FSZs are 3 - 11.5 $Å^{-1}$. Those of pretreated FMZs and their working states are 3 - 11.5 and 3 - 10 $Å^{-1}$, respectively. In all of their radial structure functions (RSFs) except for that of FMZ at the working state, two distinct peaks appeared around 1.6 and 3.3 Å. The peak around 1.6 Å is due to oxygen scatterers. The positions of the peak around 3.3 Å is higher than those of α-Fe_2O_3 and γ-Fe_2O_3, which is due to Fe atoms. Therefore, we assigned the second peak due to scattering not from Fe but from Zr atoms. In contrast to our results, Tábora *et al.* did not observe the second peak in the RSF of FMSZ.[11] The reason for the difference between our results and their work is the data reduction of EXAFS spectra. In the case of Tábora's work, it seems that the subtracted background was not adequate, especially over $k = 7$ $Å^{-1}$. In addition, they adopted k^2-weighted EXAFS, in contrast to our k^3-weighted EXAFS spectra.

To obtain further information, we performed curve-fitting analysis. The results are summarized in Table 2. As examples, the fits of Fourier filtered Fe K-edge EXAFS for pretreated and at a working state of FMSZ are shown in Figure 11. The first coordination spheres for all the catalysts could not be fit with a single Fe-O shell, but could be fit with two shell. Only that of pretreated FMZs gave a satisfactory fit with a single shell. For the first shell of all the catalyst samples, each estimated parameter is identical within calculation errors. Their interatomic distances and coordination numbers are similar to those of α-Fe_2O_3, the coordination environment of which is 6-fold.[28] An Fe atom of α-Fe_2O_3 is surrounded by six oxygen atoms, but the interatomic distances are not uniform. The bond lengths of three Fe-O pairs are ca. 1.91 Å, and those of three more Fe-O pairs are ca. 2.06 Å.[29] The estimated EXAFS parameter strongly suggests that Fe species in all the catalyst samples are present at the center of oxygen octahedron. An estimated coordination number for the first shell of pretreated FMZ is 4.6; however, the interatomic distance is 2.02 Å. For 4-fold coordination materials, the bond length between Fe and O atoms has been reported to be 1.85 Å for Fe-MFI[26] and $FePO_4$,[30] and to be 1.89 Å for Fe/Na-SiO_2.[31] The estimated distance (2.02 Å) of the Fe-O bond in pretreated FMZ is much longer than those for 4-fold coordination. Therefore, we conclude that the Fe species on pretreated FMZ is also in 6-fold coordination. From the fact that each height of the preedge peak of the catalysts is higher than those of $Fe_2(SO_4)_3$ and α-Fe_2O_3, the FeO_6 octahedra of catalyst samples are supposed to be distorted.

The peaks around 3.3 Å observed in RSFs of samples could be assigned to scatterers from Zr atoms, as shown in Table 2. The estimated interatomic distances are almost the same as each other (3.60 ± 0.02 Å). These bond lengths are close to the Zr-Zr bonding of tetragonal ZrO_2,[32] and ZS and FMSZ.[11] In our analysis, the estimated coordination number was ranged

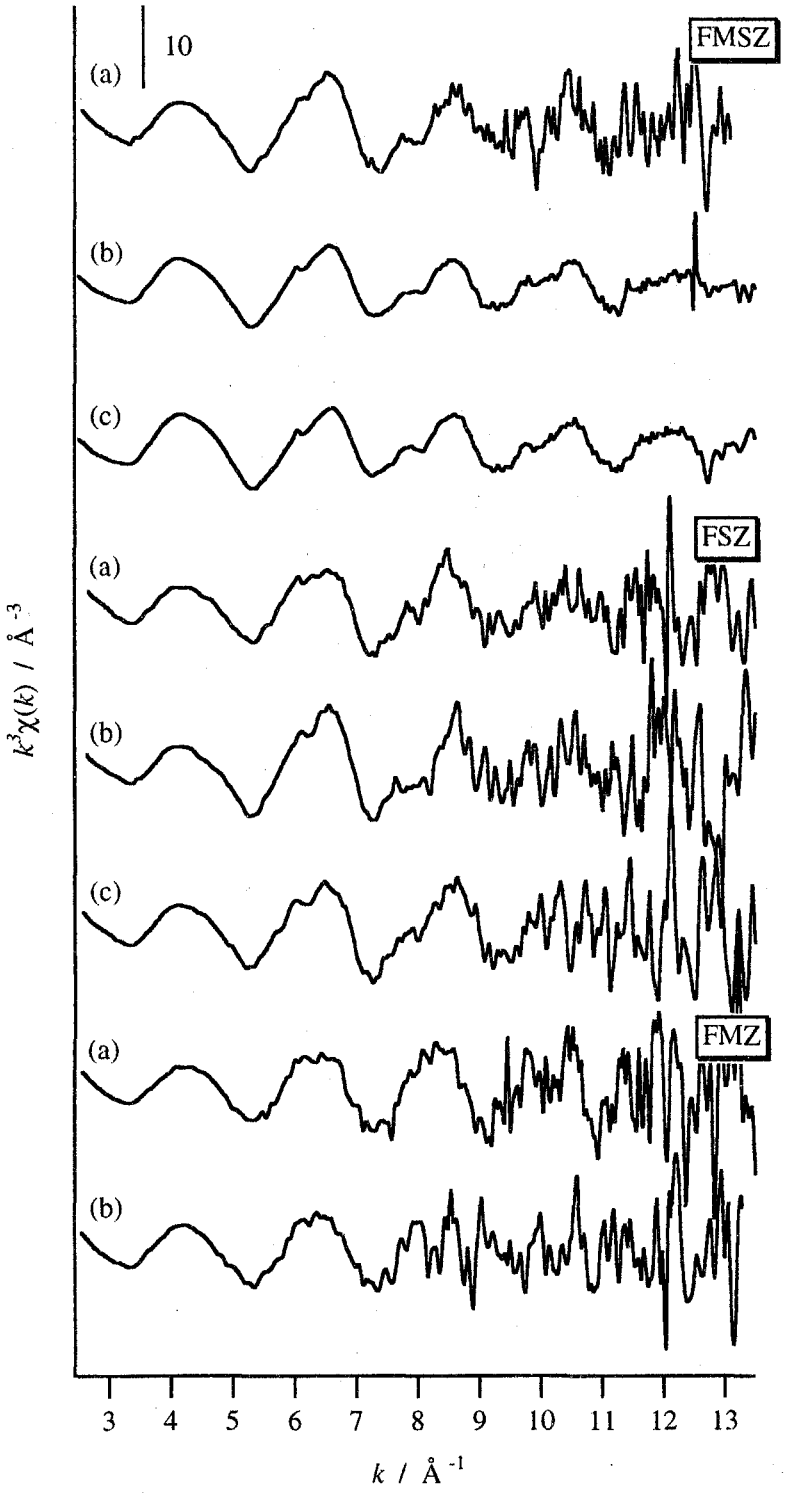

Figure 9. Fe K-edge EXAFS spectra of catalysts: evacuated at 673 K (a), at a working state (b), and evacuated at room temperature after reaction (c).

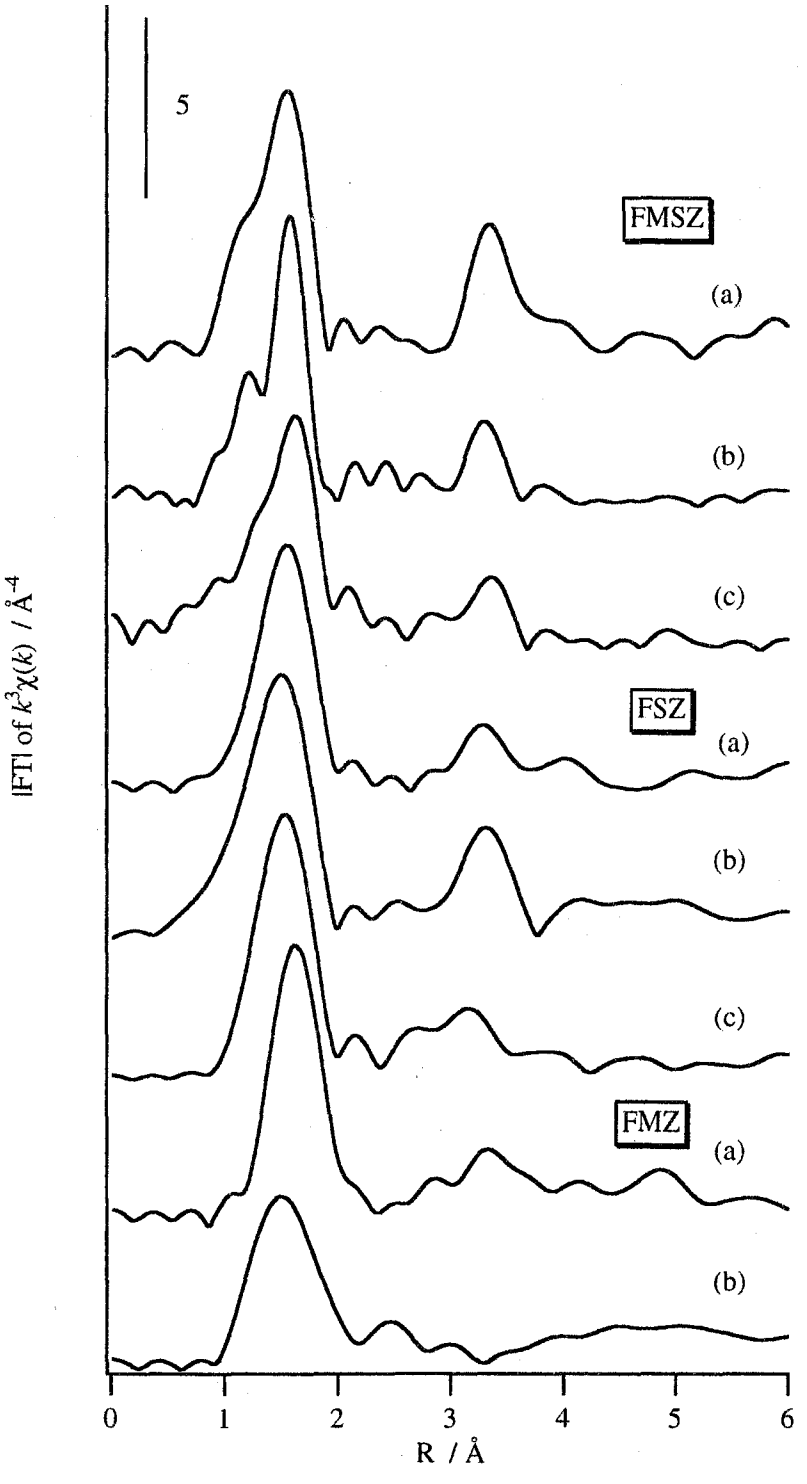

Figure 10. Fourier transforms for k^3-weighted Fe K-edge EXAFS of catalysts: evacuated at 673 K (a), at a working state (b), and evacuated at room temperature after reaction (c).

from 1.1 to 4.1. However, we recognize that the estimated coordination number is not very important. Because the noise level of the higher *k*-region of many spectra is not sufficient, the reliability of the absolute value seems not to be high. The important points are the facts that contributions from Zr were observed and that the coordination number was much smaller than 12. The reason will be discussed in the following section. A lack of the second peak in RSF of FMZ of the working state is due to the low quality of its EXAFS spectrum, not really to the lack of contribution from the second neighbors.

Discussion

Structure around Fe

XRD patterns indicate that ZrO_2 phases of all promoted catalysts are tetragonal. The phase of sulfated zirconia calcined at 873 K is reported by many researchers as tetragonal by XRD,[2,3] Raman, [13,21,22] and EXAFS characterizations.[11] In our analysis, the ZrO_2 phase of sulfate-ion-free FMZ was also tetragonal. XRD analysis suggests that iron and/or manganese atoms also affect the crystal phase of ZrO_2 to form the tetragonal metastable phase as well as sulfate ions. The similar effects were observed in WO_3-ZrO_2 and MoO_3-ZrO_2 systems.[2] According to the phase diagram for Fe-Zr-O system, Fe_2O_3 forms a solid solution with ZrO_2 when the content of Fe oxide is up to a few mol%.[33] In the case of FMSZ, an Fe fraction as Fe_2O_3 is 1.85 mol% for ZrO_2. That for FMZ is 2.08 mol%. These concentrations permit formation of a solid solution. Therefore, we conclude that Fe and Zr oxide of all the catalyst samples formed solid solution. Because the ion radius of Fe^{3+} (0.67 Å) is much smaller than that of Zr^{4+} (0.87 Å), the type of solid solution is supposed to be interstitial, not substitutional. If Fe_2O_3 and ZrO_2 formed substitutional type solid solution, Fe atom would be in 8-fold coordination and the coordination number for the Fe-Zr shell should be estimated to be 12. In fact, the Y-K edge EXAFS analysis of 3 mol% Y_2O_3-ZrO_2 revealed that the estimated coordination number for the Y-O and Y-Zr shells were 8 and 12, respectively.[32b,c] In addition, the Zr-O bond length of tetragonal ZrO_2 is 2.260 ± 0.208 Å, the coordination number of which is eight, and that for monoclinic ZrO_2 is 2.160 ± 0.085 Å, coordination number of which is seven.[32a] If the Fe atom was in 7- or 8-fold coordination, the Fe-O bond length is expected to be much longer than that of α-Fe_2O_3 of 6-fold coordination. In our analysis, however, coordination numbers for the Fe-Zr shell of all the samples were much smaller than 12, and the bond lengths for Fe-O shells were close to those for α-Fe_2O_3. These coordination numbers for Fe-Zr pairs and the bond length for Fe-O pairs support the deduction that the type of solid solution is interstitial and that Fe atoms are present inside the bulk of ZrO_2. Both sulfate and/or manganese ions, which are present on the surface of catalysts, did not affect the

TABLE 2: Results of Curve-fitting Analysis

Sample	Shell	C.N. *a*	R / Å *b*	$\Delta\sigma^2$ / Å^2 *c*
Fe, Mn-SO_4^{2-}/ZrO_2	Fe-O	3.0	1.86	-0.0048
pretreated		2.9	1.99	-0.0075
	Fe-Zr	1.5	3.62	0.0037
under reaction	Fe-O	3.0	1.85	-0.0021
		3.0	1.98	-0.0062
	Fe-Zr	1.5	3.60	0.0070
after evacuation	Fe-O	2.8	1.88	-0.0035
		2.8	2.01	-0.0064
	Fe-Zr	1.9	3.61	0.0090
Fe-SO_4^{2-}/ZrO_2	Fe-O	2.6	1.91	-0.0067
pretreated		2.6	2.03	-0.0069
	Fe-Zr	3.1	3.58	0.0127
under reaction	Fe-O	2.9	1.87	-0.0085
		2.9	2.00	-0.0090
	Fe-Zr	4.1	3.60	0.0110
after evacuation	Fe-O	2.8	1.90	-0.0081
		2.9	2.03	-0.0084
	Fe-Zr	4.3	3.53	0.0140
Fe, Mn/ZrO_2	Fe-O	4.6	2.02	-0.0037
pretreated	Fe-Zr	1.1	3.62	0.0051
under reaction	Fe-O	2.9	1.91	-0.0065
		2.9	2.07	-0.0066
	Fe-Zr	-	-	-
α-Fe_2O_3 *d*	Fe-O	3.0	1.91	0.0007
		2.9	2.04	0.0023

a Coordination number.

b Interatomic distance.

c Debye-Waller factor.

d Taken from ref. 28.

coordination environment around Fe. It is consistent with the fact that the local structure around Fe was not affected by the exposure to *n*-butane.

Formation of Solid Solution

XAFS studies of Fe-Zr-O systems have been performed by Berthet et al.[34] and Ji et al.[35] Berthet et al. prepared a cubic solid solution of $Zr_{0.70}Fe_{0.30}O_{1.85}$ by calcination of the coprecipitates of hydroxides. They observed two peaks around 1.4 and 3 Å in the RSF of the Fe K-edge EXAFS and assigned the second peak to the Fe-Zr shell. They reported that the coordination number and interatomic distance for the second shell were 4.1 and 3.29 Å, respectively. This bond length was much shorter than those of our results (3.60 Å). In their work, the molar fraction of Fe_2O_3 was 18 mol% which remarkably exceeds the limit of solid solution formation. At that fraction, a mixture of ZrO_2 solid solution and hematite solid solution will be formed, as shown in the phase diagram.[33] Therefore, the second peak they observed around 3 Å in the RSF might not be due to Zr scatterers, but to Fe scatterers.

Ji et al. prepared Fe/ZrO_2 by equilibrium adsorption of Fe ions onto ZrO_2, in which the loading amount of Fe was 0.5 wt%, followed by calcination at 773 K.[35] They observed the second peak in the RSF of Fe K-edge EXAFS around 2.6 Å and concluded that the second peak was due to Fe-Fe scatterers, the coordination number and interatomic distance of which were 1.1 and 3.11 Å, respectively.

In Ji's study, the concentration of Fe is possible to form a solid solution with ZrO_2; however, the solid solution was not formed. The difference between our result and Ji's study results from the preparation methods. For the support of Fe species, Li et al. used the ZrO_2 crystal (16 $m^2\ g^{-1}$).[36] In our study, iron was supported onto $Zr(OH)_4$ (391 $m^2\ g^{-1}$) or $SO_4^{2-}/Zr(OH)_4$. We believe that the definitive difference is whether the support was ZrO_2 or $Zr(OH)_4$. In the calcination step, $Fe/Zr(OH)_4$ or $Fe\text{-}SO_4^{2-}/Zr(OH)_4$ had transformed to Fe/ZrO_2 or $Fe\text{-}SO_4^{2-}/ZrO_2$ with formation of solid solutions. In the case of Ji's study, it seems to be difficult for Fe atoms to form a solid solution with the ZrO_2 crystal. It was supported by the results that two kinds of 7 mol% Fe_2O_3/ZrO_2 catalysts, which were prepared by the impregnation method onto the ZrO_2 crystal and the coprecipitation method, exhibit a remarkable difference in catalytic property for CO hydrogenation and reducibility of Fe atoms.[37]

Structure of Manganese Species

We have reported that the Mn atom was supported on the surface of FMSZ as $MnSO_4$.[15] From an ESR study, Scheithauer et al. concluded that Mn^{2+} atoms were supported on MSZ and FMSZ in a highly dispersed form, although their structures remained unknown.[13] In the present study, Mn K-edge XANES spectra revealed that the Mn species on MSZ and FMSZ are

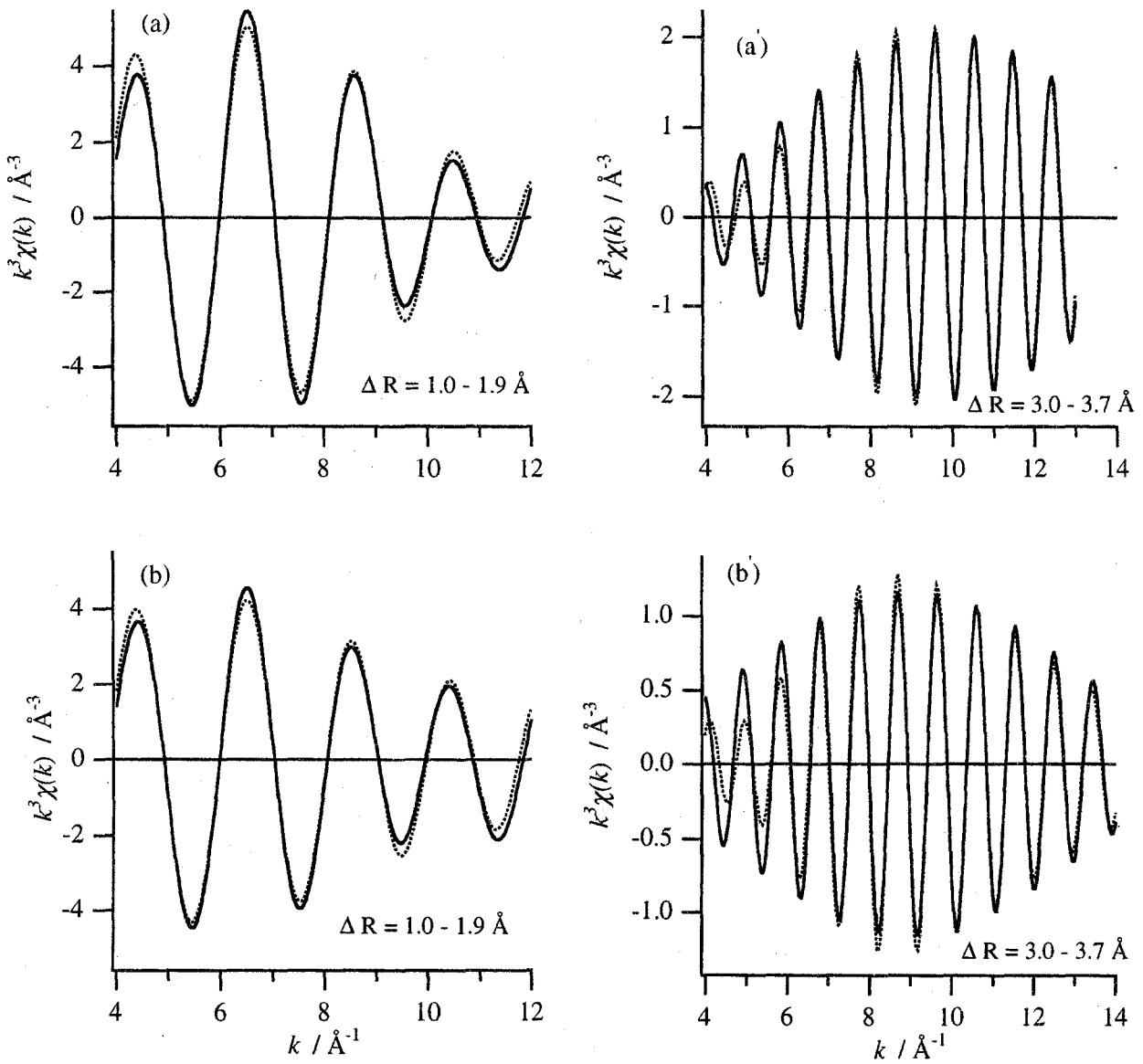

Figure 11. Fits of Fourier-filtered EXAFS of FMSZ: pretreated (a, a'); working state (b, b'). The solid curves were obtained experimentally, and the dotted ones were the fits.

present as $MnSO_4$. The calcination temperature of each sample was 873 K, which is lower than the decomposition temperature of $MnSO_4$. The decomposition temperature of $MnSO_4$ is 1123 K, while that of $Fe_2(SO_4)_3$ is 753 K.[38] Therefore, the assumption that $MnSO_4$ was present on the catalysts is adequate.

In contrast to the cases of FMSZ and MSZ, manganese species on FMZ were identified as α-Mn_2O_3. It was reported that α-Mn_2O_3 and α-Mn_3O_4 are formed by calcination of manganese salt under air at 873 and 1073 K, respectively.[23] Because the sulfate ion was free and the calcination temperature of the precursor was 873 K, α-Mn_2O_3 was formed on FMZ. In addition, MnO_2 polymorphism might be formed if the precursor of FMZ was calcined at lower than 773 K.

Role of Fe and Mn Ion

Wan et al. speculated that a high-valent iron oxy species such as the tetrahedral Fe^{4+} species have formed during calcination in air, and the site is responsible for the oxidative dehydrogenation of *n*-butane to produce butenes.[14] However, our present XANES analysis indicates that the Fe atom on each catalyst sample was invariantly trivalent. Although the reacted amounts of *n*-butane much exceeded those of Fe atoms contained in the catalyst, it is obvious that reduction of the Fe atom did not occur during reaction. Tábora stated that Fe atoms in FMSZ are not substituted isomorphously into bulk tetragonal ZrO_2 but instead are in nanometer-size oxide clusters or rafts located on the surfaces or at defects in tetragonal ZrO_2.[11] Scheithauer et al. concluded from ESR analysis that small Fe_2O_3 particles are present in FSZ and FMSZ, with some isolated Fe^{3+} ions.[13] In contrast to their opinions, we conclude that Fe^{3+} ions of FMSZ, FSZ and FMZ are present inside the bulk of tetragonal ZrO_2 to form interstitial type solid solutions, and each Fe atom is isolated from other Fe atoms. The formation of the Fe_2O_3 particle may depend on the preparation method. As discussed above, Fe atoms of all the catalyst samples are present inside the bulk phases and do not make contact with the reactant gas. It shows that the Fe atom does not directly participate in *n*-butane skeletal isomerization. Nevertheless, not only FMSZ but also FSZ exhibit quite higher activity for the isomerization than SZ. We speculate that the role of Fe ions is to influence somewhat the surface energy level of SO_4^{2-}/ZrO_2, although we do not have any evidence for it.

It is well-known that many metal sulfates exhibit solid acidity.[39,40] However, these metal sulfates merely exhibit moderate acid strength, the maximum of which are $H_0 = -3$. It is impossible to catalyze *n*-butane isomerization at around 300 K over these kinds of acid sites. This is supported by the result of catalysis that MSZ exhibited only activity similar to that of SZ. However, local structures around Mn on FMSZ and MSZ were affected by the presence of *n*-butane, as shown in XANES spectra. Therefore, it can be concluded that Mn sites on FMSZ are not active sites. Because the coordination environment around Mn was affected by the introduction of reactant gas, we propose that the role of the Mn site on Fe, Mn-SO_4^{2-}/ZrO_2

would be to accelerate transformation of reactants to active sites on SO_4^{2-}/ZrO_2. The rapid transformation of substrates results in a remarkable enhancement of the catalytic activity. The combination of two different kinds of promoters enhances remarkably the catalytic activity of SZ.

Arata et al. reported that iron oxide treated with sulfate ion exhibited solid superacidity and catalyzed *n*-butane isomerization even at 273 K.[2,41] However, in the present case of Fe, Mn-SO_4^{2-}/ZrO_2, the so-called SO_4^{2-}/Fe_2O_3 was not formed.

Conclusion

Fe oxide and Zr oxide forms interstitial-type solid solutions, regardless of the presence of sulfate and/or Mn ions. The local structures around Fe atoms in Fe, Mn-SO_4^{2-}/ZrO_2, Fe-SO_4^{2-}/ZrO_2 and Fe, Mn/ZrO_2 are quite similar to each other. Fe atoms of all the catalysts are trivalent and located at the center of oxygen octahedron. The Fe atom is present inside the bulk of ZrO2, and the local structure and the valence were not influenced by *n*-butane. Mn atoms are present as $MnSO_4$ on the surface of sulfated zirconia and as α-Mn_2O_3 on unsulfated-zirconia. Under reaction conditions, *n*-butane molecules make contact with Mn atoms and are desorbed by evacuation.

References

1 Hino, M.; Kobayashi, S.; Arata, K. *J. Am. Chem. Soc.* **1979**, *101*, 6439.

2 Arata, K. *Adv. Catal.* **1990**, *37*, 165.

3 Song, X.; Sayari, A. *Catal. Rev.-Sci. Eng.* **1996**, *38*, 329.

4 Corma, A.; Gacía, H. *Catal. Today* **1997**, *38*, 257.

5 Hsu, C.-Y.; Heimbuch, C. R.; Armes, C. T.; Gates, B. C. *J. Chem. Soc., Chem. Commun.* **1992**, 1645.

6 Tábora, J. E.; Davis, R. J. *J. Catal.* **1996**, *162*, 125.

7 Cheung, T.-K.; Gates, B. C. *Top. Catal.* **1998**, *6*, 41 and references therein.

8 Jatia, A.; Chang, C.; MacLeod, J. D.; Okubo, T.; Davis, M. E. *Catal. Lett.* **1994**, *25*, 21.

9 Adeeva, V.; de Haan, J. W.; Jänchen, J.; Lei, G. D.; Schünemann, V.; van de Ven, L. J. M.; Sachatler, W. M. H.; van Santen, A. *J. Catal.* **1995**, *151*, 364.

10 Hattori, H.; Shishido, T. *Catal. Survey Jpn.* **1997**, *1*, 205.

11 Tábora, J. E.; Davis, R. J. *J. Chem. Soc., Faraday Trans.* **1995**, *91*, 1825.

12 Milbum, D. R.; Keogh, R. A.; Sparks, D. E.; Davis, B. H. *Appl. Surf. Sci.* **1998**, *126*, 11.

13 Scheithauer, M.; Bosch, E.; Schubert, U.; Knözinger, H.; Cheung, T.-K.; Jentoft, F. C.; Gates, B. C.; Tesche, B. *J. Catal.* **1998**, *177*, 137.

14 Wan, K. T.; Knou, C. B.; Davis, M. E. *J. Catal.* **1996**, *158*, 311.

15 Yamamoto, T.; Tanaka, T.; Takenaka, S.; Yoshida, S.; Onari, T.; Takahashi, Y.; Kosaka, T.; Hasegawa, S. *J. Synchrotron Radiat.* **1999**, *6*, 425.

16 Cheung, T.-K.; d'Itri, J. L.; Gates, B. C. *J. Catal.* **1995**, *151*, 464.

17 Tanaka, T.; Yamashita, H.; Tsuchitani, R.; Funabiki, T.; Yoshida, S. *J. Chem. Soc., Faraday Trans. I* **1988**, *84*, 2987.

18 Rehr, J. J.; Mustre de Leon, J.; Zabinsky, S. I.; Albers, R. C. *J. Am. Chem. Soc.* **1991**, *113*, 5135.

19 Lange, F. C.; Cheung, T.-K.; Gates, B. C. *Catal. Lett.* **1996**, *41*, 95.

20 Mercera, P. D. L.; van Ommen, J. G.; Doesburg, E. B. M.; Burggraaf, A. J.; Ross, J. R. H. *Appl. Catal.* **1990**, *57*, 127.

21 Spielbauer, D.; Mekhemer, G. A. H.; Bosch, E.; Knözinger, H. *Catal. Lett.* **1996**, *36*, 59.

22 Li, C.; Stair, P. C. *Catal. Lett.* **1996**, *36*, 119.

23 Strohmeisr, B. R.; Herules, D. M. *J. Phys. Chem.* **1984**, *88*, 4922.

24 Bart, J. C. J. *Adv. Catal.* **1986**, *34*, 203.

25 Westre, T. E.; Kennepohl, P.; DeWitt, J. G.; Hedman, B.; Hodgson, K. O.; Solomon, E. I. *J. Am. Chem. Soc.* **1997**, *119*, 6297.

26 Bordiga, S.; Buzzoni, R.; Geobaldo, F.; Lamberti, C.; Giamello, E.; Zecchina, A.; Leofanti, G.; Petrini, G.; Tozzola, G.; Vlaic, G. *J. Catal.* **1996**, *158*, 486.

27 Brown, N. M. D.; McMonagle, J. B.; Greaves, G. N. *J. Chem. Soc., Faraday Trans. I* **1984**, *80*, 589.

28 Kanai, H.; Mizutani, H.; Tanaka, T.; Funabiki, T.; Yoshida, S.; Takano, M. *J. Mater. Chem.* **1992**, *2*, 703.

29 Wyckoff, R. W. G. *Crystal Structures,* 2nd ed.; Interscience Publishers: New York, 1986; Vol. 2, pp. 6-8.

30 Goiffon, A. *Rev. Chim. Miner.* **1986**, *23*, 99.

31 Zhang, H.; Niu, J.-Z.; Kou, Y.; Tanaka, T.; Yoshida, S. *J. Solid State Chem.* **1998**, *137*, 325.

32 (a) Li, P.; Chen, I.-W.; Penner-Hahn, J. E. *Phys. Rev. B* **1993**, *48*, 10063. (b) Li, P.; Chen, I.-W.; Penner-Hahn, J. E. *Phys. Rev. B* **1993**, *48*, 10074. (c) Li, P.; Chen, I.-W.; Penner-Hahn, J. E. *Phys. Rev. B* **1993**, *48*, 10082.

33 Jones, T. S.; Kimura, S.; Muan, A. *J. Am. Ceram. Soc.* **1967**, *50*, 137.

34 Berthet, P.; Berthon, J.; Revcolevschi, A. *Physica B* **1989**, *158*, 506.

35 Ji, W.; Kou, Y.; Shen, S.; Li, S.; Wang, H. *Proc. Int. Congr. Catal., 10th* **1993**, 2060.

36 Ji, W.; Shen, S.; Li, S.; Wang, H. *Stud. Surf. Sci. Catal.* **1991**, *63*, 517.

37 Chen, K.; Fan, Y.; Hu, Z.; Yan, Q. *Catal. Lett.* **1996**, *36*, 139.

38 Kubo, R., Nagakura, S., Iguchi, Y., Ezawa, H., Eds. *Iwanami Rikagaku-Jiten*, 4th ed.; Iwanami-Shoten: Tokyo, 1987 (in Japanese).

39 Tanabe, K. *Solid Acids and Bases;* Kodansha: Tokyo, 1970; pp 80-89.

40 Tanabe, K.; Misono, M.; Ono, Y.; Hattori, H. *New Solid Acids and Bases;* Kodansha: Tokyo, 1989; pp 185-188.

41 Hino, M.; Arata, K. *Chem. Lett.* **1979**, 1259.

Appendix

Chapter 7

XAFS Study on the Structure of Ytterbium(III) Trifluoromethanesulfonates as a New Type Catalyst

Abstract

Yb L_3-edge XAFS spectroscopy was applied to study on the local structures around Yb atoms in ytterbium(III) trifluoromethanesulfonates ($Yb(OTf)_3$) catalysts. $Yb(OTf)_3$ catalysts employed were ones dissolved in various solution and those chiral catalysts prepared by a choice of two types of achiral ligands. XAFS analyses showed the difference in the coordination number of oxygen atoms among $Yb(OTf)_3$ catalysts dissolved in aqueous and non-aqueous solutions, suggesting the activation of the $Yb(OTf)_3$ catalyst by the hydration. For the two $Yb(OTf)_3$ chiral catalysts in dichloromethane, both the catalysts were found to be present as trivalent ytterbium oligomers. Curve-fitting analysis showed that the Yb-Yb distance of the two catalyst complexes is fairly different from each other, i.e., one is 3.68 Å and the other is 4.04 Å, which is expected to explain the difference of the catalytic performance of the two chiral catalysts.

Introduction

Lewis acid-catalyzed reactions are very important in organic syntheses. In general, this type of reaction should be performed under a strict anhydrous condition, because Lewis acid catalysts are often hydrolyzed easily. On the other hand, lanthanoid(III) trifluoromethane-sulfonates ($Ln(OTf)_3$) is stable in an aqueous solution. Kobayashi found that $Ln(OTf)_3$ acts as a Lewis acid catalyst in aqueous media, which promote hydroxymethylation and aqueous aldol reactions of silyl enol ethers. In the lanthanoid series, $Yb(OTf)_3$ exhibits the highest activity.[1,2] Moreover, Kobayashi et al. found out that chiral catalysts prepared from $Yb(OTf)_3$ catalyze the enantio-selective Diels-Alder reactions of some dienophiles with cyclopentadiene. These chiral catalysts afford both enantiomer of the corresponding cyclic compounds in high enantiometric excesses by using a single chiral source and a choice of achiral ligands.[3-5] These unique properties are supposed to be related to the specific coordination number of Yb and the configuration of $Yb(OTf)_3$ in the chiral catalysts.[6] To understand the reason for the stability of the $Yb(OTf)_3$ catalyst in aqueous solution, and to clarify the effect of a choice of achiral ligands on the structure of the chiral catalysts, in the present work, we applied the X-ray absorption technique for these new type Lewis acid catalysts.

Experimental

The preparation method of $Yb(OTf)_3$ complex (catalyst) is described elsewhere.[3] The standard chiral Yb catalyst was prepared in situ from $Yb(OTf)_3$, (R)-(+)-binaphthol **1**, MS4A and cis-1,2,6-trimethylpiperidine **2**, followed by an addition of 3-acetyl-1,3-oxazolidin-2-one **3** or 3-phenylacetylacetoneton **4** in CH_2Cl_2.[3] We refer to the samples concluding the former and the latter additives as chiral catalyst A and chiral catalyst B, respectively, hereinafter. The Yb content in each catalyst was ca. 20 mmol/L. For measurements of the X-ray absorption spectrum, each the catalyst was sealed in a polyethylene bag under N_2 atmosphere.

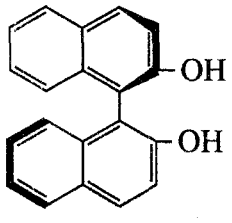

1

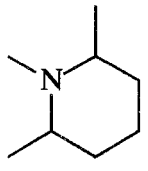

2

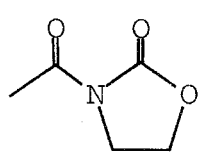

3

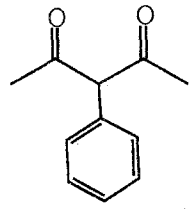

4

X-ray absorption experiments were carried out at BL-7C station at Photon Factory, Institute of Materials Structure Science, High Energy Accelerator Research Organization (KEK-PF) with a ring energy of 2.5 GeV and stored current of 250 - 350 mA. XAFS data of the samples were obtained at room temperature with a Si(111) two-crystal monochromator. Yb L_3-edge spectra of the catalyst samples and solid reference samples were measured in fluorescence and transmission modes, respectively. The curve-fitting analysis was performed for the Fourier-filtered EXAFS with the empirical parameters (the amplitudes and the phase shifts for Yb-O and Yb-Yb shells) extracted from EXAFS of c-type Yb_2O_3 by a least-squares method.

Results and Discussion

The Effect of the Kind of Solvent on the Local Structure around Yb Ions in Yb(OTf)3 Catalyst

Figure 1a shows Yb L_3-edge XANES spectra of Yb(OTf)3 solid catalyst ($Yb(OTf)_3 \cdot xH_2O$) and the Yb(OTf)3 catalysts dissolved in water, THF(tetrahydrofuran) and ethanol. Each XANES spectrum shows a similar single sharp white line at ca. 8946 eV, although white lines for Yb(OTf)3 catalysts dissolved in these solutions appear at slightly lower energy position than that of Yb(OTf)3·xH2O solid sample. Since the energy position of the white line is characteristic for Yb^{3+}, reported by some workers,[7-9] we can attribute the white line to 2p - 5d electron transitions of Yb^{3+}. This result indicates that Yb ions in the Yb(OTf)3 catalysts are trivalent states regardless of the kind of the solvent. The features of the XANES spectra for the Yb(OTf)3 catalysts in the solutions are fundamentally similar to each other, which is in contrast with the case of the YbCl3 catalyst where the catalyst reacts with water molecule to be hydrolyzed easily (Figure 1b). This result may demonstrate the stability of the Yb(OTf)3 catalyst in water. A detailed comparison of the XANES spectra lead us to notice that the intensity of the white line for the Yb(OTf)3 catalyst dissolved in water is slightly higher than those for the catalyst in non-aqueous solution such as THF or ethanol. Therefore, the kind of the solution would have a little influence on the local structure of the Yb(OTf)3 catalyst.

Figure 2 shows radial structure functions (RSFs) of Yb(OTf)3 catalysts dissolved in various solution which were obtained by Fourier-transformation on k^3-weighted Yb L_3-edge EXAFS spectra in 3.0 - 13.0 $Å^{-1}$ region. Although the pattern of RSFs of these samples is almost similar to each other, the peak around 2 Å attributed to Yb-O bond is slightly higher for the catalyst dissolved in water compared with that in non-aqueous solution. As also indicated by the curve-fitting results (Table 1), the estimated coordination number of the neighboring oxygen is larger for Yb(OTf)3 catalyst in water than that for the catalysts in non-aqueous solutions (water (10.5) > THF (9.4) > ethanol (8.8)). This relation for the coordination number probably correlates with that for the intensity of the white line appeared in XANES (water > THF > ethanol). Taking into account that the reaction rate for some aldol reactions by the

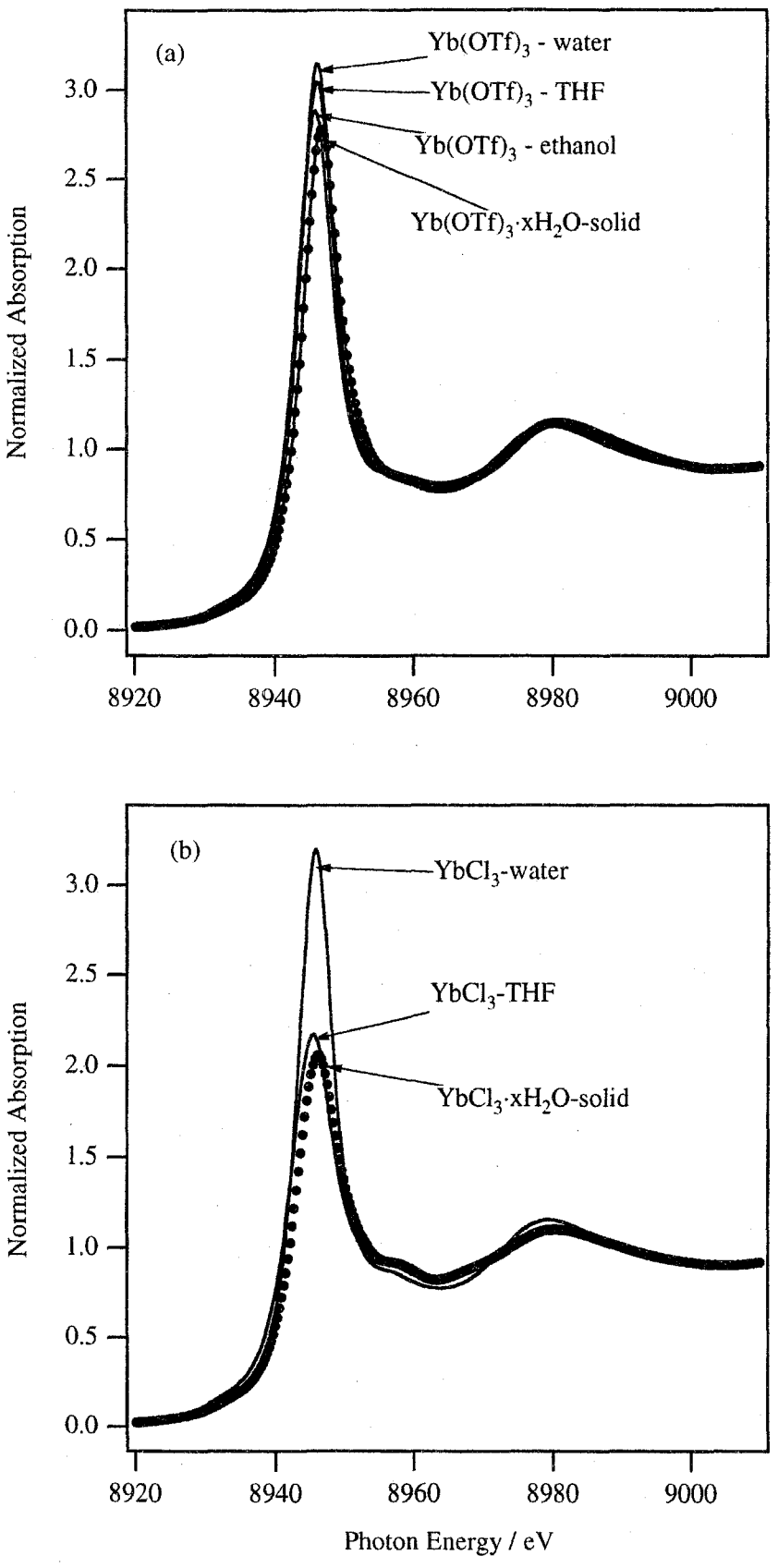

Figure 1. Yb L3-edge normalized XANES spectra of (a) Yb(OTf)3 and (b) YbCl3.

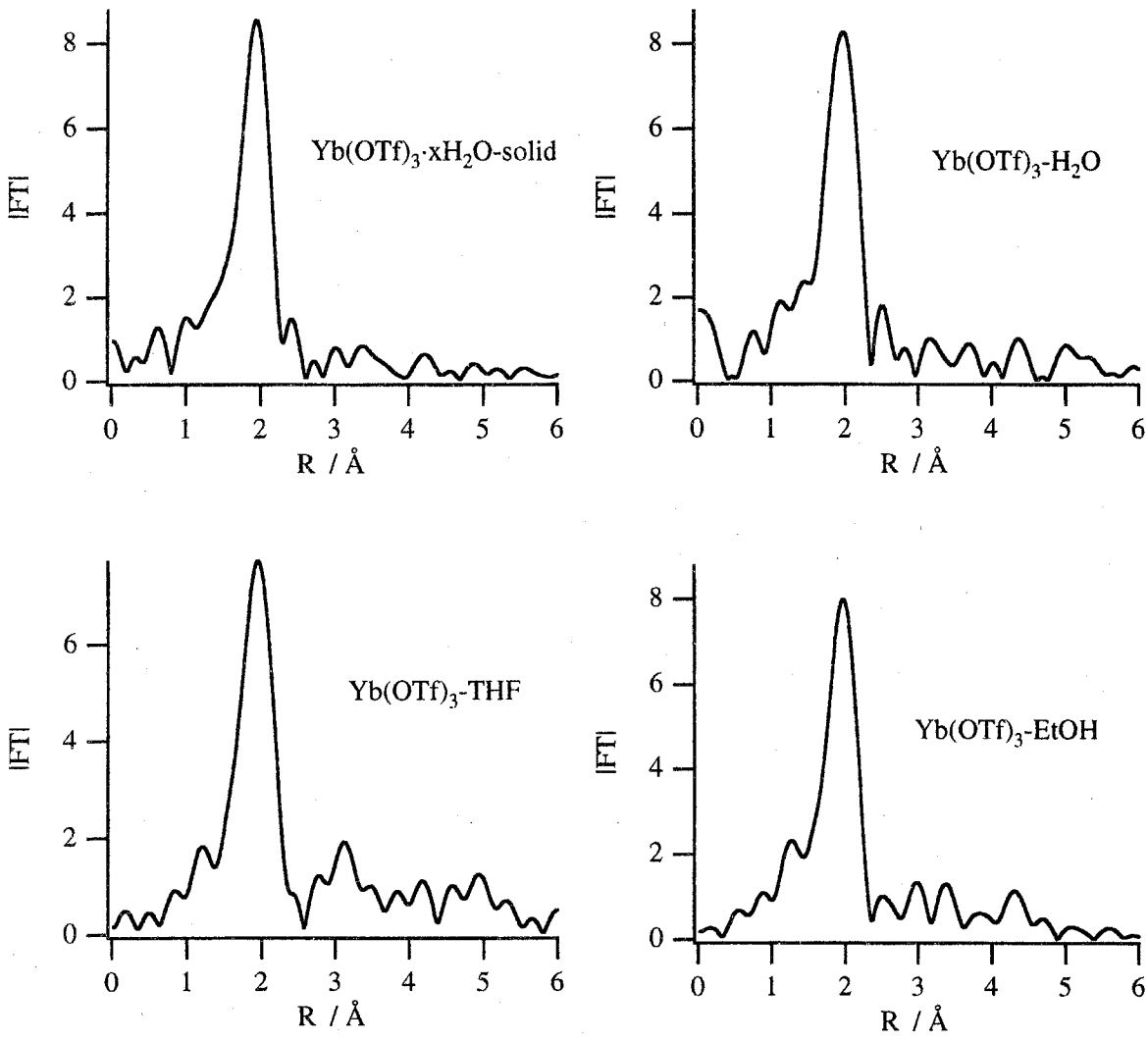

Figure 2. FT of k^3-weighted Yb L3-edge EXAFS spectra of Yb(OTf)3.

$Yb(OTf)_3$ catalyst in water is much faster than that in non-aqueous solution,[2,10] a hydration of the $Yb(OTf)_3$ catalyst (the coordination of H_2O molecules to Yb ions) may activate the catalyst.

In supplement, lanthanoid trifluoromethanesulfonate crystal $[Ln(H_2O)_9](CF_3SO_3)_3$ possesses two different kind of Ln-O distances in the coordination polyhedron.[11,12] The two inter-atomic Yb-O distances of $Yb(OTf)_3$ crystal are expected to 2.310 Å for the three pairs, and to 2.508 Å for the residual six. However, the result of curve-fitting analysis for $Yb(OTf)_3$ solid exhibited single Yb-O shell with 2.33 Å of the inter-atomic distance, which is very close to the bond length for $Yb(ClO_4)_3$ aqueous solution (2.317 Å).[13] Because XAFS spectrum measurement for $Yb(OTf)_3$ solid was performed under exposure of air, moisture might change the coordination environment to aquo complex-like structure. As a result, differences in the XANES spectra of $Yb(OTf)_3$ among solid form and each the solvents were relatively little, comparing with cases for $YbCl_3$.

TABLE 1. Results of Curve-fitting Analyses [a]

	Solvent	Shell	CN	R / Å	$\Delta\sigma^2$ [b] / Å^2
$Yb(OTf)_3$	(solid)	Yb-O	8.7	2.33	0.00079
	H_2O	Yb-O	10.5	2.33	0.00176
	THF	Yb-O	9.4	2.33	0.00147
	EtOH	Yb-O	8.8	2.34	0.00070
chiral cat. A	CH_2Cl_2	Yb-Yb	2.4	3.68	0.00011
		Yb-O	7.6	2.33	0.00147
chiral cat. B	CH_2Cl_2	Yb-Yb	3.3	4.04	0.00289
		Yb-O	9.5	2.32	0.00213
Yb_2O_3[c]	(solid)	Yb-O	6.0	2.26	0.00000
		Yb-Yb	12.0	3.69	0.00000

[a] The errors in CN(coordination number) and R (interatomic distance) are ± 10% and ± 0.02 Å, respectively.

[b] $\Delta\sigma 2$ is the difference between the Debye-Waller factors of the sample and the reference sample Yb_2O_3.

[c] Yb-O and Yb-Yb shells were extracted from EXAFS of Yb_2O_3.

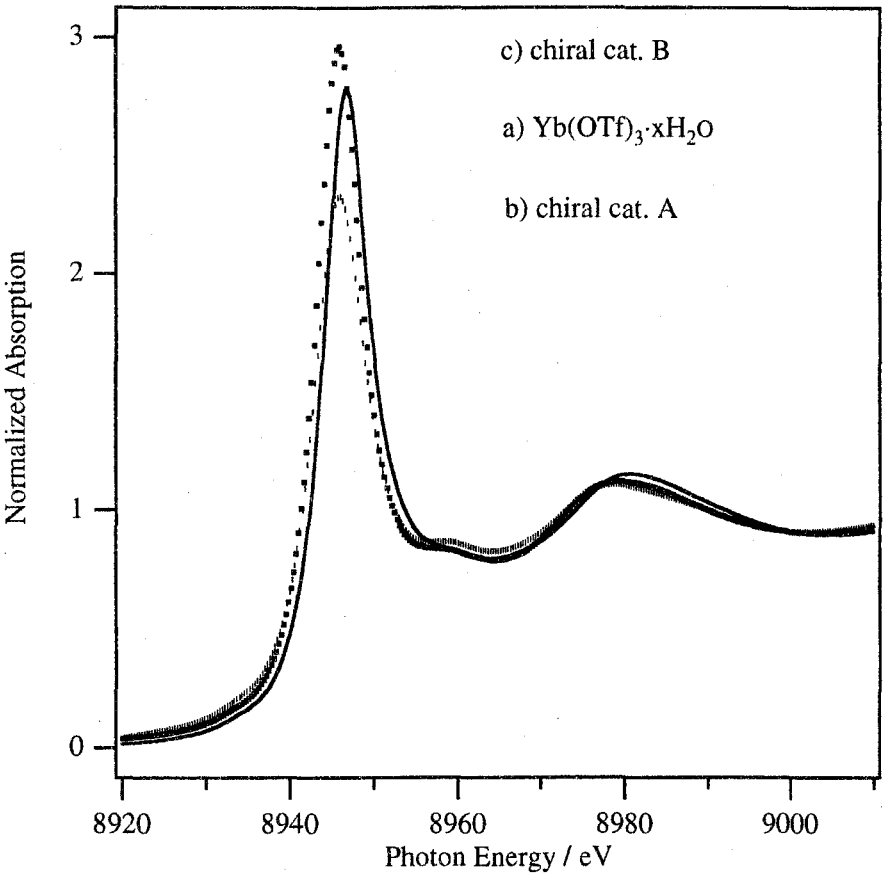

Figure 3. Yb L3-edge normalized XANES spectra of a) $Yb(OTf)_3 \cdot xH_2O$, b) chiral cat. A and c) chiral cat. B.

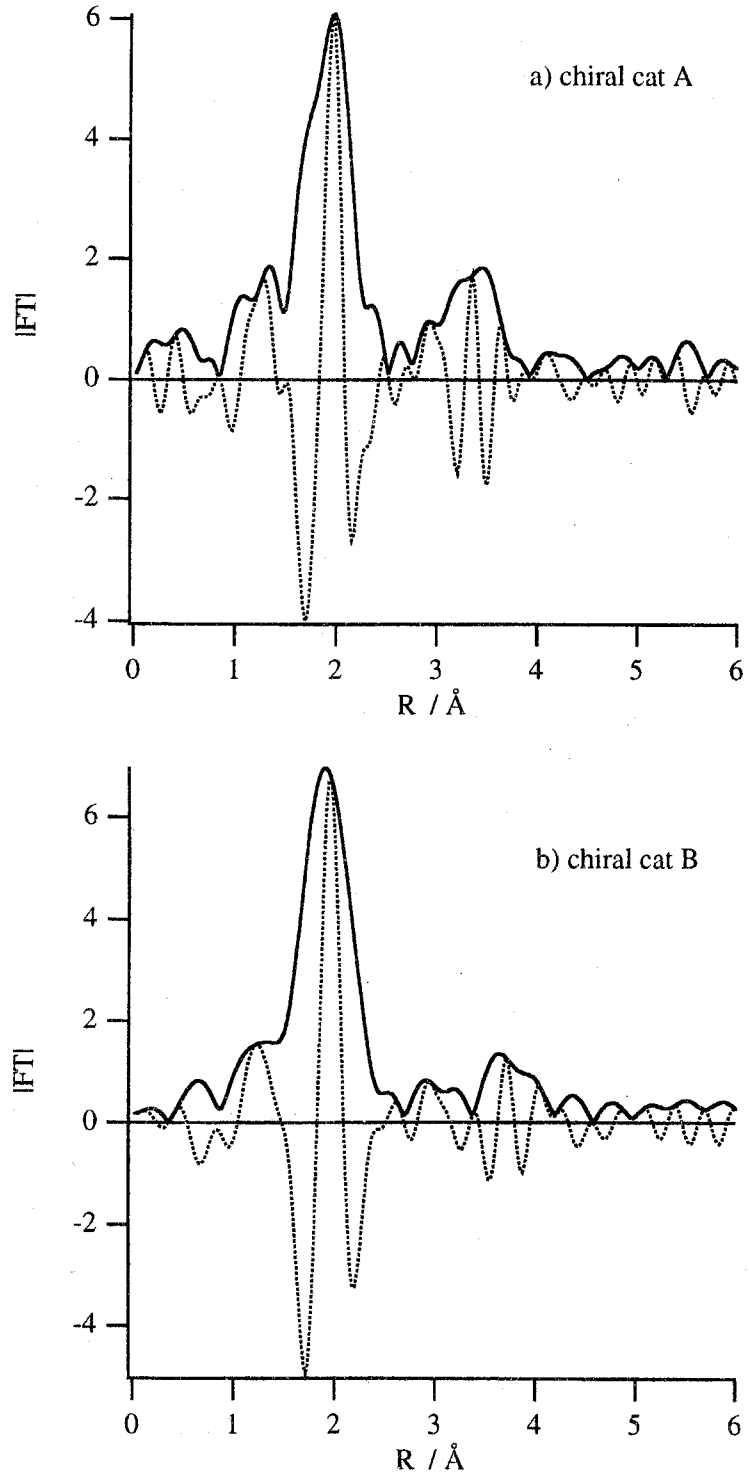

Figure 4. FT of k^3-weighted Yb L3-edge EXAFS of a) $Yb(OTf)_3 \cdot xH_2O$, b) chiral cat. A and c) chiral cat. B.

Figure 3 shows Yb L_3-edge XANES spectra of $Yb(OTf)_3$ solid catalyst, chiral catalyst A and chiral catalyst B. Each XANES spectrum showed a single sharp white line at the same energy position around 8946 eV, indicating that Yb ions in both chiral catalysts are also in a trivalent state in a similar manner as $Yb(OTf)_3$ solid catalyst. However, for the intensity of the white line, that of chiral catalyst A reduces compared with that for chiral catalyst B, suggesting that the surroundings around Yb atoms are different in these two chiral catalysts.

To elucidate the difference in the local structure around Yb atoms, k^3-weighted Yb L_3-edge EXAFS spectra of these samples were measured. The characteristics of the EXAFS spectra for the two chiral catalysts became clearer when Fourier-transformation was performed on the EXAFS in 3.0 - 13.0 $Å^{-1}$ region to obtain their RSFs. In RSFs of both chiral catalysts (Figure 4), small but distinct peaks around 3 - 4 Å can be seen. The peaks were attributed to the neighboring Yb atoms, coordination numbers of which were evaluated to be ca. 2 - 3 by the curve-fitting analyses (Table 1). These results should reflect that both Yb chiral catalysts exist as dimer or trimer complexes in dichloromethane solution. As for the difference in the local structure of these chiral catalysts, coordination numbers of neighboring oxygen (Yb-O) and ytterbium (Yb-Yb) for chiral catalyst A are estimated at slightly lower compared with those for chiral catalyst B. On the other hand, the difference in the interatomic distance of Yb-Yb, i.e., 3.68 Å for chiral catalyst A and 4.04 Å for chiral catalyst B is obvious. A choice of achiral ligands should mainly affect the distance of Yb-Yb in a chiral catalyst and control the selectivity of enantiomer of the corresponding cyclic compounds in the Diels-Alder reactions.

References

1 Kobayashi,S.; Hachiya, I.; Takahori, T.; Araki, M.; Ishitani, H. *Tetrahedron Lett.* **1992**, *33*, 6815.

2 Kobayashi, S.; Hachiya, I. *J. Org. Chem.* **1994**, *59*, 3590.

3 Kobayashi, S.; Ishitani, H. *J. Am. Chem. Soc.* **1994**, *116*, 4083.

4 Kobayashi, S.; Hachiya, I.; Ishitani, H.; Araki, M. *Tetrahedron Lett.* **1993**, *34*, 4535.

5 Kobayashi, S.; Hachiya, I.; Ishitani, H.; Araki, M. *Tetrahedron* **1994**, *50*, 11623.

6 Cotton, F. A.; Wilkinson, G. *Advanced Inorganic Chemistry*, Fifth edition, John Wiley and Sons, New York, 1988, p. 955.

7 Prabhawalkar, V.; Padalia, B. D. *Current Science* **1983**, *52*, 799.

8 Rao, R.; Sarman, D. D.; Sarode, P. R.; Sampathkumaran, E.; Guputa, L. C.; Vijayaraghavan, R. *Chem. Phys. Lett* **1980**, *76*, 413.

9 Tanaka, T.; Hanada, T.; Yoshida, S.; Baba, T.; Ono, Y. *Jpn. J. Appl. Phys., Suppl.* **1993**, *32*, 481.

10 Kobayashi, S.; Hachiya, I. *Synthesis* **1993**, 371.

11 Harrowfield, J. M.; Kepert, D. L.; Patrick, J. M.; White, A. H. *Aust. J. Chem.* **1983**, *36*, 483.

12 Santos, C. O. P.; Castellano, E. E. *Inorg. Chim. Acta* **1985**, *110*, 83.

13 Ishiguro, S.; Umebayashi, Y.; Kato, K.; Takahashi, R.; Ozutsumi, K. *J. Chem. Soc., Faraday Trans.* **1998**, *94*, 3607.

Summary

The author has investigated catalysis by new solid acid catalysts, and their chemical and physical properties. In Part I, the acidic property of siliceous FSM-16 was described. In Part II, acidic properties of silica-supported rare earth oxides were described and discussed by their detailed structural characterizations. In Part III, the characterization of iron- and manganese-promoted sulfated zirconia (Fe-Mn-SO_4^{2-}/ZrO_2) was described to clarify the role and structure of the promoters. The main results are summarized as follows.

In Chapter 1, the existence of acid sites on siliceous FSM-16 was proposed. The acidic property was characterized with acid-catalyzed reactions, a pyridine-adsorption experiment, IR spectroscopy and H_2O desorption experiment. The maximum acid strength was estimated with Hammet indicators. Siliceous FSM-16 catalyzes but-1-ene isomerization at 323 K and α-pinene isomerization at 303 K, selectivities of which indicate that both the reactions are catalyzed over acid sites. Catalytic activity varied with heat treatment, and reached a maximum at 673 K. Maximum acid strength was invariably $-5.6 < H_0 \leq -3.0$, independent of pretreatment temperatures. Both Brønsted and Lewis acid sites are confirmed on FSM-16 from IR spectra of adsorbed pyridine. Only Lewis acid sites were confirmed on FSM-16 pretreated at 1073 K, which scarcely catalyzes both the reactions. The H_2O desorption experiments and IR characterization of silanol groups gave a conclusion that the active sites on FSM-16 for olefin isomerizations are weakly perturbed silanol groups which act as Brønsted acid. When FSM-16 was pretreated at a temperature below 673 K, significant amounts of H_2O cover the active sites. If FSM-16 was pretreated higher temperature than 673 K, the active silanol groups are dehydroxylatively eliminated, resulting in a deactivation. The activity was much reduced by calcination at higher temperatures, but restored by water treatment at 353 K as long as FSM-16 retained its structure.

In Chapter 2, formation of Lewis acid sites was confirmed on FSM-16 by high-temperature treatment. The Lewis acid sites on FSM-16 were characterized with pyridine-TPD experiments and a Lewis-acid catalyzed reaction of methylamine synthesis. The structural stability of FSM-16 and/or the transformation upon thermal treatment were investigated with IR and nitrogen adsorption-desorption experiments. The pyridine TPD characterization revealed that new acid sites form on FSM-16 with increasing pretreatment temperatures. It was shown that the temperature of pyridine-adsorption process remarkably influences the desorption profiles. IR characterization demonstrated that surface silanol groups on FSM-16 was dehydroxylatively condensed to form highly strained siloxane bridges, which act as Lewis acids. The Lewis acid sites formed on FSM-16 catalyze methylamine synthesis, and the initial rates is enhanced with increasing pretreatment temperatures up to 1273 K. The structure of

FSM-16 completely retained throughout a pretreatment at 1273 K as well as a reaction for methylamine synthesis at 673 K.

Acidic property of siliceous mesoporous silica described in Part I was discovered by the author. Both Lewis and Brønsted acid sites on FSM-16 exhibit mild acid strength of $-5.6 < H_0 \leq -3.0$. When FSM-16 was pretreated at 673 K, activity of Brønsted acid-catalyzed reactions were exhibited the highest. On the other hand, the activity of Lewis acid-catalyzed reactions were enhanced at higher pretreatment temperature than 873 K. The regularly ordered mesopore of FSM-16 with medium acid strength opens the possibility that FSM-16 is promising for the application to synthetic processes of fine-chemicals.

Chapter 3 dealt with silica-supported ytterbium oxide catalysts (Yb/SiO_2), loading amounts of which ranged from 25 μmol - 8.4 mmol $g(SiO_2)^{-1}$. Various loading amounts of ytterbium oxides supported on silica catalyzed α-pinene isomerization at 323 K. The main products were limonene and camphene, the selctivities to which were 67 and 20%, respectively. The catalytic activity depended on a loading amount and pretreatment temperature, and reached the highest when the loading amount and pretreatment temperature were 3.4 mmol $g(SiO_2)^{-1}$ and 1073 K, respectively. On the other hand, the selectivity was independent of the loading amount and pretreatment temperature. Structural characterizations revealed that each ytterbium atom is widely spread over silica as a YbO_6 octahedron which connects with SiO_4 tetrahedra with forming Yb-O-Si linkage. The acid strength and catalytic activity per one active site are independent on loading amount. When loading amount of Yb exceeded the amount where YbO_6 unit can form monolayer on SiO_2, the apparent turn over frequency decreased.

In Chapter 4, local structure around Yb on Yb/SiO_2 catalysts was analyzed by X-ray absorption spectroscopy, in comparison with four kinds of crystalline ytterbium oxides. XANES and EXAFS spectra of all the Yb/SiO_2 catalysts were identical to each other, regardless of the loading amount and various procedures of treatment. It was concluded that amorphous Yb-O-Si species of the active sites had formed in a sample preparation step. The first coordination sphere around Yb was quite similar to those for Yb_2O_3 and all the Yb/SiO_2 catalysts. On the other hand, the second derivatives of Yb-L_{III} edge XANES spectra for all the Yb/SiO_2 showed that the XANES is comprised of a single peak, while that for Yb_2O_3 is double peaks. Referring to the XANES spectra of $YbNbO_4$, $YbPO_4$ and $Yb_3Al_5O_{12}$, the coordination environment around Yb species on SiO_2 was supposed to be highly symmetric.

Chapter 5 dealt with various kinds of rare earth elements (Ln/SiO_2; Ln = La, Ce, Pr, Sm, Eu, Tb, Yb and Y) to elucidate a general feature of rare earth supported on silica. The loading amount of each catalyst was adjusted to be 3.4 mmol Ln g(support)$^{-1}$. The reason for decrease of catalytic activity of Yb/SiO_2, resulting from excess loading and high temperature-treatment, was clarified by Raman spectroscopy. In the series of lanthanide, the activity for α-pinene isomerization increases monotonously with the atomic number from ^{57}La through ^{70}Yb, except ^{58}Ce. Although the catalytic activity over each Ln/SiO_2 catalyst was significantly

varied with the lanthanide elements, the selectivity of each the catalyst was almost the same. Although cerium was present as crystallites on silica, the other rare earth elements were supported on silica in an amorphous state. From XAFS characterizations, it was concluded that the acidity of Ln-O-Si linkage is independent of the lanthanide species, and only the number of Ln-O-Si species affects the activity. The affinity of LnO_n unit to SiO_4 tetrahedra depends on the size of Ln^{3+}, and influenced the number of Ln-O-Si linkages. Y/SiO_2 catalyst, (the ion radius of Y^{3+} is similar to that of Yb^{3+}), exhibited the same activity and EXAFS spectrum as Yb/SiO_2 catalyst. In the Raman spectrum of 3.4 mmol Yb/SiO_2 catalyst pretreated below 1073 K, no bands other than the typical ones to amorphous SiO_2 were detected, whereas many bands were observed on that pretreated at 1273 K. In a case of 8.4 mmol Yb/SiO_2 catalyst, a weak band assigned to Yb_2O_3 crystal was confirmed, in addition to that for silica gel. Excess Yb atoms loaded on SiO_2 block the active Yb-O-Si linkage by forming inactive Yb_2O_3 fine crystallites. The thermal treatment of Yb/SiO_2 catalyst at 1273 K changes the active amorphous Yb-O-Si structure to inactive ytterbium silicate crystallite.

Followings are conclusions of Part II. Each rare earth element is easily spread on SiO_2 to form amorphous Ln-O-Si and/or Ln-O-Ln linkages. The maximum acid strengths and the structure of active sites were independent of the kind of rare earth elements. The differences in catalytic activity among the elements are due to the ion radii of Ln^{3+}, which relates to the number of Ln-O-Si units on the surface of each catalyst. The geometry and electric configuration of each supported rare earth oxide are quite different from that of the rare earth oxide crystal itself.

In Chapter 6, *in situ* XAFS, XRD and Raman techniques were applied to the characterization of $Fe\text{-}Mn\text{-}SO_4^{2-}/ZrO_2$, $Fe\text{-}SO_4^{2-}/ZrO_2$, $Mn\text{-}SO_4^{2-}/ZrO_2$, $Fe\text{-}Mn/ZrO_2$ and ZrO_2 catalyst samples. The *in situ* XANES spectra at Fe-K edge of $Fe\text{-}Mn\text{-}SO_4^{2-}/ZrO_2$ did not change throughout *n*-butane isomerization, while those at Mn-K edge were reversibly affected by introduction of reaction gas. According to the XRD and Raman results, it was concluded that Fe^{3+} ions in $Fe\text{-}Mn\text{-}SO_4^{2-}/ZrO_2$ are present inside the ZrO_2 as an interstitial ions and the ions do not directly participate in the super acidic reaction. The redox of iron ions in the catalyst, which has been speculated by other research groups, does not take place throughout the reaction. Even in the absence of sulfate and/or manganese ions, iron and zirconium oxide form interstitial-type solid solution as well, and the local structure around iron is quite similar to each other and to $Fe\text{-}Mn\text{-}SO_4^{2-}/ZrO_2$. Mn ions are present on the surface as $MnSO_4$, and are the sites of adsorption of reactant gas molecules. Without sulfate ions, manganese species is present as Mn_2O_3.

List of Publications

Part I

Chapter 1.

1 Acidic Property of FSM-16
Takashi Yamamoto, Tsunehiro Tanaka, Takuzo Funabiki, Satohiro Yoshida
The Journal of Physical Chemistry B, **1998**, *102*, 5830-5839.

Chapter 2.

2 Acidic Property of FSM-16 (2): Generation of Lewis Acid Sites and Catalysis
Takashi Yamamoto, Tsunehiro Tanaka, Shinji Inagaki, Takuzo Funabiki, Satohiro Yoshida
The Journal of Physical Chemistry B, **1999**, *103*, 6450-6456.

Part II

Chapter 3.

3 Silica-Supported Ytterbium Oxide Characterized by Spectroscopic Methods and Acid-Catalyzed Reactions
Takashi Yamamoto, Takahiro Matsuyama, Tsunehiro Tanaka, Takuzo Funabiki, Satohiro Yoshida
Journal of Molecular Catalysis A, **1999**, in press.

Chapter 4.

4 XAFS Study of the Structure of Silica-Supported Ytterbium Oxide Catalyst
Takashi Yamamoto, Tsunehiro Tanaka, Takahiro Matsuyama, Takuzo Funabiki, Satohiro Yoshida
Solid State Communications, **1999**, *111*, 137-142.

Chapter 5.

5 Generation of Acid Sites on Silica-Supported Rare Earth Oxide Catalysts: Structural Characterization and Catalysis for α-Pinene Isomerization
Takashi Yamamoto, Takahiro Matsuyama, Tsunehiro Tanaka, Takuzo Funabiki, Satohiro Yoshida
Physical Chemistry Chemical Physics, **1999**, *1*, 2841-2849.

Part III

Chapter 6.

6 XAFS Study of Fe- and Mn- Promoted Sulfated Zirconia
Takashi Yamamoto, Tsunehiro Tanaka, Sakae Takenaka, Satohiro Yoshida, Tsutomu Onari, Yoshiaki Takahashi, Tomomi Kosaka, Sadao Hasegawa
Journal of Synchrotron Radiation, **1999**, *6*, 425-427.

7 Structural Analysis of Iron and Manganese Species in Iron- and Manganese- Promoted Sulfated Zirconia
Takashi Yamamoto, Tsunehiro Tanaka, Sakae Takenaka, Satohiro Yoshida, Tsutomu Onari, Yoshiaki Takahashi, Tomomi Kosaka, Sadao Hasegawa, Masataka Kudo
The Journal of Physical Chemistry B, **1999**, *103*, 2385-2393.

Appendix

Chapter 7.

8 XAFS Study of Ytterbium Complexes as New Type Lewis Acid Catalysts
Tomoko Yoshida, Tsunehiro Tanaka, Takashi Yamamoto, Satohiro Yoshida, Haruro Ishitani, Shu Kobayashi
Journal of Synchrotron Radiation, **1999**, 6, 455-457.

9 XAFS Study on the Structure of Ytterbium(III) Trifluoromethanesulfonates as a New Type Catalyst
Tomoko Yoshida, Tsunehiro Tanaka, Takashi Yamamoto, Satohiro Yoshida, Haruro Ishitani, Shu Kobayashi
Japanese Journal of Applied Physics, **1999**, *Suppl. 38-1*, 59-61.

The following papers are not included in this thesis.

10 Ship-in-Bottle Synthesis of $[Pt_{15}(CO)_{30}]^{2-}$ Encapsulated in Ordered Hexagonal Mesoporous Channels of FSM-16 and Their Effective Catalysis in Water-Gas Shift Reaction
Takashi Yamamoto, Takafumi Shido, Shinji Inagaki, Yoshiaki Fukushima, Masaru Ichikawa
Journal of the American Chemical Society, **1996**, *118*, 5810-5811.

11 Ship-in-Bottle Synthesis of Pt and Ru Carbonyl Clusters in NaY Zeolite Micropore and Ordered Mesoporous Channels of FSM-16; XAFS/FTIR/TPD Characterization and Their Catalytic Behaviors
Masaru Ichikawa, Takashi Yamamoto, Wei Pan, Takafumi Shido
Studies in Surface Science and Catalysis, **1997**, *105*, 679-686.

12 XAFS Characterization of Platinum Carbonyl Clusters Synthesized in the Channel of Mesoporous Zeolite
Takafumi Shido, Takashi Yamamoto, Masafumi Harada, Masaru Ichikawa
Journal de Physique IV, **1997**, *7*, C2-855-857.

13 A Robust Platinum Carbonyl Cluster Anion $[Pt_3(CO)_6]_5^{2-}$ Encapsulated in an Ordered Mesoporous Channel of FSM-16: FTIR/EXAFS/TEM Characterization and Catalytic Performance in the Hydrogenation of Ethene and 1, 3-Butadiene
Takashi Yamamoto, Takafumi Shido, Shinji Inagaki, Yoshiaki Fukushima, Masaru Ichikawa
The Journal of Physical Chemistry B, **1998**, *102*, 3866-3875.

14 Performance of the YB_{66} Soft-X-ray Monochromator Crystal at the Wiggler Beamline of the UVSOR Facility
Toyohiko Kinoshita, Yasutaka Takata, Tokuo Matsukawa, Hirofumi Aritani, Shigehiro Matsuo, Takashi Yamamoto, Masao Takahashi, Hisao Yoshida, Tomoko Yoshida, Yüksel Ufktepe, Krishna G. Nath, Shin-ichi Kimura, Yoshinori Kitajima
Journal of Synchrotron Radiation, **1998**, *5*, 726-728.

15 Templating Fabrication of Platinum Nanoparticles and Nanowires Using the Confined Mesoporous Channels of FSM-16 - Their Structural Characterization and Catalytic Performances in Water Gas Shift Reaction
Makoto Sasaki, Mai Osada, Naonori Higashimoto, Takashi Yamamoto, Atsushi Fukuoka, Masaru Ichikawa
Journal of Molecular Catalysis A, **1999**, *141*, 223-240.

16 The XAFS Beamline BL01B1 at SPring-8
Tomoya Uruga, Hajime Tanida, Yasuhiro Yoneda, Kunikazu Takeshita, Shuichi Emura, Masao Takahashi, Makoto Harada, Yasuo Nishihata, Yoshihiro Kubozono, Tsunehiro Tanaka, Takashi Yamamoto, Hironobu Maeda, Osamu Kamishima, Yasuhiro Takabayashi, Yoshiyuki Nakata, Hidekazu Kimura, Shunji Goto, Tetsuya Ishikawa
Journal of Synchrotron Radiation, **1999**, *6*, 143-145.

17 Application of XANES Spectra to Supported Catalysts
Tsunehiro Tanaka, Takashi Yamamoto, Yoshiumi Kohno, Tomoko Yoshida, Satohiro Yoshida
Japanese Journal of Applied Physics, **1999**, *Suppl. 38-1*, 30-35.

Reviews

1 Present Status of SPring-8 (Japanese)
Tsunehiro Tanaka, Takashi Yamamoto
Shokubai, **1998**, *40*, 318-323.